NEW PIEZOELECTRIC MATERIALS AND DEVICES: FABRICATION, STRUCTURES, AND APPLICATIONS

EDITED BY: Chunlong Fei, Jianguo Ma, Lin Zhang, Yang Yang and Zeyu Chen
PUBLISHED IN: Frontiers in Materials

frontiers Research Topics

ISSN 1664-8714
ISBN 978-2-88974-394-0
DOI 10.3389/978-2-88974-394-0

About Frontiers

Frontiers is more than just an open-access publisher of scholarly articles: it is a pioneering approach to the world of academia, radically improving the way scholarly research is managed. The grand vision of Frontiers is a world where all people have an equal opportunity to seek, share and generate knowledge. Frontiers provides immediate and permanent online open access to all its publications, but this alone is not enough to realize our grand goals.

Frontiers Journal Series

The Frontiers Journal Series is a multi-tier and interdisciplinary set of open-access, online journals, promising a paradigm shift from the current review, selection and dissemination processes in academic publishing. All Frontiers journals are driven by researchers for researchers; therefore, they constitute a service to the scholarly community. At the same time, the Frontiers Journal Series operates on a revolutionary invention, the tiered publishing system, initially addressing specific communities of scholars, and gradually climbing up to broader public understanding, thus serving the interests of the lay society, too.

Dedication to Quality

Each Frontiers article is a landmark of the highest quality, thanks to genuinely collaborative interactions between authors and review editors, who include some of the world's best academicians. Research must be certified by peers before entering a stream of knowledge that may eventually reach the public - and shape society; therefore, Frontiers only applies the most rigorous and unbiased reviews.
Frontiers revolutionizes research publishing by freely delivering the most outstanding research, evaluated with no bias from both the academic and social point of view. By applying the most advanced information technologies, Frontiers is catapulting scholarly publishing into a new generation.

What are Frontiers Research Topics?

Frontiers Research Topics are very popular trademarks of the Frontiers Journals Series: they are collections of at least ten articles, all centered on a particular subject. With their unique mix of varied contributions from Original Research to Review Articles, Frontiers Research Topics unify the most influential researchers, the latest key findings and historical advances in a hot research area! Find out more on how to host your own Frontiers Research Topic or contribute to one as an author by contacting the Frontiers Editorial Office: frontiersin.org/about/contact

NEW PIEZOELECTRIC MATERIALS AND DEVICES: FABRICATION, STRUCTURES, AND APPLICATIONS

Topic Editors:
Chunlong Fei, Xidian University, China
Jianguo Ma, Beihang University, China
Lin Zhang, Media Lab, Massachusetts Institute of Technology, United States
Yang Yang, San Diego State University, United States
Zeyu Chen, Central South University, China

Citation: Fei, C., Ma, J., Zhang, L., Yang, Y., Chen, Z., eds. (2022). New Piezoelectric Materials and Devices: Fabrication, Structures, and Applications. Lausanne: Frontiers Media SA. doi: 10.3389/978-2-88974-394-0

Table of Contents

frontiers in Materials

EDITORIAL
published: 05 January 2022
doi: 10.3389/fmats.2021.824345

Editorial: New Piezoelectric Materials and Devices: Fabrication, Structures, and Applications

Chunlong Fei[1]*, *Lin Zhang*[2], *Zeyu Chen*[3], *Yang Yang*[4] and *Jianguo Ma*[5]

[1]School of Microelectronics, Xidian University, Xi'an, China, [2]Media Lab, Massachusetts Institute of Technology (MIT), Cambridge, MA, United States, [3]College of Mechanical and Electrical Engineering, Central South University, Changsha, China, [4]Department of Mechanical Engineering, San Diego State University, San Diego, CA, United States, [5]School of Instrumentation and Optoelectronic Engineering, Beihang University, Beijing, China

Keywords: piezoelectric materials (PMs), piezoelectric devices (PZDs), fabrication, structures, applications, performance simulation

Editorial on the Research Topic

New Piezoelectric Materials and Devices: Fabrication, Structures, and Applications

INTRODUCTION

Piezoelectric materials and devices are fundamental to industrial and scientific applications such as non-destructive testing, acoustic tweezers, medical imaging, and ultrasound therapy. Typical piezoelectric materials include bulk ceramics, thin films, single crystals, polymers, composites, etc., which are used for a variety of devices such as ultrasound transducers, sensors, and actuators. This Research Topic of new piezoelectric materials and devices presents two reviews and eight original research articles that give insight into new piezoelectric materials, provide a basis for equivalent models of piezoelectric devices, and summarize and prospect the research of piezoelectric devices.

OPEN ACCESS

Edited and reviewed by:
Weihua Li,
University of Wollongong, Wollongong, Australia

***Correspondence:**
Chunlong Fei
clfei@xidian.edu.cn

Received: *29 November 2021*
Accepted: *06 December 2021*
Published: *05 January 2022*

Citation:
Fei C, Zhang L, Chen Z, Yang Y and Ma J (2022) Editorial: New Piezoelectric Materials and Devices: Fabrication, Structures, and Applications. Front. Mater. 8:824345. doi: 10.3389/fmats.2021.824345

PIEZOELECTRIC MATERIALS

Piezoelectric materials have wide applications in energy conversion, sensors, drives, and frequency control. Chen et al. described rate-earth elements-doped piezoelectric materials that were categorized into ceramics, single crystals, and thin films. On this basis, the current research status and application prospects of those piezoelectric materials were summarized systematically, which can be used as the experimental design of piezoelectric materials to provide a level of theoretical reference.

Conventional lead-based piezoelectric materials for ultrasonic transducers are harmful to the human body and the environment. Consequently, Quan et al. reported the effect of Sm^{3+} modification for novel lead-free KNLN-BZ-BNT ceramics. When the temperature was raised from 30 to 180°C, the thermal stability of the d_{33} value decreased to less than 20%. These results showed that Sm^{3+} modification can improve the properties of KNLN-BZ-BNT ceramics. Furthermore, the ceramics are suitable for further applications even under high temperatures.

Composite materials combine the advantages of piezoelectric materials and polymers to achieve high electromechanical coupling coefficients and low acoustic impedance. In this study, Han et al. proposed a 64-element ultrasonic phased-array transducer with a central frequency of 9 MHz for

intracardiac echocardiography. The phased array was fabricated based on 1-3 piezoelectric composites with a flexible circuit, and exhibited a high spatial resolution and imaging performance.

DEVICES FABRICATION, STRUCTURES, AND APPLICATIONS

Jun et al. introduced an ultrahigh frequency (UHF) ultrasonic transducer, and summarized the current research status from three aspects: material selection, focus design, and acoustic energy transmission matching. In addition, the authors also shared some views on the future development of UHF ultrasonic transducers. Shen et al. described the design and fabrication of ultrasonic transducers with different frequencies (12 and 20 MHz), different matching layers, and different cable lengths (0.5–2.5 m) to validate the effectiveness of the Leach model and the transmission line model. The results showed that in some applications, such as IVUS, the influence of the cable was not negligible, and even for high frequency transducers, different cable lengths had a significant effect on the transducer. The model of the sonotrode system was established to simulate the performance of two ultrasonic transducers and one sonotrode. Wang et al. presented the finite element model and the transfer matrix model for the sonotrode system. The vibration velocity ratio, resonance frequency, and amplitude ratio of the two models were compared. The proposed transfer matrix method is an effective method to simulate the dynamic performance of the ultrasonic welding electrode system, and provides a better basis for further optimization.

The surface acoustic wave (SAW) is an ultrasonic device which provides a wide range of applications with the use of an electronic system, including delay lines, filters, correlators, and DC to DC converters. Ma et al. explored the detailed fabrication process of a piezoelectric-on-silicon (POS) substrate, by using Smart-Cut technology, a 128°Y-X LN POS substrate with a high-quality single-crystal LN film and low surface roughness was fabricated. Compared with the LN/Si structure, the BCB layer in the POS substrate could concentrate more SAW vibration in the piezoelectric thin film layer. Traditional radio frequency filters cannot meet the demands of miniaturization, high frequency operation, integration, and broadband capacity in new-generation communication systems owing to their larger volumes. Jiang et al. first analyzed the harmonic characteristics of the FBAR and proposed the optimized structure of the FBAR by using the FEM method. Then, a 3.7 GHz FBAR was fabricated through MEMS technology based on the optimized structural parameters. The simulation result was validated by comparing it to the FBAR test results. The proposed FBAR is perfectly compatible with currently available semiconductor technologies, allowing for device miniaturization and integration.

Guanbing et al. proposed a compact five-element integrated ultrasonic transducer, which was designed and manufactured for the inspection of defects in the split pins of control rod guide tubes in nuclear power plants. The compact 5 MHz transducer has been proven to be capable of sustained operation in an underwater environment for 7 days, and can detect all the defects in the various zones of the split pin with a defect length of 10 mm and height sensitivity of 2 mm. Due to strong background signals *in vivo*, it is difficult to image the molecules of a particular marker. Wang et al. developed a semi-ring array photoacoustic system for transient triple differential (TTD) imaging. PtOEP was used as the exogenous contrast agent and black ink was used to mimic the strong light absorption of melanin. According to the different delay TTD signals, the background signal was successfully removed by the TTD imaging principle. The ratio of the PtOEP signal to black ink signal increased to about 10 times. It is proved that the use of the TTD method to image phosphorescent materials with a strong background has great potential for molecular imaging *in vivo*.

In summary, these major research and review articles make this Research Topic a collection of new insights and perspectives on piezoelectric materials and devices. We thank all authors for their efforts and wish them success in continuously pushing their respective fields forward.

AUTHOR CONTRIBUTIONS

All authors listed have made a substantial, direct, and intellectual contribution to the work and approved it for publication.

Conflict of Interest: The authors declare that the research was conducted in the absence of any commercial or financial relationships that could be construed as a potential conflict of interest.

Publisher's Note: All claims expressed in this article are solely those of the authors and do not necessarily represent those of their affiliated organizations, or those of the publisher, the editors and the reviewers. Any product that may be evaluated in this article, or claim that may be made by its manufacturer, is not guaranteed or endorsed by the publisher.

frontiers in Materials

ORIGINAL RESEARCH
published: 24 February 2021
doi: 10.3389/fmats.2021.642896

Modeling of Sonotrode System of Ultrasonic Consolidation With Transfer Matrix Method

Yin Wang, Ziyan Chen, Qing Yu and Fang Cheng*

College of Mechanical Engineering and Automation, Huaqiao University, Xiamen, China

To establish an efficient model for sonotrode system, a key part that continuously applies ultrasonic oscillation on metal foils to form solid state bond in ultrasonic consolidation equipment, this research presents modeling methods for sonotrode system. After an introduction to the construction of sonotrode system along with its operating principle, the transfer matrix method was adopted to build the model for the system consisting two ultrasonic transducers and one sonotrode. Simulation results of transfer matrix model were compared to that of finite element method. A prototype was fabricated and tested. A comparison of the resonance frequencies calculated by two modeling methods to the experimental result showed that the difference between transfer matrix model and prototype is 6.96% while the difference between finite element model and prototype is 9.26%. The proposed transfer matrix method is an efficient way to simulate dynamic performances for sonotrode system, which provide a better foundation for further optimization.

Keywords: ultrasonic consolidation, transfer matrix model, piezoelectric transducer, sonotrode, finite element model

OPEN ACCESS

Edited by:
Zeyu Chen,
Central South University, China

Reviewed by:
Xiaoniu LI,
Nanjing University of Aeronautics and Astronautics, China
Jun Huang,
Jiangsu University, China
Weidong Liu,
Hohai University, China

****Correspondence:***
Yin Wang
yin.wangyin@hqu.edu.cn

Specialty section:
This article was submitted to Smart Materials, a section of the journal Frontiers in Materials

Received: *17 December 2020*
Accepted: *07 January 2021*
Published: *24 February 2021*

Citation:
Wang Y, Chen Z, Yu Q and Cheng F (2021) Modeling of Sonotrode System of Ultrasonic Consolidation With Transfer Matrix Method. Front. Mater. 8:642896. doi: 10.3389/fmats.2021.642896

INTRODUCTION

Ultrasonic consolidation (UC) was developed based on metal ultrasonic additive manufacturing (UAM) which was mainly used for welding the congeneric metal and heterogeneous metal foil (Mariani and Ghassemieh, 2010; Jiao et al., 2019; Wang et al., 2019b). In UC process, high-power ultrasonic energy is transmitted to layers of metal foil through an ultrasonically vibrating sonotrode, pressed onto them, resulting in metallurgical bonding between atoms and interfaces of metal layers (Li and Soar, 2008; Li and Soar, 2009). This process avoids the high temperature needed for recrystallization, thus no protecting atmosphere is necessary for avoiding oxidization and smaller thermal deformation is arisen (Foster et al., 2013; Obielodan and Stucker, 2014). UC has shown unique advantages and broad prospects in metal composite material manufacturing, intelligent structure processing, and complex functional structure manufacturing (Zhang et al., 2009; Zhang and Li, 2009; Zhang and Li, 2010; Panteli et al., 2012). In the past, the researches on ultrasonic consolidation mainly focused on the exploration of consolidation principle, numerical simulation, and thermal analysis of consolidation process, as well as the evaluation of the quality and process parameters of consolidated foil (Dehoff and Babu, 2010; Friel et al., 2010; Koellhoffer et al., 2011; Schick et al., 2011; He et al., 2013; Zhang et al., 2015; Han et al., 2020). However, as the core element of UC, the study of consolidation equipment is also important (Kelly et al., 2015). The first ultrasonic consolidation equipment is a single transducer structure invented by White. D et al., which can achieve continuous seam welding with the power of 3 KW. Later, the Edison Welding Institution

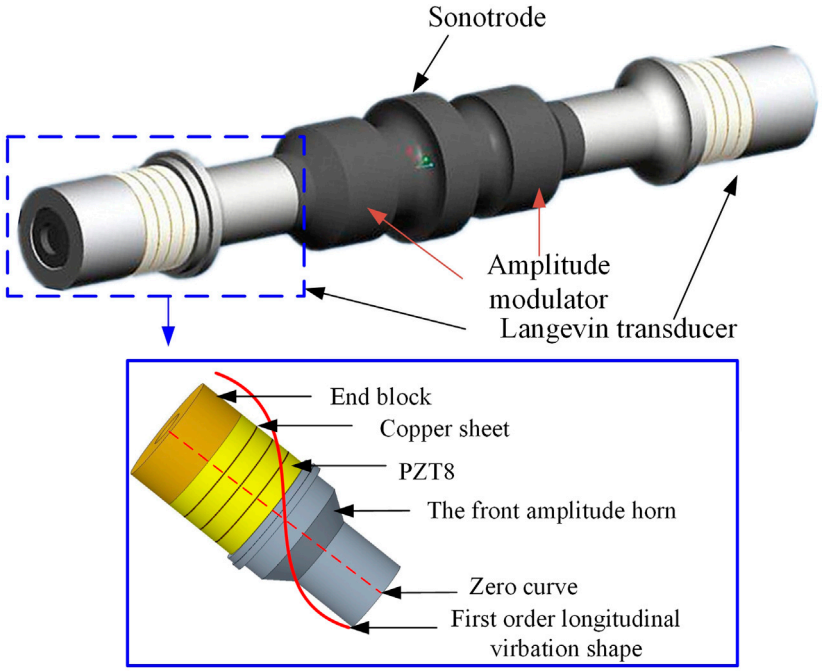

FIGURE 1 | Construction of the sonotrode system.

proposed a high-power composite vibration mode piezoelectric vibrator with two transducers in series with welding power of 9 KW (Sriraman et al., 2010). With the gradual improvement in this technology, Fabrisonic company combined the consolidation equipment with CNC machine tools and developed an ultrasonic consolidation automation equipment that can realize the one-step forming. Piezoelectric vibrator as the key energy conversion component of sonotrode system for ultrasonic consolidation equipment, the establishment of piezoelectric vibrator model is convenient for its optimal design and dynamic design, which is one of the key technologies in the development of this kind of equipment.

In the studies on the vibration characteristics of ultrasonic systems, the modeling methods commonly used for a piezoelectric vibrator include equivalent circuit method, transfer matrix method (TMM), and finite element method (FEM). In most cases, piezoelectric transducers can be modeled with the finite element method. The FEM can provide a relatively accurate solution. However, the customized TMM for a certain geometry model can significantly reduce computing time. As a result, the TMM is gradually adopted by researchers (Feyzollahzadeh and Bamdad, 2020). The TMM is more convenient for the optimization of ultrasonic systems in the circumstance of repeatedly modeling a single system with the same geometry (Wang et al., 2019a).

This work aimed at an efficient dynamic model for a push-pull transducer adopted in high-power ultrasonic welding equipment and a transfer matrix model for its sonotrode was proposed. In the model, the transducer was divided into three kinds of longitudinal vibration elements: the elastic bar with constant cross-section, elastic bar with variable cross-section, and the piezoelectric element. Besides, a finite element model of the same sonotrode was also built for comparison. Finally, a push-pull transducer prototype is manufactured and its impedance test was carried out. The feasibility of the two modeling methods was verified and the possible factors of errors were analyzed.

CONSTRUCTION AND WORKING PRINCIPLE

Construction

The requirement of consolidation equipment for ultrasonic consolidation is a high power, large output vibration amplitude, and stable operation. The design consists of two sandwich piezoelectric transducers with symmetrical sonotrode. The structural parameters of the left and right transducers are identical, as shown in **Figure 1**. The sonotrode includes a welding head in the middle and amplitude adjusters on both sides. In order to achieve the purpose of continuous welding, the sonotrode is a wheel disc type, with grooves on both sides to facilitate the loading of static pressure. The sandwich transducer consists of three parts: piezoelectric element, metal front cover plate directly contacting with the horn end, and metal back cover plate connecting the ultrasonic generator. The energy generated by the transducer radiates the longitudinal vibration efficiently to the horn end through the front cover plate, while the back cover plate contacts the air directly. The whole piezoelectric vibrator uses the first-order longitudinal vibration to generate axial vibration, so as to obtain high-frequency vibration at the welding head and achieve consolidation effect through friction.

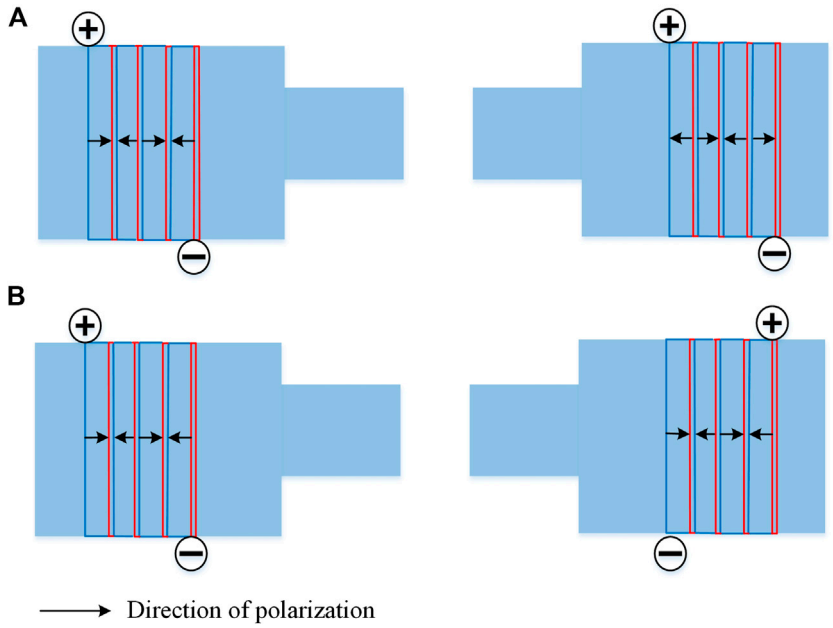

FIGURE 2 | Push-pull excitation **(A)** The piezoelectric ceramics polarized in opposite direction with the same voltage **(B)** The piezoelectric ceramics polarized in same direction with two voltage excitation of reverse phases.

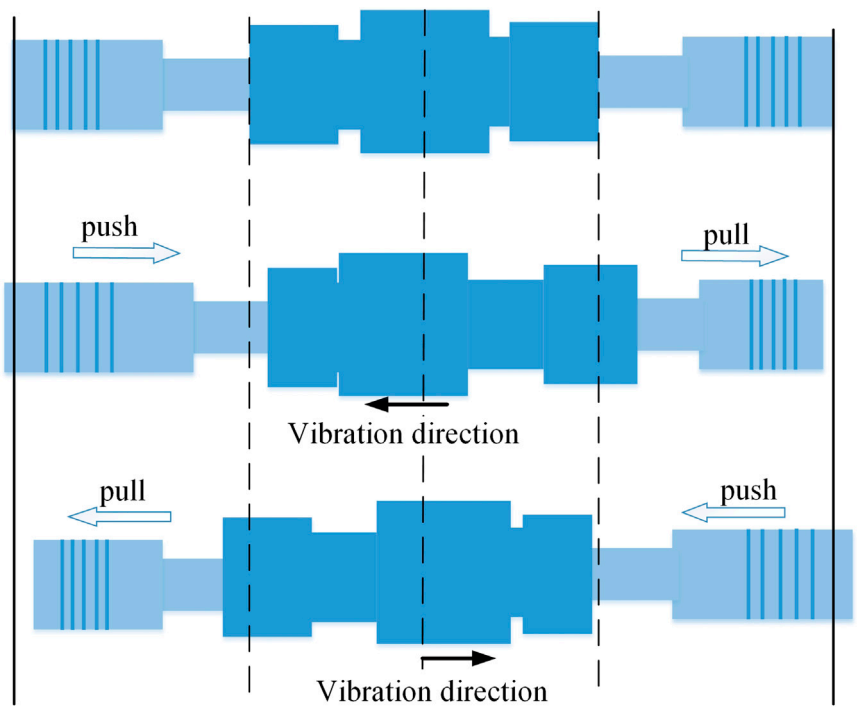

FIGURE 3 | Working principle of sonotrode system.

Working Principle

The movement direction of the left and right sandwich transducers of push-pull piezoelectric vibrator keeps the same direction all the time. When one side shrinks, the other side stretches, and the transducers produce longitudinal vibration as a whole. To realize the push-pull excitation, two sandwiched transducers are applied with two voltage excitation of reverse phases, or the piezoelectric ceramics in the two transducers are

TABLE 1 | Parameters of piezoelectric ceramics.

Parameters	Dielectric constant matrix (F/m)	Piezoelectric constant matrix (C/m^3)	Stiffness matrix(N/m^2)
PZT8	$\begin{bmatrix} 6.04 & & \\ & 6.04 & \\ & & 6.04 \end{bmatrix} \times 10^{-9}$	$\begin{bmatrix} 0 & 0 & -5.2 \\ 0 & 0 & -5.2 \\ 0 & 0 & 15.1 \\ 0 & 12.7 & 0 \\ 12.7 & 0 & 0 \\ 0 & 0 & 0 \end{bmatrix}$	$\begin{bmatrix} 120 & 53.5 & 51.5 & 0 & 0 & 0 \\ 53.5 & 120.6 & 51.5 & 0 & 0 & 0 \\ 51.5 & 120.6 & 51.5 & 0 & 0 & 0 \\ 0 & 0 & 0 & 31.3 & 0 & 0 \\ 0 & 0 & 0 & 0 & 31.3 & 0 \\ 0 & 0 & 0 & 0 & 0 & 31.3 \end{bmatrix} \times 10^{10}$

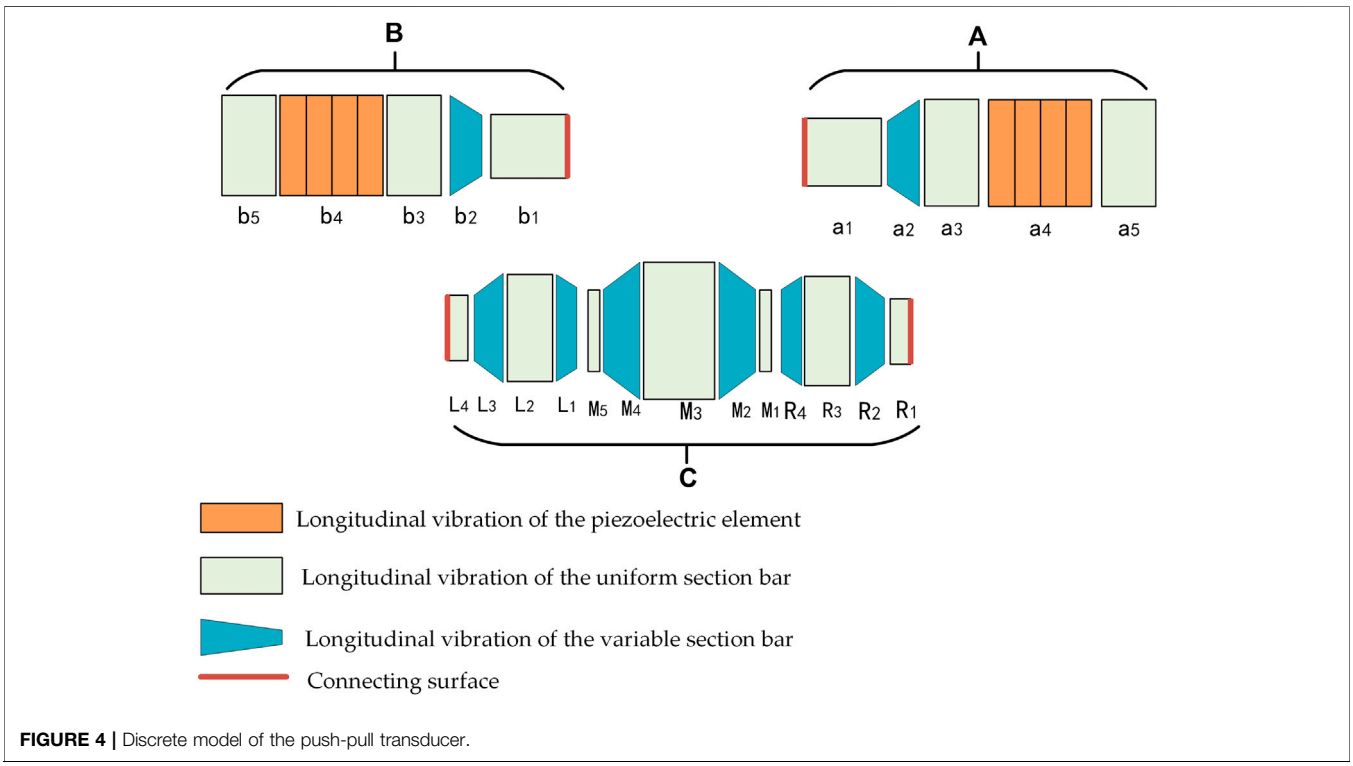

FIGURE 4 | Discrete model of the push-pull transducer.

polarized in opposite directions, as shown in **Figure 2**.The working principle is shown in **Figure 3.**

The specific materials to be fixed are mainly aluminum foil and titanium alloy, and the working frequency of the ultrasonic vibration system is aimed at about 20 kHz. The parameters of PZT8 are shown in **Table 1**.

MODELING

Transfer Matrix Modeling

The transfer matrix method discretizes the complex system and then connects them through the transfer connection between each discrete element (Eduard, 1963). The TMM can obtain the accurate solution of the vibration velocity of each discrete element with the resonance frequency of the system, which plays a key role in analyzing whether the frequency of the designed transducer and the vibration velocity of the welding head meet the requirements. Since there is only one vibration form of longitudinal vibration in the whole sonotrode system, the longitudinal vibration wave equations of elastic rod and piezoelectric element were established, and its transfer matrix can be obtained, and simple boundary conditions can be set up to solve the problem.

As shown in **Figure 4**, the piezoelectric vibrator was mainly divided into the right transducer (A), the left transducer (B), and the sonotrode (C). According to symmetry, the sonotrode can be divided into three parts: left amplitude modulator, right amplitude modulator, and M-type welding head. All the discrete elements can be divided into three types: the longitudinal vibration of the constant cross-section bar, the longitudinal vibration of the variable cross-section bar, and the longitudinal vibration of the piezoelectric element.

Longitudinal Vibrations of Elastic Rod

The longitudinal vibration of elastic rod was divided into constant cross-section and variable cross-section, as shown in **Figure 5**.

According to Newton's second law, the wave equation of elastic rod with constant cross section in free boundary can be formulated as:

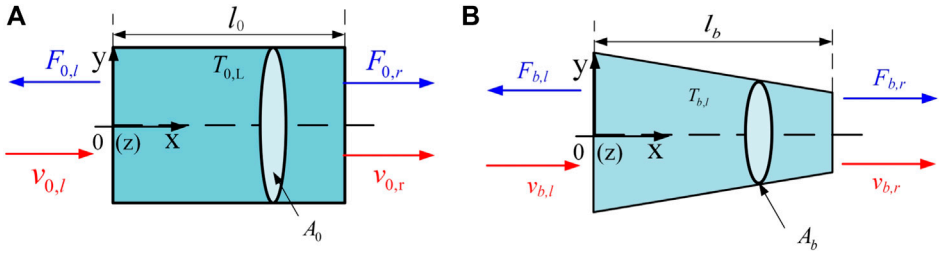

FIGURE 5 | Longitudinal vibrations of tapered sticks **(A)** constant cross-section rob **(B)** variable cross-section rob.

$$\frac{\partial^2 u(x,t)}{\partial x^2} = \frac{1}{c_0^2}\frac{\partial^2 u(x,t)}{\partial t^2} \tag{1}$$

$u(x,t)$ is vibrational displacement function. c_0 is the wave velocity of the elastic rod. The transfer matrix model of the elastic rod with constant cross-section can be obtained with the theory of the separated variable method as follow:

$$Z_{0,r} = T_{0,l}Z_{0,l} = \begin{bmatrix} \cos(k_0 l_0) & -\dfrac{\sin(k_0 l_0)}{jA_0 z_0} \\ jA_0 z_0 \sin(k_0 l_0) & \cos(k_0 l_0) \end{bmatrix} Z_{0,l} \tag{2}$$

$T_{0,l}$ is the longitudinal vibration transfer matrix of elastic rod. $Z_{0,r} = [\, v_{0,l} \quad F_{0,l} \,]^T$ and $Z_{0,r} = [\, v_{0,r} \quad F_{0,r} \,]^T$ represent the input state vector and the output state vector, respectively. $c_0 = \sqrt{E_0/\rho_0}$ is the wave velocity. E_0 is the elastic modulus of rod. ρ_0 is the density of rod. $k_0 = \omega/c_0$ is the wave beam. $z_0 = \sqrt{\rho_0 E_0}$ is the impedance. A_0 is the section area of rod and l_0 is the length of the rod.

The wave equation of variable cross-section can be formulated as.

$$\frac{\partial}{\partial x}\left[E_b A_b(x)\frac{\partial u(x,t)}{\partial x}\right] = \rho_b A_b(x)\frac{\partial^2 u(x,t)}{\partial t^2} \tag{3}$$

where $A_b(x) = (ax+b)^n$ is the section area of rod, $\rho_b$is the density of rod, and the transfer matrix model as follow:

$$Z_{b,r} = T_{bl}Z_{b,l} = \begin{bmatrix} \dfrac{a\sin(\xi l_b) + b\xi\cos(\xi l_b)}{(al_b+b)\xi} & \dfrac{j\omega\sin(\xi l_b)}{bE\xi(al_b+b)} \\ \dfrac{E_b a^2 l_b \xi\cos(\xi l_b) - E_b\left[a^2 + b\xi^2(al_b+b)\right]\sin(\xi l_b)}{j\omega\xi} & \dfrac{\xi(al_b+b)\cos(\xi l_b) - a\sin(\xi l_b)}{b\xi} \end{bmatrix} \tag{4}$$

where $Z_{b,r} = [\, v_{b,l} \quad F_{b,l} \,]^T$ and $Z_{b,r} = [\, v_{b,r} \quad F_{b,r} \,]^T$ represent the input state vector and the output state vector of variable cross-section rob, respectively. $T_{b,l}$ is the longitudinal vibration transfer matrix of variable cross-section rob. $\xi = \omega\sqrt{\rho_b/E_b}$, E_b is the elastic modulus of the rod and l_b is the length of rob.

Longitudinal Vibrations of Piezoelectric Element

In the sandwich transducer structure, the piezoelectric element with d_{33} vibration mode is mainly used, and its polarization direction is along the thickness direction. To maximize the amplitude of piezoelectric ceramics, the polarization direction of two adjacent ceramic sheets was opposite. The thickness of the copper electrode is so thin that it can be ignored. The model is shown in **Figure 6**, which is the transfer matrix model of two ceramic plates.

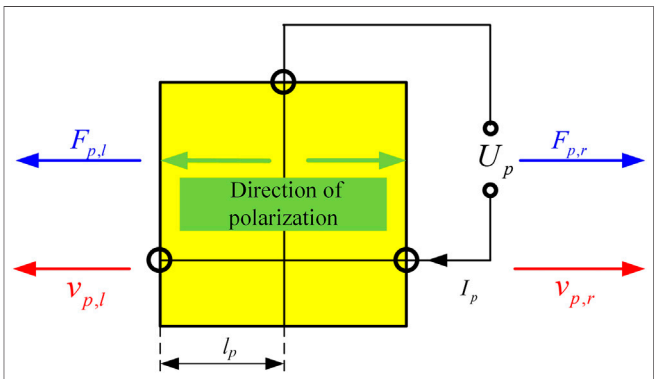

FIGURE 6 | Longitudinal vibration of piezoelectric element.

The elastic coupling matrix, dielectric coupling matrix and piezoelectric coupling matrix of PZT8 were written as a whole, and the relationship among strain, stress, electric field and potential shift (j_1 = 1,2,3,4,5,6) of piezoelectric element can be obtained intuitively:

$$\begin{Bmatrix} S_{1,p} \\ S_{2,p} \\ S_{3,p} \\ S_{4,p} \\ S_{5,p} \\ S_{6,p} \\ D_{1,p} \\ D_{2,p} \\ D_{3,p} \end{Bmatrix} = \begin{bmatrix} s_{11}^E & s_{12}^E & s_{13}^E & 0 & 0 & 0 & 0 & 0 & d_{31} \\ s_{12}^E & s_{22}^E & s_{23}^E & 0 & 0 & 0 & 0 & 0 & d_{32} \\ s_{13}^E & s_{23}^E & s_{33}^E & 0 & 0 & 0 & 0 & 0 & d_{33} \\ 0 & 0 & 0 & s_{44}^E & 0 & 0 & 0 & d_{24} & 0 \\ 0 & 0 & 0 & 0 & s_{55}^E & 0 & d_{15} & 0 & 0 \\ 0 & 0 & 0 & 0 & 0 & s_{66}^E & 0 & 0 & 0 \\ 0 & 0 & 0 & 0 & d_{15} & 0 & \varepsilon_{11}^T & 0 & 0 \\ 0 & 0 & 0 & d_{24} & 0 & 0 & 0 & \varepsilon_{22}^T & 0 \\ d_{31} & d_{32} & d_{33} & 0 & 0 & 0 & 0 & 0 & \varepsilon_{33}^T \end{bmatrix} \times \begin{Bmatrix} T_{1,p} \\ T_{2,p} \\ T_{3,p} \\ T_{4,p} \\ T_{5,p} \\ T_{6,p} \\ E_{1,p} \\ E_{2,p} \\ E_{3,p} \end{Bmatrix} \tag{5}$$

$S^E_{j_1j_2}$ (j_2 = 1, 2, 3, 4, 5, 6) is the compliance coefficient, $\varepsilon^T_{j_1j_2}$ is the dielectric constant and $d_{j_1j_2}$ is the piezoelectric constant of PZT ceramic.

Wave equation of PZT element is similar to the elastic rod which can be formulated as:

$$\frac{\partial^2 u_p(x,t)}{\partial x^2} = \frac{1}{c_p^2}\frac{\partial^2 u_p(x,t)}{\partial t^2} \tag{6}$$

And the transfer matrix of PZT element is:

$$Z_{p,r} = T_p Z_{p,l} = \begin{bmatrix} \cos(L_p k_p) & -\frac{\sin(L_p k_p)}{jA_p z_p} & \frac{\alpha_p \sin(L_p k_p)}{jA_p z_p} \\ jA_p z_p \sin(L_p k_p) & \cos(L_p k_p) & \alpha_p[\cos(L_p k_p) - 1] \\ \alpha_p[\cos(L_p k_p) - 1] & -\frac{\alpha_p \sin(L_p k_p)}{jA_p z_p} & j\omega C_{0p} - \frac{\alpha_p^2 \sin(L_p k_p)}{jA_p z_p} \end{bmatrix} \tag{7}$$

where $Z_{p,l} = [\, v_{p,l} \quad F_{p,l} \quad U_{p,l} \,]^T$ and $Z_{p,r} = [\, v_{p,r} \quad F_{p,r} \quad U_{p,r} \,]^T$ are the input state vector and the output state vector of PZT element, respectively. $A_p = \pi(R_p^2 - r_p^2)$ is the cross sectional area of PZT sheet. L_p is the thickness of PZT sheet. $k_p = \omega/c_p$ is the beam of piezoelectric element. $z_P = \sqrt{\rho_P/S^E_{33}}$ is the impedance of piezoelectric element. $C_{0P} = 4A_P\left(\varepsilon^T_{33} - \frac{d^2_{33}}{S^E_{33}}\right)\Big/L_p$ is the blocked piezoelectric capacitance. $\alpha_p = A_p d_{33}/L_p S^E_{33}$ is the electromechanical translation factor.

Transfer Conditions

After the whole transducer was discretized, according to the two key conditions that the resultant force is zero and the velocity is equal between adjacent elements on their contact interface, each vibration unit is connected with the state vector. Each discretized part of the push-pull piezoelectric transducer was connected in series, which can be divided into two types. Type1 is the series connection of elastic rod and elastic rod, and Type2 is the series connection of piezoelectric element and elastic rod as expressed:

$$\begin{cases} C_e Z_{e,i+1} - C_e Z_{e,i} = 0 \\ C_p Z_{p,i+1} - C_{el} Z_{e,i} = 0 \end{cases} \tag{8}$$

Where $Z_{e,i}$ and $Z_{e,i+1}$ represent the input state vector and the output state vector of variable cross-section rob *i* and *i+1*, respectively. C_e is the longitudinal vibration condition matrix between two adjacent elastic bars with a dimension of 2 × 2. $Z_{p,i+1} = [\, v_{e,i+1} \quad F_{e,i+1} \,]^T$ represent the input state vector and the output state vector of piezoelectric element *i+1*. C_p is the longitudinal vibration transfer condition matrix of piezoelectric element and C_{el} is the longitudinal vibration transfer condition matrix of rob as expressed:

The Total Transfer Matrix Equation

The discrete model of the whole sonotrode system with boundary conditions is shown in **Figure 7** and structural parameters are also given. The solution direction is from element one to element 23. Each element has input and output state vectors.

The sandwich transducer A and B have the same transfer matrix. Based on the transfer matrix of each element and the transfer condition matrix between elements, a simple boundary condition matrix was added. The boundary conditions are mechanically free and voltage is applied to the piezoelectric ceramic element. The transfer matrix equation of transducer is obtained as:

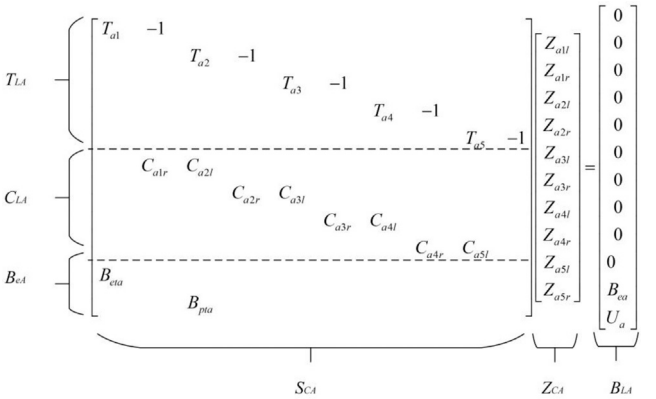

(9)

Where T_{LA} is the physical matrix of transducer A, C_{LA} is the transfer condition matrix of transducer and B_{eA} is the boundary condition matrix of transducer. The three matrixes constitute the total systematic transfer matrix of transducer S_{CA}. Z_{CA} concludes the total input and output mechanical state vectors of transducer and B_{LA} represents the total boundary condition values.

The sonotrode C can be divided into three parts as shown in **Figure 8**.

The right amplitude modulator (R_1~R_4) and the left one (L_1~L_4) have the same transfer matrix can be expressed:

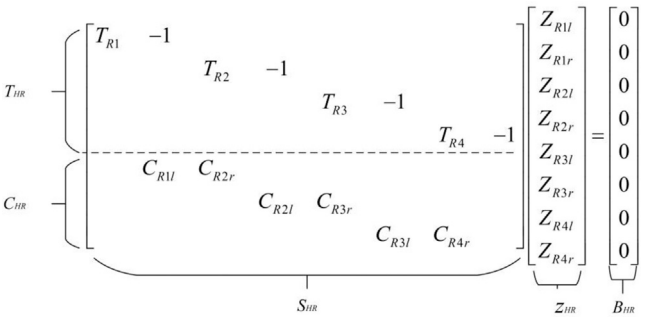

(10)

Where T_{HR} is the physical matrix of amplitude modulator, C_{HR} is the total transfer condition matrix of amplitude modulator. The three matrixes constitute the total systematic transfer matrix of transducer S_{HR}. Z_{HR} concludes the total input and output mechanical state vectors of transducer and B_{HR} represents the boundary condition values.

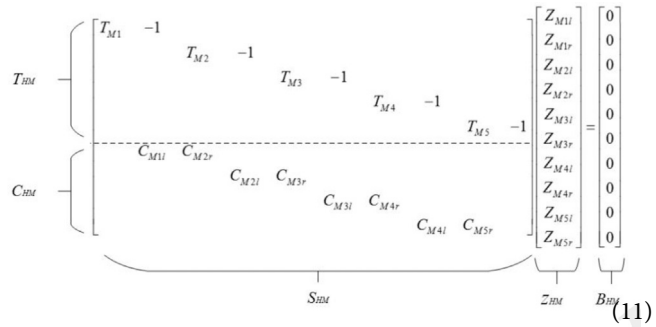

(11)

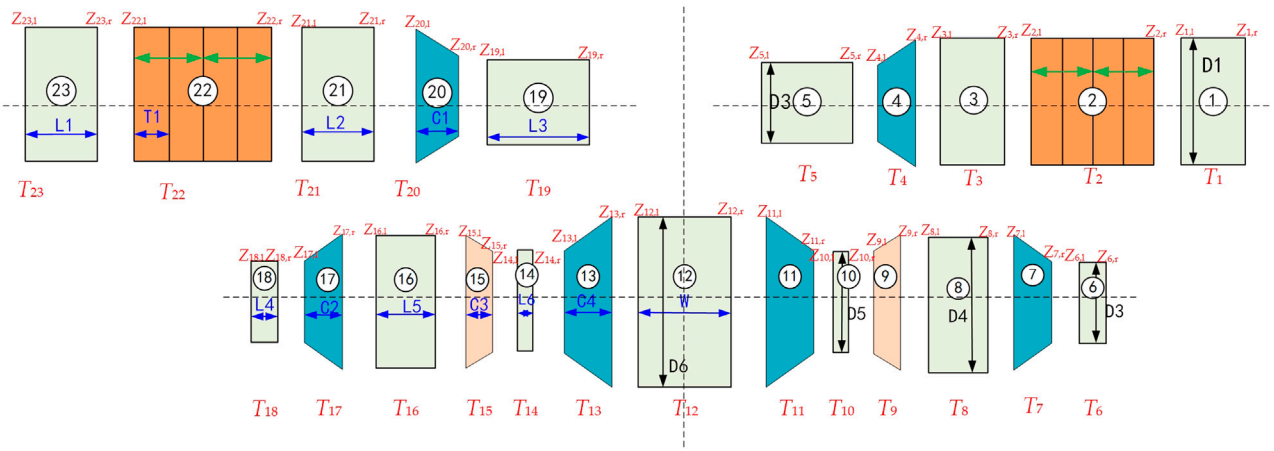

FIGURE 7 | Integral transfer matrix model of sonotrode system.

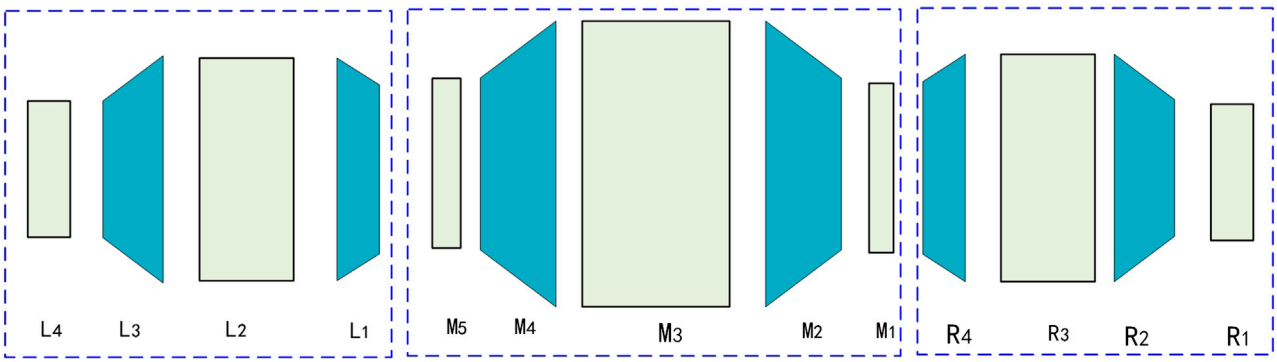

FIGURE 8 | Discrete model of sonotrode.

Where T_{HM} is the physical matrix of M-type welding head, C_{HM} is the transfer condition matrix of welding head. The three matrixes constitute the total systematic transfer matrix of welding head S_{HM}. Z_{HM} concludes the total input and output mechanical state vectors of welding head and B_{HM} represents the boundary condition values.

So the transfer matrix model of the sonotrode can be expressed.

$$\begin{bmatrix} S_{HR} & & & \\ & S_{HM} & & \\ & & S_{HL} & \\ C_{RM1} & C_{RM2} & & \\ & C_{ML1} & C_{ML2} & \end{bmatrix} \begin{bmatrix} Z_{HR} \\ Z_{HM} \\ Z_{HL} \end{bmatrix} = \begin{bmatrix} 0 \\ 0 \\ 0 \\ 0 \\ 0 \end{bmatrix} \tag{12}$$

S_{HL} is total physical matrix of the left amplitude modulator. C_{RM1}, C_{RM2} is the total transfer condition matrix with a dimension of 2×2 between the right amplitude modulator and the welding head. C_{ML1}, C_{ML2} is the total transfer condition matrix a dimension of 2×2 between the welding head and the left amplitude modulator. Z_{HR}, Z_{HM} and Z_{HL} three matrixes constitute the total input and output mechanical state vectors.

From above, the sonotrode system is divided into three parts and the transfer matrix model of the piezoelectric vibrator is expressed:

$$\begin{bmatrix} S_{CA} & & \\ & S_{CC} & \\ & & S_{CB} \\ C_{AC} & C_{CA} & \\ & C_{CB} & C_{BC} \end{bmatrix} \begin{bmatrix} Z_{CA} \\ Z_{CC} \\ Z_{CB} \end{bmatrix} = \begin{bmatrix} B_{LA} \\ B_{LC} \\ B_{LB} \\ 0 \\ 0 \end{bmatrix} \tag{13}$$

S_{CA} is the total physical matrix of the right transducer, S_{CC} is the total physical matrix of the sonotrode and S_{CB} is total physical matrix of the left transducer. C_{AC}, C_{CA} is the total transfer condition matrix with a dimension of 2×2 between the right transducer amplitude and the sonotrode. C_{CB}, C_{BC} is the total transfer condition matrix a dimension of 2×2 between the sonotrode and the left transducer. Z_{CA}, Z_{CC} and Z_{CB} three matrixes constitute the total input and output mechanical state vectors. B_{LA}, B_{LC}, B_{lB} are right side matrix including all boundary conditions of the entire piezoelectric vibrator.

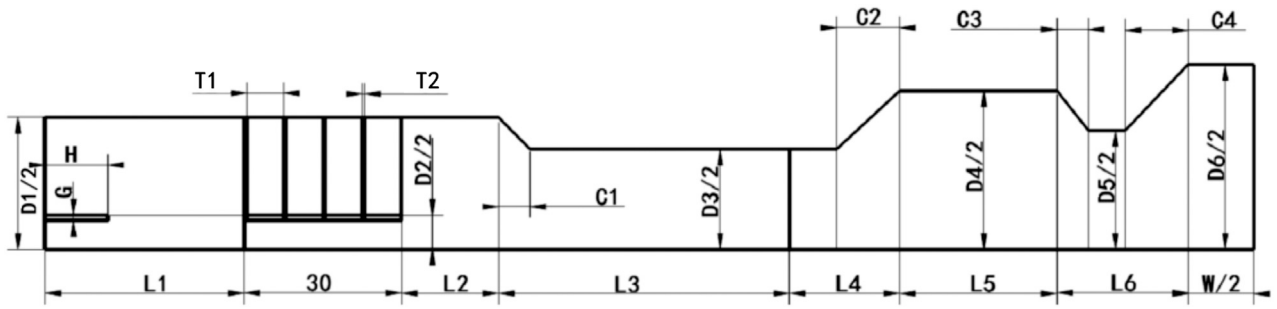

FIGURE 9 | Parameter diagram of quarter section model of piezoelectric vibrator.

TABLE 2 | Geometrical sizes of the piezoelectric vibrator.

Parameter	D1	D2	D3	D4	D5	D6	L1	L2	L3	T1	L4	L5	L6	C1	C2	C3	C4	W	H	G
Value (mm)	60	16	40	80	46	90	18	18.5	39.5	10	18	35	33	6	12	6	12	25	4	1

TABLE 3 | Material properties of piezoelectric vibrator.

Structure	Materials	Density (kg/m^3)	Elastic modulus (Gpa)	Longitudinal wave velocity (m/s)	Element
Piezoelectric ceramics	PTZ-8	7.5	—	3,100	Solid5
Front cover	Al	2.7	71	5,100	Solid45
End block	45# steel	7.8	200	3,940	Solid45

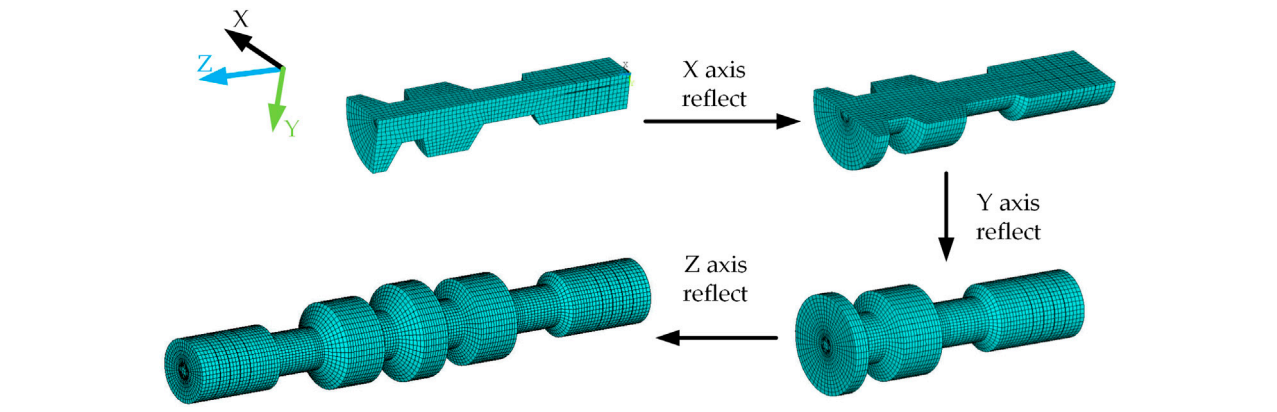

FIGURE 10 | Establishment of finite element model.

Finite Element Modeling

The FEM of sonotrode system was established by ANSYS finite element analysis software. The quarter section of the piezoelectric vibrator is shown in **Figure 9** and its geometrical sizes of the piezoelectric vibrator are listed in **Table 2**. Solid five was selected as piezoelectric ceramic and solid 45 was selected as other metal parts which are shown in **Table 3.** To model the preloading bolt, a slot with a width of *G* and length of *H* was built at the back cover plate. Moreover, due to the existence of preloading bolts, there is a gap with the width of *G* at the exit of the PZT sheets, which makes the piezoelectric ceramic sheet and the middle bolt not connect together on the grid.

To make the mesh more regular, the 1/4 model of the piezoelectric vibrator was first established, then the three element symmetry was adopted to obtain the finite element model of the whole piezoelectric vibrator, which is shown in **Figure 10**.

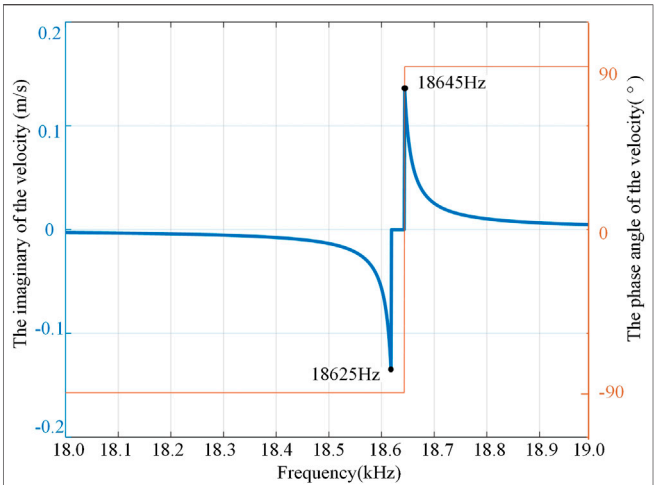

FIGURE 11 | The vibration velocity of the TMM.

RESULT AND DISCUSSION

Through the calculation of the transfer matrix in *Transfer matrix modeling Section*, the relationship between the vibration velocity and frequency of the sonotrode system is shown in **Figure 11**. It can be seen that when the frequency is near 18645 Hz, there is a peak value of vibration velocity which gets its resonant frequency.

After the finite element model was obtained, the modal analysis of the piezoelectric vibrator was carried out. Taking the symmetry center as the origin, the longitudinal displacement of the nodes on the axis of the piezoelectric vibrator was extracted, and the vibration mode of the piezoelectric vibrator was obtained as shown in **Figure 12**. The resonant frequency of the longitudinal mode is 18,187 Hz. It can be seen that the model obtained a longitudinal vibration mode. The maximum displacement is at the sonotrode. When the transducer on one side is extended, the other side is shortened. It can be seen from the modal shape in the figure that both of them are close to the sinusoidal mode and are similar.

Apply the voltage with a phase difference of 180° and peak to peak value of 200 V on the left and right transducers to obtain the amplitude of the two models, respectively, as shown in **Table 4**. The absolute errors between them were also calculated.

It can be seen the frequency difference between the two models is small, but the amplitude difference is large. The amplitude of the FEM is related to the excitation, while the amplitude of the TMM is the theoretical value derived from the vibration rate.

Experiment

To verify the effectiveness of the two modeling methods, a prototype of sonotrode system was established as shown in **Figure 13**. The material and structural parameters were consistent with the proposed above. Two supporting flange plates were attached to the base and installed at the nodes of the transducer.

In order to obtain the resonant frequency of the push-pull transducer, the impedance experiment was carried out. An impedance analyzer ZX70A was used for the impedance test. The basic accuracy of the impedance analyzer is 0.05%, and the frequency accuracy is 1 mHz. Because the left and right transducers are the same, only one section of the transducer was connected to the impedance analyzer. The frequency range of 10 kHz–80 kHz and the number of scanning points 1,556 were set. It can be seen that the transducer has resonant frequencies in each frequency band. Then take the frequency close to 20 kHz, and set the number of scanning points 1,001. The admittance of the prototype was obtained. As shown in **Figure 14**, the maximum admittance frequency is 20,042 Hz. According to the resonance theory, there is a resonance frequency of the piezoelectric vibrator near and below this frequency.

DISCUSSION

Comparison of experimental results, the relative error of the resonant frequency of TMM model is 6.96% and that of the FEM model is 9.26%. The error of TMM is smaller and closer to the actual characteristics of the prototype. The reason for the error of TMM can be attributed to the fact that the chamfering was regarded as a variable cross-section. The reason for the error of the FEM may be the grid and the selected elements have an impact on the model. When building a finite element model, the preloading force between the preloading bolt and the piezoelectric ceramics sheet cannot be reflected after assembly. Besides, the processing technology still affects the properties of the material, thus affecting the solution of the vibration calculation. In order to compact the assembly of the transducer and the sonotrode, holes were punched in both the output amplitude horn and the modulator of the transducers, and the existence of such holes was not considered in both two models.

By comparing the two models and the experiment, it can be found that the TMM seems more accurate. When studying this kind of sandwich piezoelectric transducer, it's found that the FEM is difficult to calculate very accurately, and the preload on the piezoelectric ceramic is very exquisite. In the FEM, the gap between the preloading bolt and the PZT sheet was simulated, and the joint end face was connected together, there are still some inevitable errors. In general, the FEM and the TMM have similar calculation themes, both of which discretizes the target object. FEM is very particular about grid division and the density and the size of mesh determine the solution accuracy. However, the TMM only needs to decompose the vibrating body according to its different vibration modes. Compared with the traditional finite element modeling method, the transfer matrix modeling method can indeed shorten the calculation time and intuitively obtain the working frequency. The TMM can intuitively reflect the relationship between the structural parameters and the resonant frequency.

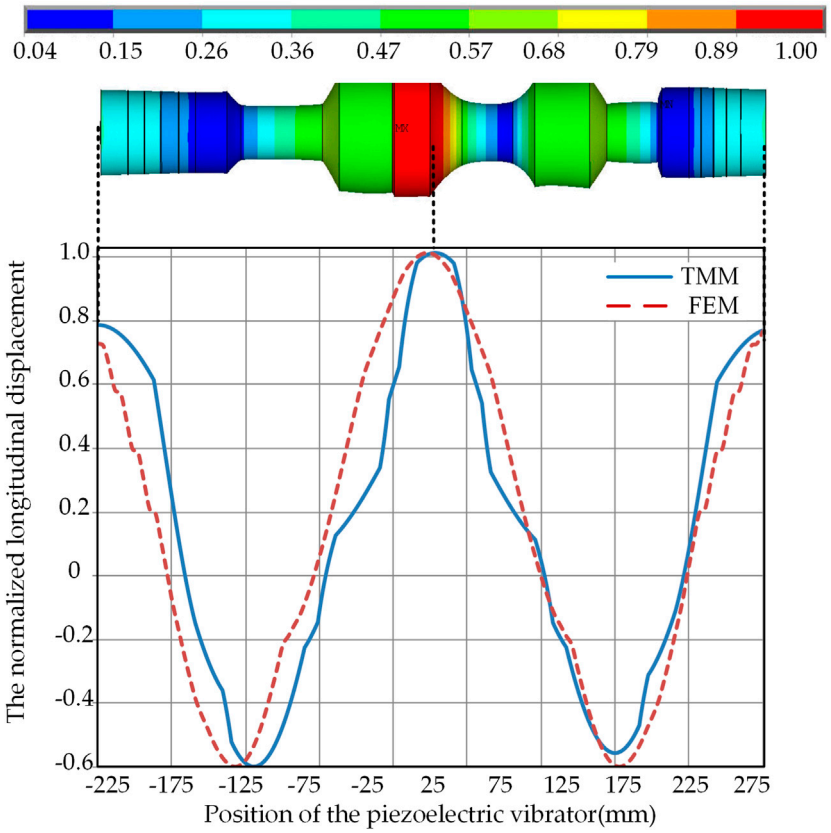

FIGURE 12 | Modal analysis of piezoelectric vibrator.

TABLE 4 | Comparison of two models.

Model types and errors	Resonant frequency (Hz)	The ratio of speed of vibration	Amplitude of sonotrode (μm)
TMM model	18,645	1.5898	10.1
FEM model	18,187	1.5333	10.8
Relative error	2.5	3.6%	6.4

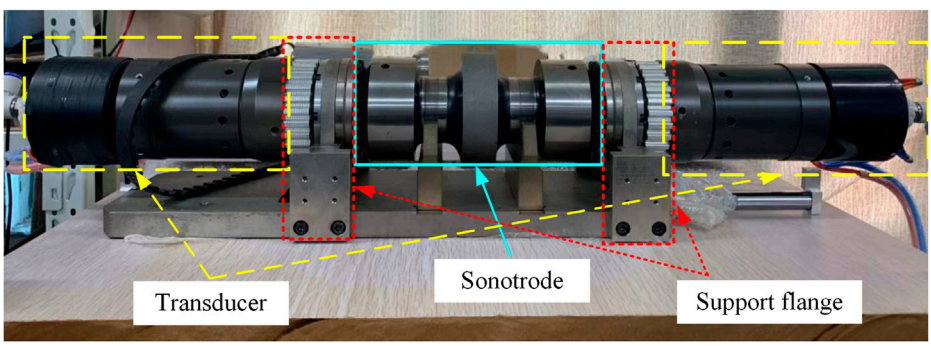

FIGURE 13 | The prototype of sonotrode system.

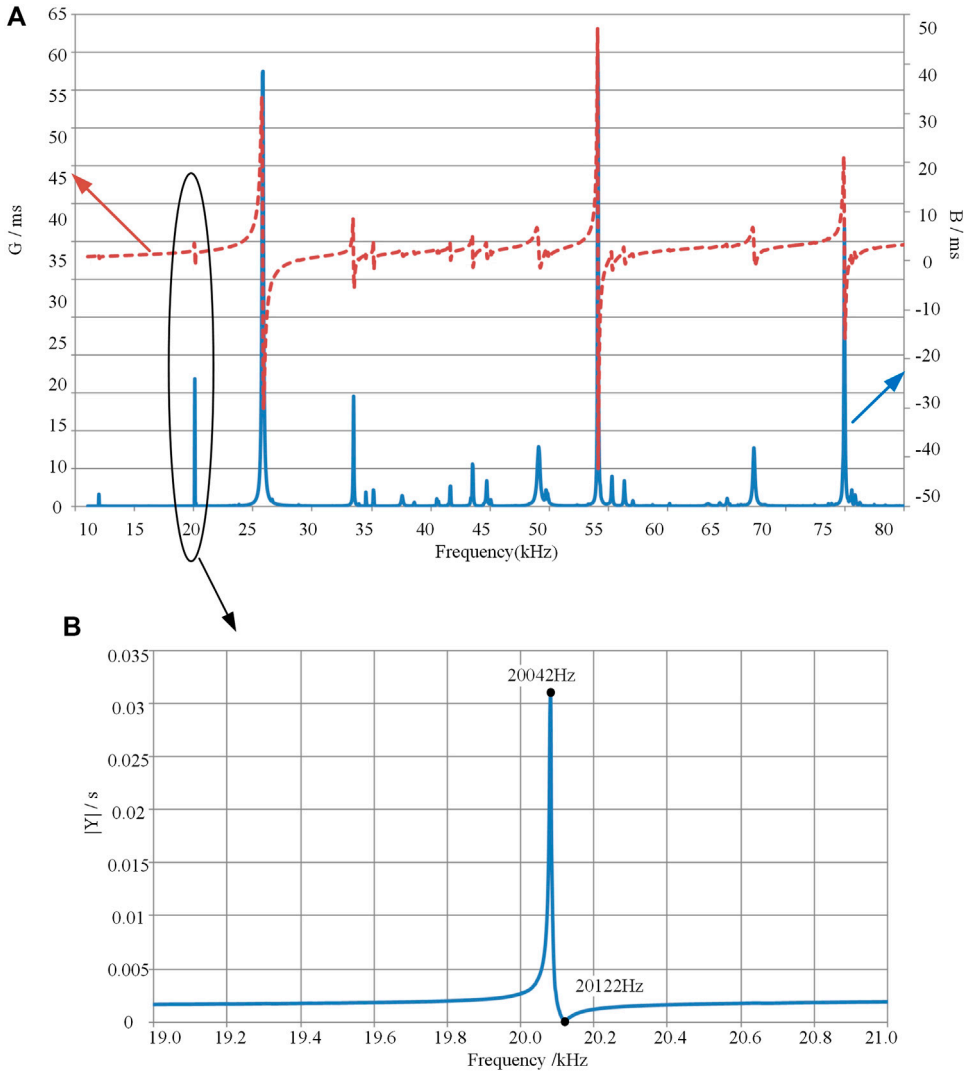

FIGURE 14 | Impedance and phase curve of prototype **(A)** Impedance curve at full frequency **(B)** Impedance curve around 20 kHz.

CONCLUSION

Based on the sonotrode system for ultrasonic consolidation, two models were established, that is, the finite element model and the transfer matrix model. The ratio of the speed of vibration, resonant frequency, and amplitude ratio of the two models were compared. The prototype was made and its testing results verified the results of modeling. The dynamic performances calculated by both models were compared with the experimental results, which show that the transfer matrix method has the same feasibility as the finite element model and can achieve higher efficiency.

DATA AVAILABILITY STATEMENT

The original contributions presented in the study are included in the article/Supplementary Material, further inquiries can be directed to the corresponding author.

AUTHOR CONTRIBUTIONS

YW came up with the idea. ZC and YW carried out the experiments. ZC analyzed the experimental results. ZC, QY, and FC wrote the manuscript. All authors contributed to the article and approved the submitted version.

FUNDING

This research was funded by the National Natural Science Foundation of China (Grant No.: 51505161), Natural Science Foundation of Fujian province (Grant No.: 2016J01236), the Promotion Program for Young and Middle-aged Teacher in Science and Technology Research of Huaqiao University (Grand No.: ZQN-PY604), and the Subsidized Project for Postgraduates' Innovative Fund in Scientific Research of Huaqiao University (Grant No.: 18013080054).

REFERENCES

Dehoff, R. R., and Babu, S. S. (2010). Characterization of interfacial microstructures in 3003 aluminum alloy blocks fabricated by ultrasonic additive manufacturing. *Acta Mater.* 58, 4305–4315. doi:10.1016/j.actamat.2010.03.006

Eduard (1963). *Matrix methods in elastomechanics*. New York, NY: McGraw-Hill.

Feyzollahzadeh, M., and Bamdad, M. (2020). A modified transfer matrix method to reduce the calculation time: a case study on beam vibration. *Appl. Math. Comput.* 378, 125238. doi:10.1016/j.amc.2020.125238

Foster, D. R., Dapino, M. J., and Babu, S. S. (2013). Elastic constants of ultrasonic additive manufactured Al 3003-H18. *Ultrasonics* 53, 211–218. doi:10.1016/j.ultras.2012.06.002

Friel, R. J., Johnson, K. E., Dickens, P. M., and Harris, R. A. (2010). The effect of interface topography for Ultrasonic Consolidation of aluminium. *Mater. Sci. Eng.* 527, 4474–4483. doi:10.1016/j.msea.2010.03.094

Han, T., Kuo, C.-H., Sridharan, N., Headings, L. M., Babu, S. S., and Dapino, M. J. (2020). Effect of preheat temperature and post-process treatment on the microstructure and mechanical properties of stainless steel 410 made *via* ultrasonic additive manufacturing. *Mater. Sci. Eng.* 769, 138457. doi:10.1016/j.msea.2019.138457

He, X.-H., Shi, H.-J., Zhang, Y.-D., Fu, W.-X., Yang, Z.-G., and Wilkinson, C. E. (2013). *In-situ* scanning electron microscopy studies of small fatigue crack growth in ultrasonic consolidation bonded aluminum 2024 laminated structure. *Mater. Lett.* 112, 47–50. doi:10.1016/j.matlet.2013.08.093

Jiao, F., Liu, M., Jiang, F., Zhao, J., Li, P., and Wang, Z. (2019). Continuous carbon fiber reinforced Ti/Al3Ti metal-intermetallic laminate (MIL) composites fabricated using ultrasonic consolidation assisted hot pressing sintering. *Mater. Sci. Eng.: A* 765, 138255. doi:10.1016/j.msea.2019.138255

Kelly, G. S., Advani, S. G., and Gillespie, J. W. (2015). A model to describe stick-slip transition time during ultrasonic consolidation. *Int. J. Adv. Manuf. Technol.* 79, 1931–1937. doi:10.1007/s00170-015-6939-z

Koellhoffer, S., Gillespie, J. W., Advani, S. G., and Bogetti, T. A. (2011). Role of friction on the thermal development in ultrasonically consolidated aluminum foils and composites. *J. Mater. Process. Technol.* 211, 1864–1877. doi:10.1016/j.jmatprotec.2011.06.011

Li, D., and Soar, R. C. (2008). Plastic flow and work hardening of Al alloy matrices during ultrasonic consolidation fibre embedding process. *Mater. Sci. Eng.: A* 498, 421–429. doi:10.1016/j.msea.2008.08.037

Li, D., and Soar, R. (2009). Influence of sonotrode texture on the performance of an ultrasonic consolidation machine and the interfacial bond strength. *J. Mater. Process. Technol.* 209, 1627–1634. doi:10.1016/j.jmatprotec.2008.04.018

Mariani, E., and Ghassemieh, E. (2010). Microstructure evolution of 6061 O Al alloy during ultrasonic consolidation: an insight from electron backscatter diffraction. *Acta Mater.* 58, 2492–2503. doi:10.1016/j.actamat.2009.12.035

Obielodan, J., and Stucker, B. (2014). A fabrication methodology for dual-material engineering structures using ultrasonic additive manufacturing. *Int. J. Adv. Manuf. Technol.* 70, 277–284. doi:10.1007/s00170-013-5266-5

Panteli, A., Robson, J. D., Brough, I., and Prangnell, P. B. (2012). The effect of high strain rate deformation on intermetallic reaction during ultrasonic welding aluminium to magnesium. *Mater. Sci. Eng.: A* 556, 31–42. doi:10.1016/j.msea.2012.06.055

Schick, D., Suresh Babu, S., Foster, D. R., Dapino, M., Short, M., and Lippold, J. C. (2011). Transient thermal response in ultrasonic additive manufacturing of aluminum 3003. *Rapid Prototyping. J.* 17, 369–379. doi:10.1108/13552541111156496

Sriraman, M. R., Babu, S. S., and Short, M. (2010). Bonding characteristics during very high power ultrasonic additive manufacturing of copper. *Scr. Mater.* 62, 560–563. doi:10.1016/j.scriptamat.2009.12.040

Wang, L., Hofmann, V., Bai, F., Jin, J., and Twiefel, J. (2019a). A novel additive manufactured three-dimensional piezoelectric transducer: systematic modeling and experimental validation. *Mech. Syst. Signal Process.* 114, 346–365. doi:10.1016/j.ymssp.2018.05.025

Wang, Y., Yang, Q., Liu, X., Liu, Y., Liu, B., Misra, R. D. K., et al. (2019b). Microstructure and mechanical properties of amorphous strip/aluminum laminated composites fabricated by ultrasonic additive consolidation. *Mater. Sci. Eng.* 749, 74–78. doi:10.1016/j.msea.2019.01.039

Zhang, C., Deceuster, A., and Li, L. (2009). A method for bond strength evaluation for laminated structures with application to ultrasonic consolidation. *J. Mater. Eng. Perform.* 18, 1124–1132. doi:10.1007/s11665-008-9342-1

Zhang, C., and Li, L. (2009). A coupled thermal-mechanical analysis of ultrasonic bonding mechanism. *Metall. Mater. Trans. B* 40, 196–207. doi:10.1007/s11663-008-9224-9

Zhang, C. S., and Li, L. (2010). Effect of substrate dimensions on dynamics of ultrasonic consolidation. *Ultrasonics* 50, 811–823. doi:10.1016/j.ultras.2010.04.005

Zhang, S., Yi, D., Zhang, H., Zheng, L., Zhang, Y., Yang, Z., et al. (2015). Towards understanding of ultrasonic consolidation process with "process map". *Rapid Prototyp. J.* 21, 461–468. doi:10.1108/RPJ-05-2014-0067

Conflict of Interest: The authors declare that the research was conducted in the absence of any commercial or financial relationships that could be construed as a potential conflict of interest.

frontiers in Materials

ORIGINAL RESEARCH
published: 08 March 2021
doi: 10.3389/fmats.2021.643703

Compact Multi-Element Ultrasonic Transducer for Inspecting Split Pins in Nuclear Power Plants

Ma Guanbing[1,2]*, *Ding Hui*[1]*, *Wang Weiqiang*[2], *Ma Chao*[2], *Yan Jingli*[1], *Zhu Chuanyu*[2] and *Tang Jianbang*[2]

[1]School of Materials Science and Engineering, Southeast University, Nanjing, China, [2]CGN Inspection Technology Co., Ltd., Suzhou, China

A compact five-element integrated ultrasonic transducer was designed and manufactured for the inspection of defects in the split pins of control rod guide tubes in nuclear power plants. The transducer consists of three types of ultrasonic elements to detect cracks in the entire volume of the split pins. In the transducer design, two main factors were investigated: the coupling of elements in confined space and measurement sensitivity. The experimental results demonstrated that the developed transducer has good acoustic performance and defect response capabilities and can detect 10 mm × 2 mm × 0.5 mm notches in the three areas of the split pins. This work provides a foundation for applications in nuclear site inspections.

Keywords: ultrasonic transducer, pins inspection, nuclear application, defect detection, underwater testing

OPEN ACCESS

Edited by:
Chunlong Fei,
Xidian University, China

Reviewed by:
Kwok Ho Lam,
Hong Kong Polytechnic University, Hong Kong
Qifa Zhou,
University of Southern California, Los Angeles, United States

***Correspondence:**
Ma Guanbing
maguanbing@cgnpc.com.cn
Ding Hui
dinghui@seu.edu.cn

Specialty section:
This article was submitted to Smart Materials, a section of the journal Frontiers in Materials

Received: *18 December 2020*
Accepted: *01 February 2021*
Published: *08 March 2021*

Citation:
Guanbing M, Hui D, Weiqiang W, Chao M, Jingli Y, Chuanyu Z and Jianbang T (2021) Compact Multi-Element Ultrasonic Transducer for Inspecting Split Pins in Nuclear Power Plants. Front. Mater. 8:643703. doi: 10.3389/fmats.2021.643703

INTRODUCTION

Ultrasonic testing (UT) (Shung, 2011) has become indispensable in nuclear power plants for regular health status monitoring of in-service equipment because of its ability to locate minor defects in materials and structures non-destructively without detrimental environmental effects. To improve the efficiency and safety of nuclear power generation, components with complex geometries and special materials are used in next-generation nuclear power units. Ultrasonic testing of these complex structures places high requirements on ultrasonic transducers. Meanwhile, the development of a high-efficiency transducer is always important for reducing the radiation dose to which the ultrasonic testing operator is exposed (Xia and Han, 2016; Yuan et al., 2011; Guo et al., 2012). In recent years, many researchers have focused on the development of ultrasonic array probes and ultrasonic phased array technology to improve the efficiency of ultrasonic detection for key components in nuclear power plants (Norris et al., 1999; Chikazawa and Yoshiuji, 2015; Trampus, 2014; Drinkwater and Wilcox, 2006; Kim et al., 2016a; Shi et al., 2014; Fu et al., 2019). Trampus (Trampus, 2019) adopted a smart phase array UT probe to detect radial fatigue cracks in a nozzle radius. Yamamoto et al. (Yamamoto et al., 2016) developed a phased array ultrasonic inspection technique for monitoring cast austenitic stainless steel parts in nuclear power plants. Fu et al. (Fu et al., 2019) designed a 2.5 MHz 64 el dual-element matrix array probe and a 2.25 MHz 64 el single-linear array probe for the inspection of vertical defects in the butt-joint welds of CFETR vacuum vessel port stubs.

However, the ultrasonic phased array probes are too large to reach the surfaces of the components in complex structures with narrow scanning spaces. Even if the transducer could reach these components, the ultrasonic beams could not cover the target inspection area because of the limited scanning space. Compact ultrasonic probes have emerged as a solution to this problem (Yoon et al.,

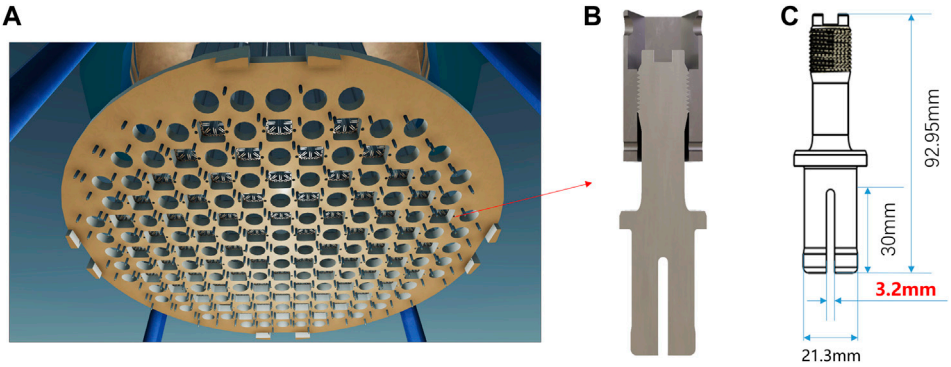

FIGURE 1 | Structure of the split pin: **(A)** postion of the split pin; **(B)** cross section; **(C)** geometry.

2014; Erhard et al., 2001; Song et al., 2002; Kim et al., 2016b; Abdallah and Namgung 2018). Pajnić et al. (Pajnić et al., 2009) developed a slim sword-like trinary probe with a pair of time-of-flight diffraction (TOFD) transducers for the detection and sizing of circumferential and axial cracks in the 3 mm gap between the inner surface of the penetration nozzle and the thermal sleeve. Glass et al. (Glass et al., 2011) proposed a 4-element probe to detect cracks inside nuclear reactors.

In this study, a compact multi-element ultrasonic transducer was designed and fabricated for the inspection of split pins, which are the key connecting parts of the internal components in the reactor core of a nuclear power plant. The spectrum performance and defect detection ability of the ultrasonic transducer were quantified. A mockup of the interior of a reactor core containing the split pins was designed and produced to simulate the actual engineering inspection environment. An underwater robot was developed to carry the transducer for underwater testing.

EXPERIMENTS

Split pin Inspection Requirements

A split pin is the key component for connecting and ensuring the accurate positioning of the control rod guide tube and the upper grid plate (IAEA, 2007; Andresen et al., 2012), as shown in **Figure 1A**. Nuts are used to fasten the split pins to the control rod guide tubes, as shown in **Figure 1B**. The material of the split pin is the alloy Inconel X-750. Solid solution and surface shot peening treatments were performed on the pin during the manufacturing process. The structure of the split pin is shown in **Figure 1C**. The total length of the split pin is 92.95 mm, and the free state diameter of the open end is 21.3 mm. Its diameter after compression is 20.5 mm. The width of the middle open slot is only 3.2 mm, and its length is 30 mm.

The structure of the split pin can be divided into the leaf zone, transition zone, shrank zone, and thread zone, as shown in **Figure 2**. Part failures mainly occur in the root of the open leaf area, the transition area between the shrank and leaf zones, and the first buckled area in the thread zone at three positions. The most common type of failure is cracks. The orientation of the cracks occurring in the thread and leaf zones is perpendicular to the axis of the split pin, while in the transition zone it is in the range of 30–60° along the axial direction.

Compact Transducer Design

Three types of conventional ultrasonic transducers are needed for the inspection of cracks in the three zones mentioned above. For cracks in the leaf zone, two semi-circular elements utilizing a 0° longitudinal wave are aligned along the bottom plane of the split pin, as shown in **Figure 2A**. For cracks in the threaded zone, a long strip element utilizing a 0° longitudinal wave is aligned on the top of the middle open slot, and the two semi-circular elements choosing emit-receive mode are also been used, as shown in **Figure 2B**. For tilt cracks in the transition zone, a send-and-receive mode transducer with two tandem elements are aligned on the side of the open slot in the leaf area, as shown in **Figure 2C**. A 45° transverse wave is used to detect the tilt cracks. It is time-consuming to use conventional ultrasonic transducers because changing the transducer takes place in cumbersome steps during the automatic scanning. To improve inspection efficiency, a compact five-element plug-in integrated transducer was designed to detect cracks in the entire volume of the split pins, as shown in **Figure 2D**.

The design details are as follows:

(1) Element frequency and size design: The split pin is made of a nickel-based material, which has higher acoustic attenuation compared to carbon steel. Therefore, a low-frequency wave should be chosen for inspecting the high-attenuation material. However, the length of the split pin is only 92.95 mm. The element frequency was set to 5 MHz in consideration of the tradeoff between the resolution and sensitivity. The elements were designed to be as large as possible to provide maximum detection coverage. Elements E4 and E5 were designed as semi-circles with a diameter of 16 mm. Elements E2 and E3 were designed as rectangles with a size of 2.4 mm × 8 mm. The size of element E1 is 2.2 mm × 8 mm. The design of element frequency and size is validated by CIVA, a professional sound field simulation software. The results show that the selected frequency and size can effectively cover the area need to be detected in the maximum sound pressure-6dB range, as shown in

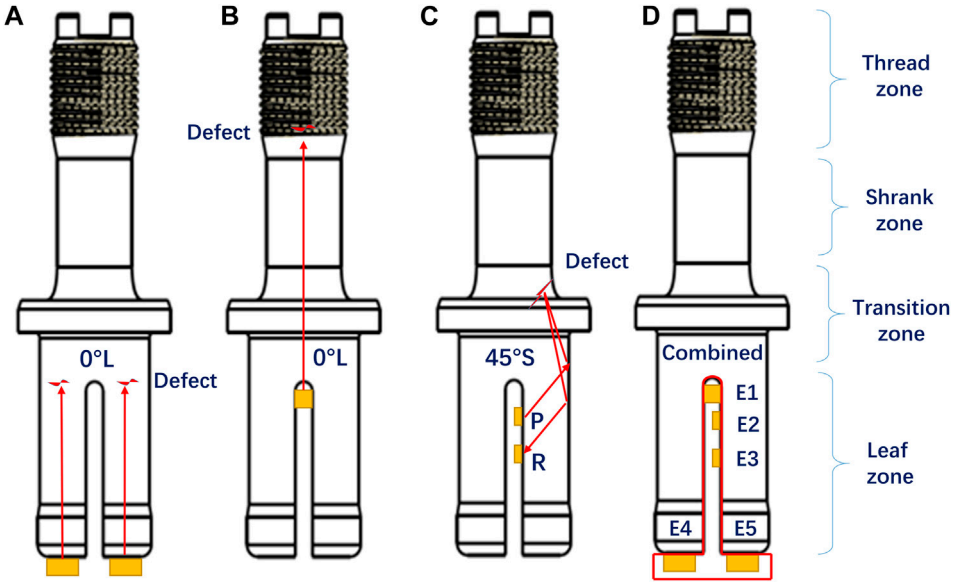

FIGURE 2 | Ultrasonic inspection strategies: **(A)** 0° L for leaf zone; **(B)** 0° L for thread zone; **(C)** 45° S for transition zone; **(D)** combined design.

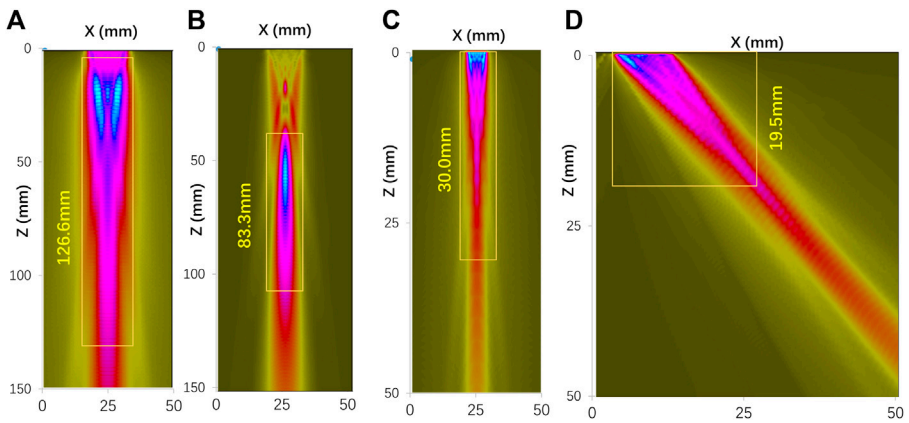

FIGURE 3 | Sound field coverage simulation: **(A)** E4/E5 for leaf zone; **(B)** E4/E5 for thread zone; **(C)** E1 for thread zone; **(D)** E2/E3 for transition zone.

Figure 3. Other frequencies such as 3, 4, and 6 MHz are also simulated. The sound field distribution simulation in the leaf zone of E4 or E5 in the split pin was shown in **Figure 4**. taking the leaf zone for example. The calculation results show that 5 MHz is a suitable frequency.

(2) Angle design: The defects in the thread and leaf area occur mainly in the direction perpendicular to the axis of the split pin. Therefore, the E4, E5, and E1 elements utilize a 0° longitudinal wave to detect defects at the leaf zone and the thread zone. The E2 and E3 elements were designed to utilize a transverse wave mode with a refraction angle of 45° to detect defects with axial directions of 30–60° at the transition zone. The distance between the E2 and E3 elements was designed to be 15 mm. The reason for this design is: The beam path of the 45° elements can detect transition zone 30–60° defects approximately vertically, through the split pin side-wall reflection, and the tandem detection pattern can be used for adapting to the change of the angle of the defect, therefore, it has a high probability of detection (POD).

(3) Coupling matching design: The inspection of the split pin was performed in an underwater environment. Water can, therefore, be used as the ultrasonic testing couplant. To ensure full coupling of the element, the size of the inserted chip was designed to meet strict requirements. The length of the inserted chip was accurately designed to be 30 mm to ensure full contact between the elements E4, E5, and E1. For the transition zone inspection, the element needs to be inserted into the opening slot, which has a width of 2.4 mm. Therefore, the thickness of the designed insert was

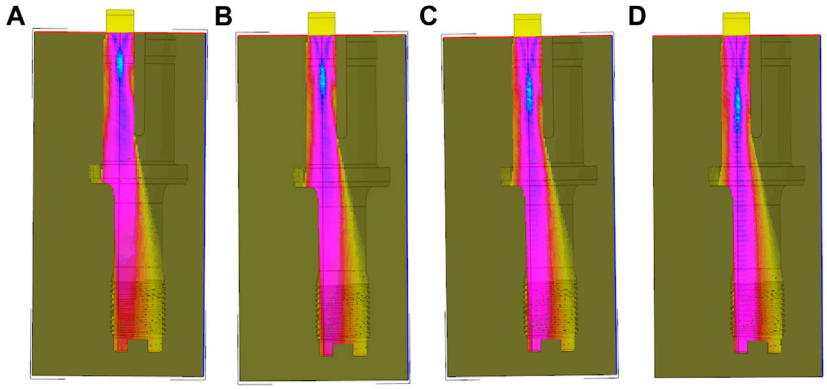

FIGURE 4 | Sound field distribution simulation of E4 or E5: **(A)** 3 MHz; **(B)** 4 MHz; **(C)** 5 MHz; **(D)** 6 MHz.

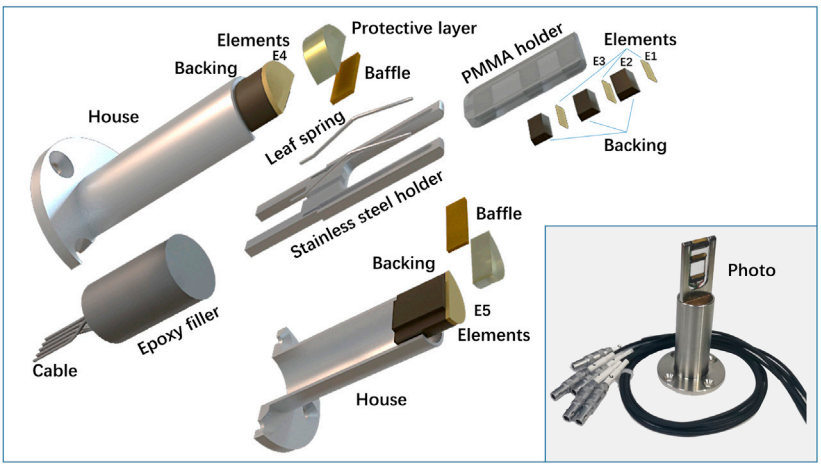

FIGURE 5 | Exploded device structure of the ultrasonic transducer.

made to be 2.2 mm, and a compressible spring was incorporated into the design on one side of the insert. The compressible spring fitting method was adopted to ensure the quality of the coupling and improve the safety performance of the transducer.

(4) Transducer housing design: The length of the transducer housing is same as the thickness of the upper grid plate, which is 45 mm. Four bolt holes were incorporated into the design to fix the transducer.

Compact Transducer Assembly

The ultrasonic transducer element, damping, cable, and connector were selected based on the design of the ultrasonic transducer, and the housing of the transducer was fabricated. The split pin ultrasonic integrated transducer was then assembled. The process is shown in **Figure 5**.

The piezoelectric ceramic PZT (1–3 composite, Changzhou ultrasonic electronics Co., LTD) was chosen for the transducer element considering the vibration characteristics. The protective film was made of polymethyl methacrylate (PMMA), which has good sound permeability, wear resistance, chemical stability, and radiation resistance. The PMMA thickness of the E4 and E5 is 5 mm E1 protective layer adopts a semi-circular structure adapted to the bottom arc end of the split pin, and the maximum thickness of PMMA, is the radius of the arc 1.6 mm E2 and E3 protective layer thickness design is mainly considered its 45° refractive angle in the split pin. According to Snell's law of refraction, the E2 and E3 in PMMA has a tilt of 38.5°, therefore, the thickness of the protective layer is 1–2.4 mm.

The transducer damping stops the vibration of the piezoelectric element quickly, reduces the pulse width, improves the resolution, and absorbs the ultrasonic waves emitted from the back of the element to reduce the initial pulse noise. The damping is made of a 35% tungsten powder +65% epoxy resin composite material.

A RG178 cable is used as the transducer cable partly because of its flexibility and resistance to electromagnetic interference, moisture, and temperature extremes. The length of the cables is 2.2 m. The connector uses a 50 Ω LEMO 00 coaxial connector.

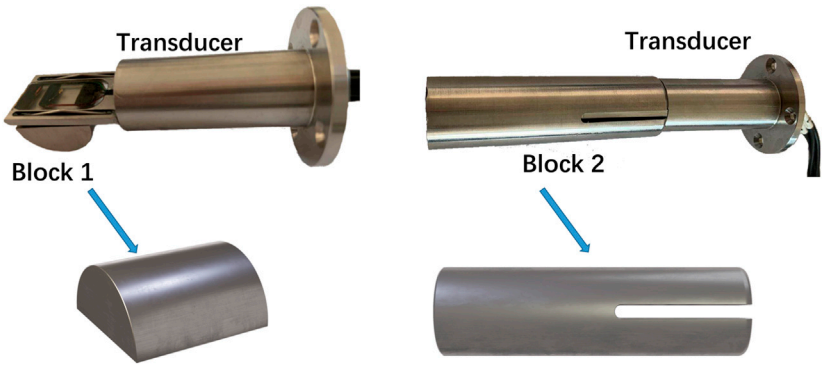

FIGURE 6 | Transducer testing using the designed blocks.

SUS304 stainless steel is used for the transducer housing owing to its ease of decontamination in a radioactive environment. The processing accuracy was precisely controlled, and the sharp edges were blunted during shell processing to prevent the edges from damaging the inspected component.

The overall assembly process of the probe is as follows: E1, E2, and E3 were first fixed on the PMMA holder. The whole assembly was then installed on the stainless steel holder together with the leaf spring. The probe wires of E1, E2, and E3 were placed through the stainless steel holder slot. The protective layer, baffle, E4, and backing were then installed into the housing, which was then filled with an epoxy filler. The 2.2 m long cable of the five elements was then connected to the BNC-type LEMO 00 cable.

Transducer Performance Tests

The electrical impedance characteristics were measured using an impedance analyzer (Agilent 4294A). The center frequency and bandwidth (BW) of the transducers were characterized using a pulse-echo response arrangement and two self-designed blocks. The material of the test blocks was X750, which is the same as that of the split pins. Test block 1 was a semi-cylindrical block with a diameter of 10 mm and a height of 22 mm. Test block 2 was a cylindrical block with an opening width of 3.2 mm, diameter of 21.3 mm, and length of 73 mm. Test block 1 was mainly used to evaluate the performance of E2 and E3, and test block 2 was mainly used to evaluate the performance of E1, E4, and E5. The experimental setups are shown in **Figure 6**.

Three types of defects were introduced to evaluate the detection performance of the ultrasonic transducer. The defects were made by wire-electrode cutting and were located at the leaf zone, transition zone, and thread zone of the split pin. The depth of the three defects was 2 mm and the outer arc length was 10 mm. The gap of the defect is 0.2 mm. The distribution of the defects is shown in **Figure 7**.

RESULTS AND DISCUSSION

Impedance and Pulse Echo

The measured impedance of the compact transducer is shown in **Figure 8**. All five elements had a nominal frequency of 5 MHz when the impedance was 50 Ω. The time domain and frequency domain pulse echoes are shown in **Figure 9**. The ultrasonic transducer was excited by an ultrasonic pulser and receiver (DPR300) with a pulse energy of 170 μJ and a repetition rate of 200 Hz. An acquisition card (NI PXIe-5260) was used for data acquisition at a sampling frequency of 1.25 GHz. A fast Fourier transform (FFT) was used to obtain the frequency spectrum of the pulse-echo signal. The central frequencies of the five elements are all located between 4 and 4.5 MHz. The two semicircular elements (E4 and E5) have similar wave forms, and the peak-to-peak amplitude is approximately 110 dB, which is the highest among the five elements. This is because the elements E4 and E5 are larger than the other. The amplitude of the signals received from elements E2 and E3 is approximately 50 dB, which is much lower than that from the other elements. This is because the two elements were used to emit shear waves. Acoustic attenuation occurred during the mode conversion at the interface between the PMMA wedge and the specimen when the ultrasound wave propagated into the wedge.

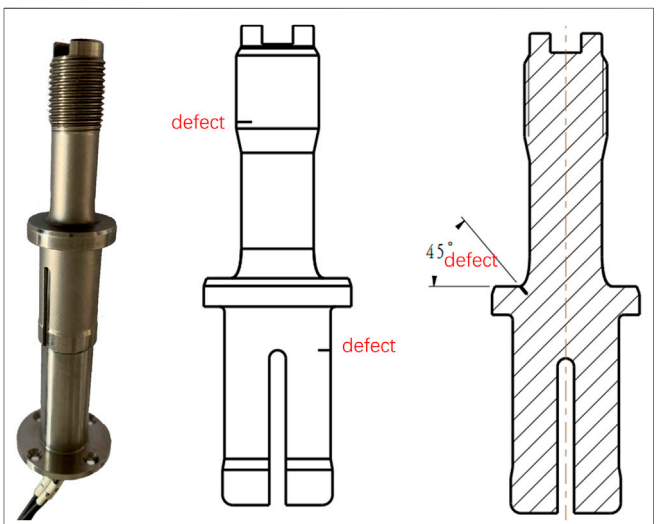

FIGURE 7 | Transducer testing using the blocks with defects.

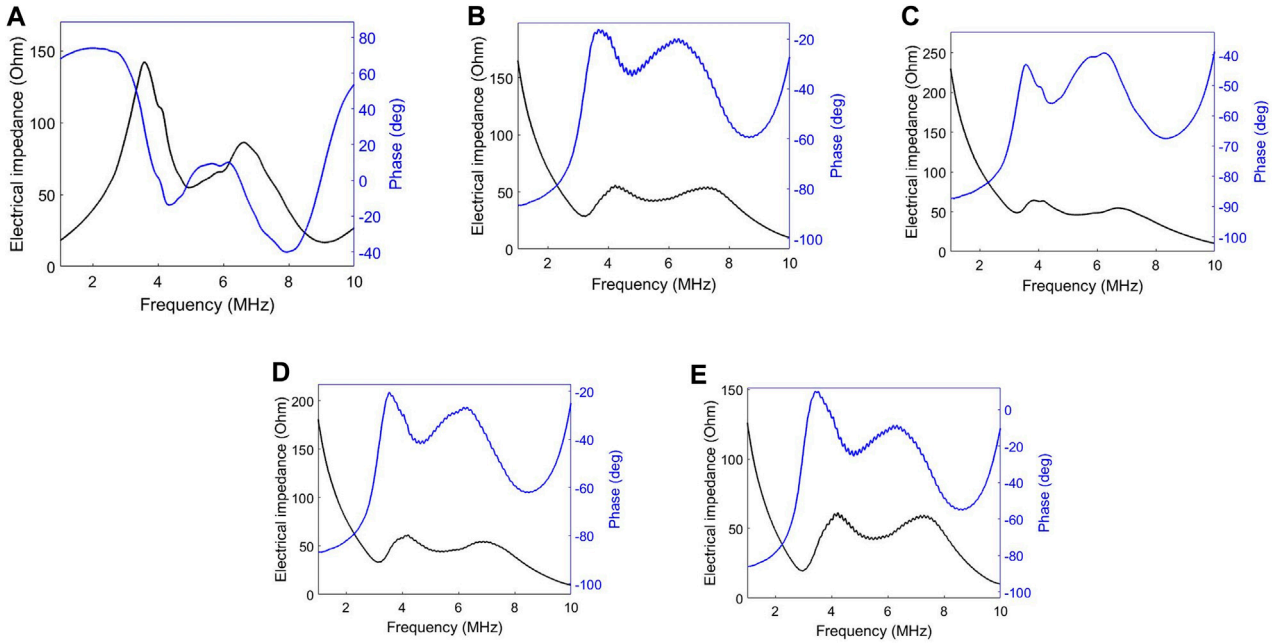

FIGURE 8 | Impedance and phase spectra of ultrasonic transducer: **(A)** element 1; **(B)** element 2; **(C)** element 3; **(D)** element 4; and **(E)** element 5.

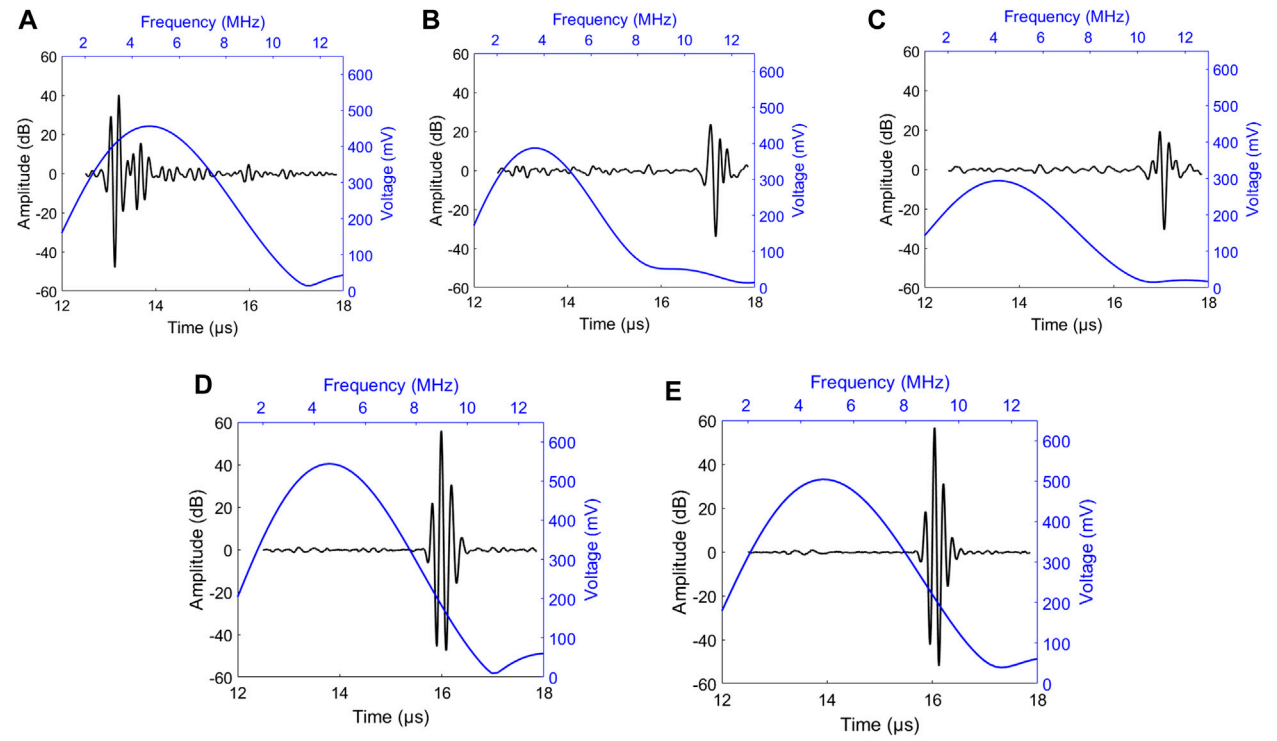

FIGURE 9 | Pulse-echo waveforms and frequency spectra of the transducer: **(A)** element 1; **(B)** element 2; **(C)** element 3; **(D)** element 4; **(E)** element 5.

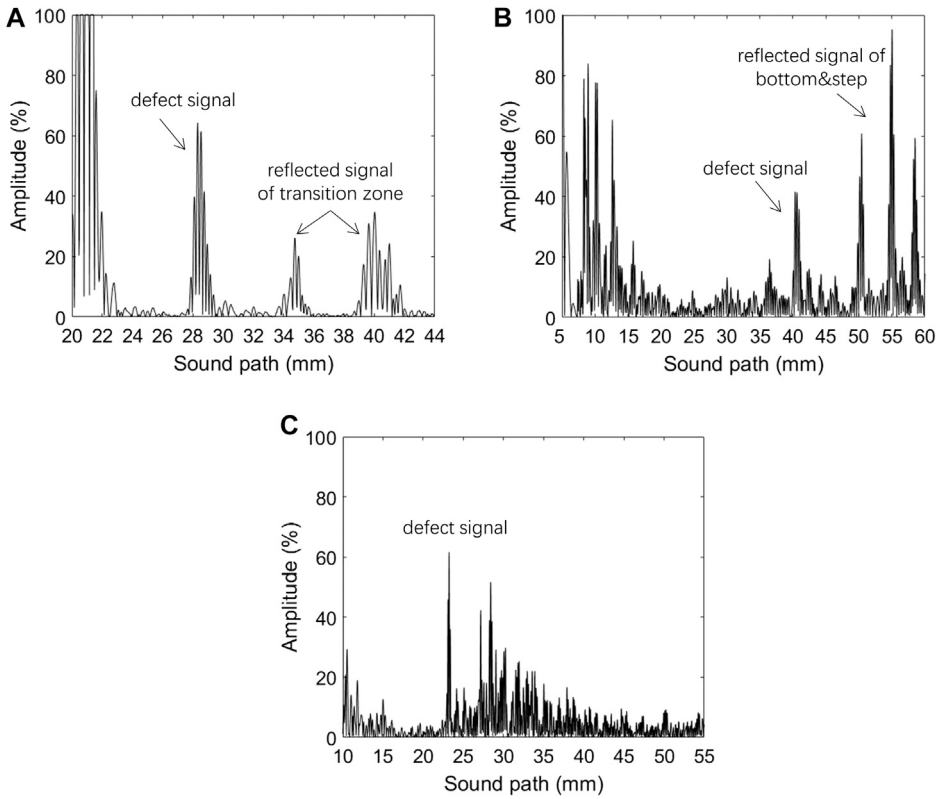

FIGURE 10 | Defect detection capability of transducer. **(A)** leaf zone; **(B)** thread zone; **(C)** transition zone.

Defect Detection Results

The detection performance of the probe was tested with split pins containing defects. The results show that the defects in the three zones could be accurately detected. The defect 3 in the leaf zone could be detected clearly, as shown in **Figure 10A**. The strong echo signal after the notch signal was caused by the reflected signal in the variable diameter area of the split pin transition zone. The notch signal in the threaded area could also be clearly detected by E1. The two signals with higher amplitudes seen after the notch signal are the reflected signals formed by the bottom surface of the split pin and the steps on the bottom surface. These two signals can be used as structure signals to characterize the performance of the transducer, as shown in **Figure 10B**. For the detection of defects in the transition zone, elements E2 and E3 were used for tandem ultrasonic inspection. When a defect is encountered, the incident wave is reflected and received by the receiving probe, and there is a defect echo displayed at a fixed sound path position. This is because the ultrasonic propagation sound path between the transmitting element and the receiving element is fixed. The sound path can be calculated by $S = 2T/\cos\beta$, where T is the thickness of the split pin leaf, and β is the refraction angle of the probe. As the thickness of the split pin leaf was T = 8.7 mm, and the refraction angle was $\beta = 45^{\circ}$, the defect sound path was calculated to be

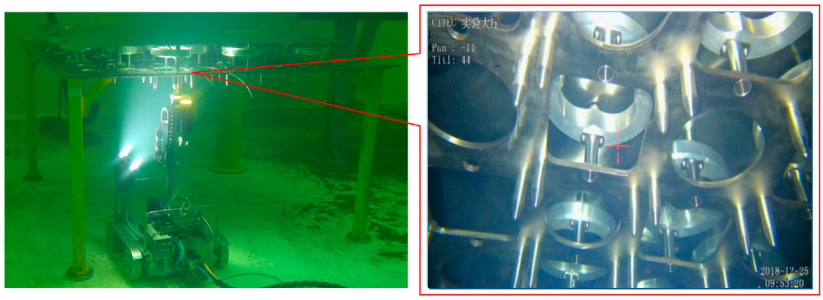

FIGURE 11 | Robot with transducer for underwater inspection.

approximately 24.5 mm, which is consistent with the notch signal shown in **Figure 10C**. In summary, the test results on the split pins with defects show that the compact multi-element ultrasonic transducer could detect all the designed defects in different zones.

FIELD APPLICATION AND FUTURE PROSPECTS

To assess the robustness of the compact transducer for field applications, a mockup of the interior of the upper reactor containing the control rod guide tube split pins was designed and fabricated. An underwater robot was also developed to carry the compact multi-element ultrasonic transducer to the target inspection area. The test was performed in a water-filled pool, as shown in **Figure 11**. The compact transducer could perform inspection tasks underwater for seven days without interruption. There are 32 split pins fixed on the mockup, of which 16 split pins have 50 crack defects in sensitive areas, and all defects can be detected using the developed compact multi-element ultrasonic transducer. This ability to work for long durations is highly advantageous for the inspection of control rod guide tube split pins in third-generation advanced pressurized water reactor (PWR) nuclear power plants in the future.

CONCLUSION

A compact five-element compact ultrasonic transducer was designed and produced for the inspection of split pins in control rod guide tubes in nuclear power plants. The experimental results show that the central frequencies of all five elements were controlled to be approximately 4–4.5 MHz. The compact transducer can detect all the defects in the various zones of the split pin with a defect length and height sensitivity of 10 mm length and 2 mm, respectively. The compact transducer has been proven to be capable of sustained operation in an underwater environment for seven days. This capability lays the foundation for further implementation and applications in nuclear power plants.

DATA AVAILABILITY STATEMENT

The raw data supporting the conclusions of this article will be made available by the authors, without undue reservation.

AUTHOR CONTRIBUTIONS

MG: transducer design DH: funding receiver WW: block design MC: impedance analysis YJ: pulse echo analysis ZC: under water testing. TJ: sound field simulation.

FUNDING

The study was supported by the National Key Research and Development Program of China (no. 2018YFB1106100).

REFERENCES

Abdallah, K. A. A., and Namgung, I. (2018). Virtual reality development and simulation of BMI nozzle inspection system for use during regular refueling outage of APR1400 family of reactors. *Ann. Nucl. Energ.* 116, 235–256. doi:10.1016/j.anucene.2017.12.010

Andresen, P. L., Flores-Preciado, J., Martin, M. M., and Robert, C (2012). "Microstructure and SCC of alloy X-750," in 15th international conference on environmental degradation of materials in nuclear power systems water reactors, Salt Lake City, Utah, April 2, 2012 (Wiley), 719–740.

Chikazawa, Y., and Yoshiuji, T. (2015). Water experiment on phased array acoustic leak detectionsystem for sodium-heated steam generator. *Nucl. Eng. Des.* 289, 1–7. doi:10.1016/j.nucengdes.2015.04.008

Drinkwater, B. W., and Wilcox, P. D. (2006). Ultrasonic arrays for non-destructive evaluation: a review. *NDT E Int.* 39, 525–541. doi:10.1016/j.ndteint.2006.03.006

Erhard, A., Schenk, G., Hauser, T., and VÖlz, U. (2001). New applications using phased array techniques. *Nucl. Eng. Des.* 206, 325–336. doi:10.1016/S0029-5493(00)00419-2

Fu, Y., Wu, J., Liu, Z., Wang, R., Jiang, B., and Wen, W. (2019). Phased array ultrasonic test of vertical defect on butt-joint weld of CFETR vacuum vessel port stub. *Fusion Eng. Des.* 141, 1–8. doi:10.1016/j.fusengdes.2019.02.010

Glass, S. W., Thigpen, B., and Renshaw, J. (2011). "Ultrasound and nonlinear resonant testing of nuclear reactor internals bolts," in Proceedings of the ASME 2011 pressure vessels and piping conference, Baltimore, Maryland, July 17–21, 2011 (Baltimore, MD: ASME), 185–189.

Guo, Y., Yuan, Q., Sun, Z., Logan, K., and Lam, C. (2012). Development of ultrasonic phased array systems for applications in tube and pipe inspection. *AIP Conf. Proc.* 1430, 1897. doi:10.1063/1.4716442

IAEA (2007). *Assessment and management of ageing of major nuclear power plant componets important to safety: PWR vessel internals*. Vienna, Austria: International Atomic Energy Agency, 74.

Kim, G. H., Park, C. K., Jin, S. W., Kim, H. S., Hong, K. H., Lee, Y. J., et al. (2016a). Qualification of phased array ultrasonic examination on T-joint weld of austenitic stainless steel for ITER vacuum vessel. *Fusion Eng. Des.* 109 (111), 1099–1103. doi:10.1016/j.fusengdes.2016.01.015

Kim, H.-H., Kim, H.-J., Song, S.-J., Kim, K.-C., and Kim, Y.-B. (2016b). Simulation based investigation of focusing phased array ultrasound in dissimilar metal welds. *Nucl. Eng. Technol.* 48, 228–235. doi:10.1016/j.net.2015.10.011

Norris, W. E., Naus, D. J., and Graves, H. L., III (1999). Inspection of nuclear power plant containment structures. *Nucl. Eng. Des.* 192, 303–329. doi:10.1016/S0029-5493(99)00125-9

Pajnić, M., Franjić, H., Gabrijel, S, and Jarnjak, F. (2009). "Advanced approach of reactor pressure vessel head inspection and repair/removal of RPVH J-weld indications," in Proceedings of the international conference nuclear energy for new Europe, Bled, Slovenia, September 14–17, 2009 (Dubrovnik, Croatian: Croatian Nuclear Society), 112.

Yamamoto, S., Semboshi, J., Sugawara, A., and Ochiai, M. (2016). "Phased array ultrasonic inspection technique for cast austenitic stainless steel parts of nuclear power plants," in 2016 24th international conference on nuclear engineering, Charlotte, North Carolina, June 26–30, 2016 (ASME), 6.

Shi, J., Hou, D., Guo, W., Zhou, Y., Chen, X., and Zheng, J. (2014). "Ultrasonic inspection of large diameter polyethylene pipe used in nuclear power plant," in American society of mechnical Engineering, vessels and piping division, Anaheim, California, July 20–24, 2014 (ASME), 8.

Shung, K. K. (2011). Diagnostic ultrasound: past, present, and future. *J. Med. Biol. Eng.* 3, 1371–1374. doi:10.5405/jmbe.871

Song, S.-J., Shin, H. J., and Jang, Y. H. (2002). Development of an ultrasonic phased array system for nondestructive tests of nuclear power plant components. *Nucl. Eng. Des.* 214, 151–161. doi:10.1016/S0029-5493(02)00024-9

Trampus, P. (2014). Ensuring safety of structures and components at nuclear power Plants,1st international conference on structural integrity, ICONS-2014. *Procedia Eng.* 86, 486–495. doi:10.1016/j.proeng.2014.11.062

Trampus, P. (2019). Role and importance of NDE in nuclear power plant life extension. *Procedia Struct. Integr.* 16, 161–168. doi:10.1016/j.prostr.2019.07.036

Xia, J. W., and Han, C. (2016). Ultrasound inspection of zirconium alloy cladding tube for nuclear fuel. *Nucl. Power Eng.* 3, 122–126. doi:10.13832/j.jnpe.2016.03.0122

Yoon, B., Kim, Y., and Lee, J. (2014). Steam generator small bore piping socket weld inspection using the phased array ultrasonic technique. *J. Nucl. Sci. Technol.* 51 (2), 231–239. doi:10.1080/00223131.2014.855151

Yuan, Q., Guo, Y., Sun, Z., and Lam, C. (2011). Development of an ultrasonic phased array for nondestructive testing of pipes: theory and practice. *Mater. Eval.* 69 (4), 501–506.

Conflict of Interest: Authors MG, WW, MC, ZC, and TJ were employed by company CGN Inspection Technology Co., Ltd.

The remaining authors declare that the research was conducted in the absence of any commercial or financial relationships that could be construed as a potential conflict of interest.

frontiers in Materials

ORIGINAL RESEARCH
published: 09 April 2021
doi: 10.3389/fmats.2021.663109

An Improved Equivalent Circuit Simulation of High Frequency Ultrasound Transducer

Zhitian Shen[1,2], Jie Xu[2,3], Zhangjian Li[2], Youwei Chen[2], Yaoyao Cui[2] and Xiaohua Jian[2]**

[1] School of Biomedical Engineering (Suzhou), Division of Life Sciences and Medicine, University of Science and Technology of China, Suzhou, China, [2] Medical Acoustic Department, Suzhou Institute of Biomedical Engineering and Technology, Chinese Academy of Sciences, Suzhou, China, [3] Academy for Engineering and Technology, Fudan University, Shanghai, China*

The equivalent circuit simulation plays an important role in the design of ultrasound transducer. However, the existing methods are difficult to achieve the effect of matching and backing layer, and not able to accurately simulate the transducer with cable. Especially in the application of high frequency ultrasound, the long cable has a great influence on the performance of the transducer. To overcome these limitations, this paper proposed an improved equivalent circuit method, which combined Leach model and transmission line model. It can realize the complete simulation of ultrasound transducer with a long cable, matching layer, and backing layer in PSPICE circuit simulation software when the parameters were measured. Its principles were briefly introduced, and ultrasound transducers with different frequencies (12 and 20 MHz), different matching layers, and different cable lengths (0.5–2.5 m) were designed and fabricated to verify the effectiveness of the method, which is also compared with the traditional KLM method using PiezoCAD. The experiment results showed that the long cable, matching layer, and backing layer have a significant impact on the performance of high frequency ultrasound transducers, and this proposed method has good agreement with these results. Moreover, for the simulation of the complete transducer, the effect of this method is better than KLM model. Besides, this method does not need to know the specific equivalent circuit of matching, backing layer, or cable wire, it can accurately predict the impedance and phase of the transducer through the material parameters, which is very helpful for the material selection and optimization of subsequent transducer design and fabrication. The study indicates that this improved equivalent circuit method is suitable to be applied in the general circuit simulation software and provides strong support for the high frequency transducer and system design.

Keywords: equivalent circuit, simulation, high frequency, transducer, cable, PSPICE

OPEN ACCESS

Edited by:
Chunlong Fei,
Xidian University, China

Reviewed by:
Laiming Jiang,
University of Southern California, Los Angeles, United States
Venu Gopal Madhav Annamdas,
Continental (Germany), Germany

****Correspondence:***
Xiaohua Jian
jianxh@sibet.ac.cn
Yaoyao Cui
cuiyy@sibet.ac.cn

Specialty section:
This article was submitted to Smart Materials, a section of the journal Frontiers in Materials

Received: *02 February 2021*
Accepted: *22 March 2021*
Published: *09 April 2021*

Citation:
Shen Z, Xu J, Li Z, Chen Y, Cui Y and Jian X (2021) An Improved Equivalent Circuit Simulation of High Frequency Ultrasound Transducer. Front. Mater. 8:663109. doi: 10.3389/fmats.2021.663109

INTRODUCTION

Simulation plays an important role in the design of ultrasound transducers and helps designers to understand the effects of system parameters (Tarpara and Patankar, 2018). Excellent simulation can usually obtain very accurate results, save the time and cost consumed in the experimental development of prototype equipment, and also reduce the number of iterations of the product (Jensen, 2004).

However, with the emergence of high-frequency and even ultra-high-frequency ultrasound applications, such as intravascular ultrasound imaging, ophthalmic ultrasound imaging, small animal ultrasound imaging, ultrasound microscopy, etc (Pandian et al., 1990; Turnbull et al., 1993; Pavlin and Foster, 1998; Sahai, 1998), the design of transducers has become more complex. The number of matching layers is increasing and the materials are not readily available. This leads to the need to estimate the impedance of the transducer based on the material or for establishing impedance matching networks (Wu and Chen, 1999). Therefore, high requirements are put forward to the simulation.

The design and performance prediction of ultrasound transducers require appropriate software tools, which involve a variety of knowledge of acoustics, electronics, and ultrasonic properties of the propagation medium (Merdjana et al., 2014; Rathod, 2020). The finite element model and equivalent circuit model are the main research methods (Zheng et al., 2018). For example, Comsol, a commercial software based on the finite element model, divides the transducer into many small units for calculation (Fan et al., 2014). This method has high precision, but it requires a lot of computation time and computation resources. In contrast, the equivalent circuit model has a very fast calculation speed and high calculation accuracy. The classical equivalent circuit model of the transducer was first proposed by Mason (1942). The equivalent circuit uses an ideal transformer to separate the piezoelectric material into an electrical port and two acoustic ports, which describes the conversion of mechanical quantity to electrical quantity (Tarpara and Patankar, 2018). Later, Redwood (1961) introduced the transmission line model to solve the transient response of the transducer on this basis, and described the propagation of mechanical signals from one surface of the transducer to another. Krimholtz et al. (1970) proposed a different equivalent circuit model for piezoelectric transducers. Its circuit consists of a transformer connected to the middle of a transmission line. It is suitable for the simulation of multi-layer structure (Van Deventer and Lofqvist, 2000; Kim et al., 2020). BVD (Butterworth-Van Dyke) model is the simplest model (Aouzale et al., 2008; Kim et al., 2020; Zhou et al., 2020), which only needs four common components to realize the transducer simulation, and the implementation of multi-frequency BVD model is also very simple. In 1994, Leach proposed to replace the frequency-dependent transformer in Mason's model with a controllable current source and a controllable voltage source to simulate the transducer, and achieved good results (Leach, 1994). However, these models have some limitations. The negative capacitance C_0 contained in Mason model and the frequency dependent transformer contained in KLM model are difficult to be realized in PSPICE software. BVD model is not suitable for high frequency transducer performance from material parameters. Leach model is widely used, but most of the applications lack the modeling of matching layer, backing layer and cable (Van Deventer and Lofqvist, 2000; Johansson and Martinsson, 2001; Roa-Prada et al., 2007; Aouzale et al., 2008; Chahal and Reddy, 2013; Tarpara and Patankar, 2018; Takahashi et al., 2019; Zheng et al., 2019).

Moreover, high frequency ultrasound transducer usually consists of a piezoelectric ceramic layer, a matching layer, a backing layer, and a cable. Performance is easily affected by long cables and systems (Jian et al., 2018). Therefore, it is necessary to establish a complete equivalent circuit model of the transducer, which can be implemented in PSPICE circuit simulation software, to complete the simulation and performance prediction of the transducer. Based on Leach model and transmission line theory, this paper established a complete equivalent circuit model to study the performance of high frequency transducers. The simulation of a transducer with a long cable, matching layer, and backing layer was realized. Based on the measured material parameters, this model predicted the impedance of the transducer with and without cable. The actual measured results were compared with the theoretical calculation results. For transducers with different lengths of cable, the simulation results were verified that the long cables have a great effect on the performance, and the simulation results accorded with the measured results. It is also compared with PiezoCAD software based on KLM model and achieved better results. For high frequency ultrasound transducer, this method allows researchers to consider the influence of cable and system while studying the performance of the transducer, and even further adjust the circuit design of the transducer.

THEORY

In order to establish the equivalent circuit model of the multi-layer ultrasound transducer structure, the controlled source model and the lossy transmission line are used to simulate the physical structure of the piezoelectric ultrasound transducer and cable which is bonded to the transducer. The theory uses a typical structure of transducer consisted of a piezoelectric ceramic layer as the active layer, a matching layer, a backing layer, and a cable.

Leach Model

Figure 1 shows the controlled source model used to simulate the sensor.

In the model, B, E, and F are the ports of the piezoelectric ultrasonic transducer. Port E is used to connect the excitation

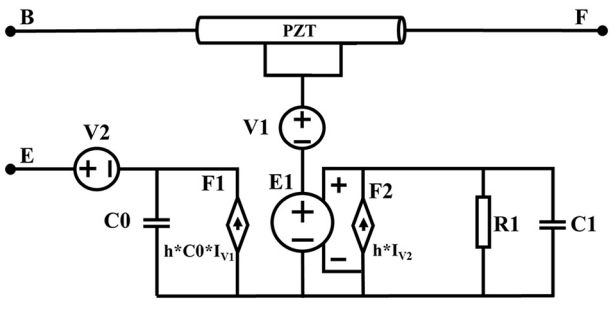

FIGURE 1 | The Leach model of transducer.

source of the transducer, port B is used to connect the backing layer, and port F is used to connect the matching layer. The model uses the controllable voltage and current sources to model the piezoelectric phenomenon. By comparing the wave equation and the telegraph equation of the acoustic wave in the piezoelectric material, the controllable source equivalent circuit model of the piezoelectric ultrasonic transducer is established. The specific derivation can be found in reference (Leach, 1994). So, the piezoelectric effect simulation is realized. All parameters in the model are derived from the material characteristics of the transducer. The required parameters in the model are as follows:

$$\mathbf{f} = \frac{\mathbf{c}}{\mathbf{2d}} \tag{1}$$

$$\mathbf{C0} = \frac{\boldsymbol{\varepsilon}^{\mathbf{S}}\mathbf{A}}{\mathbf{d}} \tag{2}$$

$$\mathbf{h} = \frac{\mathbf{e_{33}}}{\boldsymbol{\varepsilon}^{\mathbf{S}}} \tag{3}$$

Where, $\mathbf{d(m)}$ represents the thickness of piezoelectric ceramics, which determines the center frequency of the sensor $\mathbf{f(Hz)}$, $\mathbf{c}$*(m/s)* represents the speed of sound in piezoelectric ceramics, $\mathbf{C0(F)}$ represents the static capacitance, ε^S is the relative clamped dielectric constant, $A(m^2)$ represents the cross-sectional area of the piezoelectric material along the direction of sound wave propagation, $h(N/C)$ represents piezoelectric constant, $e_{33}(10^{-12}m^2/N)$ represents the short circuit elastic constants, $R1$ and $C1$ represent an integrator, which is 1 $k\Omega$ and 1 F, respectively.

The PZT part in **Figure 1** can be simulated as a lossy transmission line by comparing the propagation equations of wave in electric transmission line and acoustic medium (Van Deventer and Lofqvist, 2000), we can use a lossy transmission line to simulate the propagation of the acoustic wave in the medium. To simulate the propagation of sound waves through the transducer, the parameters of the piezoelectric ceramic transmission line are calculated as follows:

$$\mathbf{L} = \mathbf{A}\boldsymbol{\rho} \tag{4}$$

$$\mathbf{C} = \frac{\mathbf{1}}{\mathbf{A}\boldsymbol{\rho}\mathbf{c^2}} \tag{5}$$

$$\mathbf{R} = \mathbf{2}\boldsymbol{\rho}\mathbf{c}A\boldsymbol{\alpha} \tag{6}$$

$$\mathbf{G} = \frac{\mathbf{2}}{\boldsymbol{\rho}\mathbf{c}A}\boldsymbol{\alpha} \tag{7}$$

Where $\boldsymbol{\rho}(\mathbf{kg/m^3})$ represents the density of piezoelectric materials, $\boldsymbol{\alpha}(\mathbf{NP/m})$ represents the attenuations.

Transmission Line Model

The electric transmission line model is usually described in **Figure 2**.

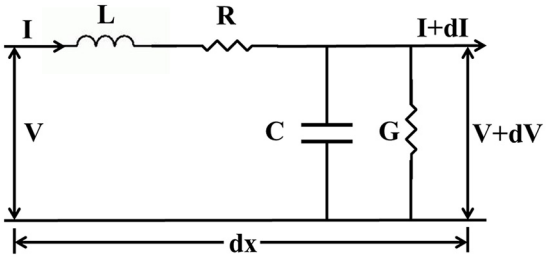

FIGURE 2 | The transmission line model of cable.

The telegraph equation can be derived that (Magnusson et al., 2000):

$$\boldsymbol{\gamma} = \sqrt{(\mathbf{R} + \mathbf{j}\boldsymbol{\omega}\mathbf{L})\,(\mathbf{G} + \mathbf{j}\boldsymbol{\omega}\mathbf{C})} = \boldsymbol{\alpha} + \mathbf{j}\beta \tag{8}$$

$$\mathbf{Z_0} = \sqrt{\frac{\mathbf{R} + \mathbf{j}\boldsymbol{\omega}\mathbf{L}}{\mathbf{G} + \mathbf{j}\boldsymbol{\omega}\mathbf{C}}} \tag{9}$$

Where γ represents the propagation constant, α represents attenuation constant, β represents phase constant, Z_0 represents the characteristic impedance.

The input impedance of the cable is (Peres and Lopes, 1998; de Souza et al., 2003):

$$\mathbf{Z_{in}} = \frac{\mathbf{Z_L} + \mathbf{Z_0}\mathbf{tanh}(\boldsymbol{\gamma}\mathbf{L})}{\mathbf{Z_0} + \mathbf{Z_L}\mathbf{tanh}(\boldsymbol{\gamma}\mathbf{L})}\mathbf{Z_0} \tag{10}$$

The L is the length of the cable, Z_0 is the characteristic impedance, Z_L is the load impedance.

When the load circuit is short and open, respectively, we can measure the input impedance of the transmission line. When the terminal of the cable is short, the load impedance of the cable Z_L is 0. In the same way, when the terminal of the cable is open, the load impedance Z_L is infinite. According to Eq. 10, the two variables could derive the characteristic impedance Z_0 and γ. And then, according to Eqs. 8 and 9, the lumped circuit parameters could also be derived. Further, the distribution parameters of the transmission line can be calculated:

$$\mathbf{R} = \mathbf{real}(\mathbf{Z_0}\boldsymbol{\gamma}) \tag{11}$$

$$\mathbf{L} = \mathbf{imag}\,(\mathbf{Z_0}\boldsymbol{\gamma}) \tag{12}$$

$$\mathbf{G} = \mathbf{real}(\frac{\boldsymbol{\gamma}}{\mathbf{Z_0}}) \tag{13}$$

$$\mathbf{C} = \mathbf{imag}(\frac{\boldsymbol{\gamma}}{\mathbf{Z_0}}) \tag{14}$$

An Improved Equivalent Circuit Simulation

The complete ultrasound transducer includes the matching layer, piezoelectric ceramic, backing layer, adhesive layers, and

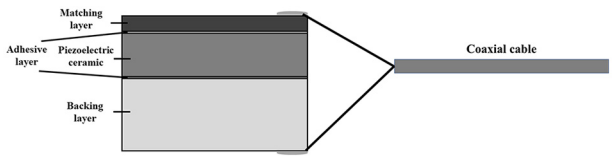

FIGURE 3 | The structural diagram of complete transducer.

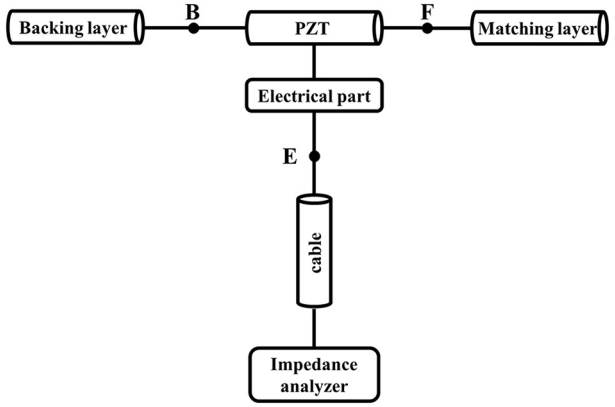

FIGURE 4 | The improved equivalent circuit simulation diagram of complete transducer.

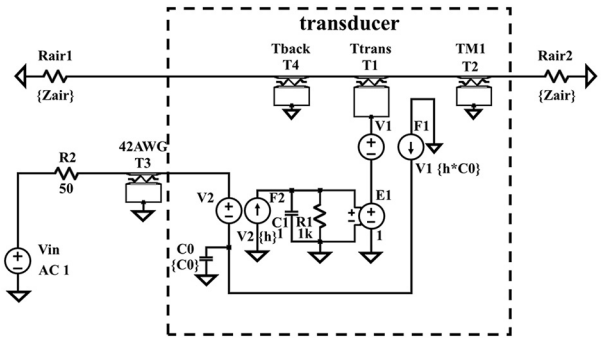

FIGURE 6 | The equivalent circuit simulation diagram by using LTspice software.

TABLE 1 | The parameters of PZT-5H for Leach model.

	PZT-5H	Matching Layer 1	Matching Layer 2	Backing Layer
$\rho(kg/m^3)$	7,850	1,773	2,025	3,200
$A(m^2)$	4.5 μ	4.5 μ	4.05 μ	4.5 μ
$c(m/s)$	4,600	3,300	2,874	2,250
$\alpha(NP/m)$	160	427	850	4,272
ε^S	1,050	/	/	/
$e_{33}(10^{-12}m^2/N)$	21	/	/	/

cable. The typical structural diagram of a transducer is shown in **Figure 3**.

According to this diagram, we established the improved equivalent circuit simulation in **Figure 4**.

In general, the adhesive layer is very thin, which has little effect on the performance of the piezoelectric ultrasonic transducer. So, the adhesive layers are ignored in this model.

SIMULATIONS AND EXPERIMENTS

The Established Model Includes a Transducer and a Cable

To verify above theoretical equivalent circuit simulation model, the high frequency transducers were fabricated in **Figure 5** and their models in **Figure 3** were also established.

It consists of a piezoelectric ceramic layer, a matching layer, a backing layer, and a long cable. Among them, the PZT part is PZT-5H (CTS Electronic Components, Inc., Elkhart, IN, United States), the backing layer part is the conductive silver epoxy (E-Solder 3022, Von Roll Insulation, Isola, MS, United States), the matching layer is self-made materials, and the cable is a 42 AWG coaxial wire. Adhesive layers are made of epoxy (epo–tek 301, Epoxy Technology, Billerica, MA, United States). Usually, these layers are very thin so that it has little effect on the performance of the transducer and these will be ignored in our model. According to the structure, the equivalent circuit model of this transducer was established using LTspice software (Analog Device, Norwood, MA, United States), as shown in **Figure 6**.

The equivalent circuit model is composed of three parts: piezoelectric material part, backing part, and matching layer part. The piezoelectric material is composed of T1 and a controlled source model (E1, F1, F2) to complete the simulation

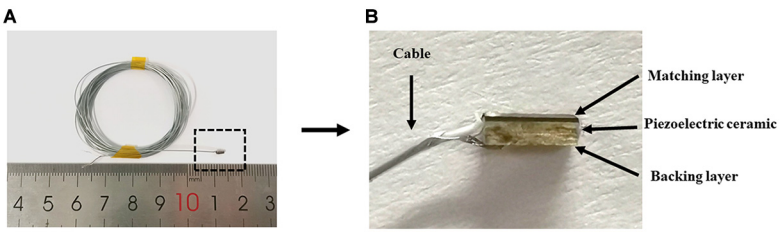

FIGURE 5 | (A) the complete transducer **(B)** the detail of transducer.

TABLE 2 | The input impedance of the open circuit and short circuit.

Fc	Zs	Zo	Z0	R(Ω)	L(nH)	C(pF)	G(S)
12M	55.07+78.36i	26.99+16.69i	40.11 +37.82i	11.72	442.47	59.68	0.011
20M	83.89–116.72i	9.51+1.61i	34.46–14.14i	5.27	172.78	109.72	0.008

of the piezoelectric effect of piezoelectric materials. T2 and T4 were used to simulate the matching layer and the backing part, respectively. A lossy transmission line model was used to simulate the cable. In the experiment, the impedance analyzer was used to measure the impedance curves at both ends of the transducer. LTspice software is used to realize the equivalent circuit simulation of the transducer. Finally, the measured results were compared with the simulation results to verify the feasibility of the model. To verify the practicability of the model for transducers of different frequencies, different matching layers, and different cable lengths, two kinds of frequency transducers were made, and two kinds of matching layer materials were used. The simulation was carried out in the case of cable and without cable, respectively, and made the comparison with the actual test.

The Transducers Without Cable

In this experiment, the practicability of the model for the transducer without cable is verified. Two kinds of frequency transducers are made. The piezoelectric ceramic part used the same material, PZT-5H. The matching layer part used two kinds of self-made materials, and the backing layer was also made of the same material. At the same time, considering the influence of technology in the process of making the transducer, the parameters will be slightly adjusted during the actual simulation. The measured parameters of the material are shown in **Table 1**. For No. 1 transducer, the thickness of piezoelectric ceramic part is 170 μm, and the matching layer is 57 μm thick; For No. 2 transducer, the PZT layer is 185 μm, and the matching layer is 53 μm; For No. 3 transducer, the PZT layer is 100 μm, and the matching layer is 35 μm.

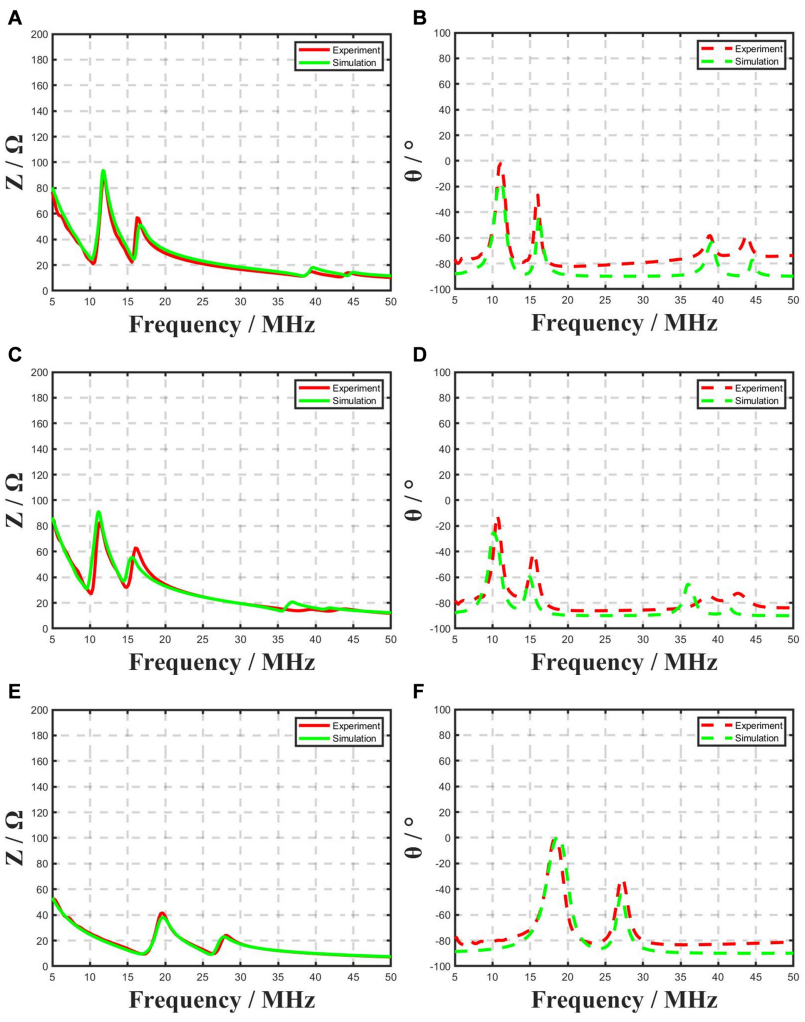

FIGURE 7 | The simulated and measured results of transducers without cable **(A)** the amplitude of No. 1 transducer **(B)** the phase of No. 1 transducer **(C)** the amplitude of No. 2 transducer **(D)** the phase of No. 2 transducer **(E)** the amplitude of No. 3 transducer **(F)** the phase of No. 3 transducer.

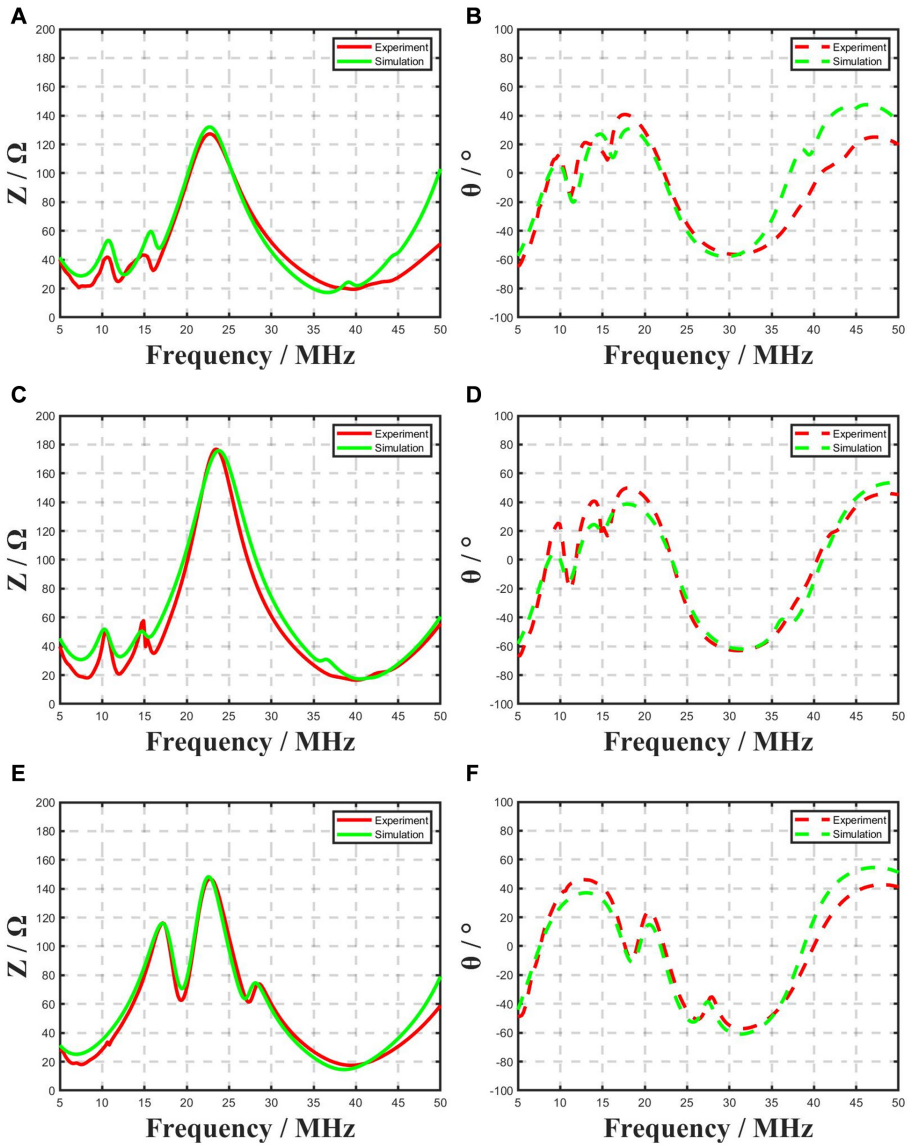

FIGURE 8 | The simulated and measured results of transducer with cable **(A)** the amplitude of No. 1 transducer **(B)** the phase of No. 1 transducer **(C)** the amplitude of No. 2 transducer **(D)** the phase of No. 2 transducer **(E)** the amplitude of No. 3 transducer **(F)** the phase of No. 3 transducer.

The Transducers With Cable

In this experiment, three transducers in the previous section were used to bond long cable and carried out measurements. A 42 AWG cables were used and the length of cables was 2.5 m. For the cable, we used the impedance analyzer to measure the input impedance of the open circuit and short circuit. According to equation 10, γ, and Z_0 can be derived. The required parameters of the transmission line can also be derived according to equation 11∼14. Typical parameters are shown in **Table 2**.

The Transducer With Different Cable Lengths

Because the different lengths of cable have a great impact on the high frequency transducers, it has to study the transducer performance at different cable lengths. In this experiment, we measured the open circuit and short circuit input impedance of 42AWG cable at 20 MHz and calculated the lumped circuit parameters to support the transmission line model in LTspice software. The parameters which used in Leach model were close to those mentioned in **Table 1**. To verify the practicability of the model for transducers of different cable lengths, the aforementioned No. 3 transducers with 42 AWG cables of different lengths were used. The cable lengths were 0.5, 1.5, and 2.5 m, respectively. The impedance of the transducer was measured and compared with the simulation results. The consistency between the simulation results and the measured results of transducers with different lengths confirms that the model can be used to simulate transducers of different lengths, not just one length.

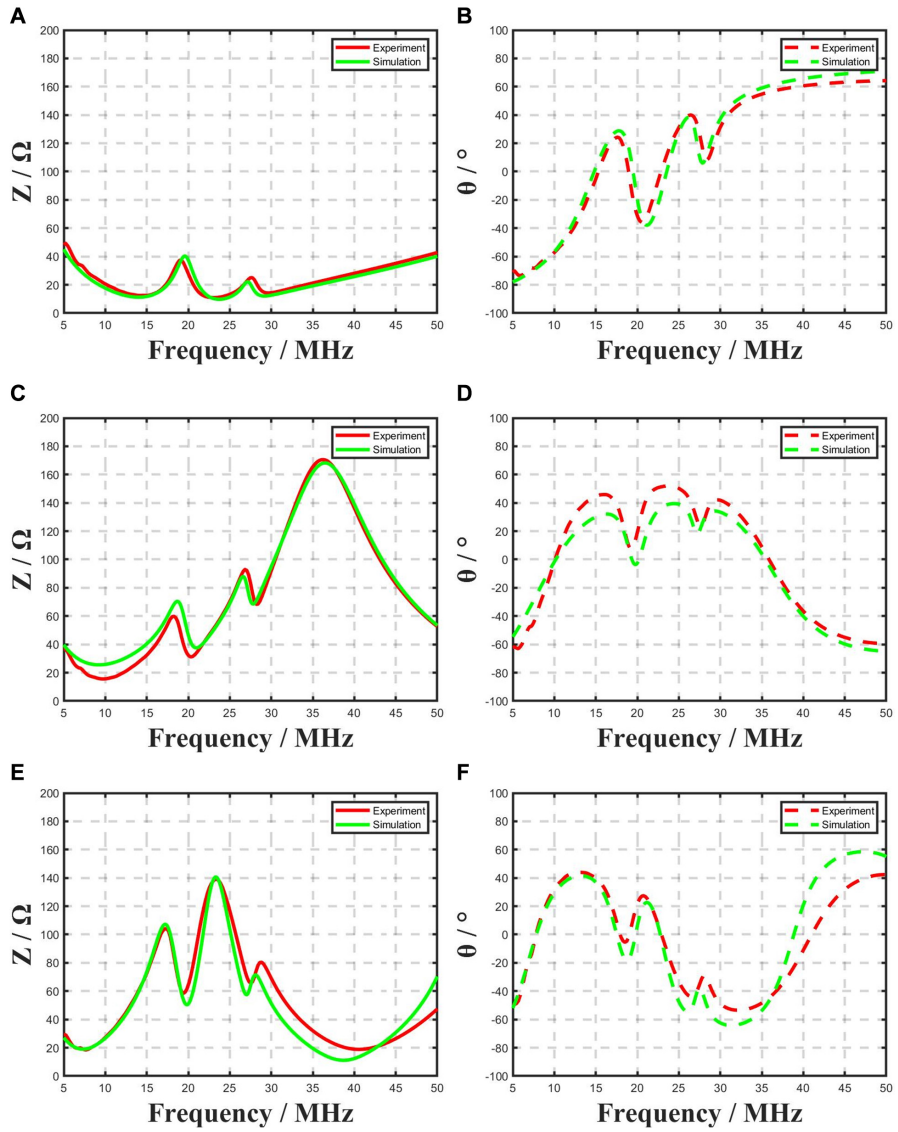

FIGURE 9 | The simulated and measured results of **(A)** the amplitude of 20MHz transducer with 0.5 m cable **(B)** the phase of 20MHz transducer with 0.5 m cable **(C)** the amplitude of No. 3 transducer with 1.5 m cable **(D)** the phase of 20MHz transducer with 1.5 m cable **(E)** the amplitude of No. 3 transducer with 2.5 m cable **(F)** the phase of 20MHz transducer with 2.5 m cable.

RESULTS AND DISCUSSION

The Results of Transducer Without Cable

In the experiment of the transducer without cables, we compared the simulation results of the three transducers with the measured results, as shown in **Figure 7**. It can be seen that the simulation results are in good agreement with the measured results, especially at the position of the resonance. The simulated and measured center frequencies of the No. 1 transducer are 11.76 MHz and 11.75 MHz. The amplitudes at the center frequencies are 93.76Ω and 89.58Ω. The phases at the center frequencies are −46.90° and −34.35°. The errors of frequency, amplitude, and phase are, respectively, 0.08%, 4.18Ω, and 12.55°. The simulated and measured center frequencies of the No. 2 transducer are 11.13 MHz and 11.3MHz. The amplitudes are 91.2Ω and 82.65Ω. The phases are −53.07° and −43.95°. The errors are 1.5%, 8.55Ω, and 9.12°. The simulated and measured center frequencies of the No. 3 transducer are 19.68Ω and 19.63MHz. The amplitudes are 38.04Ω and 41.67Ω. The phases are −47.08° and −43.35°. The errors are 0.25%, 3.63Ω, and 3.73°. It is obvious that the simulation results are close to the measured results. Besides, because of the addition of the matching layer, the second resonance peak appears in all three transducers.

The Results of Transducer With Cable

In the experiment of transducer with cable, we compared the simulation results and measured results of three kinds of

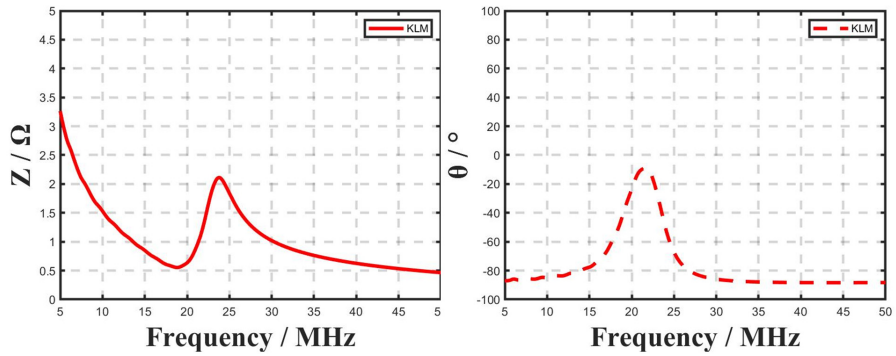

FIGURE 10 | The amplitude and phase of 20M transducer by using PiezoCAD.

TABLE 3 | The comparison of the improved model and PiezoCAD.

	Error of Fc	Error of amplitude	Error of phase @Fc	Second resonance	Cable
Improved model	0.25%	3.63Ω	3.73°	Appear	Considered
PiezoCAD	>10%	>10Ω	14.31°	Not appear	Not considered

transducers, as shown in **Figure 8**. Under the influence of the long cable, the resonance was shifted, and the simulation results of the three transducers matched well with the measured results. In **Figure 8B** the phase of No. 1 transducer has a high deviation above 35MHz because in our experiments, the parameters of cable were measured and calculated at the center frequency of transducer, which is 12MHz. So, when the frequencies reach 35MHz, the parameters of the cable will become different. But in the software, the used parameters of the transmission line were not frequency dependent. So, the deviation is bigger in higher frequencies. Besides this, the individual differences between transducers we make, the processing methods, and the uniformity of the materials will all have an impact on the phase, especially the high frequency part. Moreover, the phase results are also easily affected by test conditions, polarization, and other conditions, so these factors lead to relatively large phase deviation.

The Results of Transducer With Different Cable Lengths

In experiments with different cable lengths, we compared the simulation results and measured results of three kinds of wire length transducers, as shown in **Figure 9**. It can be seen that for high frequency transducers, the cable length has a significant effect on the transducer. The longer cable length is, the greater influence of performance is made. Especially at the center frequency, the amplitude of the impedance has been increased. It means that the attenuation of the center frequency is also influenced by the cable.

DISCUSSION

In the experiment, we compared the simulation results and the measured results of the transducer with and without cables, respectively. Obviously, in the simulation results without cable, no matter what frequency or any kind of matching layer, the resonance impedances matched well with the actual results. Among them, the designed center frequencies calculated according to Eq. 1 are 13.5Ω, 12.4Ω, and 23 MHz, respectively. The measured values are 11.75Ω, 11.3Ω, and 19.63 MHz. These results are also close to the theoretical values. Moreover, due to the existence of the matching layer, the second resonance appeared in both the measured results and the simulation results. In addition, the part above 25 MHz in the simulation results did not match the measured parameters. That's because in our experiment, some parameters like attenuations which the Leach model part used are measured and calculated at a fixed frequency and not changed by frequencies. It will have impact on the simulation results. Besides this, some parameters cannot be measured, and there is deviation between the theoretical value and the actual value. During the model optimization, we selected the impedance of the transducer as the optimization benchmark, so our impedance simulation results were closer to the measured value than the phase simulation results. Of course, if the phase is selected for model parameter optimization, the result can be closer to the actual value. In the following research, we will further improve our model, so that the simulation can be done well in both phase and impedance amplitude. So, it caused that the deviations about phase are higher than amplitude in **Figure 7**. We used the same material parameters to simulate 20 MHz transducer with PiezoCAD software. The results are shown in **Figure 10**, at the position of the resonance, the center frequency is 23.72 MHz, the amplitude is 2.11Ω and lower than the measured values, the phase is −44.04°. The compared results between this improved model and PiezoCAD are shown in **Table 3**. It is showed that the effect of this improved model is more suitable for complete transducer than PiezoCAD software based on KLM model. In KLM model, a frequency dependent transformer was used and it is not easy to achieve in PSPICE software. One of the main advantages in Leach model is easy to achieve.

Besides, for the high frequency transducers, the different lengths of cable have a great impact on the transducers. In traditional KLM model, the influence of cable has not been considered because most transducers' applications did not include long cable. But in some applications like IVUS, the influence of cable cannot be ignored. So, the biggest difference between this model and KLM model is that this model contained cable model. It could give the simulation results of transducer with cable, and use the circuit simulation software to achieve the circuit simulation.

CONCLUSION

Simulation is important for the design of high frequency ultrasound transducer. Considering the influence of transmission lines, backing and matching layers, this paper established an improved complete ultrasound transducer model which can be realized in the circuit simulation software LTspice. This improved model can be used to predict the performance of transducer by measuring the parameters of material. And it includes the simulation of piezoelectric ceramic, matching layer, backing layer, and cable. In this paper, the model was simulated and compared with the measured results. This paper tested the comparison between the transducer and the actual situation under various circumstances. The results showed that the proposed model is in good agreement with the actual results for various frequencies, various matching layer materials, and various cable lengths. The errors of the simulated center frequencies are less than 1.5% and the errors of amplitudes are less than 10Ω. The simulation results are closer to the measured results than those of PiezoCAD based on KLM model. In conclusion, the complete transducer simulation model can be implemented in general circuit simulation software. The influence of cable and system can also be considered, which can be better used in the simulation of the whole system including the transducers.

DATA AVAILABILITY STATEMENT

The original contributions presented in the study are included in the article/supplementary material, further inquiries can be directed to the corresponding authors.

AUTHOR CONTRIBUTIONS

ZS proposed the concept and performed the simulations. JX and ZL fabricated the transducer. YCh contributed to the PiezoCAD simulation. YCu contributed to the discussions on the concept. XJ supervised the project and contributed to the writing of the manuscript. All authors contributed to the article and approved the submitted version.

FUNDING

This work was supported in part by the National Key Research and Development Program of China (Grant Nos. 2019YFC0120500 and 2018YFC0116201), National Natural Science Foundation of China (Grant Nos. 21927803 and 11704397), the Funds of Youth Innovation Promotion Association, Chinese Academy of Sciences (Grant Nos. Y201961, 20A122062ZY, and YJKYYQ20180031), and Funds of Suzhou Science and Technology Project (SS202062).

REFERENCES

Aouzale, N., Chitnalah, A., Jakjoud, H., and Kourtiche, D. (2008). PSpice modelling of an ultrasonic setup for materials characterization. *Ferroelectrics* 372, 107–114. doi: 10.1080/00150190802382058

Chahal, J. S., and Reddy, C. C. (2013). Modeling and simulation of pulsed electroacoustic measurement method. *IEEE Syst. J.* 8, 1283–1292. doi: 10.1109/jsyst.2013.2292452

de Souza, C. R., Peres, P. L. D., and Bonatti, I. S. (2003). ABCD matrix: a unique tool for linear two-wire transmission line modelling. *Int. J. Elect. Eng. Educ.* 40, 220–229. doi: 10.7227/ijeee.40.3.5

Fan, X., Ma, S., and Zhang, X. (2014). Simulation analysis of piezoelectric ceramic chip PZT based on Ansys. *Piezoelectr. Acoustooptics* 36, 416–420.

Jensen, J. A. (2004). Simulation of advanced ultrasound systems using Field II. *2 IEEE Int. Symp. Biomed. Imag. Macro Nano* 1-2, 636–639.

Jian, X., Li, Z., Han, Z., Xu, J., Liu, P., Liu, Y., et al. (2018). The study of cable effect on high frequency ultrasound transducer performance. *IEEE Sens. J.* 18, 5265–5271. doi: 10.1109/jsen.2018.2838142

Johansson, J., and Martinsson, P.-E. (2001). "Incorporation of diffraction effects in simulations of ultrasonic systems using PSpice models,' in *Proceedings of the 2001 IEEE Ultrasonics Symposium: An International Symposium (Cat. No. 01CH37263)*, Vol. 1, (New York, NY: IEEE), 405–410.

Kim, G., Hwang, Y.-I., Seo, M.-K., and Kim, K.-B. (2020). Electrical tuning for sensitivity enhancement of a piezo-electric ultrasonic transducer: Simulation and fabrication. *J. Mech. Sci. Technol.* 34, 3155–3164. doi: 10.1007/s12206-020-0707-1

Krimholtz, R., Leedom, D. A., and Matthaei, G. L. (1970). New equivalent circuits for elementary piezoelectric transducers. *Electr. Lett.* 6, 398–399. doi: 10.1049/el:19700280

Leach, W. M. (1994). Controlled-source analogous circuits and spice models for piezoelectric transducers. *IEEE T Ultrason. Ferr.* 41, 60–66. doi: 10.1109/58.265821

Magnusson, P. C., Weisshaar, A., Tripathi, V. K., and Alexander, G. C. (2000). *Transmission Lines and Wave Propagation*. Boca Raton, FL: CRC press.

Mason, W. P. (1942). *Electromechanical Transducers and Wave Filters*. New York, NY: Van Nostrand.

Merdjana, T., Chaabi, A., and Rouabah, S. (2014). "VHDL-AMS and PSPICE modeling of ultrasonic piezoelectric transducer for biological mediums application," in *Proceedings of the 2014 International Conference on Advanced Technologies for Signal and Image Processing (ATSIP)*. (Sousse: IEEE)

Pandian, N. G., Weintraub, A., Kreis, A., Schwartz, S. L., Konstam, M. A., and Salem, D. N. (1990). Intracardiac, intravascular, two-dimensional, high-frequency ultrasound imaging of pulmonary artery and its branches in humans and animals. *Circulation* 81, 2007–2012. doi: 10.1161/01.cir.81.6.2007

Pavlin, C. J., and Foster, F. S. (1998). Ultrasound biomicroscopy: high-frequency ultrasound imaging of the eye at microscopic resolution. *Radiol. Clin. North Am.* 36, 1047–1058.

Peres, P. L. D., and Lopes, B. A. (1998). Transmission line modeling: a circuit theory approach. *Siam Rev.* 40, 347–352. doi: 10.1137/s0036144597316048

Rathod, V. T. (2020). A review of acoustic impedance matching techniques for piezoelectric sensors and transducers. *Sensors (Basel)* 20:4051. doi: 10.3390/s20144051

Redwood, M. (1961). Transient performance of a piezoelectric transducer. *J. Acoustic. Soc. Am.* 33, 527–536. doi: 10.1121/1.1908709

Roa-Prada, S., Scarton, H. A., Saulnier, G. J., Shoudy, D. A., and Gavens, A. J. (2007). "Modeling of an ultrasonic communication system," in *Proceedings of the Asme International Mechanical Engineering Congress & Exposition*, (New York, NY: *ASME*), 133–146.

Sahai, A. (1998). Prospective assessment of the ability of endoscopic ultrasound to diagnose, exclude, or establish the severity of chronic pancreatitis found by endoscopic retrograde cholangiopancreatography. *Gastrointest Endosc.* 48, 18–25. doi: 10.1016/s0016-5107(98)70123-3

Takahashi, V. L., Kubrusly, A. C., Braga, A., Quintero, S. M., Figueiredo, S. W., and Domingues, A. B. (2019). Ultrasonic power and data transfer through multiple curved layers applied to pipe instrumentation. *Sensors* 19:4074. doi: 10.3390/s19194074

Tarpara, E. G., and Patankar, V. (2018). Lossless and lossy modeling of ultrasonic imaging system for immersion applications: Simulation and experimentation. *Comput. Electr. Eng.* 71, 251–264. doi: 10.1016/j.compeleceng.2018.07.054

Turnbull, D. H., Starkoski, B. G., Harasiewicz, K. A., Lockwood, G. R., and Foster, F. S. (1993). "A 40–100 MHz B-scan ultrasound backscatter microscope for skin imaging," in *Proceedings of the IEEE Ultrasonics Symposium*, (New York, NY: IEEE)

Van Deventer, J., and Lofqvist, T. (2000). PSpice simulation of ultrasonic systems. *IEEE Trans. Ultrason. Ferroelectr. Freq. Control* 47:1014. doi: 10.1109/58.852085

Wu, L., and Chen, Y. C. (1999). PSPICE approach for designing the ultrasonic piezoelectric transducer for medical diagnostic applications. *Sens. Actuat. A Phys.* 75, 186–198. doi: 10.1016/s0924-4247(99)00067-9

Zheng, D.-D., Mao, Y., and Lv, S.-H. (2019). Research and validation of design principles for PVDF wideband ultrasonic transducers based on an equivalent circuit model. *Measurement* 141, 324–331. doi: 10.1016/j.measurement.2019.04.050

Zheng, D.-D., Mao, Y., Cui, Z., and Lv, S.-H. (2018). "Optimization of equivalent circuit model for piezoelectric ultrasonic transducer," in *2018 IEEE International Instrumentation and Measurement Technology Conference (I2MTC)*, (New York, NY: IEEE), 1–5.

Zhou, H., Huang, S., and Li, W. (2020). Electrical Impedance Matching between Piezoelectric Transducer and Power Amplifier. *IEEE Sens. J.* 20, 14273–14281. doi: 10.1109/jsen.2020.3008762

Conflict of Interest: The authors declare that the research was conducted in the absence of any commercial or financial relationships that could be construed as a potential conflict of interest.

frontiers in Materials

ORIGINAL RESEARCH
published: 22 April 2021
doi: 10.3389/fmats.2021.663926

Phased-Array Transducer for Intracardiac Echocardiography Based on 1–3 Piezocomposite

Zhile Han[1], Ninghao Wang[2], Zhangjian Li[2], Xinle Zhu[2], Youwei Chen[2], Xiaohua Jian[2] and Yaoyao Cui[1]**

[1] Academy for Engineering & Technology, Fudan University, Shanghai, China, [2] Medical Ultrasound Department, Suzhou Institute of Biomedical Engineering and Technology, Chinese Academy of Sciences, Suzhou, China

In this study, an ultrasonic phased-array transducer was proposed, which could effectively improve the imaging performance by using 1–3 piezocomposite. The piezocomposite consists of PZT and epoxy, with a pitch of 70 μm, kerf of 20 μm, and thickness of 170 μm. The phased-array transducer has 64 elements; the size of each element is 85 μm × 1.3 mm; the pitch of the transducer is 100 μm; and the kerf between the elements is only 15 μm. To minimize the transducer size, the 1–3 composite uses an encase structure, which connects the upper surface of the composite directly to the flexible circuit board bonded to the lower surface as the ground electrode. The size of the final fabricated transducer is 2 mm × 7.4 mm, and the transducer is mounted on a 9 F (3 mm diameter) catheter, which can bend in four directions and is primarily used for intracardiac echocardiography (ICE). The acoustic and electrical properties of the transducer were tested, including impedance, echo sensitivity, center frequency (9 MHz), bandwidth (BW) (55%), and consistency. Finally, the wire phantom experiments were carried out to demonstrate the spatial resolutions and imaging performance. This study shows that this transducer with compact design and construction can bring higher performance for the single-use disposable ICE catheter.

Keywords: 1–3 composite, phased array, intracardiac echocardiography, high frequency, miniature transducer

OPEN ACCESS

Edited by:
Zeyu Chen,
Central South University, China

Reviewed by:
Benpeng Zhu,
Huazhong University of Science and Technology, China
Wei Ren,
Xi'an Jiaotong University, China
Ruimin Chen,
Zhejiang Lab, China

****Correspondence:***
Yaoyao Cui
cuiyy@sibet.ac.cn
Xiaohua Jian
jianxh@sibet.ac.cn

Specialty section:
This article was submitted to Smart Materials, a section of the journal Frontiers in Materials

Received: *04 February 2021*
Accepted: *01 April 2021*
Published: *22 April 2021*

Citation:
Han Z, Wang N, Li Z, Zhu X, Chen Y, Jian X and Cui Y (2021) Phased-Array Transducer for Intracardiac Echocardiography Based on 1–3 Piezocomposite. Front. Mater. 8:663926. doi: 10.3389/fmats.2021.663926

INTRODUCTION

Intracardiac echocardiography (ICE) has become a widely used imaging tool in the past decades (Hijazi et al., 2009). The visualization of the heart becomes possible due to the application of ICE and ICE has become an indispensable equipment for various percutaneous, interventional, and electrophysiological procedures (Bartel et al., 2014; Enriquez et al., 2018). ICE catheters can be divided into rotational catheters and phased-array catheters (Vitulano et al., 2015). Among them, the phased-array catheter has wider application potential because of its higher frequency range and ability of Doppler and color flow imaging. With the large-scale application of ICE, it is essential to develop a single-use disposable phased-array catheter with excellent performance and low cost (Bartel et al., 2014).

The miniaturized phased-array transducer has a complicated and challenging fabrication process because the pitch and the kerf must be small enough to avoid spurious modes.

Currently, many researchers have focused their efforts on the development of miniaturized phased-array transducer (Bezanson et al., 2014; Chiu et al., 2014; Basij et al., 2019; Cabrera-Munoz et al., 2019). The current manufacturing process of the transducer is rather cumbersome. For example, sputtering Au/Cr layer needs to be performed multiple times to connect the ground of array elements (Cannata et al., 2006), and individual element electrodes are separated by removing the gold layer by using photolithography or Cr/Au etching and carefully aligned with the electrode patterns on the flexible circuit (Chen et al., 2014; Chiu et al., 2014), using conductive epoxy to bond the bent ground electrode on the circuit to the matching layer (Cabrera-Munoz et al., 2019). All these extra processes not only increase the cost of the transducer but also cause the instability of the electrical connection.

The active material is another critical restricting factor for the ICE phased-array probe. The piezoelectric ceramic (Cannata et al., 2008; Kim H. H. et al., 2010) and single crystal (Sung Min et al., 2003; Chen et al., 2012; Wong et al., 2017) have been widely used in array transducer applications. However, these two homogeneous materials will bring lateral mode to interfere between phased-array elements (Yang et al., 2012). Besides, the piezoelectric ceramic is hard to fulfill the requirements of high performance for the phased-array probe though it has stable performance and cost effective (Kim K. B. et al., 2010). In addition, the single crystal is limited by its delicate and expensive cost for disposable catheter applications (Luo et al., 2010). At the same time, 1–3 piezoelectric composite has minimum lateral mode interference, increased electromechanical coupling efficiency, and better acoustic matching (Brown et al., 2007). It is more suitable in the application of ICE phased-array probe.

In this study, a high-performance 1–3 composite is employed to realize an ICE 64-element phased-array transducer. The encase structure is adopted to minimize the transducer size and reduce the complexity of the fabrication process. The working frequency of the probe is chosen as 9 MHz to achieve a higher spatial resolution and ensure a penetration depth of at least 10 cm, which can cover most of the applications of ICE (Alkhouli et al., 2018). The design, fabrication, and characterization of the phased array are then presented. The wire phantom imaging experiments are carried out to demonstrate the spatial resolutions and imaging performance.

DESIGN AND FABRICATION

1–3 Piezocomposite Material

The 1–3 piezocomposite was processed by the "dice-and-fill" technique; a mechanical cutting saw (DAD3221, Disco Co., Tokyo, Japan) was used to cut kerfs into a piece of bulk piezoelectric ceramic; and the kerfs were backfilled with epoxy. In the 1–3 composite, the generation of spurious resonances within the designed operating bandwidth (BW) should be avoided. To avoid the problems with lateral modes, the pillars in the composite should have a width that is lower than half of the pillar height. The generation of the first two spurious Lamb wave mode frequencies, f_{L1} and f_{L2}, can be predicted using the following equation:

$$f_{L1} = \frac{\upsilon_{\text{phase}}}{d}$$
$$f_{L2} = \frac{\sqrt{2}\upsilon_{\text{phase}}}{d} \quad (1)$$

where υ_{phase} is the phase velocity in the transverse direction across the piezocomposite and d is the pillar-to-pillar spacing within the composite. The phase velocity in low fractional ceramic-volume composites is predominantly determined by the shear wave velocity of the filler epoxy. To push the lateral modes outside the operating BW of the transducer, the composite in this study is designed with 50 μm height, 20 μm width (Brown et al., 2007), and 51% volume fraction. The composite was finally grounded to a thickness of 170 μm. The PZT-5H (3203HD, CTS [Tianjin] Electronics Company Ltd., Tianjin, China) was chosen as the active material of 1–3 composite because of its wide application and high price–performance ratio. A simulation model was built to analyze the piezoelectric characters of the 1–3 composite material, as shown in **Figure 1**, a part of the composite material structure was built, and its outer boundary was set as symmetric to simulate the whole characteristics of composite material.

For the phased-array transducer with central frequency around 9 MHz, the element pitch should be less than λ (wavelength in water, 167 μm), which is 100 μm in our design, and the kerf is 15 μm. In order to make the distribution of the piezoelectric column in each array element as consistent as possible, the element pitch value needs to be designed to equal cutting kerf plus piezoelectric pillar width (Zhou et al., 2011, 2020; Zhang et al., 2020), and the composite material is diced in a direction parallel to the edge of the pillars. This traditional method limits the design of element size. When the material is diced parallel to the edge of the ceramic pillar, due to the epoxy bumps at the interface between the ceramic pillar and bulk epoxy caused by the differences in the mechanical properties of ceramic and polymers (Cochran et al., 2006; Boonruang et al., 2019), the

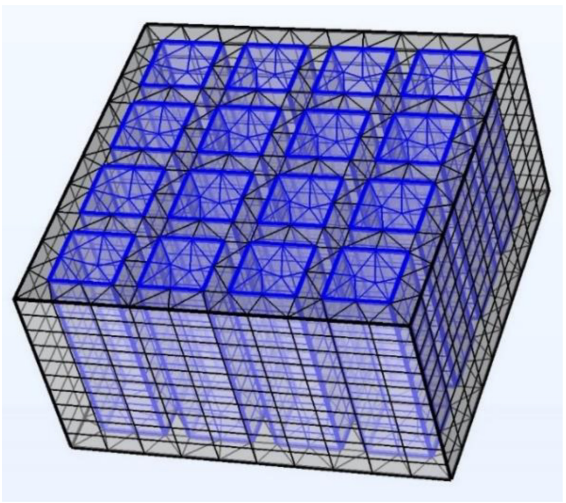

FIGURE 1 | The simulation model of 1–3 piezoelectric material.

bumps are easy to cause the fracture of the electrode Au/Cr layer, so a more suitable dicing method need to be designed.

In this study design, to make the distribution of the piezoelectric column in each array element as consistent as possible, it is necessary to cut the composite material along with a specific angle.

The specific angle is calculated as follows:

(1) Select a_1 as the initiated centered position and draw a circle with a radius of 100 μm.
(2) Look for points that are most similar to a_1. As shown in **Figure 2A**, point a_2 has the same location features as point a_1.
(3) Draw a tangent line to the circle along point a_2. The angle between the tangent line and the horizontal direction is the specific dicing angle.

It is straightforward that the optimal angle can be calculated as 46°. After dicing the material and sputtering the Au/Cr layers on the surface of the 1–3 composite, the designed material was diced into a size of 1.3 × 7.4 mm, with an encase electrode layer structure, as shown in **Figure 2B**, which was connected along the short side from the upper surface to the lower surface.

Each element of the transducer has an area of 0.085 mm × 1.3 mm and is composed of several ceramic pillars and epoxy. The consistency of the array elements depends on the active volume of the pillars contained in each array element, and it can be calculated using AutoCAD software (Auto CAD 2012, Autodesk Inc., San Rafael, CA, United States), as shown in **Figure 2C**. Compared with the dicing method parallel to the edge of the pillar (0°) or the diagonal of the pillar (45°), the current method can achieve higher consistency, with a volume fraction of 50.95% ± 1.61% of piezoelectric ceramic.

Array Acoustic Stack

The phased-array transducer was fabricated using a novel transducer technology, and it had a total active azimuth aperture of 6.4 mm and an active elevation aperture of 1.3 mm.

As shown in **Figure 3**, first, both sides of the encase structure of composite were cleaned by applying the acetone and reagent alcohol with a cotton swab, and then the structure was bonded

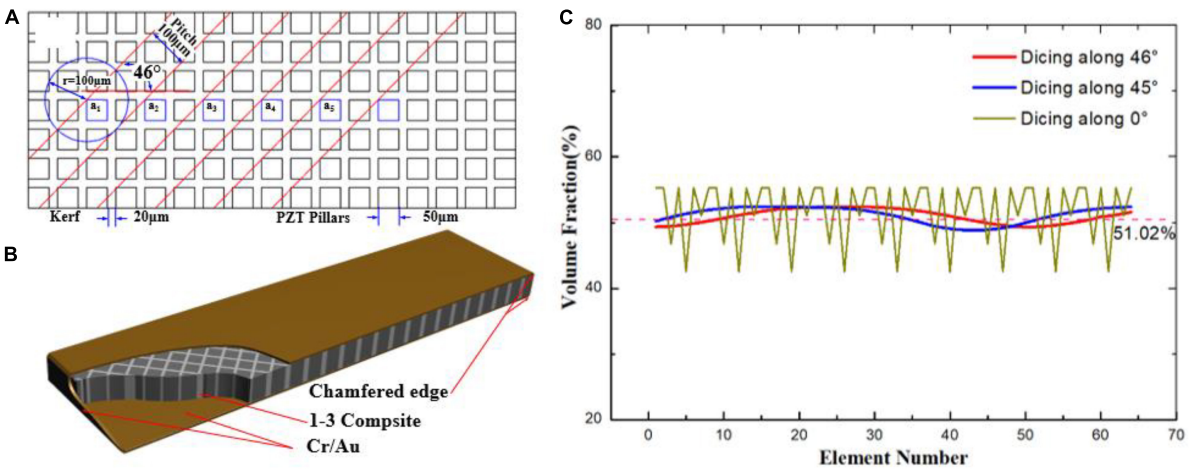

FIGURE 2 | (A) Dicing methods, **(B)** model of 1–3 piezocomposite, and **(C)** volume fraction comparison of each element.

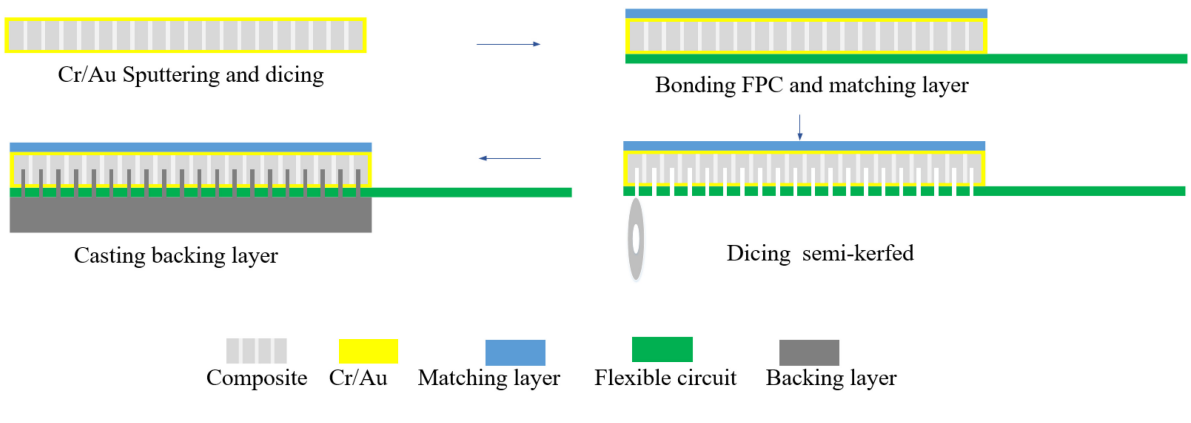

FIGURE 3 | Fabrication process of the phased-array transducer.

TABLE 1 | Design parameters of the phased-array transducer.

Specifications	Values
Designed center frequency	9 MHz
Pitch	0.1 mm
Kerf	0.015 mm
Elevation	1.3 mm
Number of elements	64
Thickness of matching layer (polyimide, 3.16 MRayls)	0.04 mm
Thickness of FPC (Cu+ polyimide)	0.04 mm
Thickness of backing material (Epo-Tek 301 + 70% Tungsten powder, 7.9 MRayls)	0.6 mm

using nonconductive epoxy (Epo-Tek 301, Epoxy Technology Inc., Billerica, MA, United States), to the polyimide matching layer and custom-designed flexible circuit (FPC), which was consisted of a polyimide base material and a layer of copper foil. After cured overnight at 50°C, the dicing process was performed by using a 15-μm width dicing saw from the FPC side and the depth of dicing was set to 0.12 μm into the center of the composite material. Finally, a compound mixed with epoxy resin and tungsten powder was employed as the backing layer; its weight ratio was 3:7; and after removing bubbles by vacuuming, the backing material was poured on the backside of the transducer and cured at 60°C for 12 h. It was cast on the acoustic stack. The Au/Cr layer on the upper surface of the composite as a ground electrode was connected to the FPC board bonded to the lower surface in order to lead out through the traces on the flexible circuit. The array design parameters and material properties are shown in **Table 1**. The acoustic impedances of the materials were measured through a pulse-echo method (Zhangjian et al., 2020).

The composite was diced in an oblique direction of 46°, which caused multiple pillars half-cut in each element although the material is composite. However, several phased-array transducers have been designed in many studies with the half-cut technology, and the beam performance test indicated that the focusing and steering ability was satisfactory (Zhang et al., 2011; Bezanson et al., 2014, 2020). Compared with wire bonding the array elements to the thickness dimension of flexible circuit boards or other methods, the acoustic stack with encase structure and the half-cut elements reduced the interconnect size, allowing for significantly reduced cost and complexity of manufacturing.

Probe Packaging

The acoustic stack was assembled at the distal end of an ICE catheter; the pads on the FPC end were welded to the 48 American Wire Gauge (AWG) coaxial cable inserted inside the catheter, as shown in **Figure 4A**; and the other end of the cable was connected to the breakout board of an imaging system by a customized connector.

The outside of the transducer except for the imaging window was cast with Pebax 2533 material for medical applications. The custom-designed catheter (ICE, Xinhuajia Technology Co., Shenzhen, China) was a long, thin, flexible multilayer plastic tubes, with four pull wires spaced apart 90° along the cross section connect the distal end to handle, and had an insertable length of 900 mm, as shown in **Figure 4B**. The catheter was manually manipulated by grasping the catheter handle and actuating each of the four degrees of freedom (left/right and anterior/posterior), and able to bend up to an angle of 160°, with a minimum bending radius of 27 mm.

The fabricated ICE transducer, as shown in **Figure 5A**, is the structure of 1–3 composite materials under a microscope, and **Figure 5B** shows a customized flexible circuit board, which is mainly composed of two parts, namely the transducer assembly

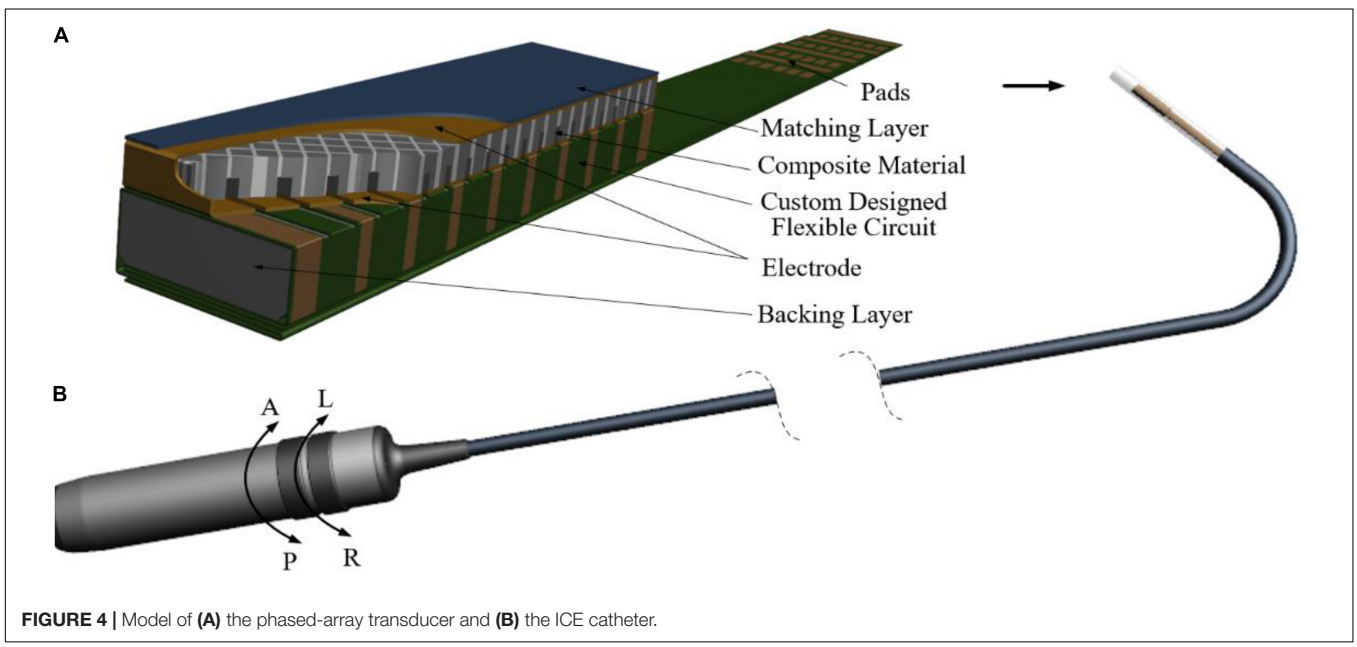

FIGURE 4 | Model of **(A)** the phased-array transducer and **(B)** the ICE catheter.

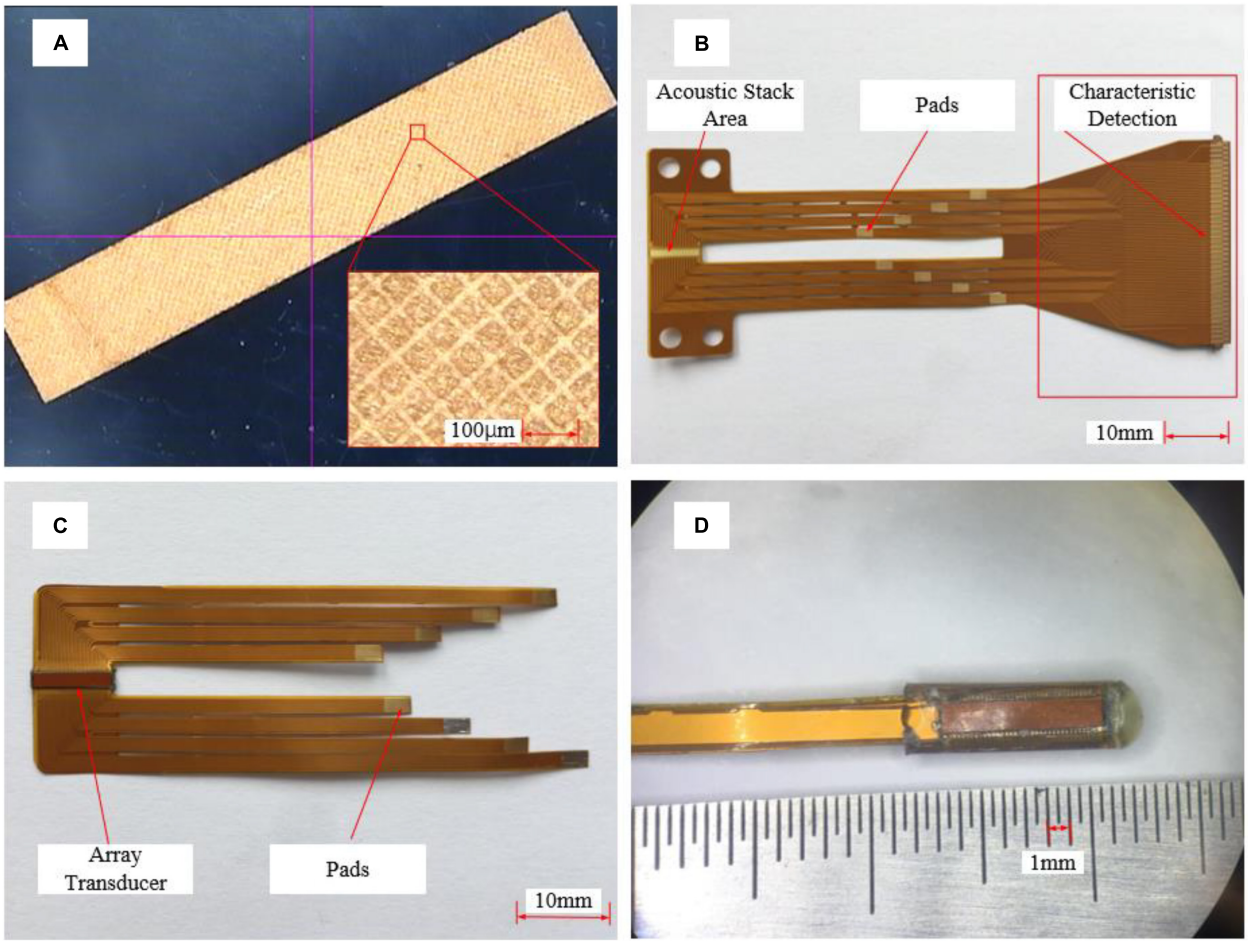

FIGURE 5 | Photograph image of **(A)** 1–3 composite material, **(B)** FPC board, **(C)** fabricated transducer, and **(D)** probe cast with Pebax.

part and the characteristic detection part, where the latter is used to test the characteristics of the transducer and will be removed in the subsequent process. **Figure 5C** shows the manufactured transducer, the remaining FPC board can be folded and cast with Pebax 2533 as protection, and the total structural size of the transducer is 3 mm in diameter, as shown in **Figure 5D**.

A bundle of 64 individual 48-AWG micro-coaxial cables with a total outer diameter of 1.9 mm is carefully soldered to the transducer as shown in **Figure 6**, and the other ends of the cables are divided into four groups where each group is soldered on a custom L-shaped circuit board, which can be connected to a commercial Verasonics Vantage 128 System (Vantage 128, Verasonics Inc., Kirkland, WA, United States).

CHARACTERIZATION AND DISCUSSION

Performance of the 1–3 Composite Material

The simulation result and the test result of the composite material are shown in **Figure 7**. The simulation impedance curves are almost the same as the measurement result. It can be noticed that the magnitude value of the simulation impedance curve is much larger than the measurement result, and the reason is due to that the area of the simulation model is much smaller than the tested area.

According to the measured electrical impedance spectrum, the center frequency of the fabricated 1–3 composite is 10.2 MHz, and its electromechanical coupling coefficient (k_t) is 0.66, which is higher than 0.55 of pure PZT-5H (CTS, 2021). Besides, according to the 1–3 composite thickness mode (Smith and Auld, 1991), the main piezoelectric properties of the 1–3 composite including longitudinal velocity, density, and acoustic impedance are listed in **Table 2**.

Basic Performance of Phased-Array Transducer

Each of the elements was repolarized in the polarizing fluid under an electric field of 2 kV/cm for 3 min using a high-voltage power supply before testing. Then the electrical impedance was measured using an impedance analyzer (E4991A, Keysight Technologies Inc., Santa Rosa, CA, United States) before

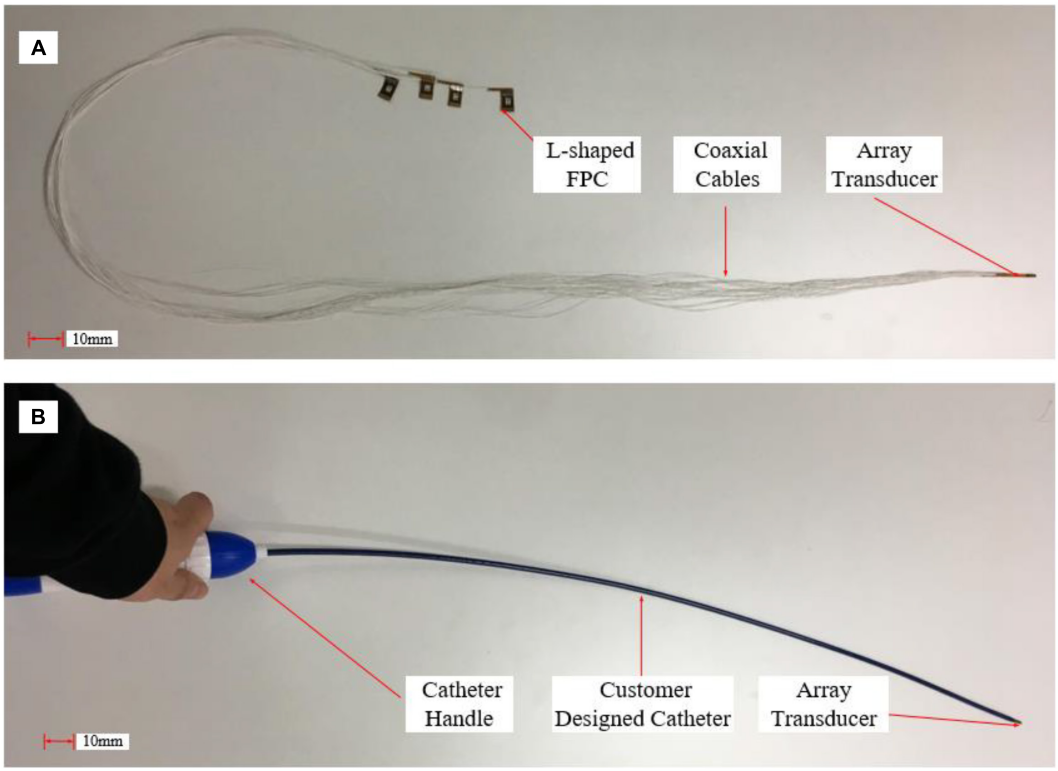

FIGURE 6 | Photograph image of **(A)** ultrasound probe with cables and **(B)** ICE catheter.

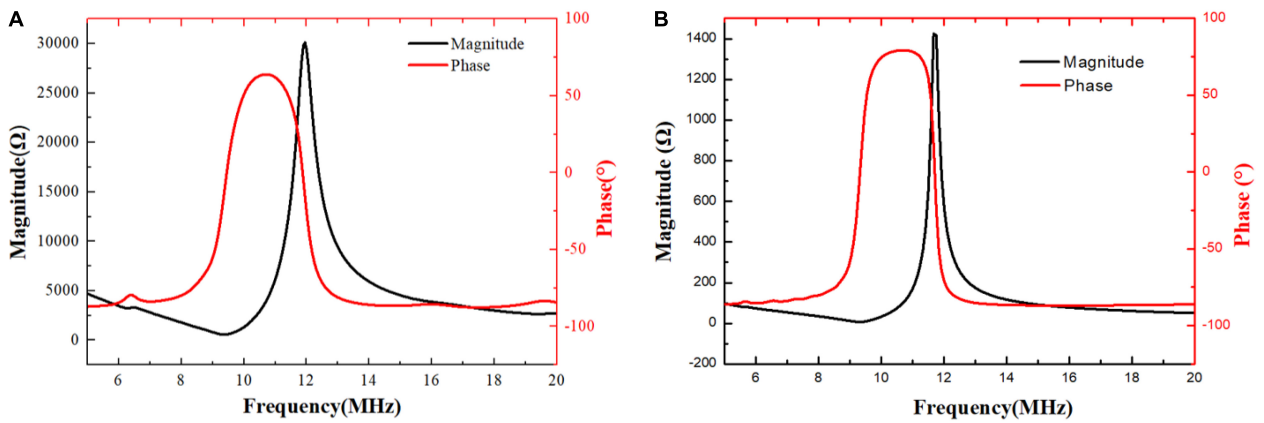

FIGURE 7 | (A) Simulated and **(B)** measured impedance and phase of 1–3 composite.

connecting each element to the coaxial cable assembly; both the impedance magnitude and phase angle were recorded over the range of 5–15 MHz.

The measured values of all 64 elements are shown in **Figure 8**, and the average value and SD of electrical impedance at 9 MHz were 288.48 ± 27.24 Ω and 72.35° ± 2.92°, respectively. Since the electrical impedance was measured by connecting each pad on the transducer to the impedance analyzer, a 20-mm homemade electrical probe was used in the test and brought the smaller resonance peak located at around 6 MHz.

After completing the cable welding and fabrication of the catheter, the pulse-echo response was performed in deionized water at room temperature for the characterization. A device (DPR 500, JSR Ultrasonics Inc., Pittsford, NY, United States) with a remote pulser RP-H4 was used to excite the elements of the transducer: the voltage amplitude of the pulser was set as 330 V, the PRF was 200 Hz, and the echo was received by the device with 0 dB gain. The waveforms were recorded and processed by an oscilloscope (DPO5034, Tektronix Inc., Beaverton, OR, United States). Each

TABLE 2 | Properties of 1–3 piezoelectric composite.

Specifications	Values
Longitudinal velocity	3,789 m/s
Density	4.58 g/cm^3
Electromechanical coupling coefficient (k_t)	0.66
Acoustic impedance	17.3 MRayls
Volume fraction	51.02%

element was connected in series with a 1.2 μH inductor for impedance matching.

Figure 9A shows the measurement results of a representative array element, and the uniformity of the calculated center frequency (F_c), − 6 dB BW, and peak-to-peak sensitivity of the phased-array transducer are illustrated in **Figure 9B**, which are about 9 MHz, 55%, and 150 mV, respectively. It can be found that the acoustic performance of the phased array exhibits a good uniformity. In **Figure 9A**, ringing and bumpy spectrum are observed, and it might be caused by the FPC layer between the backing and composite materials. A single matching layer may also lead to insufficient BW.

For the two-way insertion loss (IL) measurement, the transducer was excited with a 5-Vpp, four-cycle sinusoidal tone-burst signal at 9 MHz, and the reflected echo was received from a polished steel reflector. The echo signal (V_o) was measured by the oscilloscope with a 1 MΩ coupling, and the driving signal (V_i) was then measured with a 50 Ω coupling. The measured value was corrected for loss due to attenuation in water (2.2×10^{-4}dB mm^{-1} × MHz^2) and reflection from the steel target (0.6 dB) (Cannata et al., 2006). The IL was calculated using the following equation:

$$\mathrm{IL} = 20log\frac{V_o}{V_i} + 0.6 + 2.2 \times 10^{-4} \times 2d \times f_c^2 \quad (2)$$

where f_c is the center frequency and d is the distance between the transducer and steel reflector. The IL value of the array is measured to be 39.1 dB, which is somewhat higher than other

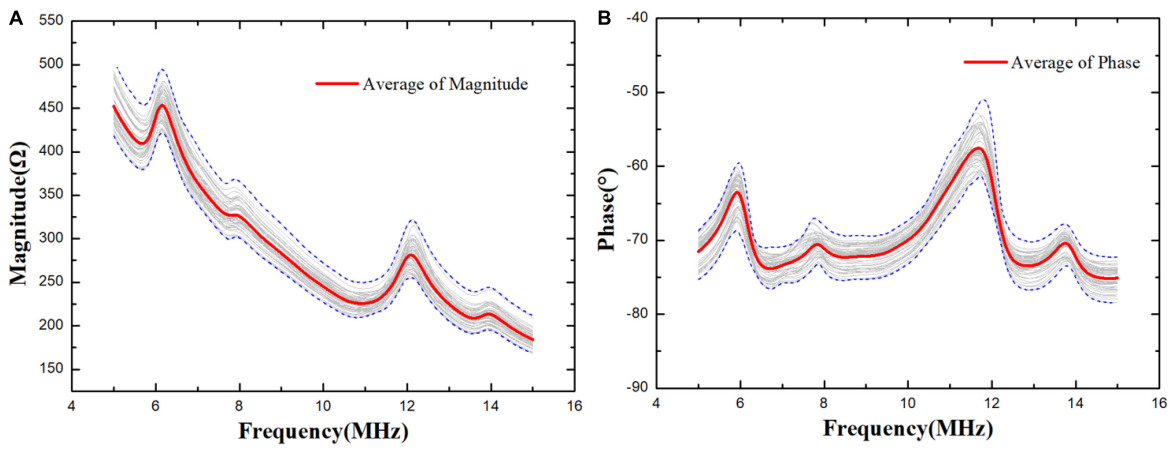

FIGURE 8 | Electrical impedance **(A)** magnitude and **(B)** phase as a function of frequency for 64 elements.

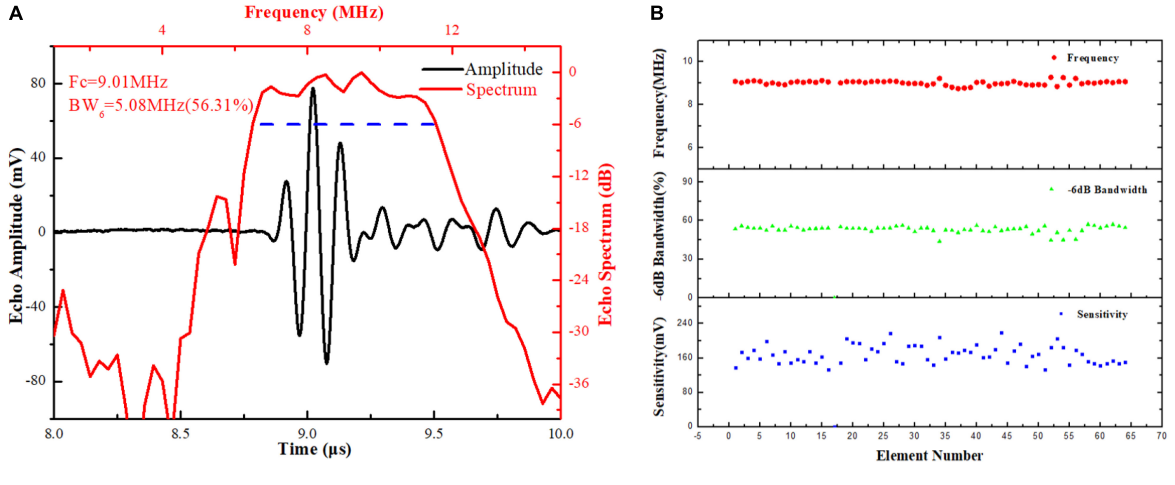

FIGURE 9 | Measured **(A)** pulse-echo response performance of element 17 and **(B)** frequency, bandwidth, and sensitivity of the pulse-echo signal for each element.

reported transducers, and this might be due to the relatively low g_{33} coefficient of piezoelectric composite material (Dias and Das-Gupta, 1994). Besides, it is not easy to obtain high sensitivity by monolayer matched layer. The sensitivity can be improved by increasing the piezoelectric volume ratio and adopting multilayer matching.

For the cross-talk measurement, a 5-Vpp, 20-cycle sinusoidal tone-burst signal generated by a function generator (33250A, Keysight Technologies Inc.) was used to excite one representative element (element 23) in the phased array with a frequency range from 3 to 15 MHz in steps of 2 MHz. The voltages across the first, second, and third adjacent elements were measured and the cross talk was calculated as reference (Cannata et al., 2006).

The measured cross talk is shown in **Figure 10**. As shown in the figure, the maximum cross-talk values at the center frequency were −34.5, −36.4, and −38.9 dB for the first, second, and third adjacent elements respectively. Considering the simplicity of array design and construction, these values are considered satisfactory (Lukacs et al., 2006).

The cross talk decreased fast in the lower frequency and almost no change in the higher frequency. This phenomenon may be caused by the parasitic capacitance formed by the array elements. The parasitic capacitance is a high-pass filter for the cross talk.

The long wire electrode binding and flexible circuit affected the electrical impedance characteristics of the transducer, resulting in the lower value of peak-to-peak voltage in the measurement. The electrical impedance curve can be used to analyze the impact of wire (Jian et al., 2018) and the FPC board.

The one-way azimuthal directivity response of the phased-array transducer was measured by exciting the one-array element (element 23) using the pulser/receiver DPR500. The element was rotated around an axis with a precise rotating device (QRP02, Thorlabs, Newton, NJ, United States) in a step of 3°, along its center and length, and the amplitudes of the response were acquired at discrete angular positions by a hydrophone (NH0200, Precision Acoustic, Dorset, United Kingdom) with 0.2 mm diameter. For the transducer, the measurement of − 6 dB directivity was ± 30°, as shown in **Figure 11**, which can serve satisfactorily in the performance of phased-array beam. Similar results were reported with directivity of approximately ±25° for a 2–2 composite phased array (Bezanson et al., 2014; Cabrera-Munoz et al., 2019).

Imaging Performance of Phased-Array Transducer

The authors utilized Verasonics Vantage 128 System to determine the imaging capability of the phased array. The probe is driven by a single-cycle sinusoidal tone-burst signal with an amplitude of 50 V, and the DELAY-AND-SUM (DAS) beamforming method is used in the system, which is the most basic digital beamformer for medical ultrasound imaging (Friis and Feldman, 1937; Mailloux, 1982), and the phantom images are presented in a 50-dB dynamic range. The catheter can operate at frequencies of 6.5–11.5 MHz.

To evaluate the performance, the custom-made wire phantoms were used to carry out the image tests. The lateral resolution and axial resolution were detected by wire phantom (Foster et al., 2002) at the central frequency of 9 MHz of the catheter. We can calculate the theoretical spatial resolution using the following equations based on pulse-echo response:

$$R_A = PL/2 \tag{3}$$

where PL is the − 6 dB spatial pulse length of the received echo and the measured value is 217 μm, and the theoretical axial spatial resolution R_A is 108.5 μm.

$$R_L = F\# \times \lambda \tag{4}$$

where $F\#$ is the F number of the transducer (1.9) and λ is the sound wavelength in the medium (167 μm in water); therefore, the theoretical lateral spatial resolution R_L is 317 μm.

The 50-μm diameter wires phantom was immersed in a tank and imaged with gray scale in a 50-dB dynamic range as shown in **Figure 12**. The spread functions of A wire image axial and lateral line were plotted and are shown in **Figure 13**.

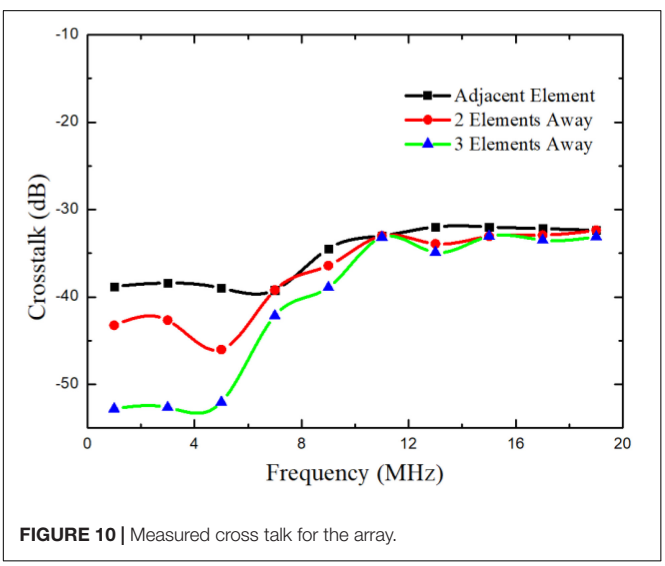

FIGURE 10 | Measured cross talk for the array.

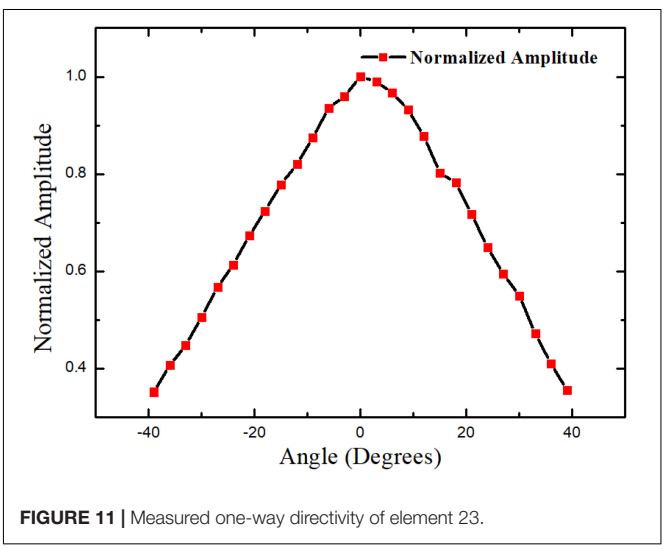

FIGURE 11 | Measured one-way directivity of element 23.

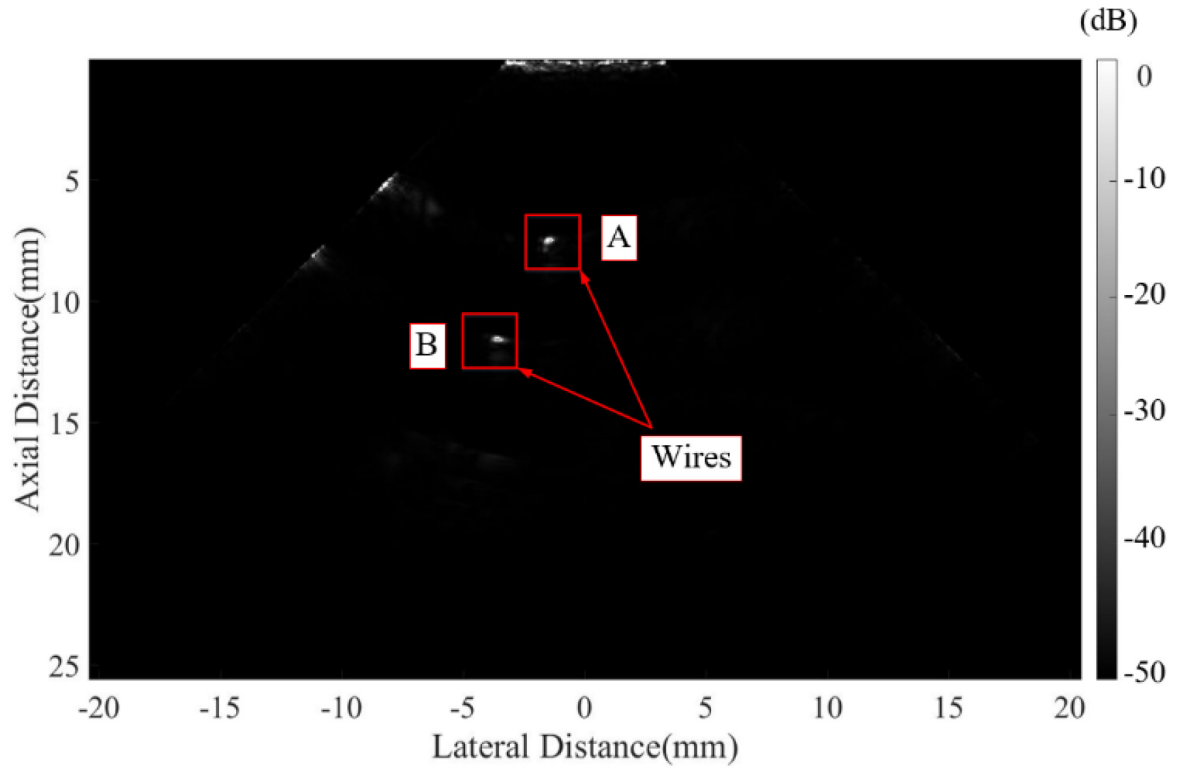

FIGURE 12 | Image of wire phantom.

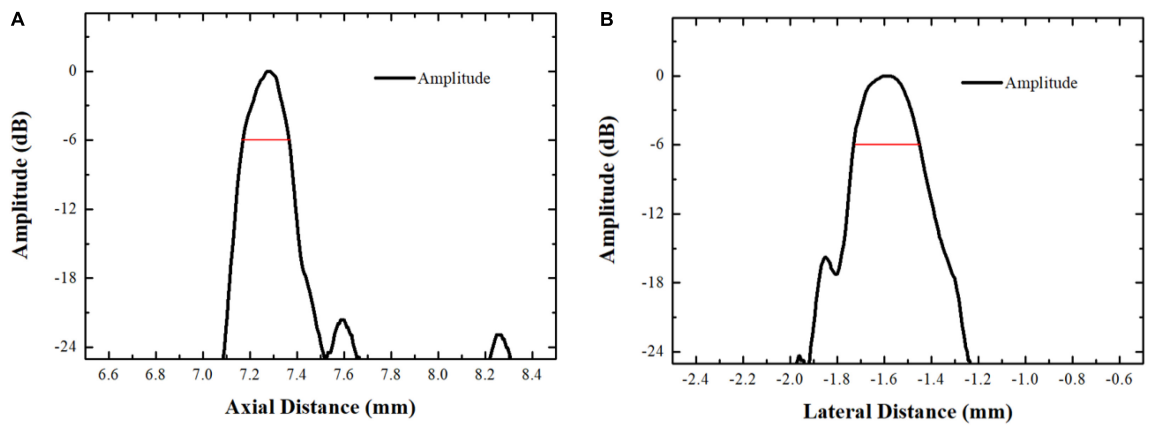

FIGURE 13 | (A) Axial and **(B)** lateral line spread functions.

The measured axial and lateral resolutions at −6 dB are 188 and 321 μm, respectively, and the lateral value is close to its theoretical value, but the axial value has a large deviation because the wire is difficult to be placed in the theoretical focus position.

Figure 14 shows an ultrasonic image of a phantom with 10 evenly 10-mm-spaced tungsten wires immersed in a tank with deionized water, and it is clear to find that the wire at a penetration depth of 100 mm can be easily observed with reasonable image quality. The SNR of the wires image was analyzed according to the RF data acquired by the Vantage system, which is higher than 30 dB. The spatial resolutions and penetration performance are satisfactory and can meet the requirements of ICE imaging.

A commercial phantom (KS107BG, Institute of Acoustics, Beijing, China), as shown in **Figure 15A**, was also employed in the experiment. It can be observed from **Figure 15B** that the wires in the distal area have a superior resolution (<0.5 mm), which shows that the transducer has an excellent beam steering performance.

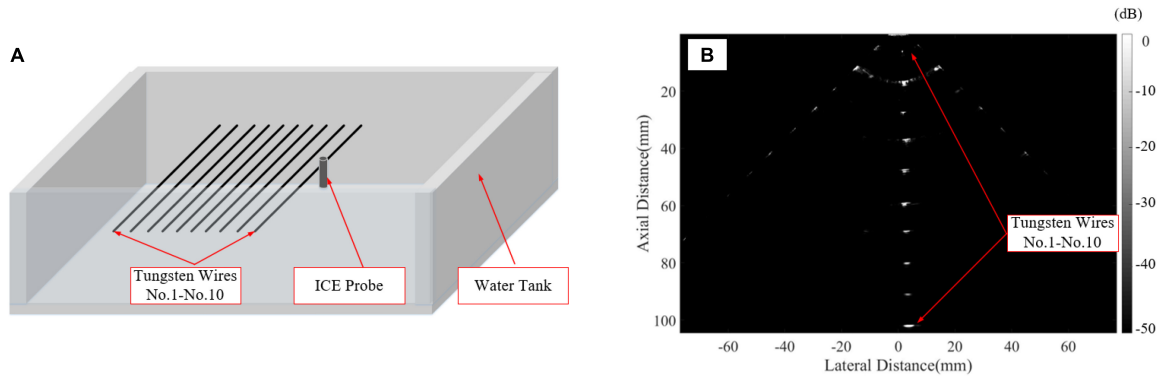

FIGURE 14 | (A) The image of wires phantom and **(B)** the wire phantom images of penetration depth.

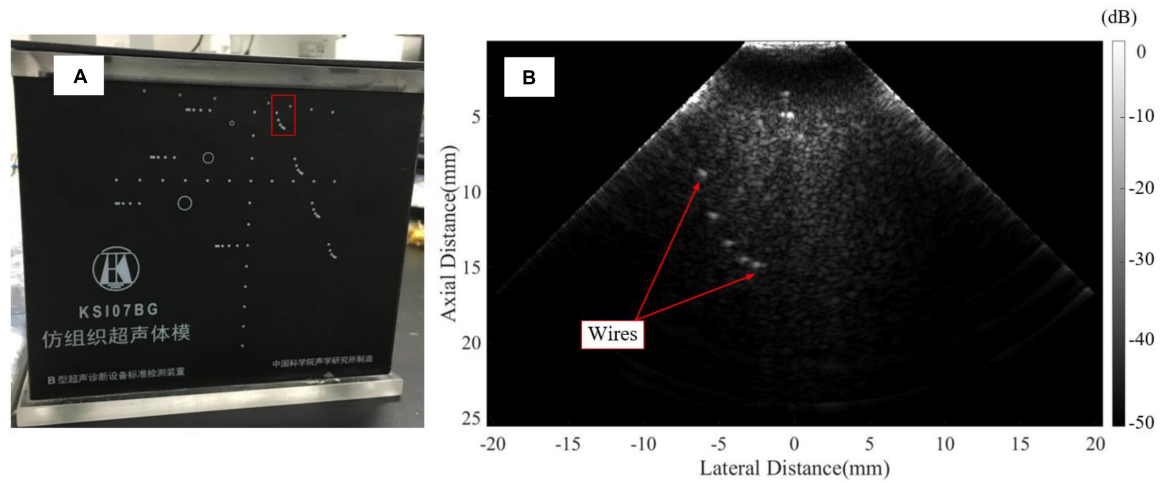

FIGURE 15 | (A) A commercial phantom (KS107BG, Institute of Acoustics, Beijing, China), and **(B)** The commercial wire phantom image.

CONCLUSION

This study described the development of a 1–3 piezocomposite-based phased-array transducer fit inside of a four-direction steerable ICE catheter. The dice-and-fill technique was used to produce the 1–3 piezocomposite material, and an encase structure and half-cut methods were developed to reduce the complexity of the fabrication process. Utilizing fabricated 1–3 piezocomposite, a transducer with a size of 2 mm × 7.4 mm with a central frequency of 9 MHz and −6 dB BW of 55% was prototyped. According to the echo and wire phantom experiments, the basic performance of the phased array was excellent. The experimental results suggest that a novel fabricated process of 1–3 composite phased array is competent for the single-use disposable ICE catheter in the future.

DATA AVAILABILITY STATEMENT

The original contributions presented in the study are included in the article/supplementary material, further inquiries can be directed to the corresponding authors.

AUTHOR CONTRIBUTIONS

ZH, ZL, XJ, and YCu conceived and designed the research work. NW, ZL, and YCh analyzed the data. ZH and XZ performed the experiments. All authors contributed to the article and approved the submitted version.

FUNDING

This work was supported in part by the National Key Research and Development Program of China (Grant Nos. 2019YFC0120500 and 2018YFC0116201), the Funds of Youth Innovation Promotion Association, Chinese Academy of Sciences (Grant Nos. Y201961, 20A122062ZY, and YJKYYQ20180031), and Funds of Suzhou Science and Technology Project (SS202062).

REFERENCES

Alkhouli, M., Hijazi, Z. M., Holmes, D. R. Jr., Rihal, C. S., and Wiegers, S. E. (2018). Intracardiac echocardiography in structural heart disease interventions. *JACC Cardiovasc. Interv.* 11, 2133–2147. doi: 10.1016/j.jcin.2018.06.056

Bartel, T., Müller, S., Biviano, A., and Hahn, R. T. (2014). Why is intracardiac echocardiography helpful? Benefits, costs, and how to learn. *Eur. Heart J.* 35, 69–76. doi: 10.1093/eurheartj/eht411

Basij, M., Yan, Y., Alshahrani, S. S., Helmi, H., Burton, T. K., Burmeister, J. W., et al. (2019). Miniaturized phased-array ultrasound and photoacoustic endoscopic imaging system. *Photoacoustics* 15:100139. doi: 10.1016/j.pacs.2019.100139

Bezanson, A., Adamson, R., and Brown, J. A. (2014). Fabrication and performance of a miniaturized 64-element high-frequency endoscopic phased array. *IEEE Trans. Ultrason. Ferroelectr. Freq. Control* 61, 33–43. doi: 10.1109/TUFFC.2014.6689774

Bezanson, A., Garland, P., and Brown, J. (2020). "A comparison study between high-frequency kerfless and fully-kerfed ultrasonic phased arrays," in *Proceedings of the 2020 IEEE International Ultrasonics Symposium (IUS)* (Las Vegas, NV: IEEE), 1–5.

Boonruang, A., Thongchai, T., Button, T., and Cochran, S. (2019). "Microfabrication of 1-3 composites with photolithographically defined electrode patterns for kerfless microultrasound arrays," in *Proceedings of the 2019 IEEE International Ultrasonics Symposium (IUS)* (Glasgow: IEEE), 1746–1749.

Brown, J. A., Foster, F. S., Needles, A., Cherin, E., and Lockwood, G. R. (2007). Fabrication and performance of a 40-MHz linear array based on a 1-3 composite with geometric elevation focusing. *IEEE Trans. Ultrason. Ferroelectr. Freq. Control* Vol. 54, 1888–1894. doi: 10.1109/TUFFC.2007.473

.Cabrera-Munoz, N. E., Eliahoo, P., Wodnicki, R., Jung, H., Chiu, C. T., Williams, J. A., et al. (2019). Fabrication and characterization of a miniaturized 15-MHz side-looking phased-array transducer catheter. *IEEE Trans. Ultrason. Ferroelectr. Freq. Control* 66, 1079-1092. doi: 10.1109/tuffc.2019.2906134

Cannata, J. M., Williams, J. A., Chang-Hong, H., and Shung, K. K. (2008). "Development of high frequency linear arrays using interdigital bonded composites," in *Proceedings of the2008 IEEE Ultrasonics Symposium* (Beijing: IEEE), 686–689.

Cannata, J. M., Williams, J. A., Qifa, Z., Ritter, T. A., and Shung, K. K. (2006). Development of a 35-MHz piezo-composite ultrasound array for medical imaging. *IEEE Trans. Ultrason. Ferroelectr. Freq. Control* Vol. 53, 224–236. doi: 10.1109/TUFFC.2006.1588408

Chen, R., Cabrera-Munoz, N. E., Lam, K. H., Hsu, H. S., Zheng, F., Zhou, Q., et al. (2014). PMN-PT single-crystal high-frequency kerfless phased array. *IEEE Trans. Ultrason. Ferroelectr. Freq. Control* Vol. 61, 1033–1041. doi: 10.1109/tuffc.2014.2999

Chen, R., Wu, J., Ho Lam, K., Yao, L., Zhou, Q., Tian, J., et al. (2012). Thermal-independent properties of PIN-PMN-PT single-crystal linear-array ultrasonic transducers. *IEEE Trans. Ultrason. Ferroelectr. Freq. Control* Vol. 59, 2777–2784. doi: 10.1109/TUFFC.2012.2519

Chiu, C. T., Williams, J. A., Kang, B. J., Abraham, T., Shung, K. K., and Kim, H. H. (2014). "Fabrication and characterization of a 20 MHz microlinear phased array transducer for intervention guidance," in *Proceedings of the 2014 IEEE International Ultrasonics Symposium* (Chicago, IL: IEEE), 2121–2124.

Cochran, S., MacLennan, D., Button, T. W., Hughes, H., Ponting, M., and Sweet, J. (2006). "P3Q-1 ultra precision grinding in the fabrication of high frequency piezocomposite ultrasonic transducers," in *Proceedings of the 2006 IEEE Ultrasonics Symposium* (Vancouver, BC: IEEE), 2353–2356.

CTS (2021). *Piezoelectric Polycrystalline (PZT) Components and Wafers*. Available online at: www.ctscorp.com/wp-content/uploads/CTS-Corporation-Piezoelectric-Polycrystalline-PZT-Components-and-Wafers.pdf).

Dias, C. J., and Das-Gupta, D. K. (1994). "Electroactive polymer-ceramic composites," in *Proceedings of the 1994 4th International Conference on Properties and Applications of Dielectric Materials (ICPADM)*), Vol. 1 (Brisbane, QLD: IEEE), 175–178.

Enriquez, A., Saenz, L. C., Rosso, R., Silvestry, F. E., Callans, D., Marchlinski, F. E., et al. (2018). Use of intracardiac echocardiography in interventional cardiology: working with the anatomy rather than fighting it. *Circulation* 137, 2278–2294. doi: 10.1161/circulationaha.117.031343

Foster, F. S., Zhang, M. Y., Zhou, Y. Q., Liu, G., Mehi, J., Cherin, E., et al. (2002). A new ultrasound instrument for in vivo microimaging of mice. *Ultrasound Med. Biol.* 28, 1165–1172. doi: 10.1016/s0301-5629(02)00567-7

Friis, H. T., and Feldman, C. B. (1937). A multiple unit steerable antenna for short-wave reception. *Bell Syst. Tech. J.* 16, 337–419. doi: 10.1002/j.1538-7305.1937.tb00425.x

Hijazi, Z. M., Shivkumar, K., and Sahn, D. J. (2009). Intracardiac echocardiography during interventional and electrophysiological cardiac catheterization. *Circulation* 119, 587–596. doi: 10.1161/circulationaha.107.753046

Jian, X., Li, Z., Han, Z., Xu, J., Liu, P., Liu, Y., et al. (2018). the study of cable effect on high-frequency ultrasound transducer performance. *IEEE Sens. J.* 18, 5265–5271. doi: 10.1109/JSEN.2018.2838142

Kim, H. H., Hu, C., Park, J., Kang, B. J., Williams, J. A., Cannata, J. M., et al. (2010). "Characterization and evaluation of high frequency convex array transducers," in *2010 IEEE International Ultrasonics Symposium* (San Diego, CA: IEEE), 650–653.

Kim, K.-B., Hsu, D. K., Ahn, B., Kim, Y.-G., and Barnard, D. J. (2010). Fabrication and comparison of PMN-PT single crystal, PZT and PZT-based 1-3 composite ultrasonic transducers for NDE applications. *Ultrasonics* 50, 790–797. doi: 10.1016/j.ultras.2010.04.001

Lukacs, M., Yin, J., Pang, G., Garcia, R. C., Cherin, E., Williams, R., et al. (2006). Performance and characterization of new micromachined high-frequency linear arrays. *IEEE Trans. Ultrason. Ferroelectr. Freq. Control* 53, 1719–1729. doi: 10.1109/TUFFC.2006.105

Luo, L., Zhao, X., and Luo, H. (2010). "Chapter 7 - single crystal PZN-PT, PMN-PT, PSN-PT, and PIN-PT-based piezoelectric materials," in *Advanced Piezoelectric Materials (Second Edition)*, ed. K. Uchino (Sawston: Woodhead Publishing), 271–318. doi: 10.1016/b978-0-08-102135-4.00007-2

Mailloux, R. J. (1982). Phased array theory and technology. *Proc. IEEE* 70, 246–291. doi: 10.1109/PROC.1982.12285

Smith, W. A., and Auld, B. A. (1991). Modeling 1-3 composite piezoelectrics: thickness-mode oscillations. *IEEE Trans. Ultrason. Ferroelectr. Freq. Control* 38, 40–47. doi: 10.1109/58.67833

Sung Min, R., Hyung Ham, K., Ho, J., Seduk, K., and Sang-Goo, L. (2003). "A 128 channel 7.5 MHz linear array ultrasonic probe using PMN-PT single crystal," in *Proceedings of the IEEE Symposium on Ultrasonics, 2003*, Vol. 781 (Honolulu, HI: IEEE), 782–785.

Vitulano, N., Pazzano, V., Pelargonio, G., and Narducci, M. L. (2015). Technology update: intracardiac echocardiography - a review of the literature. *Med Devices* 8, 231–239. doi: 10.2147/mder.S49567

Wong, C. M., Chen, Y., Luo, H., Dai, J., Lam, K. H., and Chan, H. L. (2017). Development of a 20-MHz wide-bandwidth PMN-PT single crystal phased-array ultrasound transducer. *Ultrasonics* 73, 181–186. doi: 10.1016/j.ultras.2016.09.012

Yang, H. C., Cannata, J., Williams, J., and Shung, K. K. (2012). Crosstalk reduction for high-frequency linear-array ultrasound transducers using 1-3 piezocomposites with pseudo-random pillars. *IEEE Trans. Ultrason. Ferroelectr. Freq. Control* 59, 2312–2321. doi: 10.1109/tuffc.2012.2456

Zhang, J. Y., Xu, W. J., Carlier, J., Ji, X. M., Nongaillard, B., Queste, S., et al. (2011). "Fabrication and characterization of half-kerfed LiNbO3-based high-frequency (>100MHz) ultrasonic array transducers," in *Proceedings of the 2011 IEEE International Ultrasonics Symposium*) (Orlando, FL: IEEE), 1727–1730.

Zhang, Q., Li, Y., Liu, J., Huang, J., Tan, Q., Wang, C., et al. (2020). A PMN-PT composite-based circular array for endoscopic ultrasonic imaging. *IEEE Trans. Ultrason. Ferroelectr. Freq. Control* 67, 2354–2362. doi: 10.1109/TUFFC.2020.3005029

Zhangjian, L., Zhile, H., Xiaohua, J., Weiwei, S., Yang, J., and Yaoyao, C. (2020). Pulse-echo acoustic properties evaluation method using high

frequency transducer. *Meas. Sci. Technol.* 31:125011. doi: 10.1088/1361-6501/aba0d8

Zhou, D., Cheung, K. F., Chen, Y., Lau, S. T., Zhou, Q., Shung, K. K., et al. (2011). Fabrication and performance of endoscopic ultrasound radial arrays based on PMN-PT single crystal/epoxy 1-3 composite. *IEEE Trans. Ultrason. Ferroelectr. Freq. Control* 58, 477–484. doi: 10.1109/TUFFC.2011.1825

Zhou, W., Zhang, T., Ou-Yang, J., Yang, X., Wu, D., and Zhu, B. (2020). PIN-PMN-PT single crystal 1-3 composite-based 20 MHz ultrasound phased array. *Micromachines* 11:524. doi: 10.3390/mi11050524

Conflict of Interest: The authors declare that the research was conducted in the absence of any commercial or financial relationships that could be construed as a potential conflict of interest.

frontiers in Materials

ORIGINAL RESEARCH
published: 28 May 2021
doi: 10.3389/fmats.2021.695330

Enhanced Electrical Properties of Lead-Free Piezoelectric KNLN-BZ-BNT Ceramics With the Modification of Sm^{3+} Ions

Yi Quan[1], Lingyan Wang[1], Wei Ren[1]*, Jinyan Zhao[1], Jian Zhuang[1], Kun Zheng[1], Zhe Wang[1], Tomoaki Karaki[2], Zhishui Jiang[3] and Li Wen[3]*

[1]Electronic Materials Research Laboratory, Key Laboratory of the Ministry of Education and International Center for Dielectric Research, School of Electronic Science and Engineering, Xi'an Jiaotong University, Xi'an, China, [2]Department of Intelligent Systems Design Engineering, Faculty of Engineering, Toyama Prefectural University, Imizu, Japan, [3]Guangdong JC Technological Innovation Electronics Co., Ltd, Zhaoqing, China

Environment-friendly lead-free piezoelectric ceramics with great properties and high thermal stability are desired in the industry. In this work, the Sm^{3+}-modified lead-free $0.915(K_{0.45}Na_{0.5}Li_{0.05})NbO_3$–$0.075BaZrO_3$–$0.01(Bi_{0.5}Na_{0.5})TiO_3$ (KNLN-BZ-BNT) ceramics are prepared. The piezoelectric properties are improved with the introduction of Sm^{3+}, and the optimal properties (d_{33} = 325 pC/N and d_{33}^* = 384 pm/V) are achieved in the ceramic modified with 0.3 mol% Sm^{3+} ions. Meanwhile, this sample shows good thermal stability such that the values of d_{33}^* decreased less than 20% when the temperature raised from 30 to 180°C. These results show the Sm^{3+}-modified KNLN-BZ-BNT ceramics are good for further applications even under high temperature.

Keywords: lead-free piezoelectric, KNN-based ceramics, rare earth, piezoelectric properties, thermal stability

OPEN ACCESS

Edited by:
Chunlong Fei,
Xidian University, China

Reviewed by:
Wanlin Zhu,
Pennsylvania State University (PSU), United States
Jiapu Li,
Huazhong University of Science and Technology, China

****Correspondence:***
Lingyan Wang
l.y.wang@mail.xjtu.edu.cn
Wei Ren
wren@mail.xjtu.edu.cn

Specialty section:
This article was submitted to Smart Materials, a section of the journal Frontiers in Materials

Received: *14 April 2021*
Accepted: *05 May 2021*
Published: *28 May 2021*

Citation:
Quan Y, Wang L, Ren W, Zhao J, Zhuang J, Zheng K, Wang Z, Karaki T, Jiang Z and Wen L (2021) Enhanced Electrical Properties of Lead-Free Piezoelectric KNLN-BZ-BNT Ceramics With the Modification of Sm^{3+} Ions. Front. Mater. 8:695330. doi: 10.3389/fmats.2021.695330

INTRODUCTION

In recent years, environmental problems are a major concern in the whole world (Zhang et al., 2017; Zeng et al., 2020; Zheng et al., 2021). Lead is widely used in various industrial products such as glasses, gasoline, and batteries (Uchino, 1996; Shung, 2015; Wu et al., 2015). Ceramics based on lead zirconate titanate [$Pb(Zr, Ti)O_3$ (PZT)], the most widely used piezoelectric material, also contain PbO more than 60% (Saito et al., 2004; Jiang et al., 2016). The Restriction of Hazardous Substances Directive (RoHS) has been implemented to minimize the use of toxic materials in the end products (Saito et al., 2004; Zhang et al., 2007). Consequently, researches on lead-free piezoelectric materials are highly needed now (Saito et al., 2004; Zhao et al., 2017; Zhao et al., 2019). Among several lead-free piezoelectric materials, such as $BaTiO_3$-, $(Bi, Na)TiO_3$-, and $BiFeO_3$-based piezoelectric materials, the $(K, Na)NbO_3$ (KNN)-based piezoelectric materials, with high Curie temperature and high piezoelectric properties, are considered a potential candidate for PZT-based materials in the industry (Shrout and Zhang, 2007; Zhang et al., 2007).

The morphotropic phase boundary (MPB) between the rhombohedral phase and the tetragonal phase contributes to the excellent performance of PZT-based materials (Shrout and Zhang, 2007; Zhang et al., 2007). Furthermore, as to the vertical MPB, the PZT and PZT-based ceramics show excellent thermal stability. For the lead-free piezoelectric KNN ceramics, a phase boundary between the orthorhombic phase and the tetragonal phase called the polymorphic phase transition appeared at about 200°C (Egerton and Dillon, 1959; Karaki et al., 2013; Wang et al., 2013). By decreasing the

temperature to near room temperature, the electrical properties, especially the piezoelectric property, were dramatically enhanced. Unfortunately, the high piezoelectric coefficients only remain stable in a narrow temperature range (Karaki et al., 2013).

To solve this problem, Karaki et al. constructed an MPB of rhombohedral and tetragonal phases by the introduction of $BaZrO_3$ (Karaki et al., 2013). The piezoelectric properties were expectedly improved. Meanwhile, by introducing $Bi_{0.5}Na_{0.5}TiO_3$ in an appropriate amount, a vertical MPB has appeared in $0.915(K_{0.45}Na_{0.5}Li_{0.05})NbO_3$–$0.075BaZrO_3$–$0.01(Bi_{0.5}Na_{0.5})TiO_3$ (KNLN-BZ-BNT) ceramics, and excellent thermal stability was manifested. In this work, to further improve the properties of KNLN-BZ-BNT ceramics, the doped ceramics with 0.1, 0.3, and 0.5 mol% Sm^{3+} ions are prepared. The crystalline phase, micro-morphologies, electrical properties, and thermal stability are investigated. For comparison, the KNLN-BZ-BNT ceramics in our previous work are discussed together (Quan et al., 2018; Quan et al., 2019; Quan et al., 2020).

EXPERIMENTAL DETAILS

$0.915(K_{0.45}Na_{0.5}Li_{0.05})NbO_3$–$0.075BaZrO_3$–$0.01(Bi_{0.5-x}Sm_xNa_{0.5})TiO_3$, where x = 0.1, 0.3, 0.5, ceramics were synthesized by a solid oxide reaction process. Reagent-grade oxide/carbonate powders, K_2CO_3 (99%), Na_2CO_3 (99.8%), Li_2CO_3 (98%), Nb_2O_5 (99.5%), $BaCO_3$ (99%), ZrO_2 (99%), Bi_2O_3 (99%), TiO_2 (98%), and Sm_2O_3 (99%), were selected as starting raw materials. The powders were weighed according to stoichiometry and mixed through ball milling, with partially stabilized ZrO_2 balls as media, in alcohol for 15 h at 300 rpm. After drying at 80°C, the powder mixtures were calcined at 800°C for 2 h. The calcined powders were re-milled for 15 h and then pressed into disks of 8 mm diameter and 1 mm thickness at 200 MPa. The green disks were heated at 600°C for 2 h to remove the organics and then sintered at 1,200 °C for 4 h in a sealed alumina curable. To minimize the volatilization of volatile elements, the green compacts were embedded in the calcined powders during sintering. The final pellets were polished and coated with silver paste on both sides, to characterize the electrical properties.

The crystalline phase structure was evaluated using an X-ray diffractometer (D/MAX-2400, Rigaku, Cu Kα radiation, Japan). The temperature dependence of the dielectric constant and dielectric loss was measured using an LCR meter (4980A, Agilent Technologies, Inc.). A ferroelectric testing system (TF Analyzer 2000E, aixACCT) was used to characterize the piezoelectric strain and the P–E and S–E hysteresis loops. The piezoelectric coefficients were measured by a piezoelectric testing system (ZJ-1, CAS), after poling in a silicon oil bath at 30 kV/cm for 10 min.

RESULTS AND DISCUSSION

The X-ray diffraction (XRD) patterns of un-doped and doped KNLN-BZ-BNT ceramics with different amounts of Sm^{3+} ions are shown in **Figure 1A**. It can be seen that all the samples show a pure perovskite structure. The introduction of Sm^{3+} ions (less than 0.5 mol%) hardly changes the crystalline phase of ceramics. The details of (200) and (002) peaks for all samples are shown in **Figure 1B**, showing an invisible difference, attributed to fewer Sm^{3+} ions. Besides, the splits of (002) and (200) become a little bit wider with the addition of Sm^{3+}, suggesting a phase close to the tetragonal one after Sm^{3+} addition.

Figure 2A shows the room-temperature polarization–electrical field (P–E) hysteresis loops of the un-doped and doped samples with different amounts of Sm^{3+} ions. All the samples show a well-saturated P–E loop. The un-doped KNLN-BZ-BNT ceramic shows the lowest remanent polarization, P_r, of 9.70 μC/cm^2. The 0.1 mol% Sm^{3+}–doped ceramic shows the highest P_r of 12.3 μC/cm^2. The decreased P_r values for 0.3 and 0.5 mol% Sm^{3+}–doped KNLN-BZ-BNT ceramics could be attributed to the more tetragonal phase. The variation of maximum polarization (P_{max}) with the amount of Sm^{3+} ions shows the same trend as the P_r. The lowest and highest P_{max} appeared in the un-doped and 0.1 mol % Sm^{3+} ion–doped KNLN-BZ-BNT ceramics, respectively. The bipolar electric field–strain (S–E) loops are shown in **Figure 2B**. Those S–E loops show typical butterfly shapes with high strain, suggesting a typical ferroelectric property. It can be seen that the KNLN-BZ-BNT ceramics show improved piezoelectric strains after doping with Sm^{3+} ions. The highest strain appeared in the 0.3 mol% and 0.5 mol% Sm^{3+}–doped ceramics, which is around 0.12%.

The temperature dependence of dielectric constants and dielectric losses at the frequency of 1 kHz for all samples is shown in **Figure 3**. At room temperature, the dielectric constant of the un-doped KNLN-BZ-BNT ceramic is 1,441. Doping with the Sm^{3+} ions, all the ceramics show a high dielectric constant of 1800 and a low dielectric loss of ~3%, suitable for further applications. It can be noticed that introducing Sm^{3+} ions did not affect the Curie temperatures (T_C) of KNLN-BZ-BNT ceramics, and all the samples show a T_C of 240°C. On further inspection, all the samples did not show dielectric anomaly before the temperature was up to T_C, indicating a good ferroelectric-stable characteristic. The temperature of 240°C is enough for some high-temperature applications, such as actuators in car engines (Turner et al., 1994).

To measure the d_{33}* of the samples, the unipolar strains are measured and shown in **Figure 4A**. The d_{33}* was calculated by (Zhu et al., 2015; Li et al., 2018)

$$d_{33}^{*} = \frac{S}{E}, \tag{1}$$

where S is the strain under E (electric field). The un-doped KNLN-BZ-BNT ceramic shows the lowest strain of 0.087%. The Sm^{3+}-doped ceramics show the enhanced unipolar strains. The strain of the 0.1% Sm^{3+}–doped ceramic is 0.105%. A similar strain of 0.114% was obtained in the doped ceramics with 0.3 mol% and 0.5 mol% Sm^{3+}. **Figure 4B** plots the variation of d_{33} and d_{33}* of all the ceramics with the amount of Sm^{3+}. It can be seen that the lowest value

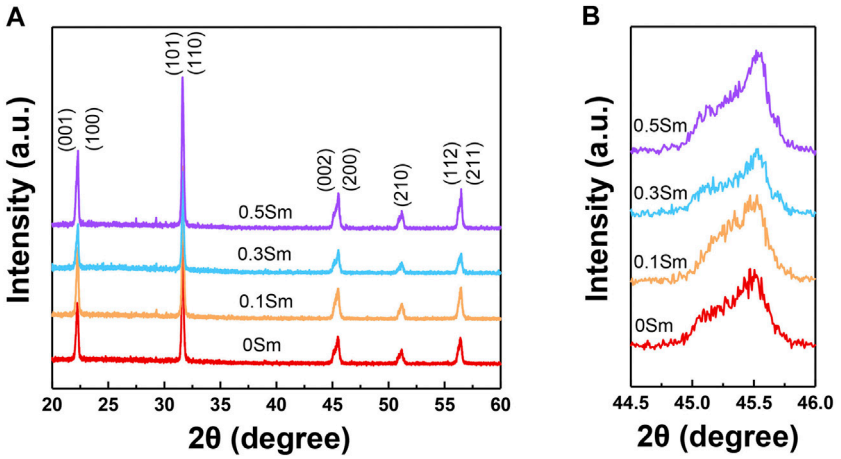

FIGURE 1 | XRD patterns of un-doped (Quan et al., 2018) and Sm^{3+}-modified KNLN-BZ-BNT ceramics. **(A)** 2θ is between 10 and 60°, and **(B)** 2θ is between 44.5 and 46°.

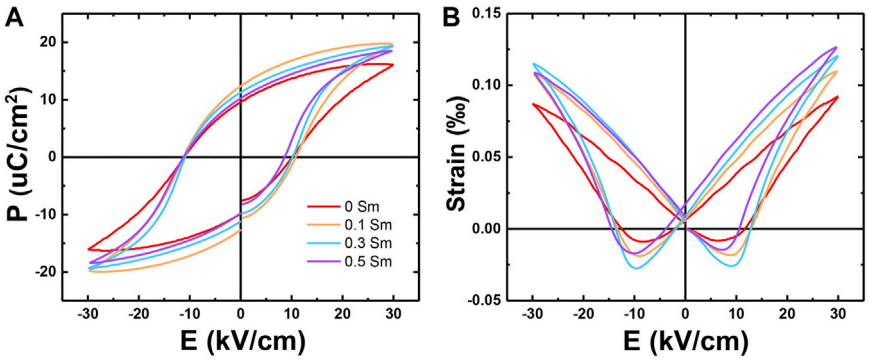

FIGURE 2 | (A) Room-temperature polarization–electrical field hysteresis loops; **(B)** bipolar electric field–strain curves of un-doped (Quan et al., 2018) and Sm^{3+}-modified KNLN-BZ-BNT ceramics.

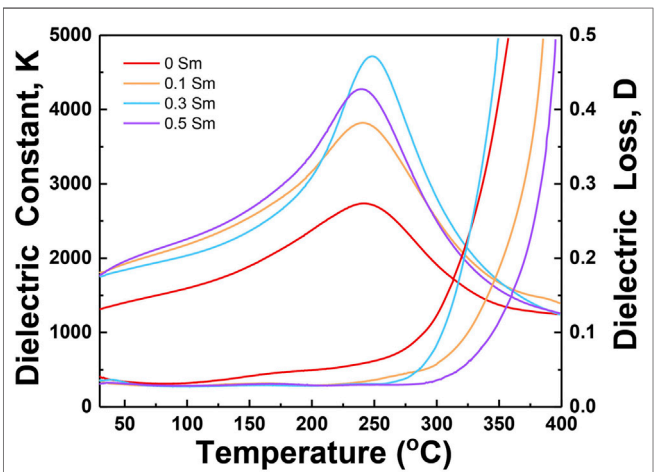

FIGURE 3 | Temperature-dependent dielectric constant and dielectric loss of un-doped (Quan et al., 2018) and Sm^{3+}-modified KNLN-BZ-BNT ceramics.

appeared in the un-doped KNLN-BZ-BNT ceramic. With the increasing amount of Sm^{3+} ions, the d_{33} and d_{33}* increased and the highest values were obtained in the ceramic doped with 0.3 mol% Sm^{3+} ions. The highest d_{33} and d_{33}* are 325 pC/N and 384 pm/V, respectively. These results indicate that the 0.3 mol% Sm^{3+} addition is the most effective way to improve the piezoelectric response of KNLN-BZ-BNT ceramics.

The doping of Sm^{3+} improved the piezoelectric and ferroelectric properties of KNLN-BZ-BNT ceramics. And the optimal performances were achieved in the sample with 0.3 mol% Sm^{3+} addition. To investigate the thermal stability of the Sm^{3+}-doped KNLN-BZ-BNT ceramics, the temperature dependence of unipolar strain and *P–E* loops is shown in **Figures 5A,B**, respectively. The strain under 30 kV/cm at room temperature is 0.114%; then, it decreased slightly with the increasing temperature. When the temperature went up to 180°C, the unipolar strain remained 0.094%, which shows good thermal stability. The samples show good ferroelectric

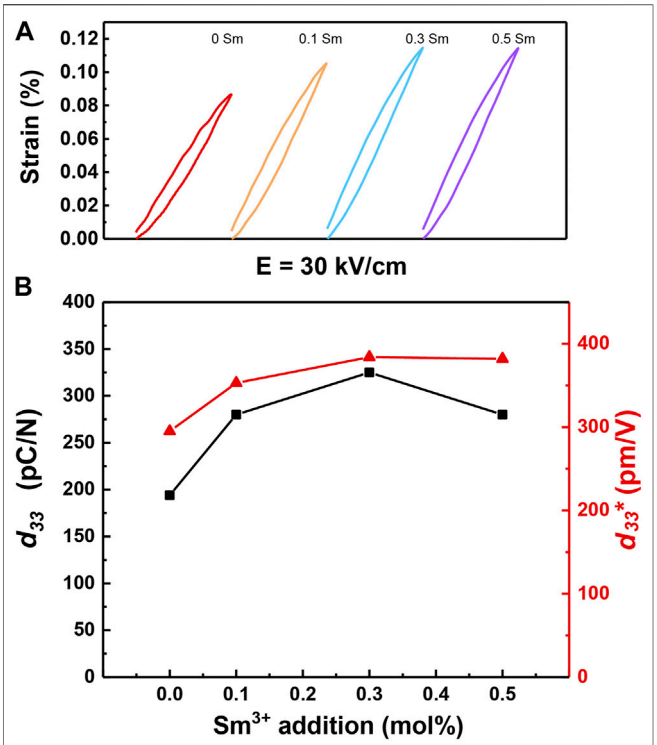

FIGURE 4 | (A) Unipolar piezoelectric strains and **(B)** variation of d_{33} and d_{33}* of un-doped (Quan et al., 2018) and Sm^{3+}-modified KNLN-BZ-BNT ceramics.

properties even at the temperature of 180°C. The P_r decreased from 11.19 μC/cm^2 at room temperature (30°C) to 7.91 μC/cm^2 at 180°C, and the P_{max} decreased from 19.29 μC/cm^2 to 16.15 μC/cm^2. To manifest the temperature dependence of ferroelectric and piezoelectric properties of KNLN-BZ-BNT with 0.3 mol% Sm^{3+} ions, the variation of P_r and normalized d_{33}* with temperature is plotted in **Figure 5C**. It can be found that the normalized d_{33}* of the sample decreased less than 20% when the temperature raised from 30 to 180°C, which is better than that in the PZT-5H ceramics (Fang et al., 2019).

CONCLUSION

The un-doped and doped KNLN-BZ-BNT ceramics with 0.1, 0.3, and 0.5 mol% Sm^{3+} ions were prepared. The remanent polarization, P_r, and piezoelectric coefficients, d_{33} and d_{33}*, were improved with the introduction of Sm^{3+} ions. The best performances appeared in the sample with 0.3 mol% Sm^{3+} ions, showing a d_{33} of 325 pC/N, a d_{33}* of 384 pm/V, a P_r of 11.19 μC/cm^2, and a high strain of 0.114% at 30 kV/cm. Furthermore, the 0.3 mol% Sm^{3+}–doped KNLN-BZ-BNT ceramic shows good thermal stability. The d_{33}* values decreased less than 20% when the temperature raised from 30 to 180°C. These excellent results show the Sm^{3+}-modified KNLN-BZ-BNT ceramics are good for further applications even under high temperature.

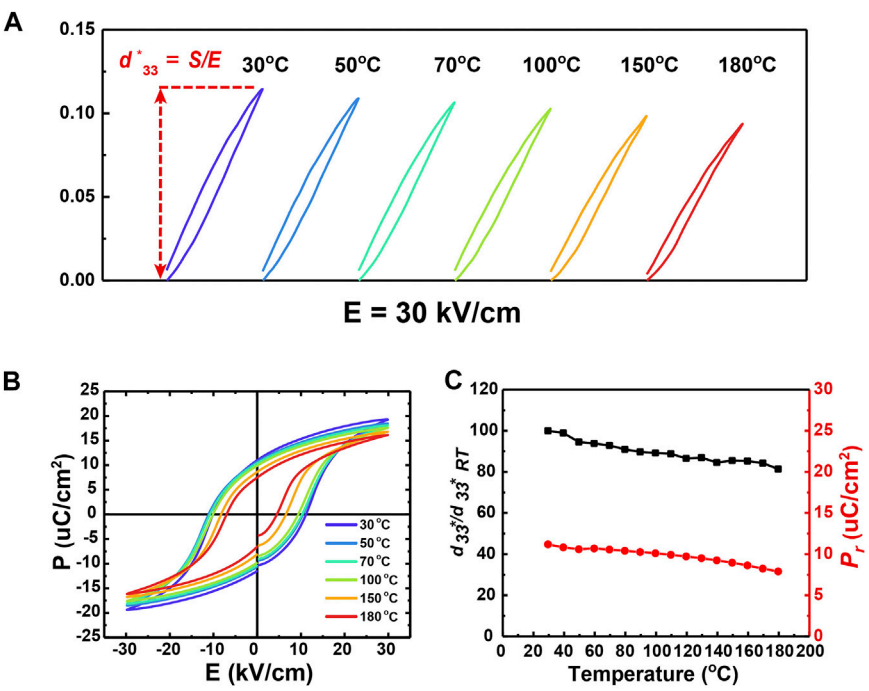

FIGURE 5 | (A) Piezoelectric strain under a 3 kV/mm unipolar field and **(B)** ferroelectric P–E hysteresis loops measured at different temperatures from 30 to 180°C; **(C)** temperature dependence of the normalized piezoelectric strain d_{33}* and P_r for the KNLN-BZ-BNT ceramic with 0.3% Sm^{3+} addition.

DATA AVAILABILITY STATEMENT

The original contributions presented in the study are included in the article/Supplementary Material, and further inquiries can be directed to the corresponding authors.

AUTHOR CONTRIBUTIONS

YQ did the experiments and wrote this article. LW (second author), WR, JZ (fourth author), JZ (fifth author), and TK designed this work and helped in writing. KZ and ZW helped in performing the experiments. ZJ and LW (10th author) helped in performing the data test.

FUNDING

This work was supported by the Natural Science Foundation of China (Grant No. 51602243, 51902246, and 51911530125), the Key Research Project of Shaanxi Province of China (Grant No. 2018ZDXM-GY-150), the Xijiang Innovation Team Introduction Program of Zhaoqing, China Postdoctoral Science Foundation (Grant No. 2018M643633 and 2019M663697), the Natural Science Fundamental Research Project of Shaanxi Province of China (No. 2019JQ590), the "111 Project" of China (B14040), and the Fundamental Research Funds for the Central Universities.

REFERENCES

Egerton, L., and Dillon, D. M. (1959). Piezoelectric and Dielectric Properties of Ceramics in the System Potassium-Sodium Niobate. *J. Am. Ceram. Soc.* 42 (9), 438–442. doi:10.1111/j.1151-2916.1959.tb12971.x

Fang, M., Rajput, S., Dai, Z., Ji, Y., Hao, Y., and Ren, X. (2019). Understanding the Mechanism of thermal-stable High-Performance Piezoelectricity. *Acta Materialia* 169, 155–161. doi:10.1016/j.actamat.2019.03.011

Jiang, L., Xing, J., Tan, Z., Wu, J., Chen, Q., Xiao, D., et al. (2016). High Piezoelectricity in (K,Na)(Nb,Sb)O3-(Bi,La,Na,Li)ZrO3 lead-free Ceramics. *J. Mater. Sci.* 51 (10), 4963–4972. doi:10.1007/s10853-016-9801-2

Karaki, T., Katayama, T., Yoshida, K., Maruyama, S., and Adachi, M. (2013). Morphotropic Phase Boundary Slope of (K, Na, Li)NbO_3-$BaZrO_3$ Binary System Adjusted Using Third Component (Bi, Na)TiO_3 Additive. *Jpn. J. Appl. Phys.* 52 (9S1), 09KD11. doi:10.7567/jjap.52.09kd11

Li, P., Zhai, J., Shen, B., Zhang, S., Li, X., Zhu, F., et al. (2018). Ultrahigh Piezoelectric Properties in Textured (K,Na)NbO3 -Based Lead-Free Ceramics. *Adv. Mater.* 30 (8), 1705171. doi:10.1002/adma.201705171

Quan, Y., Fei, C., Ren, W., Wang, L., Niu, G., Zhao, J., et al. (2020). Lead-free KNN-Based Textured Ceramics for High Frequency Ultrasonic Transducer Application. *IEEE Trans. Ultrason. Ferroelectrics, Frequency Control.* 68 (5), 1979–1987. doi:10.1109/TUFFC.2020.3039120

Quan, Y., Ren, W., Niu, G., Wang, L., Zhao, J., Zhang, N., et al. (2018). Large Piezoelectric Strain with superior thermal Stability and Excellent Fatigue Resistance of lead-free Potassium Sodium Niobate-Based Grain Orientation-Controlled Ceramics. *ACS Appl. Mater. Inter.* 10 (12), 10220–10226. doi:10.1021/acsami.8b01554

Quan, Y., Wang, L., Ren, W., Niu, G., Zhao, J., Zhuang, J., et al. (2019). Effects of MnO2 Addition on the Electrical Properties of lead-free Textured Potassium Sodium Niobate-Based Ceramics. *Ferroelectrics* 553 (1), 51–59. doi:10.1080/00150193.2019.1683495

Saito, Y., Takao, H., Tani, T., Nonoyama, T., Takatori, K., Homma, T., et al. (2004). Lead-free Piezoceramics. *Nature* 432 (7013), 84–87. doi:10.1038/nature03028

Shrout, T. R., and Zhang, S. J. (2007). Lead-free Piezoelectric Ceramics: Alternatives for PZT?. *J. Electroceram* 19 (1), 113–126. doi:10.1007/s10832-007-9047-0

Shung, K. K. (2015). *Diagnostic Ultrasound: Imaging and Blood Flow Measurements*. Boca Raton: CRC Press.

Turner, R. C., Fuierer, P. A., Newnham, R. E., and Shrout, T. R. (1994). Materials for High Temperature Acoustic and Vibration Sensors: A Review. *Appl. Acoust.* 41 (4), 299–324. doi:10.1016/0003-682x(94)90091-4

Uchino, K. (1996). *Piezoelectric Actuators and Ultrasonic Motors*. Norwell: Springer Science & Business Media.

Wang, K., Yao, F.-Z., Jo, W., Gobeljic, D., Shvartsman, V. V., Lupascu, D. C., et al. (2013). Temperature-Insensitive (K,Na)NbO3-Based Lead-Free Piezoactuator Ceramics. *Adv. Funct. Mater.* 23 (33), 4079–4086. doi:10.1002/adfm.201203754

Wu, J., Xiao, D., and Zhu, J. (2015). Potassium-Sodium Niobate Lead-Free Piezoelectric Materials: Past, Present, and Future of Phase Boundaries. *Chem. Rev.* 115 (7), 2559–2595. doi:10.1021/cr5006809

Zeng, Y., Jiang, L., Sun, Y., Yang, Y., Quan, Y., Wei, S., et al. (2020). 3D-Printing Piezoelectric Composite with Honeycomb Structure for Ultrasonic Devices. *Micromachines* 11 (8), 713. doi:10.3390/mi11080713

Zhang, M.-H., Wang, K., Du, Y.-J., Dai, G., Sun, W., Li, G., et al. (2017). High and Temperature-Insensitive Piezoelectric Strain in Alkali Niobate lead-free Perovskite. *J. Am. Chem. Soc.* 139 (10), 3889–3895. doi:10.1021/jacs.7b00520

Zhang, S., Xia, R., and Shrout, T. R. (2007). Lead-free Piezoelectric Ceramics vs. PZT? *J. Electroceram* 19 (4), 251–257. doi:10.1007/s10832-007-9056-z

Zhao, J., Ren, W., Niu, G., Zhang, N., Dong, G., Wang, L., et al. (2017). Recoverable Self-Polarization in lead-free Bismuth Sodium Titanate Piezoelectric Thin Films. *ACS Appl. Mater. Inter.* 9 (34), 28716–28725. doi:10.1021/acsami.7b04033

Zhao, J., Zhang, N., Ren, W., Niu, G., Walker, D., Thomas, P. A., et al. (2019). Polar Domain Structural Evolution under Electric Field and Temperature in the (Bi0.5 Na0.5)TiO3 -0.06BaTiO3 Piezoceramics. *J. Am. Ceram. Soc.* 102 (1), 437–447. doi:10.1111/jace.15883

Zheng, K., Quan, Y., Zhuang, J., Zhao, J., Ren, W., Wang, L., et al. (2021). Achieving High Piezoelectric Performances with Enhanced Domain-wall Contributions in -textured Sm-Modified PMN-29PT Ceramics. *J. Eur. Ceram. Soc.* 41 (4), 2458–2464. doi:10.1016/j.jeurceramsoc.2020.11.027

Zhu, B., Zhang, Z., Ma, T., Yang, X., Li, Y., Shung, K. K., et al. (2015). (100)-Textured KNN-Based Thick Film with Enhanced Piezoelectric Property for Intravascular Ultrasound Imaging. *Appl. Phys. Lett.* 106 (17), 173504. doi:10.1063/1.4919387

Conflict of Interest: ZJ and LW were employed by Guangdong JC Technological Innovation Electronics Co., Ltd.

The remaining authors declare that the research was conducted in the absence of any commercial or financial relationships that could be construed as a potential conflict of interest.

frontiers in Materials

ORIGINAL RESEARCH
published: 24 June 2021
doi: 10.3389/fmats.2021.678658

In-Situ Process and Simulation of High-Performance Piezoelectric-on-Silicon Substrate for SAW Sensor

Rui Ma[1], *Weiguo Liu*[2]*, *Xueping Sun*[2] *and Shun Zhou*[2]

[1]School of Microelectronics, Xidian University, Xi'an, China, [2]Laboratory of Thin Film Techniques and Optical Test, Xi'an Technological University, Xi'an, China

This paper studied the manufacturing process of Piezoelectric-on-Silicon (POS) substrate which integrates 128° *Y–X* Lithium niobate thin film and silicon wafer using Smart-Cut technology. The blistering and exfoliation processes of the He as-implanted LN crystal under different annealing temperatures are observed by the *in-situ* method. Unlike the conventional polishing process, the stripping mechanism of the Lithium niobate thin film is changed by controlling annealing temperature, which can improve the surface morphology of the peeling lithium niobate thin film. We prepared the 128° *Y–X* POS substrate with high single-crystal Lithium niobate thin film and surface roughness of 3.91 nm through Benzocyclobutene bonding. After simulating the surface acoustic wave (SAW) characteristics of the POS substrate, the results demonstrate that the Benzocyclobutene layer not only performs as a bonding layer but also can couple more vibrations into the LN thin film. The electromechanical coupling coefficient of the POS substrate is up to 7.59% in the Rayleigh mode when h_{LN}/λ is 0.3 and h_{BCB}/λ is 0.1. Therefore, as a high-performance substrate material, the POS substrate has proved to be an efficient method to miniaturize and integrate the SAW sensor.

Keywords: piezoelectric-on-silicon substrate, lithium niobate thin film, *in-situ* method, blistering, exfoliation, surface acoustic wave sensor

OPEN ACCESS

Edited by:
Lin Zhang,
Massachusetts Institute of Technology, United States

Reviewed by:
Wen Wang,
Chinese Academy of Sciences, China
Venu Gopal Madhav Annamdas,
Continental, Germany

***Correspondence:**
Weiguo Liu
wgliu@163.com

Specialty section:
This article was submitted to Smart Materials, a section of the journal Frontiers in Materials

Received: *10 March 2021*
Accepted: *05 May 2021*
Published: *24 June 2021*

Citation:
Ma R, Liu W, Sun X and Zhou S (2021) In-Situ Process and Simulation of High-Performance Piezoelectric-on-Silicon Substrate for SAW Sensor. Front. Mater. 8:678658. doi: 10.3389/fmats.2021.678658

INTRODUCTION

The SAW sensor is a crucial element in military and civil electrical systems, such as in communication, navigation, radars, electronic countermeasures, telecontrol, telemetric systems, etc. To realize miniaturization and integration in SAW sensor fabrication, it is necessary to have interdigital transducers (IDT) and the corresponding electronic circuit on one chip (Fu et al., 2014; Bauer et al., 2015; Dargis et al., 2020). Nowadays, most of the SAW sensors are made on the piezoelectric crystal, which brings about difficulties in the integration and miniaturization (Lu et al., 2013; Mimura et al., 2017). Using a multilayer structure to prepare the SAW sensor is considered one of the most promising techniques (Moulet et al., 2008; Maouhoub et al., 2016; Tian et al., 2016; Sun et al., 2019; Naumenko, 2020). Since the piezoelectric-on-silicon (POS) substrate bonds the piezoelectric thin film on a silicon wafer, this structure can efficiently reduce the SAW sensor's volume and weight (Abdolvand et al., 2008; Ali and Lee, 2016). Therefore, the development and optimization of the high-performance POS substrate process have become a research hotspot.

Lithium niobate ($LiNbO_3$, LN) is widely adopted in the preparation of SAW sensors due to its excellent piezoelectric properties. Several techniques are applied to fabricate LN single-crystal thin films, such as RF sputtering and sol-gel (Ishihara et al., 2003; Takahashi et al., 2004). However, the complex lattice structures in the LN crystal lead to lattice mismatching between the thin film and substrate, subsequently seriously affecting the quality of the epitaxial film. To address this problem, an emerging technique, known as "Smart-Cut," was introduced to acquire high-quality single-crystal LN thin film (Bruel, 1995; Bruel et al., 1997). This technology has proven to be very advantageous in preparing LN thin films on insulators (LNOI), which structure is similar to the POS substrate (Rabiei and Gunter, 2004; Poberaj et al., 2009; Poberaj et al., 2012; Ma et al., 2014; Wang et al., 2018; Luo et al., 2019; Michael et al., 2019).

The Smart-Cut technology transfers the peeled thin film onto a supporting substrate through bonding and crystal ion slicing. Some research groups have reported their efforts on the use of Smart-Cut technology to prepare POS substrates. The difference of the published work lies in the use of different bonding technology and surface treatment of the peeled piezoelectric thin film. Several studies on bonding technology that determine whether the thin film can be successfully transferred to the substrate have been reported. Au-Au bonding is mainly dedicated to Bulk Acoustic Resonator (BAR), where the Au layer acts as the embedded electrode (Ballandras et al., 2019). Direct bonding is very demanding on the wafer to have a surface roughness less than 0.5 nm (Pastureaud et al., 2007). Using the SiO_2 film as a middle layer is also an efficient bonding method. The LN's temperature coefficient of the frequency (TCF) can be compensated by the SiO_2 (Hori et al., 2010). The SiO_2 layer with high density is deposited on the LN substrate by plasma-enhanced chemical vapor deposition (PECVD). To reduce bond defects and strengthen the bond between the ion-sliced $LiNbO_3$ thin film and the SiO_2 layer, the surface roughness of SiO_2 should be polished to less than 1 nm. However, the required roughness is hard to achieve because a typical SiO_2 layer is 2 μm (Poberaj et al., 2012). By contrast, benzocyclobutene (BCB) bonding does not have restrictions on the surface roughness, and expensive equipment is not necessary. It has become an extremely attractive bonding solution due to the advantages of high bonding strength, low processing temperature, simple process, and so on (Shuai et al., 2018). On the other hand, the annealing temperature is another key parameter in the preparation of POS substrates, which is crucial to the smooth striping of the LN wafer. A high annealing temperature will lead to the peeled LN thin film showing parallel microcracks under thermal stress (Shuai et al., 2018), and low annealing temperature will make it so the lattice damage layer formed by the ions implantation in the LN crystal cannot be repaired. Apart from the above problems, the surface roughness of the LN thin film on the POS substrate also greatly affects the performance of the device in the preparation of the SAW sensor. However, there are few reports on how to improve the surface morphology of the peeled film. Chemical mechanical polishing (CMP) is one of the most commonly used polishing techniques, and it can reduce the root mean square (RMS) roughness of the LN thin film to 0.5 nm (Poberaj et al., 2012). However, the polishing of sub-micron thin films will increase internal stress and damage the LN thin film. Lately, some literature has reported using low-energy Ar^+ radiation as a non-contact polishing process to treat the thin film surface. When the kinetic energy of Ar^+ ions is very low, Ar^+ interacts with atoms on the surface of the LN thin film, reducing the RMS of the LN thin film from 10.81 to 4.66 nm (Luo et al., 2019). These methods all require additional polishing process steps. On the basis of ensuring performance, how to obtain higher performance POS substrates by optimizing process parameters or adopting simplified manufacturing processes is a valuable question that is worth further investigation.

In this study, the phenomena of blistering and exfoliation after ion implantation of the LN crystal were observed by *in-situ* method. Controlling the ion implantation conditions and annealing temperature can optimize the surface roughness of the stripped LN thin film. A 128° *Y–X* LN POS substrate with high-quality single crystal LN film and low surface roughness was prepared by BCB bonding. The SAW propagation characteristics of the 128° *Y–X* LN POS substrate were simulated by the finite element method (FEM).

EXPERIMENT

He ions were implanted into 2-inch 128° *Y–X* LN wafers under an energy of 200 keV. The implantation doses of He ions were 2.5×10^{16}, 4.0×10^{16}, and 6.0×10^{16} ions cm^{-2}. The LN wafers were implanted using LC-4 high-energy ion implantation equipment (Institute of semiconductors, Chinese academy of sciences). To minimize ion channeling, implantation was performed under a sample tilt of 7°. The LN wafers were cut into small pieces after ion implantation. The as-implanted LN samples were annealed in air at a temperature ranging from 30 up to 500°C. *In-situ* observation was carried out by optical microscope (DM2500, Leica) with a heating stage (THMS600, Linkam) and showed surface blistering and exfoliation. The as-implanted LN sample is bonded to the silicon wafer by BCB and annealed at a specific temperature. The morphology and surface roughness of the peeled LN thin film were measured with an atomic force microscope (AFM, Multimode8, Bruke).

The preparation process of the POS substrate by Smart-Cut technology is illustrated in **Figure 1**. The LN wafer was implanted with He ions, forming a damage layer with gaseous bubbles underneath the surface of the LN wafer. Flip the LN wafer. Next, the silicon (Si) sample was spin-coated with BCB (CYCLOTENE 3000, DOW Chemical Company), prebaking at 90°C for 3 min. The implanted surface of the LN sample and the Si wafer was then pre-bonded at 150°C for 10 min. Afterward, the LN sample/BCB/Si substrate pair was annealed in a vacuum. Eventually, the POS substrate with the LN thin film was completed. The surface of LN thin film was observed using an optical microscope. The crystalline quality of the stripping LN thin films was analyzed by X-ray diffraction (XRD) patterns. XRD was performed using a D8 Advance X-ray diffractometer. The POS structure and LN thin film thickness were estimated by field

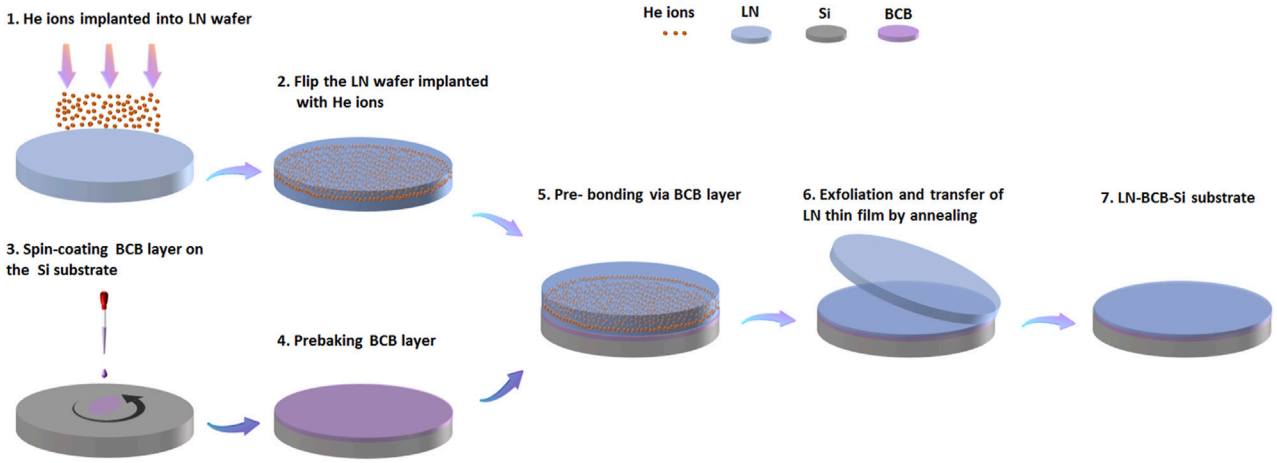

FIGURE 1 | The schematic drawing of POS substrate preparation process by smart-cut technology.

emission scanning electron microscope (FE-SEM, Zeiss GeminiSEM 500). The surface roughness of the LN thin film was measured by AFM.

RESULTS AND DISCUSSION

Blistering and Exfoliation of LN by *In-situ* Process

When He ions are implanted into the LN crystal, many nanometer-sized defects will be formed, called platelets. During the annealing process, He platelets grow laterally below the LN surface until they suddenly pop up as surface blisters due to the internal pressure after a critical size has been reached, causing blistering phenomenon (Huang et al., 1999). The time required to form optically detectable surface blisters for a given annealing temperature is termed blistering time. Since the blistering time and the annealing temperature are in accordance with the Arrhenius relationship, the change of annealing temperature has a very obvious influence on the blistering time (Tong et al., 1997). **Figure 2** shows the surface blistering of the 128° *Y–X* LN with an implantation energy of 200 KeV and a dose of 2.5×10^{16} ions cm^{-2} after annealing from 260 to 310°C. Under the same injection condition, it shows that the blistering time for the LN sample becomes shorter as the annealing temperature increases. **Figure 2A** indicates that blistering of the as-implanted LN sample started after 40 min under annealing at 260°C, while **Figure 2D** presents that blistering occurred after only heating 10 s under annealing at 310°C. Simultaneously, we have also observed that the as-implanted LN samples with the implantation dose of 2.5×10^{16} ions cm^{-2} will blister in the form of bubbles and grow larger until bubbles crack and strip off regardless of the annealing temperature.

Figure 3 presents the blistering and exfoliation phenomenon of 128° *Y–X* LN with an implantation energy of 200 KeV and a dose of 4.0×10^{16} ions cm^{-2} under annealing from 240 to 275°C. The as-implanted LN samples also comply with the rule that the higher the annealing temperature, the shorter the time for blistering. In addition, it can be seen from **Figure 3A** that obvious bubbles can be observed on the surface of the as-implanted LN sample after annealing at 240°C for 21 min. Extending annealing time, the density of bubbles on the sample surface increased significantly and the size of the bubbles also increased. Starting from 30 min, the surface of the sample was filled with bubbles, and some bubbles began to break. **Figure 3B** shows the blistering of the as-implanted LN surface annealing at 250°C. The large bubbles appeared on the surface of the LN sample within 14 min. At the 16th min, the density of the bubbles continued to increase. In addition to the small bubbles bursting, there were also larger-sized bubbles broken in the 21st min. Annealing at 260°C, **Figure 3C** shows that the surface of the LN sample blistered within 12 min. At the 19th min, the density of bubbles in the left area increased while some bubbles burst. Simultaneously, the large area of the LN thin film in the right area occurred exfoliation instead of blistering. After increasing the annealing temperature to 275°C, the LN did not blister, but exfoliation occurred directly, as shown in **Figure 3D**. Ion implantation formed plane defects, called "platelets," in the LN crystal. Platelets, acting as nucleation sites for the formation of microcracks are the origin of microcracks (Pang et al., 2012; Huang et al., 2019). In addition to lattice defects caused by implantation, strain and stress inside the crystal are also induced by ion implantation (Ofan et al., 2010). As the implantation up to a large dose of 4.0×10^{16} ions cm^{-2}, a high concentration of planar defects at the end of the ion range and large internal stress inside the LN crystal are formed. Therefore, under high-temperature annealing, gas-containing microcracks quickly propagate along the lateral direction. Due to the high concentration of the He platelets, the microcracks are easy to connect together on the same plane. In this way, large micro-cracks are formed, and regional exfoliation occurs along the domain wall. This is why the peeling presents a zigzag with regular edges. Based on the above research, the annealing temperature has a direct effect on the mechanism of blistering

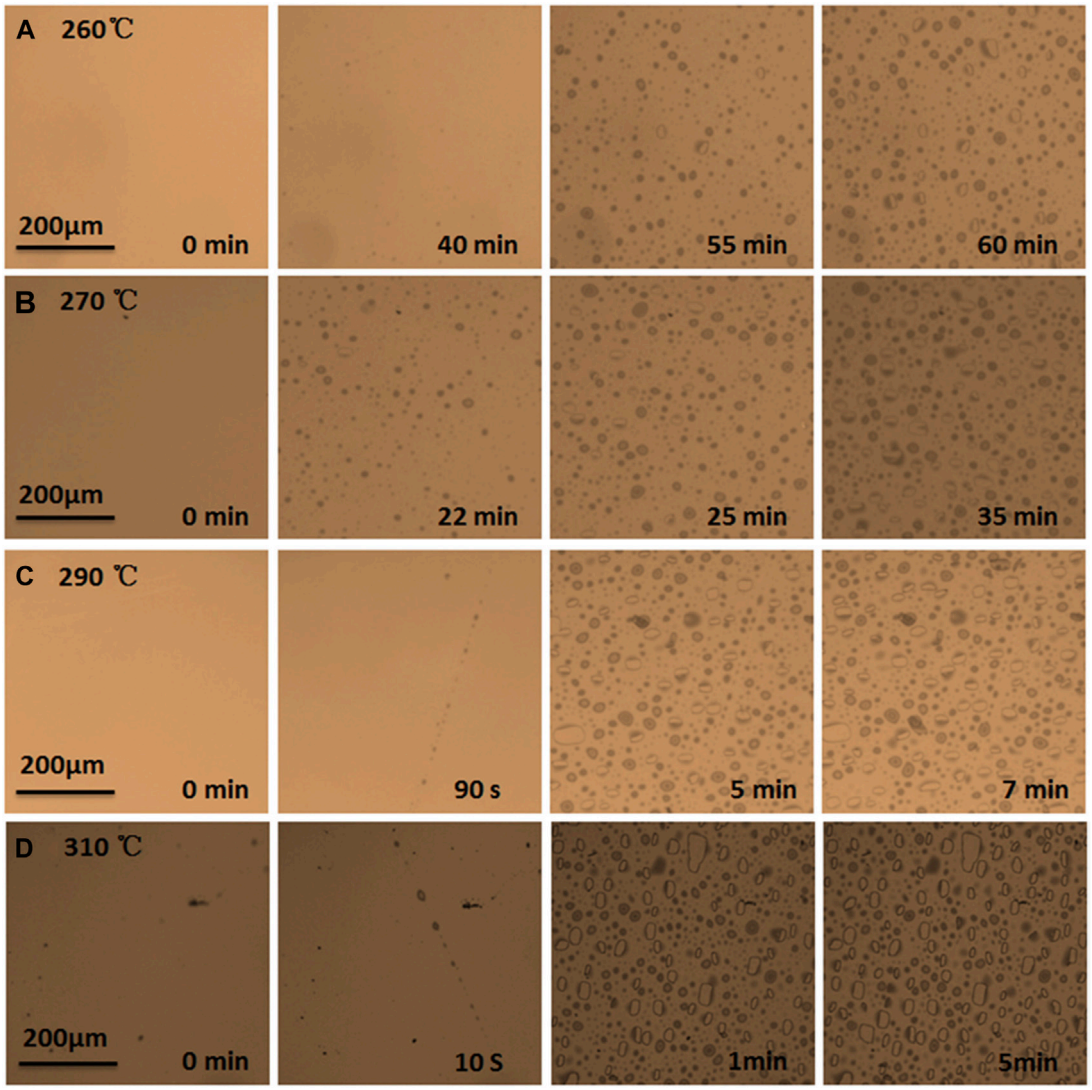

FIGURE 2 | Surface blistering of 128° *Y–X* LN implanted with a dose of 2.5 × 10^{16} ions cm^{-2} annealed at **(A)** 260°C, **(B)** 270°C, **(C)** 290°C, and **(D)** 310°C.

or exfoliation of LN crystal which implantation energy is 200 KeV and dose is 4.0 × 10^{16} ions cm^{-2}.

The residues after stripping were observed on the 128° *Y–X* LN sample surface with an implantation energy of 200 KeV and a dose of 6.0 × 10^{16} ions cm^{-2}, as shown in **Figure 4**. Notably, no blistering and exfoliation were observed on the as-implanted LN sample surface annealing from 30 to 500°C. It might be caused by the thermal effect generated during the ion implantation process. During ion implantation, the kinetic energy of He ions is transmitted to the target, and most of them are converted to thermal energy. The larger the implant dose means the more ions, the more heat it brings (Szafraniak et al., 2003; Ma et al., 2014). When the temperature of the LN sample caused by the thermal effect is higher than the blistering temperature, blistering or exfoliation will occur during the implantation process. Therefore, the temperature must be kept within a certain range, preferably at room temperature, during high-dose ion implantation.

For SAW sensors, the surface roughness of the piezoelectric thin film on the POS substrate will affect the performance of the IDT. Generally speaking, the surface of the LN thin film obtained by Smart-cut is relatively rough. The main reason for the large surface roughness of the LN thin film is that the He ion implantation into the LN crystal has a Gaussian distribution, and most of the bubbles generated during annealing are concentrated at its peak. Therefore, the thicknesses of the stripped LN thin films are not strictly equal. Base on the above research, we found that the 128° *Y–X* LN sample with an implantation energy of 200 KeV and a dose of 4.0 × 10^{16} ion cm^{-2} exhibited a large area of thin film exfoliation instead of blistering after 275°C. This stripped method inhibits the growth of bubbles in the vertical direction, accelerates the lateral spread of microcracks on the injection surface, and makes the LN thin film exfoliate in a large area. We measured the surface roughness of the stripped LN films obtained by blistering (at 240°C) and

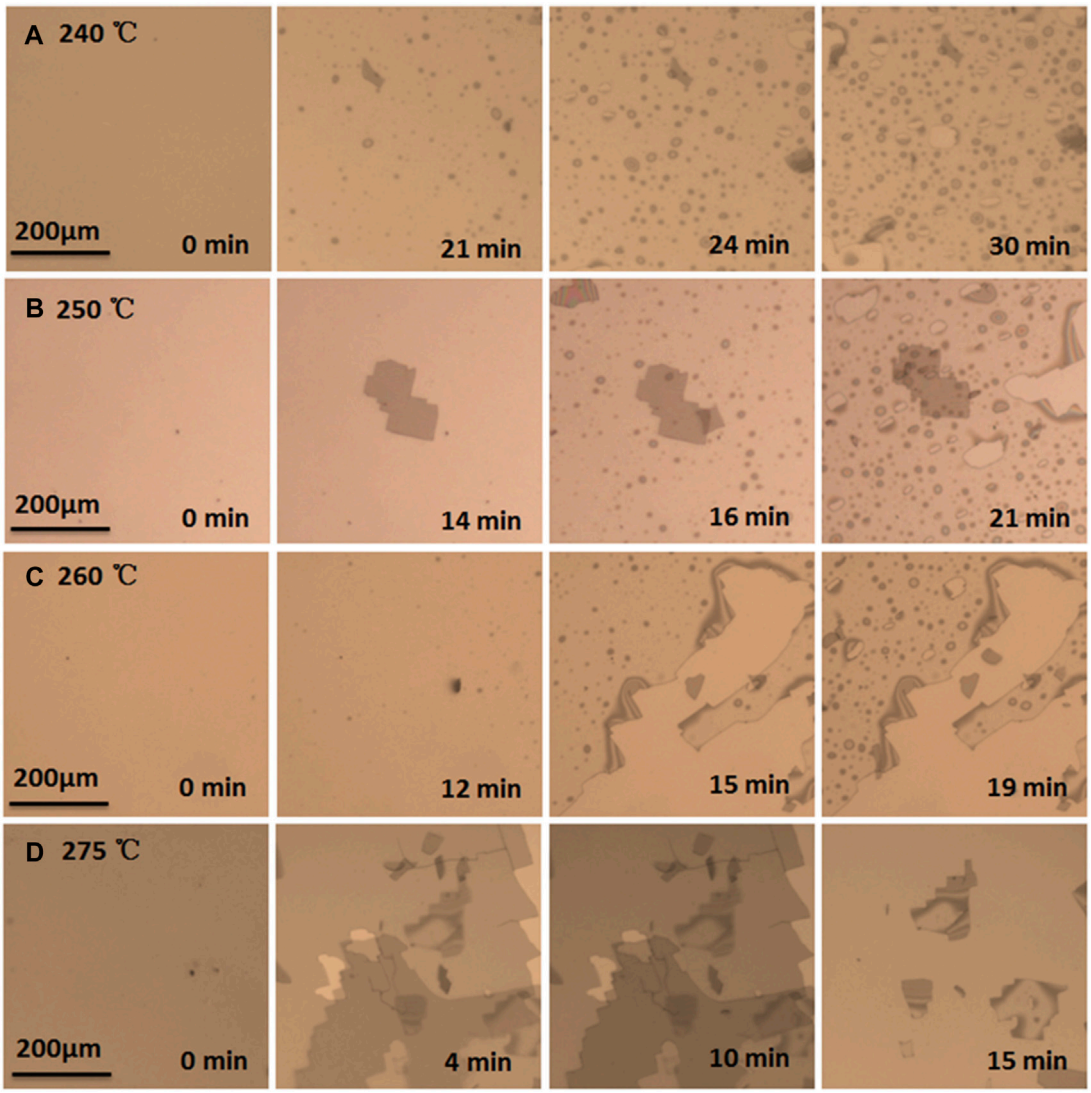

FIGURE 3 | Surface blistering of 128° *Y–X* LN implanted with a dose of 4.0 × 10^{16} ions cm^{-2} annealed at **(A)** 240°C, **(B)** 250°C, **(C)** 260°C, and **(D)** 275°C.

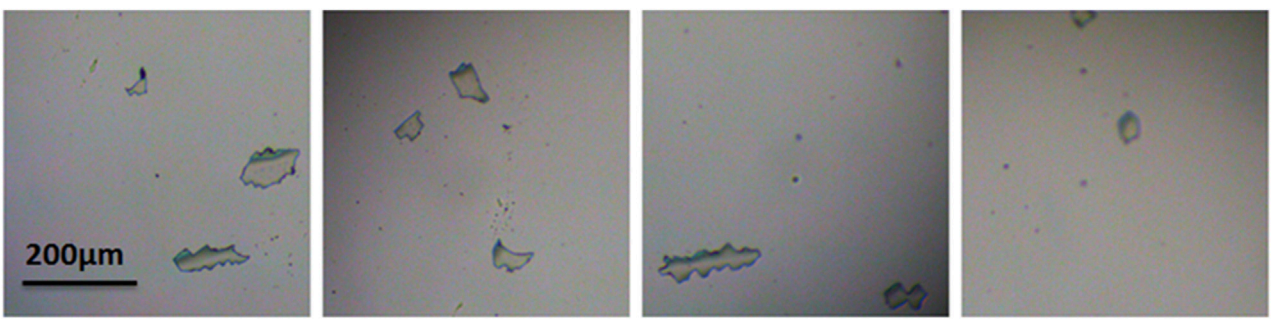

FIGURE 4 | The residues on the surface of as-implanted 128° *Y–X* LN with a He ions dose of 6.0 × 10^{16} ions cm^{-2}.

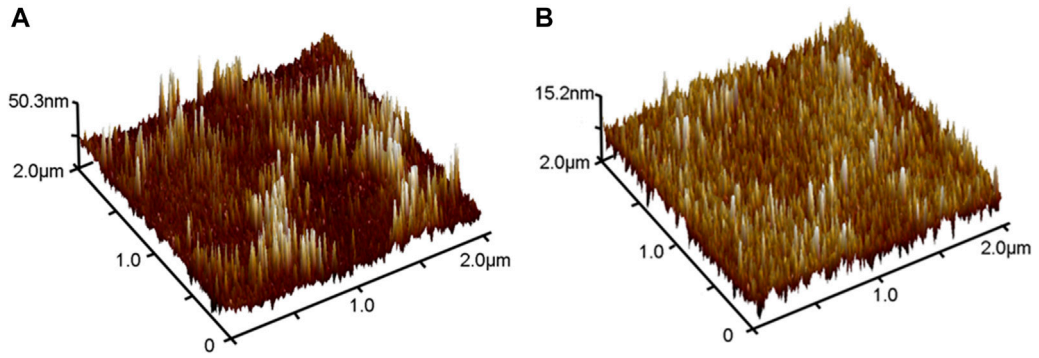

FIGURE 5 | AFM images of stripped LN thin films after annealing at **(A)** 240°C and **(B)** 275°C.

exfoliation (at 275°C) under the same injection conditions, respectively. As shown in **Figures 5A,B**, the RMS surface roughness of the LN film annealed at 240°C is 9.44 nm. By contrast, the RMS surface roughness of the LN film annealed at 275°C is as low as 3.89 nm. This result revealed that the surface roughness of the stripped LN thin film can be reduced by controlling the blistering or exfoliation method of the LN crystal after implantation.

Properties of POS Substrate

One of the aims of this work is to establish a POS substrate fabrication process using BCB bonding. The 128° *Y–X* LN with an implantation energy of 200 KeV and a dose of 4.0×10^{16} ions cm^{-2} was selected for the subsequent POS substrate fabrication. In the preparation process, annealing and bonding are crucial steps, which must be compatible with each other. After the as-implanted LN sample is bonded to a Si wafer that performs mechanical support in the following thermally induced splitting process. To achieve high-quality splitting, the bonding between the LN sample and Si wafer must be completed before the blistering of LN. Combine with the above investigation, the LN sample/BCB/Si substrate pair was annealed at 270°C for 2 h. The experimental steps of the POS substrate preparation are shown in **Supplementary Figure S1**. **Figure 6A** is an image of 128° *Y–X* LN POS substrate, which exhibits the LN thin film is exfoliated and transferred to the Si substrate. **Figure 6B** exhibits the cross-section of the 128° *Y–X* LN POS substrate with an LN thin film thickness of 692.2 nm and a BCB thickness of 3.082 μm. In the Smart-Cut technique, the thickness of exfoliated LN thin film is determined by the peak distribution of He ion implantation damage, which can be simulated using Stopping and Range of Ions in Matter (SRIM) software (Lim et al., 2020). **Figure 6C** shows the distribution of He ions and vacancies with 200 Kev implanted energy. The depth of the implanted He ions and vacancies are not strictly kept at the same level, but both followed Gaussian distribution. They are mostly gathered at a depth of 700–750 nm. Base on the thickness of LN thin films we obtained, it can be found that experimental results are consistent with the simulation results.

As shown in **Figure 7A**, the exfoliated LN thin film shows a flat surface without visible cracks or discontinuities. We take the lower annealing temperature to reduce the thermal stress in stripping of LN thin film. On the other hand, research has proved that high annealing temperature enables repairing the lattice damage which is induced by high energy ion implantation to some extent (Levy et al., 1998). Therefore, it is necessary to test the single crystalline of the LN thin film after low-temperature annealing. The XRD spectrum of the stripped LN thin film is shown in **Figure 7B**. Compared with the LN crystal standard card, the diffraction peaks of 128° *Y–X* LN thin film appear at 32.69° and 68.41°. The crystal planes are LN (104) and LN (208). The full width at half maximum (FWHM) of the LN (104) is 0.197°. The results indicate that the stripped LN thin film is a high-quality single-crystal thin film. **Figure 7C** shows the surface roughness of the 128° *Y–X* LN POS substrate, where the RMS roughness of the surface is 3.91 nm.

SAW Characteristics of POS Substrate

In addition to having smooth surface characteristics, the POS substrate is required to have as high an electromechanical coupling coefficient (K^2) as possible (Ro et al., 2009) to improve the energy conversion efficiency of the SAW sensor. The finite element analysis model is established to investigate the influence of structural parameters on SAW propagation characteristics in the POS substrate. In the multilayer structure, SAW propagation has dispersion characteristics and is related to the ratio of the thickness of the piezoelectric thin film to the SAW wavelength (El Hakiki et al., 2005). Taking 128° *Y–X* LN POS substrate as the simulation object, the model structure of IDT/LN/BCB/Si was established by COMSOL, as shown in **Supplementary Figure S2**. The detailed material constants are listed in **Supplementary Table S1** (Sun et al., 2019).

As shown in **Figures 8A,B**, the SAW phase velocity (v_p) and the K^2 of POS substrate are related to the normalized thickness of the LN thin film (h_{LN}/λ) and BCB layer (h_{BCB}/λ), where h_{LN} is the LN thin film thickness, h_{BCB} is the BCB layer thickness, λ is the SAW wavelength. The LN/Si structure without the BCB layer has been considered for comparison. The phase velocity is 3,980 m s^{-1} for the Rayleigh wave propagates in a 128° *Y–X* LN crystal (Tomar et al., 2001). The phase velocities of BCB and Si can be calculated from the Rayleigh wave equation in solids, which are 807 and 5,339 m/s, respectively (Zhou et al., 2013). Therefore, the Rayleigh mode equivalent phase velocity of the POS substrate should be between 807 and 5,339 m s^{-1}, and the

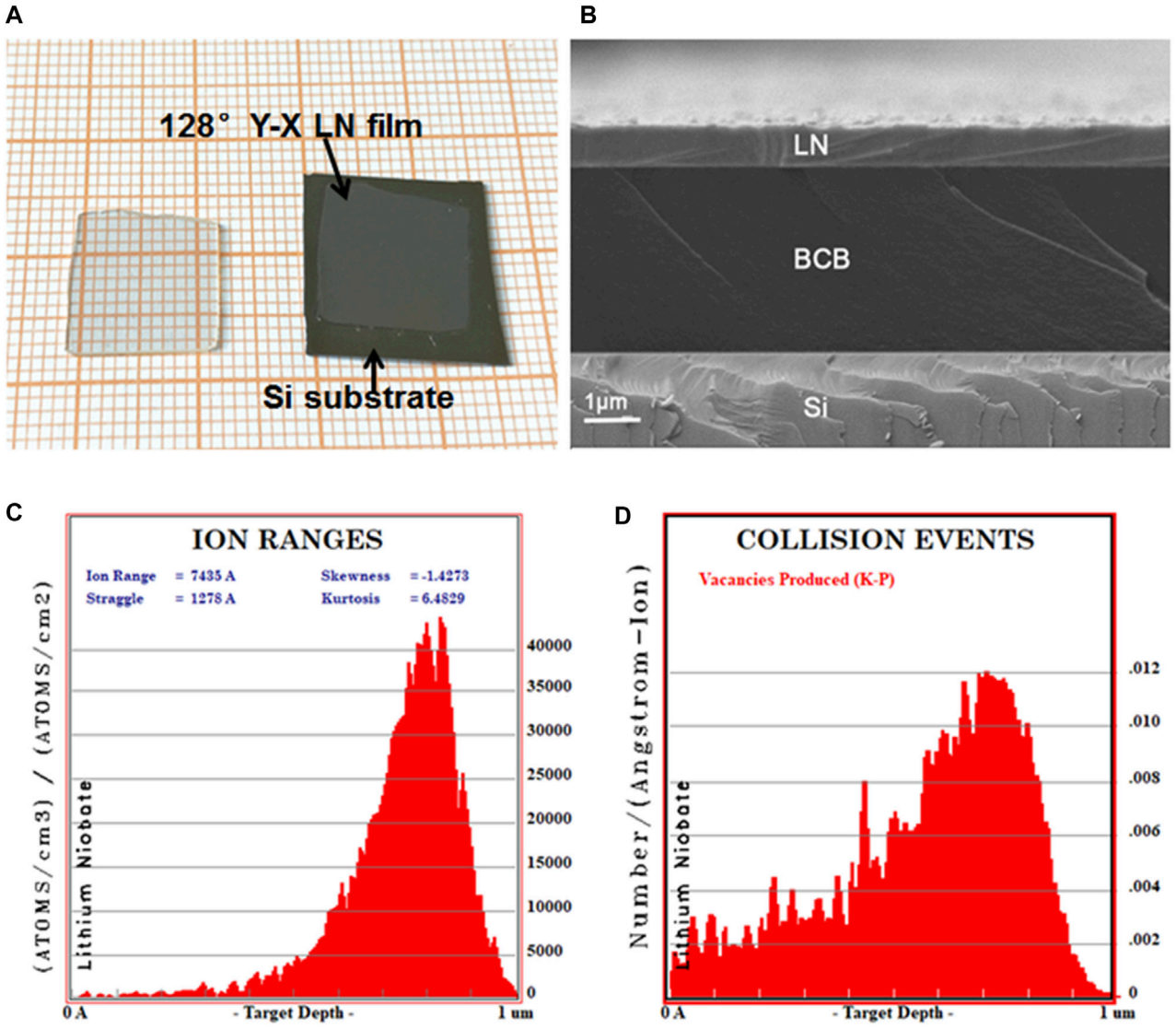

FIGURE 6 | (A) the photographs of 128° *Y–X* LN POS substrate, **(B)** The cross-section picture of 128° *Y–X* LN POS structure inspected by SEM, **(C)** He ions, and **(D)** vacancies distribution in LN crystal at 200 KeV implantation energy simulated by SRIM.

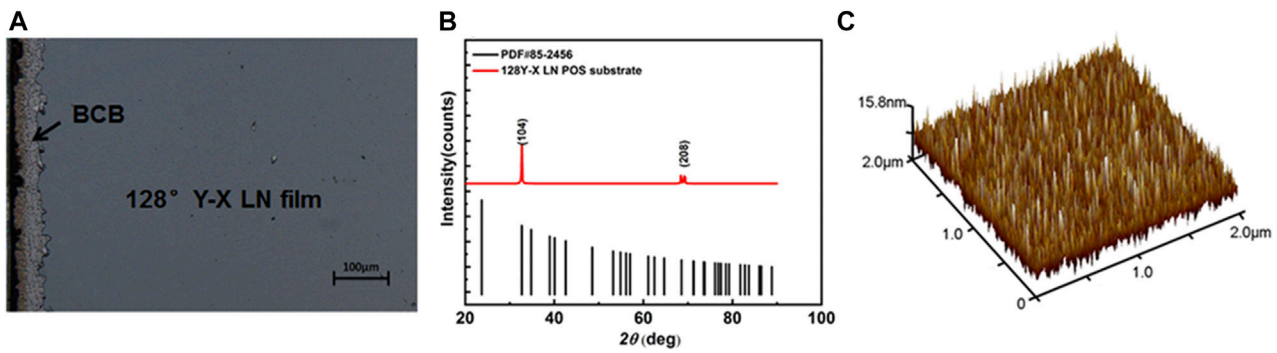

FIGURE 7 | (A) the optical microscopy images of the 128° *Y–X* LN POS substrate surface, **(B)** the XRD spectrum of the stripped LN thin film on the128° *Y–X* LN POS substrate, and **(C)** AFM images of the 128° *Y–X* LN POS substrate surface.

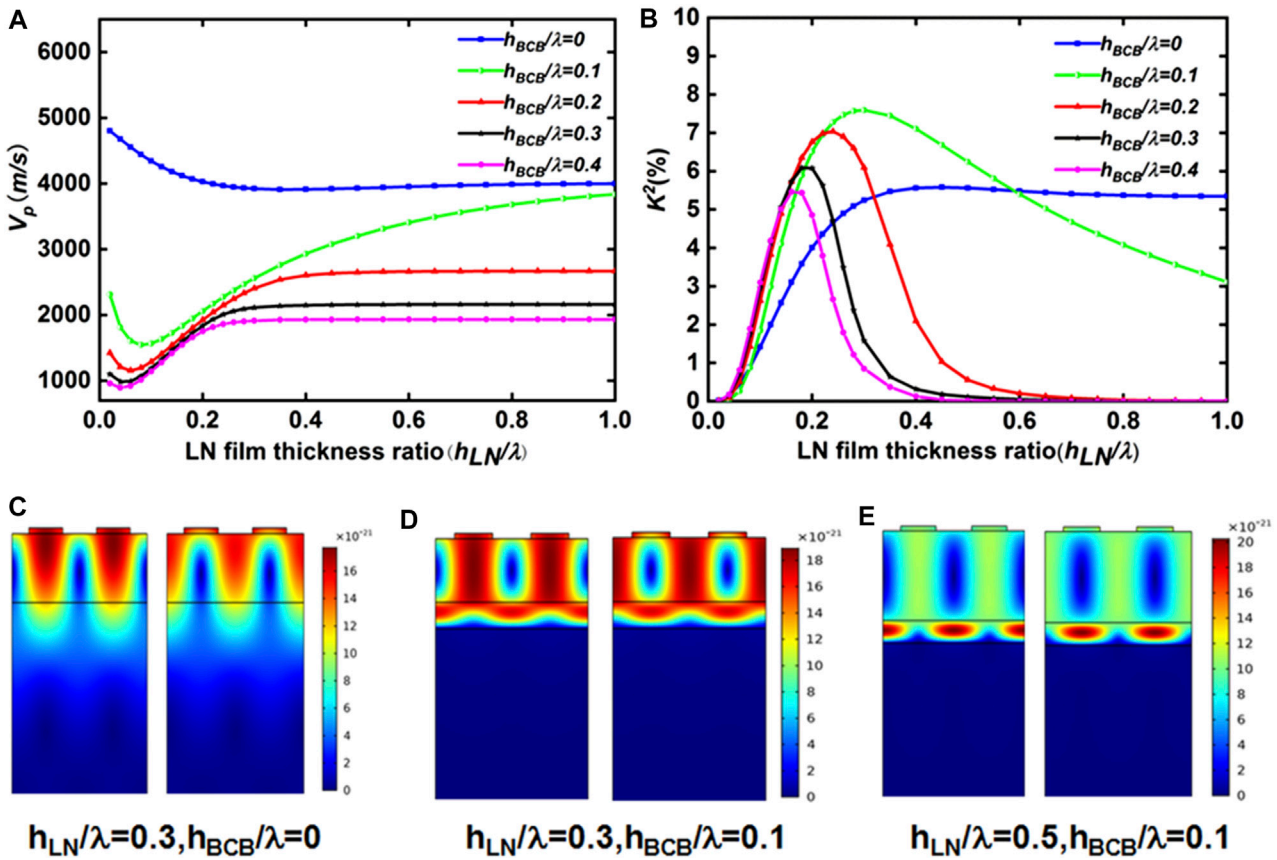

FIGURE 8 | (A) v_p dispersion curves and **(B)** K^2 dispersion curves of the 128° *Y–X* LN POS substrate, **(C)** vibration mode of POS substrates with h_{LN}/λ = 0.3 and h_{BCB}/λ = 0, **(D)** vibration mode of POS substrates with h_{LN}/λ = 0.3 and h_{BCB}/λ = 0.1, **(E)** vibration mode of POS substrates with h_{LN}/λ = 0.5 and h_{BCB}/λ = 0.1.

phase velocity of LN/Si structure is ranging from 3,980 to 5,339 m s^{-1}. Noticeable, only when h_{LN}/λ < 0.03 a*nd* h_{BCB}/λ < 0.05, the v_p of POS substrate is between 3,980 and 5,339 m s^{-1}, and the rest v_p are all between 807 and 3,980 m s^{-1}, which is confirmed by **Figure 8A**. The results demonstrate that the BCB layer has a significant effect on the v_p of POS substrate, which subsequently affects the center frequency of the SAW device. With a constant h_{BCB}/λ, the v_p of the POS substrate decreases rapidly with the thickness of the LN layer, becomes larger as h_{LN}/λ increases, and eventually remains constant when the depth reaches a specific value. When the thickness of the LN layer is constant, v_p decreases when h_{BCB}/λ increases. In **Figure 8B**, the K^2 of LN/Si structure rises with the rising h_{LN}/λ. When h_{LN}/λ > 0.3, the K^2 is approximately 5.3%, which is close to 128° *Y–X* LN crystal. When h_{BCB}/λ is constant, the K^2 of the POS substrate increases with the thickness of the LN thin film and presents an illustrative tendency to rise first and then decrease. Taking h_{BCB}/λ = 0.1 as an example, given h_{LN}/λ = 0.1, the K^2 of the POS substrate is only 1.8%, which is considered a smaller value. When h_{LN}/λ increases, the K^2 of the POS substrate increases. When h_{LN}/λ is 0.3, the K^2 of the POS substrate reaches up to 7.59%, which is higher than 5.5% of the 128° *Y–X* LN crystal (Tomar et al., 2001). When h_{LN}/λ > 0.3, the K^2 of the POS substrate dropped. The changing trend of K^2 in the POS substrate is related to its vibration mode. **Figures 8C–E** exhibit the vibration mode of POS substrates with different h_{LN}/λ and h_{BCB}/λ, respectively. When h_{LN}/λ is 0.3, h_{BCB}/λ is 0, the Rayleigh wave vibration is mainly concentrated in the LN layer, and there is also some vibration in the silicon layer. Therefore, the K^2 of the LN/Si structure is close to but not larger than the LN crystal. When h_{LN}/λ is 0.3, h_{BCB}/λ is 0.1, the Rayleigh wave's vibration is concentrated mostly in the piezoelectric thin film. Meanwhile, the vibration is restricted to the BCB layer, and there is no leaking in the Si layer. The BCB layer performs as a bonding layer and couples more SAW energy into the LN thin film. Therefore, the K^2 of the POS substrate is improved significantly. When h_{LN}/λ is 0.5, h_{BCB}/λ is 0.1, the vibration of the SAW started to concentrate on the BCB layer. The K^2 of the POS substrate has declined because the BCB does not have piezoelectric characteristics. The above simulation results indicated that the coupling effect of the BCB layer has a significant impact on the increasing of K^2 in a POS substrate under certain conditions. The thickness of the BCB layer is related to the speed of the spin coating. Moreover, LN thin films of different thicknesses can be obtained by controlling the implantation energy of He ions. Therefore, the performance of SAW propagation can be further improved by optimizing the POS structure parameters, which leads to a high-performance SAW sensor.

CONCLUSION

We proposed a preparation scheme for using Smart-Cut technology to manufacture high-quality POS substrates. Under different implantation conditions, either blistering or exfoliation of LN crystals during annealing is observed with the *in-situ* method. The results reveal the surface roughness of the peeled LN thin film can be improved by adjusting the annealing temperature. We applied BCB bonding to prepare the 128° *Y–X* LN POS substrate that proved to have good single-crystal properties and surface morphology. Compared with the LN/Si structure, the BCB layer in the POS substrate can concentrate more SAW vibration in the piezoelectric thin film layer according to the surface acoustic wave characteristics finite element analysis, which improves the K^2 of the POS substrate. When h_{LN}/λ is 0.3 and h_{BCB}/λ is 0.1, the K^2 of 128° *Y–X* LN POS substrate is as high as 7.59% in the Rayleigh mode. Overall, as a high-performance substrate material, the POS substrate is proved to be efficient in improving performance and reducing the size of the SAW sensor.

DATA AVAILABILITY STATEMENT

The original contributions presented in the study are included in the article/**Supplementary Material**, further inquiries can be directed to the corresponding author.

AUTHOR CONTRIBUTIONS

RM participated in ion implantation and annealing experiments, organized all the images and data, and fabricated the POS substrate; ZS participated in the acquisition of SEM, AFM images, and XRD data. XS participated in the simulation of POS substrate SAW characteristics and data discussion; WL proposed the study and was deeply involved in the discussion of the results and in the writing of the manuscript. All authors contributed to manuscript revision and approved the submitted version.

FUNDING

This research was supported by the National Basic Research Project (No. JCKY2016208A002), the Advanced Manufacturing Project (No. 41423020111), and the Advanced Research Fund Project (No. 6141B010271).

SUPPLEMENTARY MATERIAL

The Supplementary Material for this article can be found online at: https://www.frontiersin.org/articles/10.3389/fmats.2021.678658/full#supplementary-material

REFERENCES

Abdolvand, R., Lavasani, H., Ho, G., and Ayazi, F. (2008). Thin-film Piezoelectric-On-Silicon Resonators for High-Frequency Reference Oscillator Applications. *IEEE Trans. Ultrason. Ferroelect., Freq. Contr.* 55 (12), 2596–2606. doi:10.1109/TUFFC.2008.976

Ali, A., and Lee, J. E.-Y. (2016). "Square-extensional Mode Piezoelectric-On-Silicon Resonator for Physical Measurements of Liquids." in IEEE International Frequency Control Symposium (IFCS) (IEEE), 1–4. doi:10.1109/fcs.2016.7546823

Ballandras, S., Courjon, E., Bernard, F., Laroche, T., and Butaud, E. (2019). "New Generation of SAW Devices on Advanced Engineered Substrates Combining Piezoelectric Single Crystals and Silicon."in 2019 Joint Conference of the IEEE International Frequency Control Symposium an European Frequency and Time Forum (EFTF/IFC). doi:10.1109/fcs.2019.8855991

Bauer, T., Eggs, C., Wagner, K., and Hagn, P. (2015). A Bright Outlook for Acoustic Filtering: a New Generation of Very Low-Profile SAW, TC SAW, and BAW Devices for Module Integration. *IEEE Microwave* 16 (7), 73–81. doi:10.1109/MMM.2015.2429512

Bruel, M., Aspar, B., and Auberton-Hervé, A.-J. (1997). Smart-Cut: A New Silicon on Insulator Material Technology Based on Hydrogen Implantation and Wafer Bonding*1. *Jpn. J. Appl. Phys.* 36 (3S), 1636–1641. doi:10.1143/JJAP.36.1636

Bruel, M. (1995). Silicon on Insulator Material Technology. *Electron. Lett.* 31 (14), 1201–1202. doi:10.1049/el:19950805

Dargis, R., Clark, A., Ansari, A., Hao, Z., Park, M., Kim, D., et al. (2020). Single-Crystal Multilayer Nitride, Metal, and Oxide Structures on Engineered Silicon for New-Generation Radio Frequency Filter Applications. *Phys. Status Solidi A.* 217 (7), 1900813. doi:10.1002/pssa.201900813

El Hakiki, M., Elmazria, O., Assouar, M. B., Mortet, V., Le Brizoual, L., Vanecek, M., et al. (2005). ZnO/AlN/diamond Layered Structure for SAW Devices Combining High Velocity and High Electromechanical Coupling Coefficient. *Diamond Relat. Mater.* 14 (3-7), 1175–1178. doi:10.1016/j.diamond.2005.01.002

Fu, C., Elmazria, O., Sarry, F., Mahalingam, T., Yang, S. S., and Lee, K. (2014). Development of Wireless, Batteryfree Gyroscope Based on One-Port SAW Delay Line and Double Resonant Antenna. *Sens. Actuators A: Phys.* 220, 270–280. doi:10.1016/j.sna.2014.10.006

Hori, Y., Kobayashi, H., Tohyama, K., Iwasaki, Y., and Suzuki, K. (2010). "A Hybrid Substrate for a Temperature-Compensated Surface Acoustic Wave Filter,"in 2009 IEEE International Ultrasonics Symposium. doi:10.1109/ultsym.2009.5441626

Huang, K., Li, Z., Yan, Y., Zhao, X., Li, W., You, T., et al. (2019). Comparative Study of the Ion-Slicing Mechanism of Y-Cut LiNbO3. *AIP Adv.* 9 (8), 085001. doi:10.1063/1.5112792

Huang, L.-J., Tong, Q.-Y., Chao, Y.-L., Lee, T.-H., Martini, T., and Gösele, U. (1999). Onset of Blistering in Hydrogen-Implanted Silicon. *Appl. Phys. Lett.* 74 (7), 982–984. doi:10.1063/1.123430

Ishihara, M., Nakamura, T., Kokai, F., and Koga, Y. (2003). Preparation of Lithium Niobate Thin Films on diamond-coated Silicon Substrate for Surface Acoustic Devices. *Diam. Relat. Mater.* 12 (10-11), 1809–1813. doi:10.1016/s0925-9635(03)00212-7

Levy, M., Osgood, R. M., Liu, R., Cross, L. E., Cargill, G. S., Kumar, A., et al. (1998). Fabrication of Single-crystal Lithium Niobate Films by crystal Ion Slicing. *Appl. Phys. Lett.* 73 (16), 2293–2295. doi:10.1063/1.121801

Lim, C.-M., Zhao, Z., Sumita, K., Toprasertpong, K., Takenaka, M., and Takagi, S. (2020). Effects of Hydrogen Ion Implantation Dose on Physical and Electrical Properties of Ge-On-Insulator Layers Fabricated by the Smart-Cut Process. *AIP Adv.* 10 (1), 015045. doi:10.1063/1.5132881

Lu, X., Mouthaan, K., and Soon, Y. T. (2014). Wideband Bandpass Filters with SAW-filter-like Selectivity Using Chip SAW Resonators. *IEEE Trans. Microwave Theor. Techn.* 62 (1), 28–36. doi:10.1109/TMTT.2013.2292041

Luo, W., Luo, J., Shuai, Y., Zhang, K., Wang, T., Wu, C., et al. (2019). Infrared Detector Based on crystal Ion Sliced LiNbO3 Single-crystal Film with BCB Bonding and thermal Insulating Layer. *Microelectronic Eng.* 213, 1–5. doi:10.1016/j.mee.2019.04.004

Ma, C., Lu, F., and Ma, Y. (2014). Blistering and Cracking of LiTaO3 Single crystal under Helium Ion Implantation. *Appl. Phys. A.* 118 (4), 1233–1238. doi:10.1007/s00339-014-8821-5

Maouhoub, S., Aoura, Y., and Mir, A. (2016). FEM Simulation of AlN Thin Layers on diamond Substrates for High Frequency SAW Devices. *Diamond Relat. Mater.* 62, 7–13. doi:10.1016/j.diamond.2015.12.004

Michael, R., Peter, O., Weigel, J., Zhao, J., and Mookherjea, S. (2019). Toward 3D Integrated Photonics Including Lithium Niobate Thin Films: A Bridge between Electronics, Radio Frequency, and Optical Technology. *Nanotechnol. Mag. IEEE* 13 (4), 18–33. doi:10.1109/MNANO.2019.2916115

Mimura, M., Ajima, D., Konoma, C., and Murase, T. (2017). "Small Sized Band 20 SAW Duplexer Using Low Acoustic Velocity Rayleigh SAW on $LiNbO_3$ Substrate,IEEE International Ultrasonics Symposium (IUS) (IEEE), 1–4. doi:10.1109/ultsym.2017.8092581

Moulet, J., Pijolat, M., Dechamp, J., Mazen, F., Tauzin, A., Rieutord, F., et al. (2008). "High Piezoelectric Properties in $LiNbO_3$ Transferred Layer by the Smart Cut™ Technology for Ultra Wide Band BAW Filter Applications," in 2018 IEEE International Electron Devices Meeting, 1–4. doi:10.1109/iedm.2008.4796785

Naumenko, N. F. (2020). Advanced Substrate Material for SAW Devices Combining $LiNbO_3$ and Langasite. *IEEE Trans. Ultrason. Ferroelect., Freq. Contr.* 67 (9), 1909–1915. doi:10.1109/TUFFC.2020.2985744

Ofan, A., Zhang, L., Gaathon, O., Bakhru, S., Bakhru, H., Zhu, Y., et al. (2010). Publisher's Note: Spherical Solid He Nanometer Bubbles in an Anisotropic Complex Oxide [Phys. Rev. B82, 104113 (2010)]. *Phys. Rev. B* 82 (10), 2511–2524. doi:10.1103/PhysRevB.82.109901

Pang, L. L., Wang, Z. G., Jin, Y. F., Yao, C. F., Cui, M. H., Sun, J. R., et al. (2012). The Modification of LiTaO3 crystal by Low-Energy He-Ion Implantation. *Nucl. Instr. Methods Phys. Res. Section B: Beam Interactions Mater. Atoms* 290 (none), 54–58. doi:10.1016/j.nimb.2012.09.003

Pastureaud, T., Solal, M., Biasse, B., Aspar, B., Briot, J.-B., Daniau, W., et al. (2007). High-frequency Surface Acoustic Waves Excited on Thin-Oriented LiNbO/sub 3/Single-crystal Layers Transferred onto Silicon. *IEEE Trans. Ultrason. Ferroelect., Freq. Contr.* 54 (4), 870–876. doi:10.1109/tuffc.2007.321

Poberaj, G., Hu, H., Sohler, W., and Günter, P. (2012). Lithium Niobate on Insulator (LNOI) for Micro-photonic Devices. *Laser Photon. Rev.* 6 (4), 488–503. doi:10.1002/lpor.201100035

Poberaj, G., Koechlin, M., Sulser, F., Guarino, A., Hajfler, J., and Günter, P. (2009). Ion-sliced Lithium Niobate Thin Films for Active Photonic Devices. *Opt. Mater.* 31 (7), 1054–1058. doi:10.1016/j.optmat.2007.12.019

Rabiei, P., and Gunter, P. (2004). Optical and Electro-Optical Properties of Submicrometer Lithium Niobate Slab Waveguides Prepared by crystal Ion Slicing and Wafer Bonding. *Appl. Phys. Lett.* 85 (20), 4603–4605. doi:10.1063/1.1819527

Ro, R., Chiang, Y. F., Sung, C. C., Lee, R., and Wu, S. (2009). Theoretical Analysis of SAW Propagation Characteristics in (100) Oriented AlN/diamond Structure. *IEEE Trans. Ultrason. Ferroelectr Freq Control.* 57 (1), 46–51. doi:10.1109/TUFFC.2010.1377

Shuai, Y., Gong, C., Bai, X., Wu, C., Luo, W., Böttger, R., et al. (2018). Fabrication of Y128- and Y36-Cut Lithium Niobate Single-Crystalline Thin Films by crystal-ion-slicing Technique. *Jpn. J. Appl. Phys.* 57 (4S), 04FK05. doi:10.7567/jjap.57.04fk05)

Sun, X., Liu, W., Ge, S., Zhou, S., Li, X., and Lin, D. (2019). Achieving Both High Electromechanical Response and Stable Temperature Behavior in Si/SiO2/Al/LiTaO3 sandwich Structure. *AIP Adv.* 9 (3), 035145. doi:10.1063/1.5083128

Szafraniak, I., Radu, I., Scholz, R., Alexe, M., and Gösele, U. (2003). Single-Crystalline Ferroelectric Thin Films by Ion Implantation and Direct Wafer Bonding. *Integrated Ferroelectrics* 55 (1), 983–990. doi:10.1080/10584580390259452

Takahashi, M., Yamauchi, K., Yagi, T., Nishiwaki, A., Wakita, K., Ohnishi, N., et al. (2004). Preparation and Characterization of High-Quality Stoichiometric LiNbO3 Thick Films Prepared by the Sol-Gel Method. *Thin Solid Films* 458 (1-2), 108–113. doi:10.1016/j.tsf.2003.12.066

Tian, X.-G., Tao, L.-Q., Liu, B., Zhou, C., Yang, Y., and Ren, T.-L. (2016). Surface Acoustic Wave Devices Based on High Quality Temperature-Compensated Substrates. *IEEE Electron. Device Lett.* 37 (8), 1063–1066. doi:10.1109/LED.2016.2584785

Tomar, M., Gupta, V., Mansingh, A., and Sreenivas, K. (2001). Temperature Stability Ofc-axis Oriented LiNbO3/SiO2/Si Thin Film Layered Structures. *J. Phys. D: Appl. Phys.* 34 (15), 2267–2273. doi:10.1088/0022-3727/34/15/305

Tong, Q.-Y., Gutjahr, K., Hopfe, S., Gösele, U., and Lee, T.-H. (1997). Layer Splitting Process in Hydrogen-Implanted Si, Ge, SiC, and diamond Substrates. *Appl. Phys. Lett.* 70 (11), 1390–1392. doi:10.1063/1.118586

Wang, C., Zhang, M., Chen, X., Bertrand, M., Shams-Ansari, A., Chandrasekhar, S., et al. (2018). Integrated Lithium Niobate Electro-Optic Modulators Operating at CMOS-Compatible Voltages. *Nature* 562 (7725), 101–104. doi:10.1038/s41586-018-0551-y

Zhou, J., He, X., Jin, H., Wang, W., Feng, B., Dong, S., et al. (2013). Crystalline Structure Effect on the Performance of Flexible ZnO/polyimide Surface Acoustic Wave Devices. *J. Appl. Phys.* 114 (4), 044502. doi:10.1063/1.4816002

Conflict of Interest: The authors declare that the research was conducted in the absence of any commercial or financial relationships that could be construed as a potential conflict of interest.

frontiers in Materials

REVIEW
published: 08 July 2021
doi: 10.3389/fmats.2021.679167

Review of Research on the Rare-Earth Doped Piezoelectric Materials

Yan Chen, Donglai Zhang, Zhong Peng, Maodan Yuan and Xuanrong Ji**

State Key Laboratory of Precision Electronics Manufacturing Technology and Equipment, Guangdong University of Technology, Guangzhou, China

The piezoelectric materials, such as ceramics, crystals, and films, have wide applications in the mechanical industry, medical imaging, electronic information, and ultrasonic devices, etc. Generally, adding oxide dopants, or introducing new solid solutions to form the morphotropic phase boundary of the piezoelectric materials were common strategies to enhance the electric properties. In recent decades, rare-earth elements doped piezoelectric materials have attracted much attention due to their multifunctional performances combining piezoelectric and photoluminescence properties, which has potential applications in ultrasonics, electronics, automatic control, machinery and optoelectronic fields. An overview of the recent investigations and perspectives on rare-earth doped piezoelectric ceramics, single crystals, and films were presented.

Keywords: piezoelectric materials, rare-earth doping, electric properties, photoluminescence properties, multifunctional materials

OPEN ACCESS

Edited by:
Chunlong Fei,
Xidian University, China

Reviewed by:
Yi Quan,
Xi'an Jiaotong University, China
Tian-Long Zhao,
Xidian University, China

****Correspondence:***
Xuanrong Ji
xr.ji@gdut.edu.cn
Maodan Yuan
mdyuan@gdut.edu.cn

Specialty section:
This article was submitted to Smart Materials, a section of the journal Frontiers in Materials

Received: *11 March 2021*
Accepted: *24 May 2021*
Published: *08 July 2021*

Citation:
Chen Y, Zhang D, Peng Z, Yuan M and Ji X (2021) Review of Research on the Rare-Earth Doped Piezoelectric Materials. Front. Mater. 8:679167. doi: 10.3389/fmats.2021.679167

INTRODUCTION

Rare-earth (RE) elements contain rich structures and energy levels and exhibit excellent optical, electrical, magnetic, and nuclear properties, which were exploited in functional materials to enhance their properties and broaden applications (Singh et al., 2015; Steudel et al., 2015).

As one of the important functional materials, piezoelectric materials play a significant role in the fields of medicine, acoustics, machinery, and electronics due to the ability of mutual conversion between mechanical energy and electric energy. The electric performances of piezoelectric materials are affected by compositions, microstructure, and lattice defects like oxygen vacancies. Thus, extensive investigations have been carried out to enhance the properties of the piezoelectric materials by introducing new solid solutions or adding oxide dopants. The rare-earth ion doping may substitute the original ions and cause the formation of vacancies so that the distortion of the crystal lattices may affect the electric properties due to their unique ionic radius and different chemical valence (Qiu and Hng, 2002; Hagemann and Hennings, 2010; Singh et al., 2011). There are 17 members in the family of rare-earth elements, including 15 lanthanides (La, Ce, Pr, Nd, Pm, Sm, Eu, Gd, Tb, Dy, Ho, Er, Tm, Yb, Lu), Sc, and Y. **Figure 1** shows the rare-earth elements doped piezoelectric materials and relative properties based on the reported works. Some piezoelectric materials with certain rare-earth doping can exhibit obvious photoluminescence properties because of the ladder-shaped 4f energy level and relatively long metastable state of some rare-earth ions (Tsonev, 2008; Sun et al., 2011; Pieter, 2013; Pieter, 2017). **Figure 2A** shows the main energy flow paths during the sensitization of lanthanide (Ln) luminescence. The energy levels of Pr^{3+}, Nd^{3+}, Sm^{3+}, Eu^{3+}, Tb^{3+}, Dy^{3+}, Ho^{3+}, Er^{3+}, Tm^{3+}, and Yb^{3+} ions are also given schematically in **Figure 2B**. The electrons in the singlet (S_0) ground state absorb energy and then jump to the singlet (S1) excited state. Besides, the excitation energy of (S_1) state is transferred to the triplet state (T) based on intersystem crossing firstly and to the 4f states

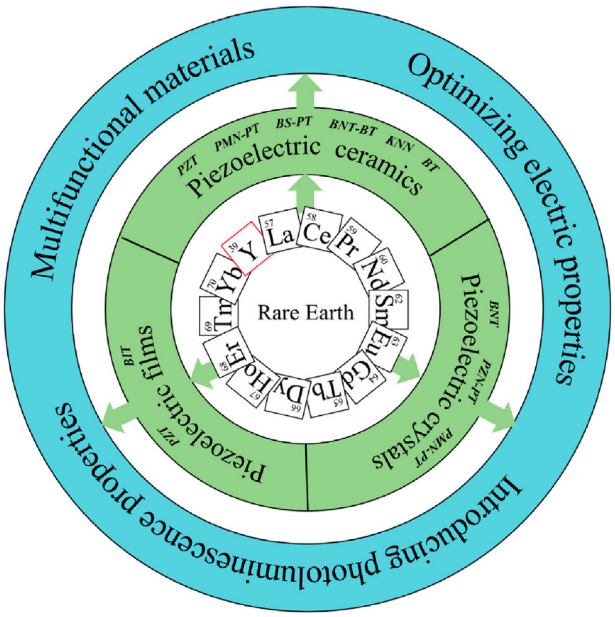

FIGURE 1 | Relationship between the rare Earth, piezoelectric materials, and properties.

subsequently. Finally, the corresponding emission of lanthanide ions can be acquired (Sun et al., 2006; Dang et al., 2008).

Although the rare-earth ion doped piezoelectric materials have attracted much attention owing to their outstanding electric and luminescence performance, there are few reviews reported in this research field. Most reviews are focused on a certain type of piezoelectric material or a fabricating method. Zheng et al. (2018) addressed the lead-free perovskite piezoelectric bulk materials. The relationships among the phase boundaries, domain configurations, and electrical properties in lead-free materials were discussed. Liu (2015) reviewed the progress on lead-free textured piezoelectric ceramics with an enhancement of the piezoelectric property. Chen et al. (2020a) paid attention to the progress of piezoelectric materials fabricated by additive manufacturing. In this paper, the effect of rare-earth doping on the electrical and optical properties of piezoelectric ceramics, crystals, and films are reviewed and discussed.

RARE-EARTH DOPED PIEZOELECTRIC CERAMICS

Rare-Earth Doped Lead-Based Piezoelectric Ceramics

Piezoelectric ceramics are a kind of piezoelectric materials with a wide range of applications due to the characteristics of good electric properties, fine optical properties, low production cost, and simple preparation. In the past few decades, lead-based piezoelectric ceramics have dominated the market due to their good properties. In the following section, the rare-earth doped lead-based ceramics were summarized.

Rare-Earth Doped PZT-Based Ceramics

$Pb(Zr_xTi_{1-x})O_3$ (PZT) ceramics are the most studied and applied piezoelectric material. The piezoelectric constant d_{33} and Curie temperature T_c of PZT-5A ceramics can reach 375 pC/N and 365°C, respectively (Shrout and Zhang, 2007; Chen et al., 2018).

Shannigrahi et al. (2004) synthesized the PZT (60/40) ceramics doped with rare-earth (La, Nd, Sm, Eu, Gd, Dy, and Er) by sol-gel growth. Among them, the ceramic doped with La has the largest dielectric constant ε_r of 3,413, and the piezoelectric constant d_{33} and the remnant polarization P_r can reach 569 pC/N and 21.9 $\mu C/cm^2$, respectively. Nevertheless, the Curie temperature T_c was lowest (~156°C). The Dy doped ceramic has the highest Curie temperature T_c of 368°C. Khazanchi et al. (2005) reported Eu doped PZT (55/45) ceramics. The dielectric constant ε_r and the remnant polarization P_r of 2 mol% Eu doped samples increased to 1,132 and 26.05 $\mu C/cm^2$, respectively. Pandey et al. (2009) developed Sm doped PZT (65/35) ceramics showing good electric properties, and the dielectric constant ε_r, the piezoelectric constant d_{33} and the planar electromechanical coupling coefficient k_p of the 6 mol% Sm doped ceramic increased to 610, 172 pC/N, and 0.42, respectively. Perumal et al. (2019) reported that the Nd doped PZT (52/48) has good electrical properties (149 pC/N) and low conductivity (~10^{-3} S/m). Guo et al. (2020) achieved Yb doped PZT based ceramics with good electric properties. The piezoelectric constant d_{33}, planar electromechanical coupling coefficient k_p, and the dielectric constant ε_r of the ceramics can reach 308 pC/N, 0.57, and 1,210, respectively. Kour et al. (2015) and Kour et al. (2016) reported that the piezoelectric constant d_{33} of the PZT ceramics with 10 mol% La doping was 381 pC/N. In conclusion, the rare-earth doped PZT ceramics exhibit good piezoelectric properties which are suitable for general applications, including sensors, actuators, and ultrasound transducers.

Except for the enhancement of electric performance after rare-earth doping, the optical properties also varied significantly. La-doped PZT (PLZT) transparent ceramics have also attracted great attention in fundamental research as well as in applications due to a wide variety of optical properties. Zhang et al. (2006) observed three emission peaks at 915, 1,066, and 1,347 nm in the Nd doped PLZT ceramics under the excitation of a continuous wave diode laser. Zeng et al. (2014) prepared the Dy doped PLZT ceramics by hot-pressing sintering. It was shown that the Dy substituting decreased the coercive field E_c, but improved the optical transmittance and electro-optic effect. Especially, the transparency can reach as high as 67% at 632.8 nm. Zhao et al. (2014) reported that the intensity of the emission peak (1800 nm) in Tm doped PLZT ceramics was obvious and strong, while the emission intensity reduced when doped with Ho. Strikingly, a quite strong emission at 1900–2200 nm emerged, whose full width at half maxima (FWHM) was up to 200 nm, which indicated Ho/Tm co-doped PLZT ceramics had potential application prospect in tunable lasers around 2000 nm. Moreover, the structural and spectroscopic properties of Nd, Er, Yb doped and co-doped PLZT ceramics were also studied as potential laser materials in the near infrared region (Camargo

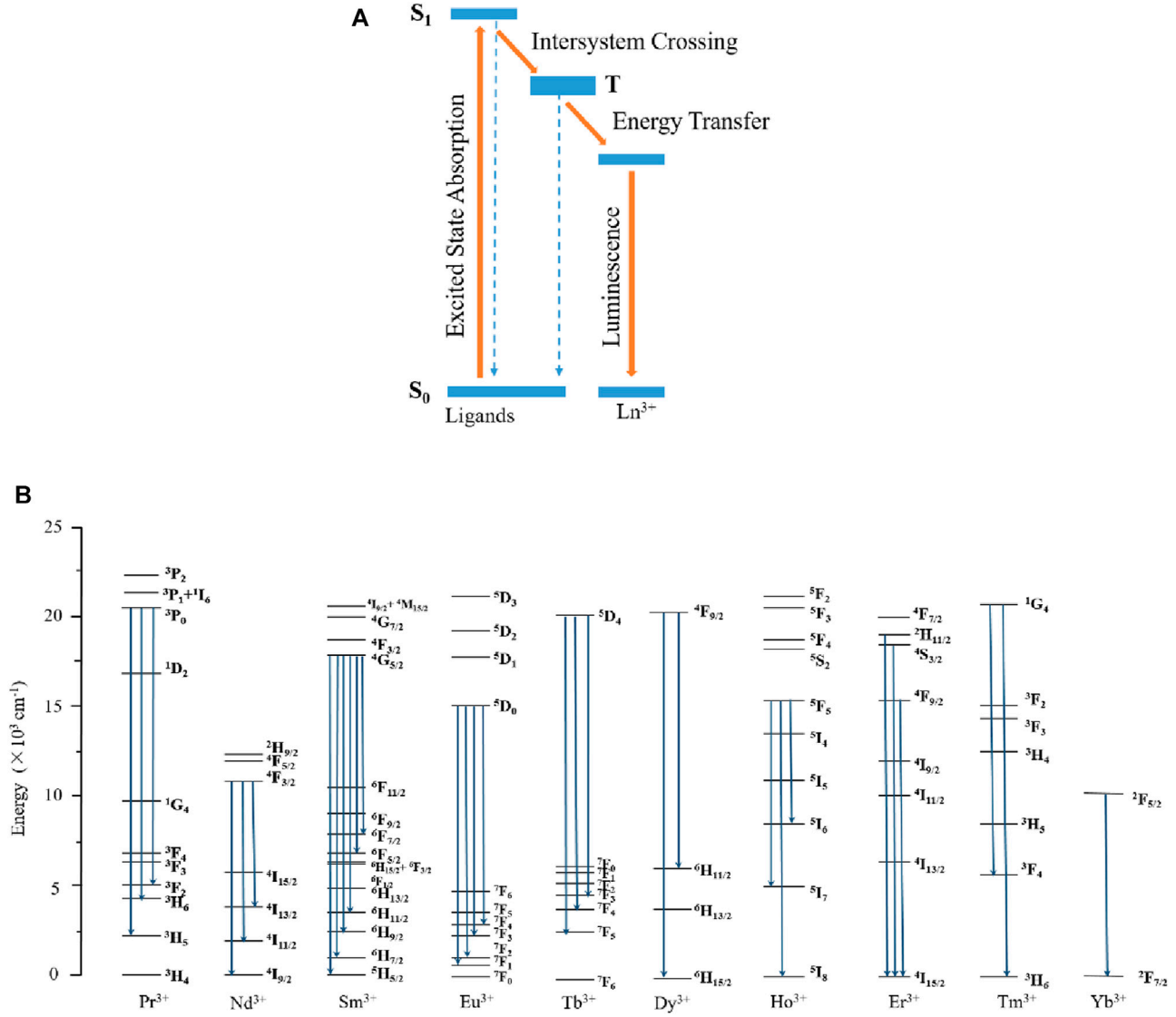

FIGURE 2 | (A) The diagram of the main energy flow paths during the sensitization of lanthanide luminescence *via* the ligands. **(B)** The diagram of the energy levels of Pr^{3+}, Nd^{3+}, Sm^{3+}, Eu^{3+},Tb^{3+}, Dy^{3+},Ho^{3+}, Er^{3+}, Tm^{3+}, and Yb^{3+} ions.

et al., 2004; Camargo et al., 2005). These studies indicated that the transparent PLZT ceramics with rare-earth doping were suitable for photonic devices, optic sensors, and multifunctional optic devices, etc.

Furthermore, the $Pb(Zn_{1/3}Nb_{2/3})O_3$-$Pb(Zr_{51}Ti_{49})O_3$ (PZN-PZT) system has recently attracted much attention owing to their better piezoelectric properties (d_{33} = 550 pC/N, k_p = 0.69) compared with traditional PZT ceramics (Vittayakorn et al., 2006; Zheng et al., 2014; Li et al., 2015a). Deng et al. (2010) reported that the piezoelectric coefficient d_{33}, dielectric constant ε_r and electromechanical coupling factor k_p of the La doped 0.3 $Pb(Zn_{1/3}Nb_{2/3})O_3$-0.7 $Pb(Zr_{0.51}Ti_{0.49})O_3$ can reach 845 pC/N, 4,088, and 0.70, respectively. Wang et al. (2012) reported that La doped 0.25 $Pb(Zn_{1/3}Nb_{2/3})O_3$-0.75 $Pb(Zr_{0.53}Ti_{0.47})O_3$ ceramics near the morphotropic phase boundary had good piezoelectric properties (d_{33} = 570 pC/N, k_p = 0.60). Fan et al. (2014) found that introducing the proper amount of Li_2CO_3 and Sm_2O_3 into 0.3PZN-0.7PZT ceramics could not only effectively improve the sinter ability and reduce the sintering temperature (~900°C), but also enhance the electric properties (d_{33} = 483 pC/N, ε_r = 2,524, tan δ = 0.0178).

Rare-Earth Doped PMN-PT Ceramics

$Pb(Mg_{1/3}Nb_{2/3})O_3$-$PbTiO_3$ (PMN-PT) ceramic is another kind of typical lead-based ceramic, which has been widely applied in multilayer capacitors, actuators, electro-optical modulators,

ultrasonic transducers, and infrared detectors due to the good electric properties (d_{33} = 663 pC/N, ε_r = 5,260) (Choi et al., 1989; Kamzina et al., 2010; Zhang et al., 2014a).

Li et al. (2018) found an ultrahigh piezoelectricity in the Sm doped 0.71 PMN-0.29 PT ceramics. The piezoelectric constant d_{33} can reach as high as 1,500 pC/N, and the dielectric constant ε_r can arrive at about 13,000. But the Curie temperature decreased to 89°C. Guo et al. (2019a) reported the enhancement of electric properties in the 0.72 PMN-0.28 PT ceramics doped with 2.5 mol % Eu. The piezoelectric constant d_{33}, dielectric constant ε_r, and electromechanical coupling coefficient k_{33} of the ceramics can reach 1,420 pC/N, 12,200, and 0.78, respectively. Guo et al. (2019b) also developed Sm doped 0.4 $Pb(Mg_{1/3}Nb_{2/3})O_3$-0.248$PbZrO_3$-0.352$PbTiO_3$ ternary system ceramics. These ceramics possess a high piezoelectric constant (d_{33} = 910 pC/N), good dielectric constant (ε_r = 4,090), and relatively high Curie temperature (T_c = 184°C). The previous studies also proved that the optical properties of PMN-PT ceramics can be also significantly improved by rare-earth doping. Wei et al. (2010) achieved a much larger Kerr effect in the La doped 0.75 PMN-0.25 PT transparent ceramic, The Kerr effect (second-order electro-optic effect) refers to the phenomenon of inductive birefringence that is proportional to the square of the electric field, providing useful devices such as light valves, deflectors and displays (Uchino, 1995). The quadratic electro-optic coefficient of the ceramics can reach as high as 66 × 10^{-6} m^2/V^2. Wei et al. (2012a) and Wei et al. (2012b) reported that the transparency of the Er doped 0.75 PMN-0.25 PT ceramics can reach 65% from visible light to infrared band. Besides, three broad peaks at 950–1,060, 1,220–1,290, and 1420–1560 nm can be observed under the excitation of a 521 nm laser. Liu et al. (2016) acquired a strong yellow-green up-conversion photoluminescence in the Ho/Yb co-doped 0.67 PMN-0.33 PT ceramics under the excited of a 980 nm laser. Ma et al. (2018) reported La doped 0.88 PMN-0.12 PT transparent ceramics. The transparency in the near infrared region increased to 70% with 1.0 mol% La doping. Fang et al. (2021) reported that the transparency and quadratic electro-optic coefficient of the Sm doped 0.88 PMN-0.21 PT transparent ceramics can reach 69.6% and 35 × 10^{-6} m^2/V^2, respectively. Lv et al. (2019) obtained strong visible up-conversion emissions at 491, 529, 539, 623, 649, 685, 710, and 737 nm and near-infrared down-conversion emissions around 1,061 nm and 1006 nm in the Pr/Yb co-doped 0.75 PMN-0.25 PT ceramics under the excitation of a 980 nm laser. These studies indicate that the rare-earth doped PMN-PT ceramics are promising multifunctional materials due to the improved electric properties, electro-optic effects, and various photoluminescence properties.

Rare-Earth Doped BS-PT Ceramics

The PMN-PT ceramics have good electric properties. However, the low Curie temperature (159°C) limits their applications. By contrast, the $BiScO_3$-$PbTiO_3$ (BS-PT) ceramics exhibit a high Curie temperature (T_c ~ 450°C) and good piezoelectric property (d_{33} ~ 460 pC/N) near the morphotropic phase boundary (Inaguma et al., 2004; Zhang et al., 2005). Yao et al. (2010) found the enhancement of the electric properties (d_{33} = 361 pC/N, k_p = 0.40) in the La doped BS-PT ceramics. The highest Curie temperature can reach 467°C. Politova et al. (2011) reported a large piezoelectric coefficient (d_{33} = 350 pC/N) and the piezoelectric coupling coefficient (k_t = 0.68) in the Nd doped BS-PT ceramics. Li et al. (2009) reported a high Curie temperature (T_c = 490°C) and good piezoelectric properties (d_{33} = 147 pC/N, k_p = 0.28) in the Y doped BS-PT ceramics. The combination of high Curie temperature and good piezoelectric properties suggested that these rare-earth modified ceramics can be a promising candidate for high-temperature actuators and transducers. **Table 1** shows the properties of some lead-based piezoelectric ceramics with rare-earth doping.

Rare-Earth Doped Lead-free Ceramics

Due to the increasing concern of lead pollution to the environment, it is significant and urgent to develop lead-free piezoelectric ceramics with good properties. There are three typical lead-free piezoelectric ceramics that have gained a lot of attention, including $(Na_{0.5}Bi_{0.5})TiO_3$-$BaTiO_3$ (NBT-BT) ceramic $(K_{0.5}Na_{0.5})NbO_3$ (KNN) based ceramic, and $BaTiO_3$ (BT) ceramic, which are considered as possible substitutes for lead-based ceramics. The following section summaries the lead-free piezoelectric ceramics with rare-earth doping.

Rare-Earth Doped BNT-BT Ceramic

BNT-BT ceramic is one of the most widely used lead-free piezoelectric ceramics owing to the good piezoelectric constant and high Curie temperature (d_{33} > 100 pC/N, T_c >280°C) (Panda, 2009; Jo et al., 2011). Li et al. (2004) reported the enhancement electric properties of the BNT-6BT ceramics doped with one at% La, showing the piezoelectric constant d_{33} increased from 117 to 125 pC/N, but the thick electromechanical coupling coefficient k_t decreased slightly from 0.43 to 0.38. Liu et al. (2008) reported that the BNT-6BT ceramics doped with 0.4 wt% CeO_2 had better performances compared to pure BNT-6BT ceramics. The piezoelectric constant d_{33} and thick electromechanical coupling coefficient k_t of the doped ceramics were 120 pC/N and 0.52, respectively. Peng et al. (2010a), Peng et al. (2010b) and Peng et al. (2010c) reported the enhancement of electric properties in the Sm doped BNT-6BT ceramics. The piezoelectric constant d_{33} and coupling coefficient k_p of the ceramics increased to 202 pC/N and 0.3, respectively. In the same year, this group found that Nd doping can also improve the electric properties of BNT-6BT ceramics. The piezoelectric constant d_{33} and planar electromechanical coupling coefficient k_p of the ceramics can reach 175 pC/N and 0.31, respectively. Besides, this group also fabricated La_2O_3 doped BNT-6BT ceramics. After 0.6 wt% La_2O_3 doping, the ceramics with showed good piezoelectric properties (d_{33} = 167 pC/N, k_p = 0.30).

Rare-earth doped BNT-BT ceramics also possess great photoluminescence properties. Jiang et al. (2018) reported the piezoelectric constant d_{33} and planar electromechanical coupling coefficient k_p of the 2.5 mol% Dy doped BNT-6BT ceramic can reach 190 pC/N and 0.372, respectively. Moreover, the ceramics excited at 426 nm also exhibited strong emissions at 478 and 575 nm. This study showed the Dy doped BNT-BT ceramics had simultaneously good piezoelectricity and photoluminescence, suggesting a promising application in the electro-optic devices.

TABLE 1 | The properties of some lead-based piezoelectric ceramics with rare-earth doping.

Composition	d_{33} (pC/N)	k_p	ε_r	T_c (°C)	Ref
(Eu,La,Nd,Sm, Gd,Dy,Er):PZT	53–569	—	187–3,413	156–368	Shannigrahi et al. (2004)
Sm:PZT	172	0.42	610	274	Pandey et al. (2009)
(Pr,Yb,Sm):PZT	—	—	210.48–7,000	314–394	Samad et al. (2017)
Sm:PMN-PT	1,510	—	13,000	89	Li et al. (2018)
Eu: PMN-PT	1,420	0.78	12,200	83	Guo et al. (2019a)
Sm-PMN-PZT	910	0.7	4,090	184	Guo et al. (2019b)
La: PZN-PZT	440–845	0.63–0.7	3,321–4,088	206–213	Deng et al. (2010)
La: PZN-PZT	570	0.6	3,900	204	Wang et al. (2012)
Sm: PNN-PZT	605	0.55	5,020	128	Peng et al. (2016)
Sm/Li:PZN-PZT	483	0.65	2,524	394	Fan et al. (2014)
La:BS-PT	361	0.4	3,500	467	Yao et al. (2010)
Y:BS-PT	147	0.28	—	490	Li et al. (2009)

Chi et al. (2015) observed visible up-conversion luminescence at 532, 540, and 600 nm, as well as near infrared (1440–1660 nm) and mid-infrared (2620–2840 nm) broadband down-conversion luminescence in the Er doped BNT-7BT ceramics under the excitation of 980 nm. Li et al. (2019a) achieved a strong orange luminescence in the Sm doped BNT-12BT ceramics when excited by blue light, and the emission intensity depends largely on the doping concentration.

Rare-Earth Doped KNN-Based Ceramics

KNN ceramics with high Curie temperature (T_c ~ 400°C) and good electric properties (d_{33} ~ 80 pC/N, k_p ~ 0.36) have been deemed as potential candidates for lead-based piezoelectric ceramics (Saito et al., 2004; Birol et al., 2006; Jaeger. 2010).

Du et al. (2017) studied the effect of the KNN ceramics doped with different rare-earth elements (Dy, Er, Eu, and Pr). The piezoelectric constant d_{33} increased slightly after doping, (KNN-Dy: 95 pC/N, KNN-Er: 91 pC/N, KNN-Eu: 84 pC/N and KNN-Pr: 94 pC/N). Wu et al. (C2017) fabricated Er doped KNN based ceramics with the piezoelectric constant of 70–90 pC/N, and the dielectric constant and loss is about 1,400 and 0.03, respectively. Zhai et al. (2019) reported good piezoelectric and ferroelectric properties in the KNN ceramics doped with Tb and Tm. The $d_{33(Tb)}$ and $d_{33(Tm)}$ can reach 140 pm/V and 127 pm/V, respectively.

In addition to studying the electric properties, the optical performances of rare-earth doped KNN ceramics were also investigated extensively. Yang et al. (2017) reported that the transparency of 1.5 mol% La_2O_3 doped KNN ceramic can reach as high as 74%). Geng et al. (2017) reported that Eu doped $K_{0.47}Na_{0.47}Li_{0.06}Nb_{0.94}Bi_{0.06}O_3$ ceramics presented high transmittance both in the near-infrared and middle infrared regions (close to 100%). Besides, the ceramics were efficiently excited by near-ultraviolet and blue light to realize strong reddish luminescence. Sun et al. (2012), and Sun et al. (2014) observed strong green (528 nm) and red (617 and 650 nm) emissions in the Pr doped KNN ceramics under the excitation of 450 nm. Two years later, this group found strong green (510–590 nm) and a relatively weak red (645–695 nm) emissions in the Er doped KNN ceramics under the 980 nm excitation, and it is possible to modulate the ratio of red to green emission by adjusting the Er concentration. Similarly, Wu et al. (2013), Wu et al. (2015a), and Wu et al. (2015b) found that the Er doped KNN ceramics fabricated by sol-gel method exhibited luminescent bands at 527, 548, 660, and 487 nm under the excitation of 980 nm. Besides, Er doping is beneficial to the formation of fine and uniform grains, which helps to enhance the up-conversion efficiency and luminous efficiency. Furthermore, seven down conversion emission bands (530, 548, 605, 618, 650, 672, and 740 nm) could be observed in the Er and Pr co-doped KNN ceramics under the excitation of 485 nm. Besides, three up-conversion emission bands (510–537 nm, 537–585 nm, and 640–690 nm), and two down-conversion emission bands (1,400–1700 nm and 2,600–2,850 nm) were found in the Er and Yb co-doped KNN ceramics. Zhang et al. (2014b) also achieved a strong orange emission in the Sm doped KNN ceramics under the excitation from 400 to 500 nm. Li et al. (2020a) also observed a bright photoluminescence with a strong orange emission in the Sm-doped $0.96(K_{0.48}Na_{0.52})(Nb_{0.95}Sb_{0.05})$-$0.04Bi_{0.5}(Na_{0.82}K_{0.18})_{0.5}ZrO_3$ ceramics under visible light irradiation.

Rare-Earth Doped BT Ceramic

BT ceramic has received much attention due to the high dielectric constant, high resistivity and outstanding insulation performance, which has been extensively applied in positive temperature coefficient of resistivity (PTCR) thermistors, multilayer ceramic capacitors (MLCC), piezoelectric devices, optoelectronic elements, and semiconductors (Zhou et al., 2001). Among them, the application of MLCC is extremely wide, for improving the dielectric constant to meet the requirements of high capacitance. It is effective in significantly increasing the dielectric constant of BT ceramics with rare-earth doping (Caballero et al., 2000; Morrison et al., 2001).

Sun et al. (2010) reported the enhancement of dielectric properties in the Sm doped BT ceramics. Sm doping can inhibit the growth of the crystal grains and make the BT ceramics possess semiconductor characteristics. Li et al. (2012) achieved a large dielectric constant (70,000 ~ 80,000) and low dielectric loss (<0.04) in the Tb doped BT ceramics. Zhang et al. (2020a) reported the Yb/Mn co-doped BT ceramic possessed a relatively good performance with dielectric constant ε_r (>2,600), low dielectric loss tanδ (0.0183) and high insulation resistivity (4.38×10^{11} Ω cm). Zhang et al. (2020b) reported the dielectric constant can reach 5,091.7 for 0.3 mol% La_2O_3 doped BT ceramic. Kumari et al. (2020) reported that the relative dielectric constant

TABLE 2 | The properties of some lead-free based piezoelectric ceramics with rare-earth doping.

Composition	d_{33} (pC/N)	k_p	ε_r	T_c (°C)	Ref
La:BNT-6BT	125	0.24	—	250	Li et al. (2004)
Ce: BNT-6BT	127	0.23	851	280	Liu et al. (2008)
Sm:BNT-6BT	202	0.3	1,200	277	Peng et al. (2010a)
Nd:BNT-6BT	175	0.31	1,400	280	Peng et al. (2010b)
La:BNT-6BT	167	0.3	1,470	272	Peng et al. (2010c)
Dy:BNT-6BT	190	0.372	1,100	275	Jiang et al. (2018)
(La,Ho,Yb,Y): BT-Mn	—	—	2,108–2,613	—	Zhang et al. (2020a)
(Dy,Er.Eu,Pr):KNN	84–95	—	—	—	Du et al. (2017)
Sm:KNN-LS	176	0.35	1,372	328	Hao et al. (2015)
(Nd, Dy, Ho):KNN-Li	68–128	—	247–807	400–433	Zhou et al. (2014)
Er: KNN-Li,Bi	89	—	1,350	350	Wu et al. (2017)

ε_r of the BT ceramics doped with Eu can increase to 8,581, and the grains of the ceramics was uniform with average grain size of 800 nm. These studies indicated that BT ceramics doped with rare-earth may be a promising candidate for MLCC applications. Besides, Battisha et al. (2010) reported the up-conversion of infrared light to visible light can be observed in Er/Yb co-doped BT ceramics. Cernea et al. (2013) observed three distinct peaks (483, 660, and 800 nm) in the BT ceramics doped with Tm under the excitation of 460 nm.

Thus, rare-earth doped piezoelectric ceramics can effectively modify the electric properties and introduce excellent photoluminescence properties, which expanded the applications of piezoelectric ceramics greatly, such as actuating device, ultrasonic transducers, electro-optical deflector, potential phosphor, and multifunctional optoelectronics. **Table 2** summarizes the properties of some lead-free based piezoelectric ceramics with rare-earth doping.

RARE-EARTH DOPED PIEZOELECTRIC SINGLE CRYSTALS

Rare-Earth Doped Lead-Based Single Crystals

In order to further improve the properties of the piezoelectric materials, the growth of piezoelectric single crystals has drawn wide concern. The discovery of relaxor-based ferroelectric single crystals represented by $Pb(Mg_{1/3}Nb_{2/3})O_3$-$PbTiO_3$ (PMN-PT) and $Pb(Zn_{1/3}Nb_{2/3})O_3$-$PbTiO_3$ (PZN-PT) are considered as a revolutionary breakthrough of piezoelectric materials, which tremendously improved the electric properties (d_{33} = 1780 pC/N) of piezoelectric materials compared to commercial piezoelectric PZT-5H ceramics (590 pC/N) (Kim et al., 2010).

Li et al. (2019b) reported a large piezoelectric constant d_{33} in the Sm doped PMN-PT single crystals, and the values (exceeding 3,400 pC/N) increased more than double compared with the Sm doped PMN-PT ceramics (1,510 pC/N). The Sm doped single crystals also showed improved compositional uniformity along the crystal boule. Furthermore, the electric field-induced strain can reach 30%, which is almost 90% higher than that of undoped PMN-PT single crystals. This study provided commercial opportunities for high-performance piezoelectric applications. Besides, PZN-9PT piezoelectric single crystal showed excellent electric properties (d_{33} > 1500pC/N, k_{33} > 90%) near the morphotropic phase boundary (Kuwata et al., 1982). However, the low coercive field (Ec ~ 3.5 kV/cm) and low Curie temperature (T_c ~ 170°C) limit the application of PZN-PT single crystal in high-power and high-temperature environments (Rajan et al., 2007). Xi et al. (2016a) and Xi et al. (2016b) reported a significantly enhanced coercive field E_c (11.6 kV/cm) in the Er doped PZN-9PT crystal. The Curie temperature T_c was around 178°C. Furthermore, the green and red up-conversion emission bands can be obtained in the ceramic under the 980 nm excitation. The group also reported the enhancement of the coercive field (E_c = 5.9 kV/cm), remnant polarization (P_r = 38.40 μC/cm^2) and Curie temperature (T_c = 175°C) in the Ho doped PZN-9PT crystal. Li et al. (2019c) also prepared Tm/Yb co-doped PZN-9PT crystal with large coercive field E_c of 12.1 kV/cm, and the value is nearly four times higher than that of PZN-9PT crystal. The Curie temperature T_c was increased to 182.5°C. Under a 980 nm laser excitation, the modified crystals produce up-conversion with three colors [blue (480 nm), strong near-infrared (804 nm), and weak red (652 nm)]. Chen et al. (2020b) and Chen et al. (2020c) reported the coercive field E_c of Eu doped PZN-9PT crystal significantly increased to 11.0597 kV/cm, and it is triple higher than that of pure PZN-9PT crystal. Besides, under the excitation of 464 nm, four broadband peaks appear at around 593 nm, 613 nm, 657 nm, and 716 nm, respectively. Furthermore, the group also achieved a high Curie temperature (T_c = 250°C) and large coercive field (E_c = 11.0597 kV/cm) in the 0.15 $Pb(Er_{1/2}Nb_{1/2})O_3$-0.63 $Pb(Zn_{1/3}Nb_{2/3})O_3$-0.22$PbTiO_3$ single crystal, and the crystal also exhibited a strong green light excited by a 980 nm laser. As mentioned above, the addition of rare-earth not only improves the temperature and electric field stability of PZN-PT single crystals but also induces photoluminescence properties, which gives the rare-earth doped PZN-PT single crystals possibilities for multifunctional optoelectronic device applications.

Rare-Earth Doped Lead-free Single Crystals

$Na_{0.5}Bi_{0.5}TiO_3$ (BNT)-based lead-free crystals were reported to have superior electric properties, large band gap and high near-visible light absorption coefficient (Hiruma et al., 2010; Li et al., 2015b). In recent years, the electric and optical properties of

the rare-earth doped BNT single crystals have been studied. Zhang et al. (2014c) prepared an Eu doped BNT single crystal by top-seeded solution growth, and observed that the crystal presented orange and red emissions under the excitation of 611 nm. The piezoelectric constant d_{33} and remnant polarization P_r of the crystal increased to 86 pC/N and 7.38 μC/cm^2, respectively. Jiang et al. (2018) achieved an extremely strong green emission in the Er doped BNT single crystal under the 980 nm near-infrared excitation. But Er doping led to a slight decreasing of dielectric constant, dielectric loss and transmittance. He et al. (2013) reported high transparency Nd doped NBT single crystal by a top seeded solution growth method. The transparency reached more than 50% above 450 nm, and a strong emission band around 1,066 nm was found under laser excitation at 808 nm. These research results may help to extend various biomedical applications including intravascular imaging, photoacoustic imaging, and microbeam applications.

RARE-EARTH DOPED PIEZOELECTRIC FILMS

Compared to piezoelectric crystal and ceramics, piezoelectric films can greatly improve the operating frequency due to unlimited size. Currently, piezoelectric films such as PZT and $Bi_4Ti_3O_{12}$ (BIT) thin films are widely applied in ferroelectric dynamic random-access memory, room temperature infrared detectors, piezoelectric motors, ultrasonic detectors, film capacitors and integrated optical waveguide devices (Xie et al., 2006).

Rare-Earth Doped PZT Films

Majumder et al. (2001) investigated rare-earth (Nd, Gd, and Ce) doped PZT (53/47) thin films by sol-gel technique, realizing an improvement of ferroelectric and dielectric properties of the PZT thin films with Ce and Gd. Nd doping was effective to increase the retained switchable polarization of PZT from 63 to 84%. Yu et al. (2003) fabricated the Eu doped PZT (52/42) thin films with an improved polarization and low leakage current by a sol-gel method. Nakaki et al. (2004) studied the effect of the PZT (40/60) thin films doped with various rare-earth elements (Y, Dy, Er, and Yb). The remnant polarization P_r of the films increased to 26 (PZT-Y), 25 (PZT-Dy) and 26 μC/cm^2 (PZT-Er), respectively, while Yb doping degraded the remnant polarization P_r down to 16 μC/cm^2. Pandey et al. (2007) reported the remnant polarization and dielectric constant of the Sm substituted PZT (65/35) thin films can reach about 52 μC/cm^2 and 1,220, respectively. Moreover, the transparency of the film was close to 80% at 1200 nm. Rath et al. (2019) reported the enhancement of piezoelectric constant d_{33} (more than 130 pm/V) in La doped PZT film. Zhang et al. (2021) achieved a large remnant polarization (22.73 μC/cm^2) in the 2 mol% Dy doped PZT (60/40) thin films. Moreover, the films also exhibited a significantly reduced leakage current density. All these studies indicated that rare-earth doping is one promising technique for improving the ferroelectric property of PZT film to meet a wide range of application requirements.

Rare-Earth Doped Lead-free Films

Due to the fatigue-free characteristics, the BIT films have been widely used in special applications, typically like nonvolatile ferroelectric random access memory. Kim et al. (2002) reported the enhancement of ferroelectric properties in the Eu doped BIT films. The remnant polarization P_r of the films was about 30 μC/cm^2. Zhang et al. (2003) reported that the remnant polarization of Nd doped BIT films increased double (8.8 μC/cm^2) compared to the pure BIT films. Ruan et al. (2008) reported a high optical transparency (>80%) in the Eu doped BIT films, and the emission spectra of the films presented two peaks at 594 and 617 nm under the excitation of 350 nm. Moreover, the films exhibited high fatigue resistance after 10^{10} switching cycles. Gao et al. (2009) observed two strong green emission bands centered at 524 and 545 nm and a weak red emission band centered at 667 nm in the Er/Yb co-doped BIT films under the excitation of 980 nm. Ding et al. (2011) observed two emission bands centered at 546 and 656 nm in the Ho/Yb co-doped BIT thin films under the excitation of 980 nm.

In addition to the research of rare-earth doped piezoelectric thin films, Xu et al. (2020) have also made remarkable achievements in the thick films. They obtained high d_{33} (343 pC/N), large P_r (12.45 μC/cm^2) and low E_c (0.63 kV/mm) in the Er doped $Ba_{0.85}Ca_{0.15}Ti_{0.9}Zr_{0.1}O_3$ textured thick films. Besides, two strong green emission bands centered at 525 and 550 nm and one weak red emission band of 660 nm were acquired under the excitation of a 980 nm laser. These results showed that rare-earth doped films significantly enhanced the electrical properties as well as the photoluminescence performances, which has high potential for multifunctional film devices applications.

DISCUSSIONS

Electrical Properties

The rare-earth doping may influence the electrical and optical performances of the piezoelectric materials significantly. Two tables (**Tables 1**, **2**) and **Figure 3** summary the piezoelectric properties of the rare-earth doped piezoelectric ceramics with perovskite (ABO_3) structure. It can be found that Sm doped PMN-PT ceramics exhibited the highest piezoelectric constants (1,510 pC/N) among the rare-earth doped ceramics listed, which may be due to the addition of aliovalent Sm^{3+} dopant on A-site of the perovskite structure with similar ion radius. It is noting that Sm^{3+} is the smallest ion among all the lanthanide rare Earth ions, which may completely occupy the A-site of PMN-PT solid solution and then replace the Pb ion (Li et al., 2020b). The significant effect on electric properties of Sm doping PMN-PT is mainly due to the local structure disorder. Besides, Eu^{3+} doped PMN-PT ceramics also exhibit excellent piezoelectric properties (d_{33}~1420pC/N). As we know, the Eu^{3+} have similar ionic radius and valence states to Sm^{3+} ions, which also proved that the rare

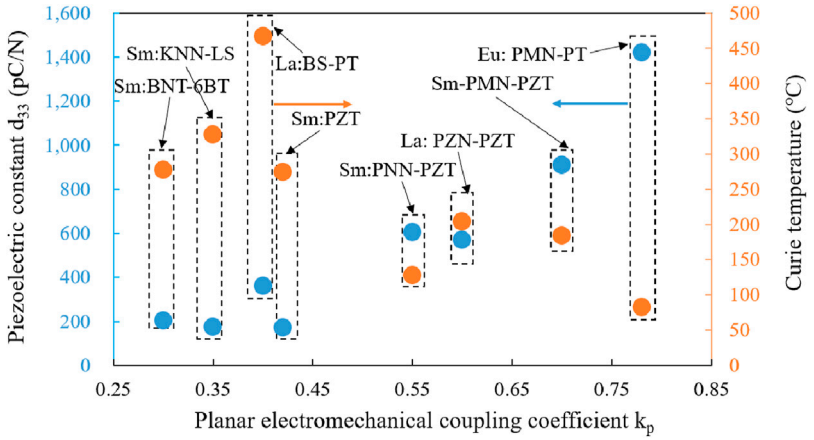

FIGURE 3 | The properties of some piezoelectric ceramics with rare-earth doping (Pandey et al., 2009; Peng et al., 2010a; Yao et al., 2010; Wang et al., 2012; Hao et al., 2015; Peng et al., 2016; Guo et al., 2019a; Guo et al., 2019b).

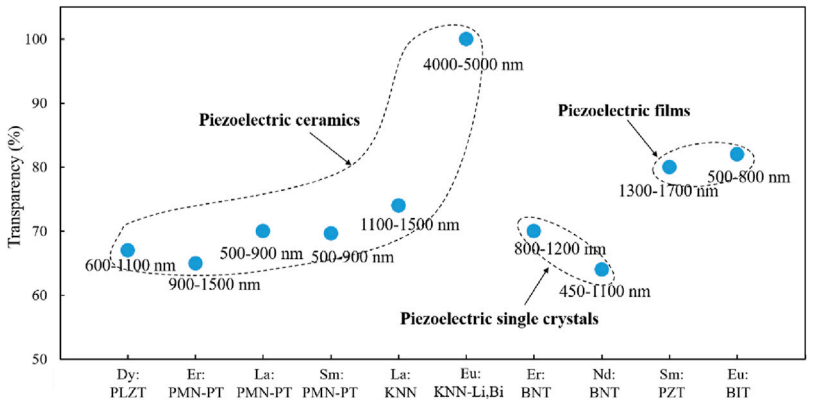

FIGURE 4 | The transmittance of some rare Earth doped piezoelectric materials in a certain wavelength range [with the thickness of 0.35 mm (Dy:PLZT); 0.6 mm (La:PMN-PT); 0.85 mm (Sm:PMN-PT); 0.5 mm (La:KNN); 0.5 mm (Eu: KNN-Li,Bi); 1 mm (Nd:BNT); 300 nm (Eu:BIT)] (Pandey et al., 2007; Ruan et al., 2008; Wei et al., 2012b; He et al., 2013; Zeng et al., 2014; Geng et al., 2017; Yang et al., 2017; Jiang et al., 2018; Ma et al., 2018; Fang et al., 2021).

Earth ions with a similar ionic radius to the A-site ions of the perovskite ferroelectric materials can be used to improve piezoelectric performance. Nevertheless, Sm doping reduced the Curie temperature of PMN-PT (89°C) that would limit their high temperature applications. The RE doped lead-based (PMN-PZT and BS-PT) and lead-free based (BNT and KNN) materials with relatively high Curie temperature were studied for enhancing piezoelectric constant. Therefore, it is difficult to obtain the samples with both excellent piezoelectric constant and high Curie temperature and more research works will be needed in the future to improve performances by regulating the local structure disorder of piezoelectric materials with a stale Curie temperature.

Optical Properties

Except for the electric properties, the optical performances were discussed. On the one hand, the rare-earth doping can obtain transparent samples with high transmittance. **Figure 4** gives the transmittance of some piezoelectric materials with rare-earth doping. It can be found that the transparency of the listed piezoelectric materials exceeds 60% in a specific wavelength range. For the ceramics, the grain boundary scattering loss is the main factor affecting the transmittance. Without exceeding the solubility limit, rare-earth can dissolve into the perovskite lattice homogeneously, meanwhile enhance the ceramic density, transparency, and other properties. However, excessive rare-earth ions may accumulate at the grain boundaries with increasing rare-earth content, which will lead to Rayleigh scattering loss due to the different refractive indices between grain boundaries and matrix. Besides, ion vacancies and crystal defects as well as the defect-induced poor crystallinity may decrease the transparency. Therefore, optimizing these factors to further improve the transparency of rare-earth doped piezoelectric materials may promote the development of multifunctional optical devices greatly.

One the other hand, the rare-earth doped piezoelectric materials can get characteristic emission spectrum after being

excited due to the ladder-shaped 4f energy level of rare-earth ions (**Figure 2**). Under the excited of 300–500 nm, some sharp down-conversion emissions can be achieved in the rare-earth doped materials. Typically, Eu^{3+} doping can acquire red (617 nm, $^5D_0 \rightarrow {}^7F_2$) emission, and Sm^{3+} doping can get red (645 nm, $^4G_{5/2} \rightarrow {}^6H_{9/2}$) and orange (563 nm, $^4G_{5/2} \rightarrow {}^6H_{5/2}$) emissions. Pr^{3+} doping can obtain green (545 nm, $^3P_0 \rightarrow {}^3H_5$) and red (617 nm, $^3P_0 \rightarrow {}^3H_6$) emissions. Besides, some sharp up-conversion emissions can be also achieved in the rare-earth doped materials under the excitation of 980 nm. Green (500 nm, $^2G_{11/2}$, $^4S_{3/2} \rightarrow {}^4I_{15/2}$) and red (670 nm, $^4F_{9/2} \rightarrow {}^4I_{15/2}$) emissions can be found for Er^{3+} doped samples, and blue (480 nm, $^1G_4 \rightarrow {}^3H_6$) and red (652 nm, $^1G_4 \rightarrow {}^3F_4$) emissions can be observed in Tm^{3+}/Yb^{3+} co-doped samples. Green (529 nm $^3P_0 \rightarrow {}^3H_5$), orange (623 nm $^3P_0 \rightarrow {}^3H_6$) and red (649 nm $^3P_0 \rightarrow {}^3F_2$) emissions were found in Pr^{3+}/Yb^{3+} co-doped materials. The introduced photoluminescence performance can significantly expand the application range of piezoelectric materials. Especially, the materials can achieve up-conversion emissions with converting long-wavelength light (invisible to the naked eye) into visible light, which will have important application in the information science and technology fields such as laser, display, anti-counterfeiting, and will also open up new research fields in biomedicine or photoacoustic multi-mode images. However, some conditions including doping concentration, sintering temperature, chemical composition and preparation process have a great influence on the electrical performance and luminescence performance of the rare-earth doped piezoelectric materials. Adjusting these conditions to obtain both good electrical and optical properties is of great significance for the development of multifunctional materials and devices.

CONCLUSION AND PERSPECTIVE

The electric and photoluminescence properties of piezoelectric materials can be significantly modified by rare-earth doping. Consequently, rare-earth doping is an effective method to fabricate multifunctional materials. The research and development trend of rare-earth doped piezoelectric materials are prospected as follows. 1) With the needs of environmental protection and sustainable development of human society, it is urgent to develop environmental friendly lead-free piezoelectric materials with excellent performance to replace traditional lead-based ceramics. The future development trend is to find an appropriate concentration of rare-earth oxide and proper lead-free piezoelectric materials to achieve excellent electric properties. 2) For the large strain and high energy conversion efficiency applications, rare-earth doped piezoelectric single crystals are superior to traditional piezoelectric ceramics due to their great electric properties. The future development trend is to optimize the growth conditions and properties of single crystals to meet increasingly demanding applications. 3) The rare-earth doped piezoelectric materials are a type of optical-mechanical-electric integrated multifunctional material. Due to the unique properties of rare-earth ions and piezoelectric materials, this type of new material has great advantages in sensing, detection, and information transmission.

AUTHOR CONTRIBUTIONS

YC and DZ wrote and edited the manuscript. ZP, MY, and XJ conceived the project and edited the manuscript.

FUNDING

This work was financially supported by National Science Foundation Grants (NSFC Grant No. 11804059, 51975131, 51805097), Guangdong Innovative and Entrepreneurial Research Team Program (Grant No. 2016ZT06G375) and Ministry of Science and Technology of China (Grant No. 2018YFF01010500).

REFERENCES

Battisha, I. K., Badr, Y., Shash, N. M., El-Shaarawy, M. G., and Darwish, A. G. A. (2010). Detection of Up-Conversion in Nano-Structure $BaTiO_3$ Co-doped with Er^{3+} and Yb^{3+} Ions. *J. Sol-gel Sci. Technol.* 53, 543–550. doi:10.1007/s10971-009-2129-5

Birol, H., Damjanovic, D., and Setter, N. (2006). Preparation and Characterization of (K0.5Na0.5)NbO3 Ceramics. *J. Eur. Ceram. Soc.* 26, 861–866. doi:10.1016/j.jeurceramsoc.2004.11.022

Caballero, A. C., Fernández, J. F., Villegas, M., Moure, C., Durán, P., Florian, P., et al. (2000). Intermediate Phase Development in Phosphorus-Doped Barium Titanate. *J. Am. Ceram. Soc.* 83, 1499–1505. doi:10.1111/j.1151-2916.2000.tb01417.x

Cernea, M., Secu, C. E., Vasile, B. S., and Secu, M. (2013). Structural and Optical Characterization of Sol-Gel Derived Tm-Doped $BaTiO_3$ Nanopowders and Ceramic. *Curr. Appl. Phys.* 13, 137–141. doi:10.1016/j.cap.2012.06.024

Chen, C., Wang, X., Wang, Y., Yang, D., Yao, F., Zhang, W., et al. (2020a). Additive Manufacturing of Piezoelectric Materials. *Adv. Funct. Mater.* 30, 2005141. doi:10.1002/adfm.202005141

Chen, Y., Bao, X., Wong, C.-M., Cheng, J., Wu, H., Song, H., et al. (2018). PZT Ceramics Fabricated Based on Stereolithography for an Ultrasound Transducer Array Application. *Ceramics Int.* 44, 22725–22730. doi:10.1016/j.ceramint.2018.09.055

Chen, Y., Xi, Z., Guo, F., Fang, P., Li, X., Long, W., et al. (2020b). Electric and Photoluminescence Properties of Eu^{3+}-Doped PZN-9PT Single crystal. *J. Mater. Sci. Mater. Electron.* 31, 11295–11302. doi:10.1007/s10854-020-03678-z

Chen, Y., Xi, Z., Guo, F., Fang, P., Li, X., Long, W., et al. (2020c). $Pb(Er_{1/2}Nb_{1/2})O_3$-$Pb(Zn_{1/3}Nb_{2/3})O_3$-$PbTiO_3$ Single Crystals with High Curie Temperature. *Crystals* 10, 22–43. doi:10.3390/cryst10010022

Choi, S. W., Shrout, R. T. R., Jang, S. J., and Bhalla, A. S. (1989). Dielectric and Pyroelectric Properties in the $Pb(Mg_{1/3}Nb_{2/3})O_3$-$PbTiO_3$ system. *Ferroelectrics* 100, 29–38. doi:10.1080/00150198908007897

Dang, S., Sun, L.-N., Zhang, H.-J., Guo, X.-M., Li, Z.-F., Feng, J., et al. (2008). Near-Infrared Luminescence from Sol–Gel Materials Doped with Holmium(III) and Thulium(III) Complexes. *J. Phys. Chem. C* 112, 13240–13247. doi:10.1021/jp8041632

de Camargo, A. S. S., Botero, É. R., Garcia, D., Eiras, J. A., and Nunes, L. A. O. (2005). Nd^{3+}-doped lead Lanthanum Zirconate Titanate Transparent Ferroelectric Ceramic as a Laser Material: Energy Transfer and Stimulated Emission. *Appl. Phys. Lett.* 86, 152905. doi:10.1063/1.1899752

de Camargo, A. S. S., de O. Nunes, L. A., Santos, I. A., Garcia, D., and Eiras, J. A. (2004). Structural and Spectroscopic Properties of Rare-Earth (Nd^{3+}, Er^{3+}, and

Yb^{3+}) Doped Transparent lead Lanthanum Zirconate Titanate Ceramics. *J. Appl. Phys.* 95, 2135–2140. doi:10.1063/1.1642285

Deng, G., Yin, Q., Ding, A., Zheng, X., Cheng, W., and Qiu, P. (2010). High Piezoelectric and Dielectric Properties of La-Doped $0.3Pb(Zn_{1/3}Nb_{2/3})O_3$-$0.7Pb(ZrxTi1-x)O_3$ Ceramics Near Morphotropic Phase Boundary. *J. Am. Ceram. Soc.* 88, 2310–2314. doi:10.1111/j.1551-2916.2005.00391.x

Ding, G., Gao, F., Wu, G., and Bao, D. (2011). Bright Up-Conversion green Photoluminescence in Ho^{3+}-Yb^{3+} Co-doped $B_{i4}T_{i3}O_{12}$ Ferroelectric Thin Films. *J. Appl. Phys.* 109, 123101. doi:10.1063/1.3596597

Du, J., Xu, Z., Chu, R., Hao, J., Li, W., Jiang, G., et al. (2017). Rare-earth Doped $(K_{0.5}Na_{0.5})NbO_3$ Multifunctional Ceramics. *J. Mater. Sci. Mater. Electron.* 28, 5288–5294. doi:10.1007/s10854-016-6186-6

Fan, G. F., Shi, M. B., Lu, W. Z., Wang, Y. Q., and Liang, F. (2014). Effects of $L_{i2}CO_3$ and Sm_2O_3 Additives on Low-Temperature Sintering and Piezoelectric Properties of PZN-PZT Ceramics. *J. Eur. Ceram. Soc.* 34, 23–28. doi:10.1016/j.jeurceramsoc.2013.07.028

Fang, Z., Jiang, X., Tian, X., Zheng, F., Cheng, M., Zhao, E., et al. (2021). Ultratransparent PMN-PT Electro-Optic Ceramics and its Application in Optical Communication. *Adv. Opt. Mater.* 2021, 2002139. doi:10.1002/adom.202002139

Gao, F., Wu, G., Zhou, H., and Bao, D. (2009). Strong Upconversion Luminescence Properties of Yb^{3+} and Er^{3+} Codoped $B_{i4}T_{i3}O_{12}$ Ferroelectric Thin Films. *J. Appl. Phys.* 106, 126104–126698. doi:10.1063/1.3273477

Geng, Z., Li, K., Li, X., and Shi, D. (2017). Fabrication and Photoluminescence of Eu-Doped KNN-Based Transparent Ceramics. *J. Mater. Sci.* 52, 2285–2295. doi:10.1007/s10853-016-0521-4

Guo, J., Zhou, H., Fan, T., Zhao, B., Shang, X., Zhou, T., et al. (2020). Improving Electrical Properties and Toughening of PZT-Based Piezoelectric Ceramics for High-Power Applications via Doping Rare-Earth Oxides. *J. Mater. Res. Tech.* 9, 14254–14266. doi:10.1016/J.JMRT.2020.10.022

Guo, Q., Hou, L., Li, F., Xia, F., Wang, P., Hao, H., et al. (2019a). Investigation of Dielectric and Piezoelectric Properties in Aliovalent Eu^{3+} -modified $Pb(Mg_{1/3}Nb_{2/3})O_3$ -$PbTiO_3$ Ceramics. *J. Am. Ceram. Soc.* 102, 7428–7435. doi:10.1111/jace.16653

Guo, Q., Li, F., Xia, F., Gao, X., Wang, P., Hao, H., et al. (2019b). High-Performance Sm-Doped $Pb(Mg_{1/3}Nb_{2/3})O_3$-$PbZrO_3$-$PbTiO_3$-Based Piezoceramics. *ACS Appl. Mater. Inter.* 11, 43359–43367. doi:10.1021/acsami.9b15424

Hagemann, H.-J., and Hennings, D. (1981). Reversible Weight Change of Acceptor-Doped $BaTiO_3$. *J. Am. Ceram. Soc.* 64, 590–594. doi:10.1111/j.1151-2916.1981.tb10223.x

Hao, J., Xu, Z., Chu, R., Li, W., and Du, J. (2015). Bright Reddish-orange Emission and Good Piezoelectric Properties of Sm_2O_3-Modified $(K_{0.5}Na_{0.5})NbO_3$-Based lead-free Piezoelectric Ceramics. *J. Appl. Phys.* 117, 194104. doi:10.1063/1.4921451

He, C., Zhang, Y., Liang, S., Wang, J., Tong, W., Feng, X., et al. (2013). Electrical and Optical Properties of Nd^{3+}-Doped $Na_{0.5}Bi_{0.5}TiO_3$ Ferroelectric Single crystal. *J. Phys. D.* 46, 245104. doi:10.1088/0022-3727/46/24/245104

Hiruma, Y., Nagata, H., Hidaka, Y., and Tsukada, S. (2010). Depolarization Temperatures and Piezoelectric Properties of $(Bi_{0.5}Na_{0.5})TiO_3$ Ceramics and Single crystal. *Ferroelectrics* 404, 815–827. doi:10.1080/00150193.2010.482854

Inaguma, Y., Miyaguchi, A., Yoshida, M., and Katsumata, T. (2004). High-pressure Synthesis and Ferroelectric Properties in Perovskite-type $BiScO_3$-$PbTiO_3$ Solid Solution. *J. Appl. Phys.* 95, 231–235. doi:10.1063/1.1629394

Jaeger, R. E. (2010). Hot Pressing of Potassium-Sodium Niobates. *J. Am. Ceram. Soc.* 45, 209–213. doi:10.1111/j.1151-2916.1962.tb11127.x

Jiang, L., Wang, Z., Chen, Y., Chen, P., Luo, L., and Chen, H. (2018). Bright Up-Conversion Emission of Er^{3+}-Doped lead-free Ferroelectric $Na_{0.5}Bi_{0.5}TiO_3$ Single crystal. *Mater. Lett.* 210, 158–160. doi:10.1016/j.matlet.2017.08.135

Jo, W., Daniels, J. E., Jones, J. L., Tan, X., Thomas, P. A., Damjanovic, D., et al. (2011). Evolving Morphotropic Phase Boundary in lead-free $(Bi_{1/2}Na_{1/2})TiO_3$-$BaTiO_3$ Piezoceramics. *J. Appl. Phys.* 109, 14110. doi:10.1063/1.3530737

Kamzina, L. S., Wei, R., Li, G., Zeng, J., and Ding, A. (2010). Electro-optical Properties of PMN-xPT Compounds: Single Crystals and Transparent Ferroelectric Ceramic. *Phys. Solid State* 52, 2142–2146. doi:10.1134/S1063783410100203

Khazanchi, R., Sharma, S., and Goel, T. C. (2005). Effect of Rare Earth Europium Substitution on the Microstructure, Dielectric, Ferroelectric and Pyroelectric Properties of PZT Ceramics. *J. Electroceram* 14, 113–118. doi:10.1007/s10832-005-0871-9

Kim, K. B., Hsu, D. K., Ahn, B., Kim, Y. G., and Barnard, D. J. (2010). Fabrication and Comparison of PMN-PT Single crystal, PZT and PZT-Based 1-3 Composite Ultrasonic Transducers for NDE Applications. *Ultrasonics* 50, 790–797. doi:10.1016/j.ultras.2010.04.001

Kim, K. T., Kim, C. I., Kang, D. H., and Shim, I. W. (2002). The Effect of Eu Substitution on the Ferroelectric Properties of $Bi_4Ti_3O_{12}$ Thin Films Prepared by Metal-Organic Decomposition. *Thin Solid Films* 422, 230–234. doi:10.1016/S0040-6090(02)00981-1

Kour, P., Kumar, P., Sinha, S. K., and Kar, M. (2015). Study of Dielectric and Impedance Spectroscopy of La Substituted Nanocrystalline $Pb(Zr_{0.52}Ti0._{48})O_3$ Ceramics. *J. Mater. Sci. Mater. Electron.* 26, 1304–1310. doi:10.1007/s10854-014-2538-2

Kour, P., Pradhan, S. K., Kumar, P., Sinha, S. K., and Kar, M. (2016). Enhanced Ferroelectric and Piezoelectric Properties in La-Modified PZT Ceramics. *Appl. Phys. A-mater.* 122, 1–7. doi:10.1007/s00339-016-0122-8

Kumari, M., Yadav, A., and Sarun, P. M. (2020). Systematic Investigation of Structural, Optical and Dielectric Properties of 0.5 Mol% Eu: $BaTiO_3$ Ceramics. *Mater. Today Proc.* 42, 2214–7853. doi:10.1016/j.matpr.2020.03.337

Kuwata, J., Uchino, K., and Nomura, S. (1982). Dielectric and Piezoelectric Properties of $0.91Pb(Zn_{1/3}Nb_{2/3})O_3$-$0.09PbTiO_3$ Single Crystals. *Jpn. J. Appl. Phys.* 21, 1298–1302. doi:10.1143/JJAP.21.1298

Lau, C. M., Xu, X. W., and Kwok, K. W. (2015). Photoluminescence, Ferroelectric, Dielectric and Piezoelectric Properties of Er-Doped BNT-BT Multifunctional Ceramics. *Appl. Surf. Sci.* 336, 314–320. doi:10.1016/j.apsusc.2014.12.105

Li, C., Xu, B., Lin, D., Zhang, S., and Li, F. (2020b). Atomic-scale Origin of Ultrahigh Piezoelectricity in Samarium-Doped PMN-PT Ceramics. *Phys. Rev. B.* 101, 140102. doi:10.1103/PhysRevB.101.140102

Li, F., Cabral, M. J., Xu, B., Cheng, Z., Dickey, E. C., Lebeau, J. M., et al. (2019b). Giant Piezoelectricity of Sm-Doped $Pb(Mg_{1/3}Nb_{2/3})O_3$-$PbTiO_3$ Single Crystals. *Science* 364, 264. doi:10.1126/science.aaw2781

Li, F., Lin, D., Chen, Z., Cheng, Z., Wang, J., Li, C. C., et al. (2018). Ultrahigh Piezoelectricity in Ferroelectric Ceramics by Design. *Nat. Mater.* 17, 349–424. doi:10.1038/s41563-018-0034-4

Li, H., Feng, C., and Yao, W. (2004). Some Effects of Different Additives on Dielectric and Piezoelectric Properties of $(Bi_{1/2}Na_{1/2})TiO_3$-$BaTiO_3$ Morphotropic-Phase-Boundary Composition. *Mater. Lett.* 58, 1194–1198. doi:10.1016/j.matlet.2003.08.034

Li, H., Zhang, Y., Zhou, J., Zhang, X., Liu, H., and Fang, J. (2015a). Phase Structure and Electrical Properties of xPZN-(1-X)PZT Piezoceramics Near the Tetragonal/rhombohedral Phase Boundary. *Ceram. Int.* 41, 4822–4828. doi:10.1016/j.ceramint.2014.12.038

Li, Q., Wei, S., Jiang, Y., Ying, P., Qiang, C., Xi, Y., et al. (2009). "Effect of Y-Doping on the Piezoelectric Properties of $(1-x)BiScO_3$-$xPbTiO_3$ High-Temperature Piezoelectric Ceramics," in 2009 18th IEEE International Symposium on the Applications of Ferroelectrics (China: Xi'an), 1–4. doi:10.1109/ISAF.2009.5307539

Li, W., Hao, J., Du, J., Fu, P., and Chu, R. (2020a). Electrical Properties and Luminescence Properties of $0.96(K_{0.48}Na_{0.52})(Nb_{0.95}Sb_{0.05})$-$0.04Bi_{0.5}(Na_{0.82}K_{0.18})_{0.5}ZrO_3$-xSm lead-free Ceramics. *J. Adv. Ceram.* 9, 72–82. doi:10.1007/s40145-019-0349-x

Li, X., Chen, C., Deng, H., Zhang, H., and Luo, H. (2015b). The Growth and Properties of lead-free Ferroelectric Single Crystals. *Crystals* 5, 172–192. doi:10.3390/cryst5020172

Li, Y., Xi, Z., Fang, P., Li, X., Long, W., He, A., et al. (2019c). Electric and Optical Properties of Tm^{3+}/Yb^{3+} Co-doped PZN-9PT Crystals. *J. Mater. Sci. Mater. Electron.* 30, 3811–3819. doi:10.1007/s10854-019-00665-x

Li, Y. X., Yao, X., Wang, X. S., and Hao, Y. B. (2012). Studies of Dielectric Properties of Rare Earth (Dy, Tb, Eu) Doped Barium Titanate Sintered in Pure Nitrogen. *Ceram. Int.* 38, S29–S32. doi:10.1016/j.ceramint.2011.04.042

Li, Y., Zhao, J., Zhang, X., Jia, Q., and Hao, X. (2019a). Tuning the Ferroelectric, Dielectric and Photoluminescence Properties of $0.88(Na_{0.5}Bi_{0.5})TiO_3$-$0.12BaTiO_3$ Ceramics by Sm Ion Doping. *J. A. D.* 9, 1950041. doi:10.1142/S2010135X19500413

Liu, L., Fan, H., Ke, S., and Chen, X. (2008). Effect of Sintering Temperature on the Structure and Properties of Cerium-Doped $0.94(Bi_{0.5}Na_{0.5})TiO_3$-$0.06BaTiO_3$ Piezoelectric Ceramics. *J. Alloys Compd.* 458, 504–508. doi:10.1016/j.jallcom.2007.04.037

Liu, L. (2015). Progress on the Fabrication of lead-free Textured Piezoelectric Ceramics: Perspectives over 25years. *J. Mater. Sci-mater El.* 26 (7), 4425–4437. doi:10.1007/s10854-015-2920-8

Liu, Z., Jiang, G., Wang, R., Chai, C., Zheng, L., Zhang, Z., et al. (2016). Temperature and Concentration Effects on Up-Conversion Photoluminescence Properties of Ho^{3+} and Yb^{3+} Co-doped $0.67Pb(Mg_{1/3}Nb_{2/3})O_3$-$0.33PbTiO_3$ Multifunctional Ceramics. *Ceram. Int.* 45, 11309–11313. doi:10.1016/j.ceramint.2016.04.049

Lv, Z., Qin, Y., Zhang, Y., Fu, J., and Lu, C. (2019). Efficient Up-Conversion Photoluminescence in Transparent Pr^{3+}/Yb^{3+} Co-doped $0.75Pb(Mg_{1/3}Nb_{2/3})O_3$-$0.25PbTiO_3$ Ferroelectric Ceramics. *Ceram. Int.* 45, 10924–10929. doi:10.1016/j.ceramint.2019.02.172

Ma, Z., Zhang, Y., Lu, C., Qin, Y., Lv, Z., and Lu, S. (2018). Synthesis and Properties of La-Doped PMN-PT Transparent Ferroelectric Ceramics. *J. Mater. Sci-mater El.* 29, 6985–6990. doi:10.1007/s10854-018-8685-0

Majumder, S. B., Dobal, P. S., Roy, B., Bhaskar, S., Katiyar, R. S., and Bhalla, A. (2001). Effect of Rare Earth Doping on Sol-Gel Derived PZT Thin Films. *Ferroelectrics Lett.* 28, 85–92. doi:10.1080/07315170108202952

Morrison, F. D., Coats, A. M., Sinclair, D. C., and West, A. R. (2001). Charge Compensation Mechanisms in La-Doped $BaTiO_3$. *J. Electroceramics* 6, 219–232. doi:10.1023/A:1011400630449

Nakaki, H., Uchida, H., Okamoto, S., Yokoyama, S., Funakubo, H., and Koda, S. (2004). Improvement of Ferroelectric Properties of lead Zirconate Titanate Thin Films by Ion-Substitution Using Rare-Earth Cations. *Mrs Proc.* 830, D3. doi:10.1557/PROC-830-D3.3

Panda, P. K. (2009). Review: Environmental Friendly lead-free Piezoelectric Materials. *J. Mater. Sci.* 44, 5049–5062. doi:10.1007/s10853-009-3643-0

Pandey, S. K., Kumar, S., Chatterjee, S. N., Kumar, U., Prakash, C., Chatterjee, R., et al. (2007). Growth and Characterization of Sm^{3+}-Substituted PZT Thin Films. *Physica B* 388, 404–411. doi:10.1016/j.physb.2006.06.167

Pandey, S. K., Thakur, O. P., Bhattacharya, D. K., Prakash, C., and Chatterjee, R. (2009). Structural and Electrical Properties of Sm^{3+} Substituted PZT Ceramics. *J. Alloys Compd.* 468, 356–359. doi:10.1016/j.jallcom.2008.01.006

Peng, F., Xu, Z., Chu, R., Wei, L., Zang, G., and Hao, J. (2010c). Piezoelectric, Ferroelectric and Dielectric Properties of La_2O_3-Doped $(Bi_{0.5}Na_{0.5})_{0.94}Ba_{0.06}TiO_3$ lead-free Ceramics lead-free Ceramics. *Mater. Des.* 31, 706–801. doi:10.1016/j.matdes.2009.07.056

Peng, F., Xu, Z., Chu, R., Wei, L., Zang, G., and Hao, J. (2010b). Piezoelectric, Ferroelectric and Dielectric Properties of Nd_2O_3-Doped $(Bi_{0.5}Na_{0.5})_{0.94}Ba_{0.06}TiO_3$ lead-free Ceramics. *Mater. Sci. Eng. B.* 167, 161–166. doi:10.1016/j.mseb.2010.01.057

Peng, F., Xu, Z., Chu, R., Wei, L., Zang, G., and Hao, J. (2010a). Piezoelectric, Ferroelectric and Dielectric Properties of Sm_2O_3-Doped $(Bi_{0.5}Na_{0.5})_{0.94}Ba_{0.06}TiO_3$ lead-free Ceramics. *Mater. Sci. Eng. B.* 124, 1065–1070. doi:10.1016/j.matchemphys.2010.08.033

Peng, G., Zheng, D., Hu, S., Zhao, H., and Cheng, C. (2016). Effects of Rare-Earth Sm_2O_3 Addition on Relaxation Behavior and Electric Properties of 0.5PNN-0.5PZT Ceramics. *J. Mater. Sci. Mater. Electron.* 27, 5509–5516. doi:10.1007/s10854-016-4577-3

Perumal, R. N., Sadhasivam, S., and Athikesavan, V. (2019). Structural, Dielectric, Ac Conductivity, Piezoelectric and Impedance Spectroscopy Studies on $PbZr_{0.52}Ti_{0.48}O_3$:Re^{3+} (Re^{3+}: La^{3+}, Nd^{3+} and Dy^{3+}) Ceramics. *Results Phys.* 15, 102729. doi:10.1016/j.rinp.2019.102729

Pieter, D. (2017). Charge Transfer Bands in Optical Materials and Related Defect Level Location. *Opt. Mater.* 69, 8–22. doi:10.1016/j.optmat.2017.03.061

Pieter, D. (2013). Lanthanide 4f-Electron Binding Energies and the Nephelauxetic Effect in Wide Band gap Compounds. *J. Lumin.* 136, 122–129. doi:10.1016/j.jlumin.2012.11.030

Politova, E. D., Egorova, B. V., Kaleva, G. M., Mosunov, A. V., and Zeng, J. (2011). Phase Transitions and the Dielectric and Piezoelectric Properties of Ceramic Solid Solutions Based on $BiScO_3$-$PbTiO_3$. *Bull. Russ. Acad. Sci. Phys.* 75, 1166–1169. doi:10.3103/S1062873811050418

Qiu, W., and Hng, H. H. (2002). Effects of Dopants on the Microstructure and Properties of PZT Ceramics. *Mater. Chem. Phys.* 75, 151–156. doi:10.1016/S0254-0584(02)00045-7

Rajan, K. K., Shanthi, M., Chang, W. S., Jin, J., and Lim, L. C. (2007). Dielectric and Piezoelectric Properties of [0 0 1] and [0 1 1]-poled Relaxor Ferroelectric PZN-PT and PMN-PT Single Crystals. *Sensor Actuat A-Phys.* 133, 110–116. doi:10.1016/j.sna.2006.03.036

Rath, M., Miryala, M., Murakami, M., and Rao, M. S. R. (2019). Controlled Piezotronic Properties on Recoverable Energy Storage Density in Rare-Earth Ions Doped Epitaxial PZT Thin Films. *J. Phys. D.* 52, 304001. doi:10.1088/1361-6463/ab1b08

Ruan, K., Chen, X., Liang, T., Wu, G., and Bao, D. (2008). Photoluminescence and Electrical Properties of Highly Transparent $(Bi,Eu)_4Ti_3O_{12}$ Ferroelectric Thin Films on Indium-Tin-Oxide-Coated Glass Substrates. *J. Appl. Phys.* 103, 627. doi:10.1063/1.2903928

Saito, Y., Takao, H., Tani, T., Nonoyama, T., Takatori, K., Homma, T., et al. (2004). Lead-free Piezoceramics. *Nature* 432, 84–87. doi:10.1038/nature03028

Samad, R., Rather, M., Asokan, K., and Want, B. (2017). Structural, Dielectric and Ferroelectric Properties of Rare Earth Substituted lead Zirconate Titanate. *J. Mater. Sci-mater El.* 29, 4226–4237. doi:10.1007/s10854-017-8368-2

Shannigrahi, R. S., Tay, F. E. H., Yao, K., and Choudhary, R. N. P. (2004). Effect of Rare Earth (La, Nd, Sm, Eu, Gd, Dy, Er and Yb) Ion Substitutions on the Microstructural and Electrical Properties of Sol-Gel Grown PZT Ceramics Science Direct. *J. Eur. Ceram. Soc.* 24, 163–170. doi:10.1016/S0955-2219(03)00316-9

Shrout, T. R., and Zhang, S. J. (2007). Lead-free Piezoelectric Ceramics: Alternatives for PZT?. *J. Electroceram* 19, 113–126. doi:10.1007/s10832-007-9047-0

Singh, D. J., Ghita, M., Fornari, M., and Halilov, S. V. (2011). Role of A-Site and B-Site Ions in Perovskite Ferroelectricity. *Ferroelectrics* 338, 73–79. doi:10.1080/00150190600732694

Singh, N., Shyam, R., Upadhyay, N. K., and Dhar, A. (2015). Development of Rare-Earth Free Mn-Al Permanent Magnet Employing Powder Metallurgy Route. *IOP Conf. Ser. Mater. Sci. Eng.* 73, 012042. doi:10.1088/1757-899X/73/1/012042

Steudel, F., Loos, S., Ahrens, B., and Schweizer, S. (2015). Quantum Efficiency and Energy Transfer Processes in Rare-Earth Doped Borate Glass for Solid-State Lighting. *J. Lumin.* 170, 157–162. doi:10.1016/j.jlumin.2015.07.032

Sun, H., Peng, D., Wang, X., Tang, M., Zhang, Q., and Yao, X. (2012). Green and Red Emission for $(K_{0.5}Na_{0.5})NbO_3$: Pr Ceramics. *J. Appl. Phys.* 111, 2087. doi:10.1063/1.3686193

Sun, H., Peng, D., Wang, X., Tang, M., Zhang, Q., and Yao, X. (2011). Strong Red Emission in Pr Doped $(Bi_{0.5}Na_{0.5})TiO_3$ Ferroelectric Ceramics. *J. Appl. Phys.* 110, 2087. doi:10.1063/1.3606425

Sun, H. Q., Wang, X. S., and Yao, X. (2010). Structure and Electric Properties of Sm Doped $BaTiO_3$ Ceramics. *Ferroelectrics* 404, 99–104. doi:10.1080/00150193.2010.482459

Sun, H., Zhang, Q., Wang, X., and Mu, G. (2014). Green and Red Up-Conversion Luminescence of Er^{3+}-Doped $K_{0.5}Na_{0.5}NbO_3$ Ceramics. *Ceram. Int.* 40, 2581–2584. doi:10.1016/j.ceramint.2013.10.089

Sun, L. N., Zhang, H. J., Peng, C. Y., Yu, J. B., Meng, Q. G., Fu, L. S., et al. (2006). Covalent Linking of Near-Infrared Luminescent Ternary Lanthanide (Er(3+), Nd(3+), Yb(3+)) Complexes on Functionalized Mesoporous MCM-41 and SBA-15. *J. Phys. Chem. B* 110, 7249–7258. doi:10.1021/jp060395u

Tsonev, L. (2008). Luminescent Activation of Planar Optical Waveguides in $LiNbO_3$ with Rare Earth Ions Ln^{3+} a Review. *Opt. Mater.* 30, 892–899. doi:10.1016/j.optmat.2007.03.011

Uchino, K. (1995). Electro-optic Ceramics and Their Display Applications. *Ceram. Int.* 21, 309–315. doi:10.1016/0272-8842(95)96202-Z

Vittayakorn, N., Rujijanagul, G., Tan, X., He, H., Marquardt, M. A., and Cann, D. P. (2006). Dielectric Properties and Morphotropic Phase Boundaries in the $xPb(Zn_{1/3}Nb_{2/3})O_3$-$(1-x)Pb(Zr_{0.5}Ti_{0.5})O_3$ Pseudo-binary System. *J. Electroceramic* 16, 141–149. doi:10.1007/s10832-006-4927-2

Wang, N., Sun, Q., Ma, W., Yong, Z., and Liu, H. (2012). Investigation of La-Doped $0.25Pb(Zn_{1/3}Nb_{2/3})O_3$-$0.75Pb(Zr_xTi_{1-x})O_3$ Ceramics Near Morphotropic Phase Boundary. *J. Electroceramics* 28, 15–19. doi:10.1007/s10832-011-9672-5

Wei, R., Li, G., Zeng, J., Bian, J., Kamzina, L. S., Zeng, H., et al. (2010). Large Electro-Optic Effect in La-Doped $0.75Pb(Mg_{1/3}Nb_{2/3})O_3$-$0.25PbTiO_3$ Transparent Ceramic by Two-Stage Sintering. *Int. J. Appl. Ceram. Tec* 93, 2128–2131. doi:10.1111/j.1551-2916.2010.03675.x

Wei, Z., Huang, Y., Tsuboi, T., Nakai, Y., Zeng, J., and Li, G. (2012a). Optical Characteristics of Er^{3+}-Doped PMN-PT Transparent Ceramics. *Ceram. Int.* 38, 3397–3402. doi:10.1016/j.ceramint.2011.12.051

Wei, Z., Tsuboi, T., Nakai, Y., Huang, Y., Zeng, J., and Li, G. (2012b). The Synthesis of Er^{3+}-Doped PMN-PT Transparent Ceramic and its Infrared Luminescence. *Mater. Lett.* 68, 57–59. doi:10.1016/j.matlet.2011.10.034

Wu, X., Chi, M. L., and Kwok, K. W. (2015a). Photoluminescence Properties of Er/Pr-Doped $K_{0.5}Na_{0.5}NbO_3$ Ferroelectric Ceramics. *J. Am. Ceram. Soc.* 98, 2139–2145. doi:10.1111/jace.13605

Wu, X., Chung, T. H., and Kwok, K. W. (2015b). Enhanced Visible and Mid-IR Emissions in Er/Yb-Codoped $K_{0.5}Na0_{.5}NbO_3$ Ferroelectric Ceramics. *Ceram. Int.* 41, 14041–14048. doi:10.1016/j.ceramint.2015.07.018

Wu, X., Kwok, K. W., and Li, F. L. (2013). Up-conversion Fluorescence Studies of Sol-Gel Derived Er-Doped KNN Ceramics. *J. Alloys Compd.* 580, 88–92. doi:10.1016/j.jallcom.2013.05.096

Wu, X., Lu, S., and Kwok, K. W. (2017). Photoluminescence, Electro-Optic Response and Piezoelectric Properties in Pressureless-Sintered Er-Doped KNN-Based Transparent Ceramics. *J. Alloys Compd.* 695, 3573–3578. doi:10.1016/j.jallcom.2016.11.409

Xi, Z., Han, A., Fang, P., Li, X., and Long, W. (2016a). Electrical Properties and Up-Conversion Luminescence of the Er^{3+}-Modified PZN-9PT Crystals. *Int. J. Mater. Res.* 31, 3044–3049. doi:10.1557/jmr.2016.311

Xi, Z., Han, A., Fang, P., Long, W., Li, X., and Bu, Q. (2016b). Structural and Electrical Properties of Ho^{3+}-Modified $Pb(Zn_{1/3}Nb_{2/3})O_3$-9$PbTiO_3$ Single Crystals. *Mater. Sci. Mater. Electron.* 27, 4223–4229. doi:10.1007/s10854-016-4286-y

Xie, D., Zhang, Z., Ren, T., Liu, T., and Liu, L. (2006). Properties of Neodymium-Doped $Bi_4Ti_3O_{12}$ Thin Films for Ferroelectric Random Access Memory. *Integrated Ferroelectrics* 84, 67–73. doi:10.1080/10584580601085230

Xu, J., Lu, Q., Lin, C., Zheng, X., Lin, T., and Wu, X. (2020). Enhanced Ferro-/piezoelectric Properties of Tape-Casting-Derived Er^{3+} -doped $Ba_{0.85}Ca_{0.15}Ti_{0.9}Zr_{0.1}O_3$ Optoelectronic Thick Films. *J. Adv. Ceram.* 9, 693–702. doi:10.1007/s40145-020-0405-6

Yang, D., Yang, Z., Zhang, X., Wei, L., Chao, X., and Yang, Z. (2017). High Transmittance in lead-free Lanthanum Modified Potassium-Sodium Niobate Ceramics. *J. Alloys Compd.* 716, 21–29. doi:10.1016/j.jallcom.2017.04.236

Yao, Z. H., Liu, H. X., Li, Y. Q., Cao, Y. Q., and Hao, H. (2010). Morphotropic Phase Boundary of $(Bi_{0.9}La_{0.1})ScO_3$-PbTi)O_3 Piezoelectric Ceramics for High-Temperature Application. *Ferroelectrics* 409, 21–26. doi:10.1080/00150193.2010.485886

Yu, Y. J., Chan, H. L. W., Wang, F. P., and Zhao, L. C. (2003). Effects of Rare Earth Eu Doping on Ferroelectric Properties of $PbZr_{0.52}Ti_{0.48}O_3$ Thin Films by Sol-Gel Methods. *Microelectron Eng.* 66, 0167–9317. doi:10.1016/S0167-9317(02)00991-7

Zeng, X., He, X., Cheng, W., Qiu, P., and Xia, B. (2014). Effect of Dy Substitution on Ferroelectric, Optical and Electro-Optic Properties of Transparent $Pb_{0.90}La_{0.10}(Zr_{0.65}Ti_{0.35})O_3$ Ceramics. *Ceram. Int.* 40, 6197–6202. doi:10.1016/j.ceramint.2013.11.074

Zhai, Y., Feng, Y., Du, J., Xue, J., Shen, J., Lu, Y., et al. (2019). The Impedance, Dielectric and Piezoelectric Properties of Tb_4O_7 and Tm_2O_3 Doped KNN Ceramics. *Mater. Sci. Mater. Electron.* 30, 4352–4358. doi:10.1007/s10854-019-00748-9

Zhang, H., Zhao, X., Hao, D., Chao, C., Di, L., Li, X., et al. (2014c). Photoluminescence and Electrical Properties of Eu-Doped $(Na_{0.5}Bi_{0.5})TiO_3$ Ferroelectric Single Crystals. *Appl. Phys. A-mater.* 114, 357–361. doi:10.1007/s00339-013-8176-3

Zhang, J. R., Zhang, Y. C., Lu, C. J., Ye, W. N., and Su, J. (2014a). Effect of La-Doping Content on the Dielectric and Ferroelectric Properties of 0.88$Pb(Mg_{1/3}Nb_{2/3})O_3$-0.12$PbTiO_3$ Ceramics. *J. Mater. Sci. Mater. Electron.* 25, 653–658. doi:10.1007/s10854-013-1688-y

Zhang, J. W., Zou, Y. K., Chen, Q., Zhang, R., Li, K. K., Jiang, H., et al. (2006). Optical Amplification in Nd^{3+} Doped Electro-Optic Lanthanum lead Zirconate Titanate Ceramics. *Appl. Phys. Lett.* 89, 411–426. doi:10.1063/1.2336216

Zhang, K., Li, L., Wang, M., and Luo, W. (2020a). Charge Compensation in Rare Earth Doped $BaTiO_3$-Based Ceramics Sintered in Reducing Atmosphere. *Ceram. Int.* 46, 25881–25887. doi:10.1016/j.ceramint.2020.07.072

Zhang, Q., Chen, J., and Che, M. (2020b). Dielectric Properties of Barium Titanium Ceramics Doped by Lanthanum Oxide. *Ferroelectrics* 566, 30–41. doi:10.1080/00150193.2020.1762427

Zhang, Q., Sun, H., Wang, X., and Zhang, T. (2014b). Highly Efficient orange Emission $(K_{0.5}Na_{0.5})NbO_3$: Sm^{3+} lead Free Piezoceramics. *Mater. Lett.* 117, 283–285. doi:10.1016/j.matlet.2013.12.026

Zhang, R., Wang, X., Zhang, S., Yang, Z., and Zou, H. (2021). Effect of Dy Doping on the crystal Orientation, Microstructure, and Electrical Properties of PDZT Thin Films Prepared by Sol-Gel Method. *J. Mater. Sci. Mater. Electron.* 32, 3612–3620. doi:10.1007/s10854-020-05108-6

Zhang, S., Alberta, E. F., Eitel, R. E., Randall, C. A., and Shrout, T. R. (2005). Elastic, Piezoelectric, and Dielectric Characterization of Modified $BiScO_3$-$PbTiO_3$ Ceramics. *IEEE Trans. Ultrason. Ferroelectrics Frequency Control.* 52, 2131–2139. doi:10.1109/TUFFC.2005.1561684

Zhang, S. T., Zhang, X. J., Cheng, H. W., Chen, Y. F., Liu, Z. G., Ming, N. B., et al. (2003). Enhanced Electrical Properties of C-axis Epitaxial Nd-Substituted $Bi_4Ti_3O_{12}$ Thin Films. *Appl. Phys. Lett.* 83, 4378–4380. doi:10.1063/1.1629372

Zhao, H., Zhang, K., Xu, L., Sun, F., Chen, X., Li, K. K., et al. (2014). Optical Amplification in Disordered Electro-Optic Tm^{3+} and Ho^{3+} Co-doped Lanthanum-Modified lead Zirconate Titanate Ceramics and Study of Spectroscopy and Communication between Cations. *J. Appl. Phys.* 115, 397–2971. doi:10.1063/1.4866000

Zheng, M., Hou, Y., Zhu, M., Zhang, M., and Yan, H. (2014). Shift of Morphotropic Phase Boundary in High-Performance fine-grained PZN-PZT Ceramics. *J. Eur. Ceram. Soc.* 34, 2275–2283. doi:10.1016/j.jeurceramsoc.2014.02.041

Zheng, T., Wu, J., Xiao, D., and Zhu, J. (2018). Recent Development in lead-free Perovskite Piezoelectric Bulk Materials. *Prog. Mater. Sci.* 98, 552–624. doi:10.1016/j.pmatsci.2018.06.002

Zhou, J., Ma, Q., Wang, P., Cheng, L., and Liu, S. (2014). Influence of Rare-Earth Nd, Dy, and Ho Doping on Structural and Electrical Properties of $(Na_{0.53}K_{0.47})$ 0.942$Li_{0.058}NbO_3$ Based lead-free Piezoceramics. *Ceram. Int.* 40, 2451–2459. doi:10.1016/j.ceramint.2013.08.020

Zhou, Z., Tang, Z. L., Zhang, Z. T., and Wlodarski, W. (2001). Perovskite Oxide of PTCR Ceramics as Chemical Sensors. *Sens. Actuators B Chem.* 77, 22–26. doi:10.1016/S0925-4005(01)00667-0

Conflict of Interest: The authors declare that the research was conducted in the absence of any commercial or financial relationships that could be construed as a potential conflict of interest.

frontiers in Materials

ORIGINAL RESEARCH
published: 02 August 2021
doi: 10.3389/fmats.2021.699433

Ultrasonic Ring Array-Based Transient Triplet Differential Photoacoustic Imaging for Strong Background Removal

Guan Wang[1], Bo Wang[1], Tong Ye[1], Congcong Wang[1], Lili Guo[2], Jiaying Xiao[1] and Zeyu Chen[3,4]**

[1]Department of Biomedical Engineering, School of Basic Medical Science, Central South University, Changsha, China, [2]Department of Biomedical Engineering, College of Biology, Hunan University, Changsha, China, [3]College of Mechanical and Electrical Engineering, Central South University, Changsha, China, [4]Dermatology Department of Xiangya Hospital, Central South University, Changsha, China*

Photoacoustic imaging (PAI) is a fast evolving imaging technology enabling *in vivo* imaging with high specificity and spatial resolution. However, due to strong background signals from various intrinsic chromospheres such as melanin, photoacoustic imaging of targeting objects labeled by contrast agents remain a challenge. The transient triplet differential (TTD) method has shown a significant potential for background-free photoacoustic imaging. Here, we develop a photoacoustic system using an ultrasonic semicircular ring array for transient triplet differential imaging. Pt(II) Octaethylporphine (PtOEP) and black ink are used as the contrast agent and the phantom of melanoma, respectively. Using the TTD method, we could remove the strong background signal from black ink. The ratio between contrast agent signal and background signal is increased to about 10 times the previous one. Our finding demonstrates the potential of the TTD method on molecular imaging for strong background removal.

Keywords: PtOEP, photoacoustic imaging, melanoma, transient triplet differential, strong background

OPEN ACCESS

Edited by:
Xun Yu,
New York Institute of Technology, United States

Reviewed by:
Hao Yang,
University of South Florida, United States
Ruimin Chen,
Zhejiang Lab, China

****Correspondence:***
Jiaying Xiao
jiayingxiao@csu.edu.cn
Zeyu Chen
zeyuchen@csu.edu.cn

Specialty section:
This article was submitted to Smart Materials, a section of the journal Frontiers in Materials

Received: *23 April 2021*
Accepted: *28 June 2021*
Published: *02 August 2021*

Citation:
Wang G, Wang B, Ye T, Wang C, Guo L, Xiao J and Chen Z (2021) Ultrasonic Ring Array-Based Transient Triplet Differential Photoacoustic Imaging for Strong Background Removal. Front. Mater. 8:699433. doi: 10.3389/fmats.2021.699433

INTRODUCTION

Photoacoustic (PA) imaging is an imaging method that images light-absorbing tissues based on the photoacoustic effect. This leads to thermoelastic expansion and propagation of ultrasound (US) waves that are then detected using a US transducer (Xu and Wang, 2006; Paul, 2011). According to the light absorption coefficient of different tissues, different ultrasonic signals are obtained, and the received signals are used for image reconstruction to get information about different organizations (Xu and Wang, 2005). Photoacoustic imaging can image endogenous tissue contrast agents or exogenous contrast agents in deep biological samples with high spatial resolution (Tsang et al., 2020). Therefore, it can track many molecular level objects, such as T cells (Zheng et al., 2018), enzymes (Zha et al., 2013), and metal ions (Liu et al., 2017), which has shown great potential in many preclinical and clinical applications.

However, due to strong background signals from various intrinsic chromospheres such as hemoglobin (Yao et al., 2015), melanin (Zhang et al., 2010), and lipids (Matthews et al., 2014), PA imaging of targeting objects labeled by contrast agents has remained a challenge. Several methods have been developed to overcome the challenge (Oh et al., 2006; Allen et al., 2012). Among these, the transient triplet differential (TTD) method has shown a significant potential for background-free molecular imaging (Tan et al., 2018).

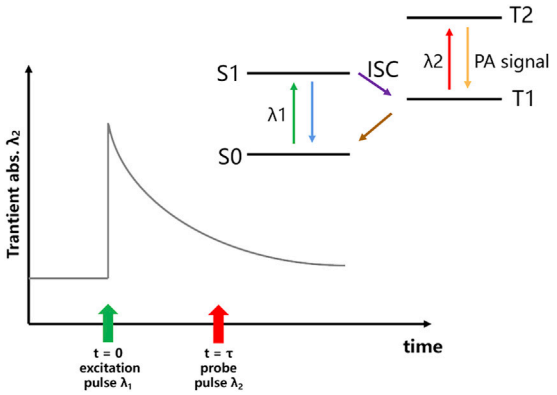

FIGURE 1 | Principle of the triplet state photoacoustic signal from phosphorescent materials.

The exogenous contrast agents for transient triplet differential (TTD) PA imaging are phosphorescent materials such as Pt(II) octaethylporphine (PtOEP) (Mills and Lepre, 1997). When the phosphorescent material is excited by a laser with specific wavelength (λ_1), the electrons in the ground state (S0) will be pumped to the singlet state (S1) and then transferred into the triplet state (T1) through intersystem crossing (ISC). Then, the electrons later decay at a much slower rate through phosphorescence, from microseconds to milliseconds. Ordinarily, the triplet state has an absorption peak (λ_2) that is well shifted from the ground state absorption peak (λ_1). By using a probe beam with the absorption peak (λ_2) of the triplet state, the electrons in the triplet state (T1) will be pumped to the second triplet state. Because the electron relaxation from T2 to T1 is a nonradioactive process, a triplet state photoacoustic signal will be generated at that time, and the principle is shown in **Figure 1** (Ashkenazi et al., 2008; Berera et al., 2009). Since only phosphorescent with electrons in the triplet state can generate the triplet state PA signal, the differential signal will exclusively come from the phosphorescent contrast agent. The difference between PA signals and triplet state PA signals allows the removal of background signals from endogenous chromospheres without phosphorescent.

Melanoma is the most dangerous type of skin cancer with high lethal rate. It develops from the cells (melanocytes) that produce melanin. Melanin has a strong absorption coefficient for light of different wavelengths in the spectrum, which enables PA imaging for boundary detection (Park et al., 2021). On the other side, due to the existence of this strong background signal from melanin, there has been a lack of PA molecular imaging studies on the proteins, biomarkers, and cells of melanoma tissue. Besides, in previous studies, melanoma phantom with black ink has been widely used to imitate the strong light absorption ability of melanin.

Ultrasonic ring array can collect the acoustic signal around the target at one time and optimize the image quality by calculating the distribution of sound velocity (Xia et al., 2013; Zhang and Wang, 2020). This study develops a transient triplet differential (TTD) PA system with a semicircular ring array. With the background of melanin phantom, we use photoacoustic imaging and transient triple difference method to image phosphorescent contrast agent separately. The results indicate that TTD can successfully remove the strong background PA signal from melanoma phantom, which can be potentially used for *in vivo* molecular imaging and molecular typing of melanoma.

MATERIALS AND METHODS

Material

In this study, octaethylporphine platinum (Pt(II) octaethylporphine, PtOEP), a transition metal complex, is used as the phosphorescent material, and the molecular structure is shown in **Figure 2**. It is in powder form at room temperature and is insoluble in water. It is easily soluble in organic solvents such as toluene (Ashkenazi et al., 2008). Research has found that PtOEP is an oxygen-sensitive material, and its luminescence will be quenched by oxygen. The peak absorption wavelengths of the singlet and triplet states of PtOEP are 532 and 740 nm, respectively. We use 10 ml of toluene solution to dissolve 7.38 mg of the PtOEP powder to obtain a mixed solution with a final concentration of 1 mM.

As mentioned before, black ink was used to imitate the melanin in-body model to test the ability of TTD to remove strong background signals.

Instruments

The semicircular ring array has 128 elements, the center frequency is 3 MHz, and the average relative bandwidth is 60%, but 32 elements of the top are hollowed out for wiring. 128 elements are equally spaced and evenly distributed on a semicircular arc with a radius of 60 mm and an angle of 180°, while ensuring the focus in the z-axis (shown in **Figure 3**). The advantage of such an array design is that for each target object, a piezoelectric element is perpendicular to its edge direction, and all the information of the target object can be obtained at one time, and the image quality can be optimized by calculating the sound velocity. The 64-channel signal passes through the port and is input to the amplifier with a multiple of 40 dB. Each amplifier contains eight input channels and four output channels. The selection of input and output channels is controlled by a

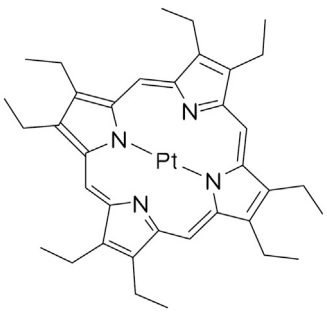

FIGURE 2 | The molecular structure formula of PtOEP.

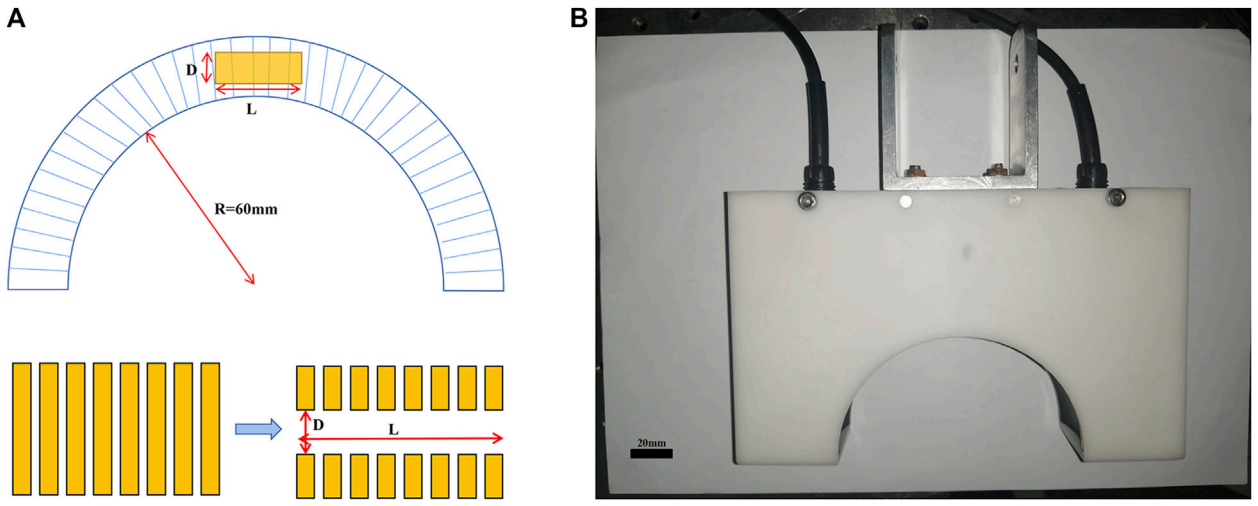

FIGURE 3 | (A) Structure diagram of circular array; **(B)** physical picture of the circular array.

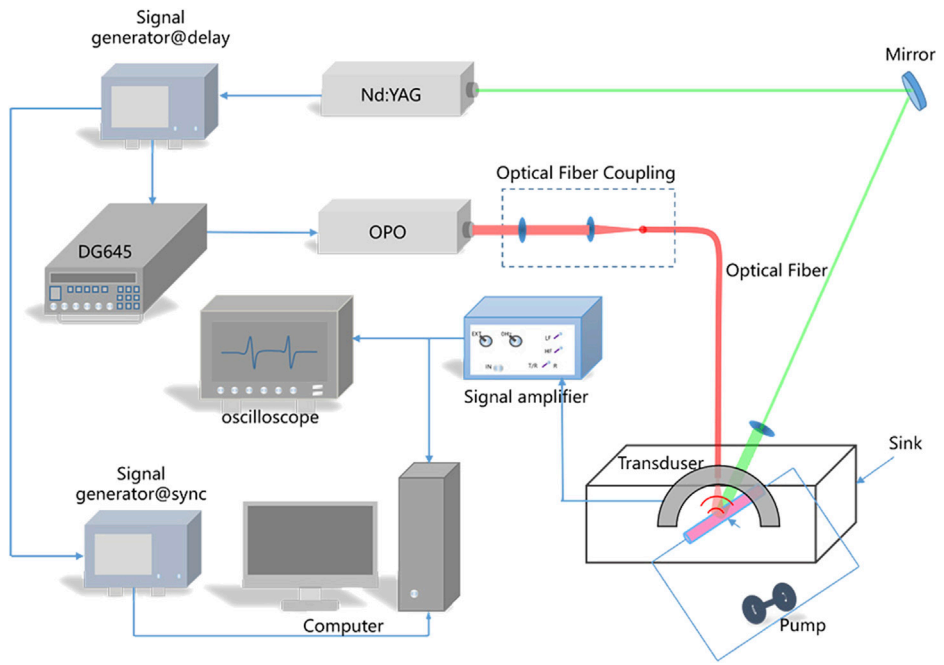

FIGURE 4 | Schematic diagram of a transient triplet differential photoacoustic imaging system.

2 1-channel selection multiplexer. 128 channels can output 64 channels at a time and can input 8 8-channel capture cards. The sampling rate of each capture card is 50 MS/s with a 24-bit resolution.

A DG645 digital delay/pulse generator (Stanford Research Systems, CA, United States) is used to control the synchronization between the two lasers. It can provide a precisely defined pulse repetition rate up to 10 MHz. The input is the synchronization trigger signal of the Nd:YAG laser. After a time delay controlled by the DG645, the OPO laser is triggered. We set different time delays ranging from −2 to 8 μs between the two lasers with ±3.5 V input signal amplitude.

System

The schematic of the system is shown in **Figure 4**. A Q-switched Nd:YAG laser (Beamtech Optronics Co., Ltd., Beijing, China) is used to generate excitation pulse with a wavelength of 532 nm, a repetition frequency of 10 Hz, a pulse width of 10 ns, an energy of 10 mJ, and a beam width of 6 mm. The SpitLight 600 OPO laser (Innolas Laser GmbH, Munich, Germany) is used to generate

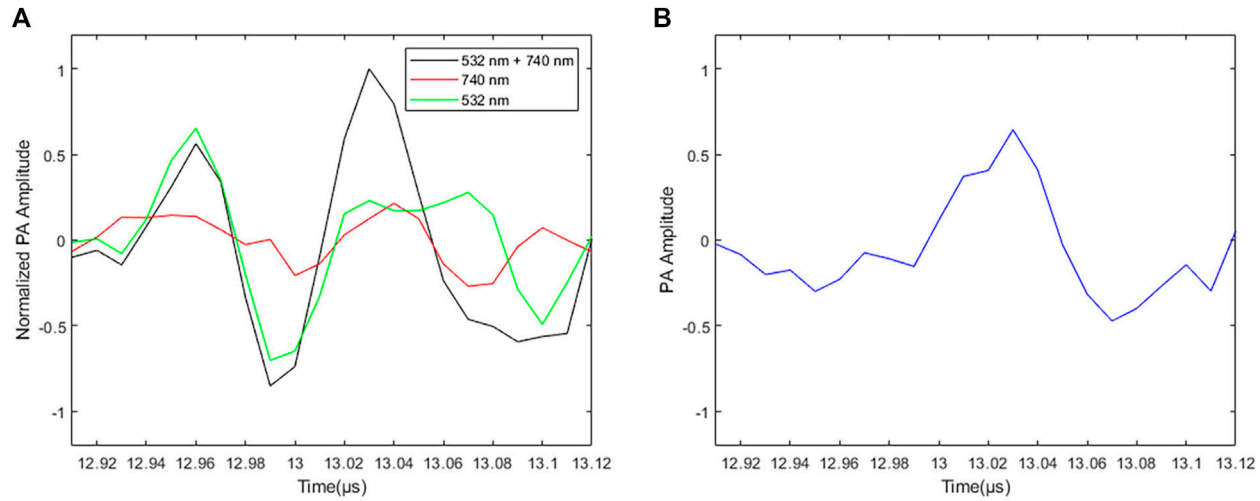

FIGURE 5 | Photoacoustic signal with 0.5 μs time delay. **(A)** Black line is the PA signal of the glass tube with PtOEP stimulated by 532 and 740 nm combined beam. Red line is the PA signal of the glass tube with PtOEP stimulated by 740 nm beam. Green line is the PA signal of the glass tube with PtOEP stimulated by 532 nm beam. **(B)** The PA signal stimulated 532 and 740 nm combined beam subtracts the PA signal stimulated by 740 nm beam and then subtracts the PA signal using 532 nm beam, which is the TTD signal.

probe pulse with 740 nm wavelength, 20 Hz repetition frequency, 5 ns pulse width, 13 mJ energy, and 2 mm beam width. The beam is focused by the lens and coupled into a quartz fiber. After the YAG laser externally triggers the DG645, DG645 generates a set of delay signals (−2, 0, 0.5, 1, 2, 4, and 8 μs) to delay the synchronous output trigger signal that controls the OPO laser to emit probe pulse. The two laser beams are directed to overlap on the target area. The ultrasonic transducer converts the acoustic signal into an electrical signal, and a digital oscilloscope is used to simultaneously observe the delays of various trigger signals amplified by the signal amplifier and the triplet state photoacoustic signals that vary with different delay times. The data are collected by a data acquisition card and analyzed by a computer.

RESULTS AND ANALYSIS

Transient Triplet Differential Signal for PtOEP

Figure 5A shows the PA signals of PtOEP excited by different wavelengths. The red line is the PA signal of the glass tube with PtOEP stimulated by 740 nm beam (PA_{740}). The green line is the PA signal of the glass tube with PtOEP stimulated by 532 nm beam (PA_{532}). The black line is the PA signal of the glass tube with PtOEP stimulated by 532 and 740 nm combined beam. The blue line is the PA signal using 532 and740 nm combined beam subtracts the PA signal stimulated by 740 nm beam and then subtracts the PA signal using 532 nm beam. This last differential PA signal is called the TTD signal ($PA_{transient}$), described as follows:

$$PA_{transient,\tau} = PA_{740+532,\tau} - PA_{532,\tau} - PA_{740,\tau}, \quad (1)$$

where τ is the pump-probe delay time:

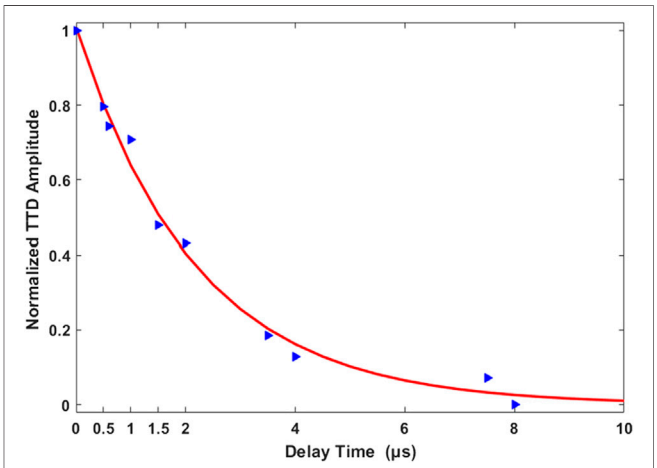

FIGURE 6 | Normalized TTD signals with varying delay times.

Because the triplet state photoacoustic signal only can be generated by the phosphorescent material, after the TTD process, the area with the phosphorescent material keeps the obvious signal (**Figure 5B**). Therefore, the obtained triplet state photoacoustic signal can be used for image reconstruction to remove the background signal.

When the excitation light is removed, the time required for the phosphorescence intensity to drop to 1/e of the maximum phosphorescence intensity during excitation is called phosphorescence lifetime; we fit the photoacoustic signals after multiple acquisitions and differentials and obtain the phosphorescence lifetime photoacoustic signal as shown in **Figure 6**. As the delay time increases, the TTD signal gradually decreases. By calculating the

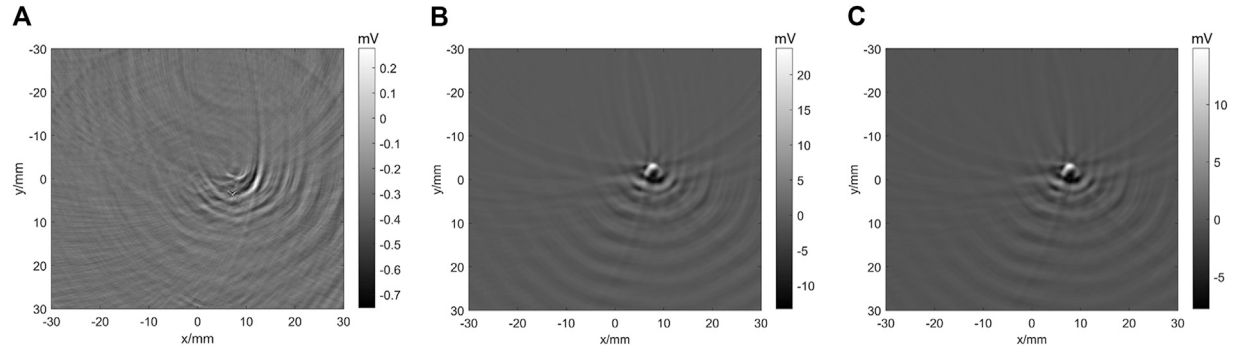

FIGURE 7 | Imaging of the TDD signal of PtOEP. **(A)–(C)** TDD signal imaging at −2, 0, and 2 μs time delay, respectively.

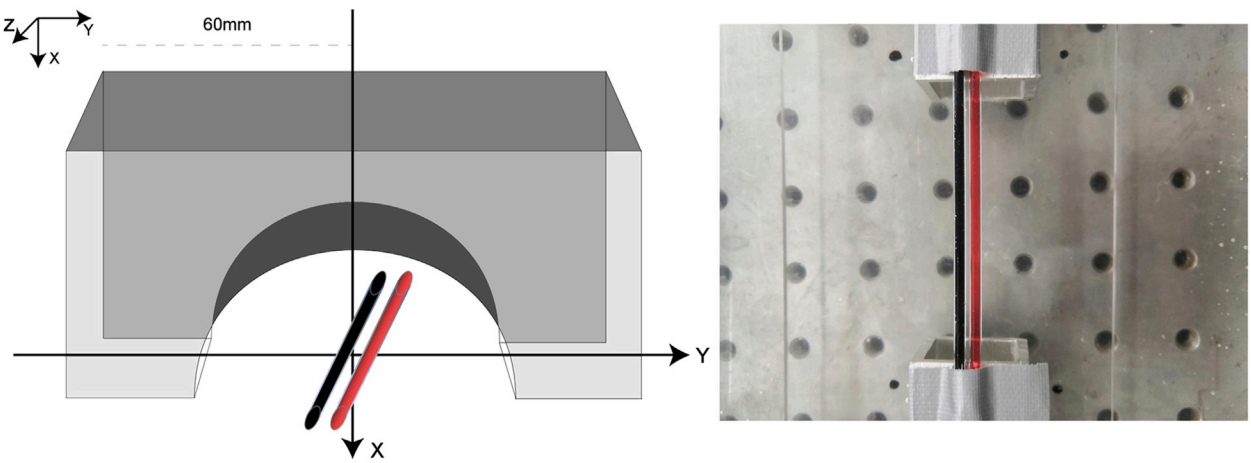

FIGURE 8 | Schematic diagram of the position of the circular array, black ink tube, and PtOEP tube.

phosphorescence lifetime according to the reference by Shaoqi (Shao et al., 2013), we collect a series of transient power amplifier signals under different pump-probe delays (τ) and fit them to an exponential decay function, as described in **Eq. 2**, and we get that the phosphorescence lifetime of PtOEP is 2.204 μs:

$$\mathrm{PA}_{transient} = \mathrm{PA}_{transient,0}\, e^{-\frac{1}{T}\tau}, \tag{2}$$

where T is the lifetime, $\mathrm{PA}_{\mathrm{transient}}$ is the transient photoacoustic signal, and $\mathrm{PA}_{\mathrm{transient},\ 0}$ is the maximum photoacoustic signal.

Transient Triplet Differential Imaging for PtOEP

Figure 7 shows the TTD imaging of PtOEP. The time delay is the period between the excitation pulse (532 nm) and probe pulse (740 nm). Minus time means the probe pulse stimulated before excitation pulse. When the time delay is −2 μs, no TTD signal can be obtained. When the time delay is 0 μs, the glass tube with PtOEP can be imaged using the semicircular ring array. As the time delay increases, the amplitude of the TTD signal decreases. The results indicate that the system and method in this study are effective for TTD imaging.

Transient Triplet Differential Imaging for Black Ink and PtOEP

In order to test the background removal ability of TTD imaging, we set a glass tube with black ink close to a tube with PtOEP (shown in **Figure 8**), the black ink with strong light absorption is widely used as the phantom of melanoma, and its absorbance at 532 nm wavelength is 3.052 and at 740 nm wavelength is 2.489. **Figure 9A** shows the PA images stimulated by 532 and 740 nm combined beam. In **Figure 9B**, we can observe the image of PtOEP because the absorption peak of PtOEP is 532 nm. In **Figure 9C**, the PA images stimulated by 740 nm are shown. Compared with the signal from black ink, the signal of PtOEP is too weak to observe. **Table 1** shows the signal amplitude of **Figure 9A**. Although the amplitude of PtOEP is 30.7718 mV, it is weak compared with the amplitude of black ink. These results imply that, even using the exogenous contrast such as PtOEP, we cannot obtain the specific molecular images with strong

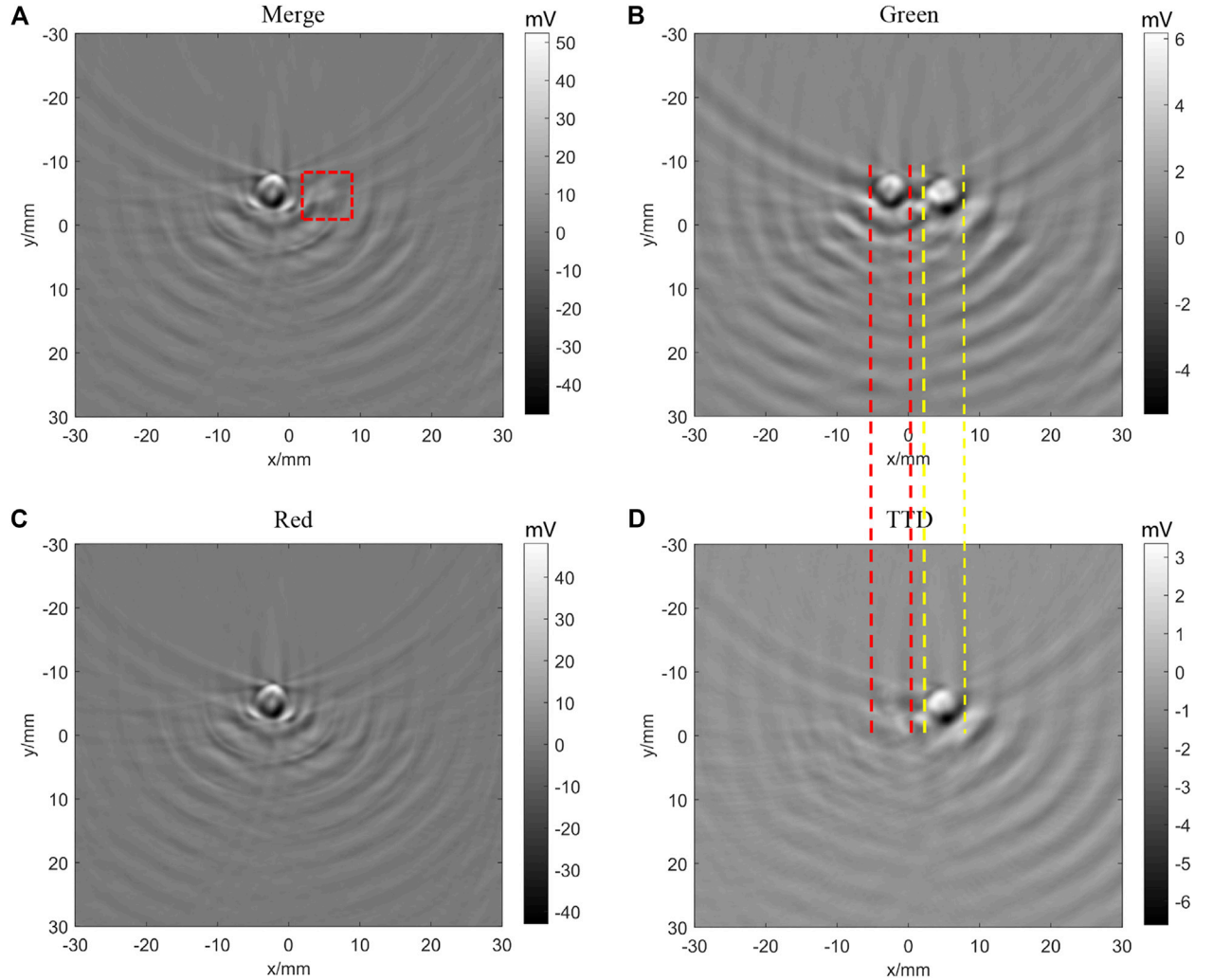

FIGURE 9 | TTD images of black ink (left) and PtOEP (right) with 0 μs time delay and 50 signal averages. **(A)** Photoacoustic image stimulated by 532 and 740 nm combined beam; the red line frame is the imaging area of PtOEP. **(B)** Photoacoustic image stimulated by 532 nm beam. **(C)** Photoacoustic image stimulated by 740 nm beam. **(D)** TTD images.

TABLE 1 | Merge image and TDD image signal value contrast.

	Merge	TTD
Black ink signal (value 1/mV)	98.9145	3.2878
PtOEP signal (value 2/mV)	30.7718	10.1934
Ratio (value 2/value 1)	0.3111	3.1003

background like melanin. **Figure 9D** shows the image after the TTD process according to **Eq. 1**, the background signal is removed successfully, and the signal of PtOEP survived. As **Table 1** shows, although the amplitude of the PtOEP signal is reduced from 30.7718 to 10.1934 mV (a reduction of about 67%), the amplitude of the strong black ink signal is reduced from 98.9145 to 3.2878 mV (a reduction of about 96%), and the ratio between PtOEP signal and black ink signal is increased from 0.3111 to 3.1003, which increases to about 10 times the previous one. Therefore, TTD imaging can successfully remove the strong background signal like black ink.

Imaging System Optimization Test

We then study the effect from signal averages. **Figure 10** shows that as the average number increases, the image intensity becomes weaker and the image quality becomes better. **Table 2** lists the signal amplitude and ratio between black ink and PtOEP. The results indicate that as the number of averages increases, the signal amplitude continues to decrease, but the ratio to the background signal continues to increase, indicating that the image signal continues to stabilize, the jitter decreases, and the signal and image are more realistic.

However, if the number of averages increases, the acquisition time will also increase. This means that more time is needed for signal acquisition, which will increase the uncertainty of the system, and due to the extension of time, the laser crystal energy will continue to decrease, which will affect the accuracy of the experiment.

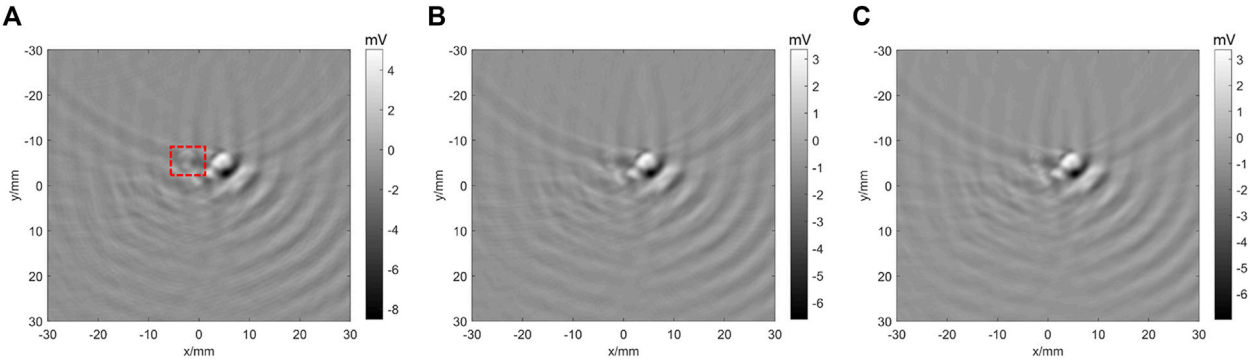

FIGURE 10 | TTD images (0 μs time delay) with different signal averages. **(A)** TTD image with 10 times signal averages; the red line frame is the imaging area of black ink. **(B)** TTD image with 50 times signal averages. **(C)** TTD image with 200 times signal averages.

TABLE 2 | TTD image signal value (0 μs time delay) with different signal averages.

	10 times	50 times	200 times
Black ink signal (value 1/mV)	4.7718	3.2878	2.2515
PtOEP signal (value 2/mV)	12.9986	10.1934	9.6715
Ratio (value 2/value 1)	2.7240	3.1003	4.2956

Based on the obtained results, we can draw the following conclusion: as the number of averaging increases, although the signal ratio continues to increase, the PtOEP signal continues to decrease, which will affect the observation of the image. In summary, choosing 50 times the average signal can not only meet the request of the imaging but also provide high contrast.

CONCLUSION

In this study, we develop a photoacoustic system with a semicircular ring array for transient triplet differential (TTD) imaging. PtOEP is used as the exogenous contrast agent and black ink was used to mimic the strong light absorption of melanin. We first obtain the TTD signal with different delay times. Then the background signal is successfully removed by TTD imaging. The ratio between PtOEP signal and black ink signal is increased to about 10 times the previous one. Besides, the effect from the signal average is studied. In summary, this study proves that the TTD method can image phosphorescent materials with strong background such as black ink which has great potential in *in vivo* molecular imaging of specific biomarkers such as protein and immune cells in melanoma.

DATA AVAILABILITY STATEMENT

The raw data supporting the conclusion of this article will be made available by the authors, without undue reservation.

AUTHOR CONTRIBUTIONS

ZC, JX, and GW contributed to the conception and design of the study. BW processed the data. TY participated in the experiment. GW wrote the first draft of the manuscript. CW, LG, and TY wrote sections of the manuscript. All authors contributed to manuscript revision and read and approved the submitted version.

FUNDING

Funding was provided by the Department of Science and Technology of Hunan Province, High-tech Industry Science and Technology Innovation Leading Program (2020SK 2003), Management Science and Technology Project of Hunan Province (2020YJ004), Central South University, Innovation Driven Program team project (2020CX004), Emergency and Fundamental Research Funds for Central Universities of the Central South University (2020zzts784).

ACKNOWLEDGMENTS

We gratefully appreciate the assistance of Lin Huang, who provided valuable discussion.

REFERENCES

Allen, T. J., Hall, A., Dhillon, A. P., Owen, J. S., and Beard, P. C. (2012). Spectroscopic Photoacoustic Imaging of Lipid-Rich Plaques in the Human Aorta in the 740 to 1400 Nm Wavelength Range. *J. Biomed. Opt.* 17, 061209. doi:10.1117/1.JBO.17.6.061209

Ashkenazi, S., Huang, S.-W., Horvath, T., Koo, Y.-E. L., and Kopelman, R. (2008). Photoacoustic Probing of Fluorophore Excited State Lifetime with Application to Oxygen Sensing. *J. Biomed. Opt.* 13, 034023. doi:10.1117/1.2927466

Berera, R., van Grondelle, R., and Kennis, J. T. M. (2009). Ultrafast Transient Absorption Spectroscopy: Principles and Application to Photosynthetic Systems. *Photosynth Res.* 101, 105–118. doi:10.1007/s11120-009-9454-y

Liu, Y., Wang, S., Ma, Y., Lin, J., Wang, H.-Y., Gu, Y., et al. (2017). Ratiometric Photoacoustic Molecular Imaging for Methylmercury Detection in Living Subjects. *Adv. Mater.* 29, 1606129. doi:10.1002/adma.201606129

Matthews, T. P., Zhang, C., Yao, D.-K., Maslov, K. I., and Wang, L. V. (2014). Label-free Photoacoustic Microscopy of Peripheral Nerves. *J. Biomed. Opt.* 19, 1016004. doi:10.1117/1.JBO.19.1.016004

Mills, A., and Lepre, A. (1997). Controlling the Response Characteristics of Luminescent Porphyrin Plastic Film Sensors for Oxygen. *Anal. Chem.* 69, 4653–4659. doi:10.1021/ac970430g

Oh, J.-T., Li, M.-L., Zhang, H. F., Maslov, K., Stoica, G., and Wang, L. V. (2006). Three-dimensional Imaging of Skin Melanoma *In Vivo* by Dual-Wavelength Photoacoustic Microscopy. *J. Biomed. Opt.* 11, 034032. doi:10.1117/1.2210907

Park, B., Bang, C. H., Lee, C., Han, J. H., Choi, W., Kim, J., et al. (2021). 3D Wide-field Multispectral Photoacoustic Imaging of Human Melanomas *In Vivo*: a Pilot Study. *J. Eur. Acad. Dermatol. Venereol.* 35, 669–676. doi:10.1111/jdv.16985

Paul, B. (2011). Biomedical Photoacoustic Imaging. *Interf. Focus.* 1, 602–631. doi:10.1098/rsfs.2011.0028

Shao, Q., Morgounova, E., Jiang, C., Choi, J., Bischof, J., and Ashkenazi, S. (2013). In Vivophotoacoustic Lifetime Imaging of Tumor Hypoxia in Small Animals. *J. Biomed. Opt.* 18, 076019. doi:10.1117/1.JBO.18.7.076019

Tan, J. W. Y., Lee, C. H., Kopelman, R., and Wang, X. D. (2018). Transient Triplet Differential (TTD) Method for Background Free Photoacoustic Imaging. *Sci. Rep.* 8, 9290. doi:10.1038/s41598-018-27578-9

Tsang, V. T. C., Li, X., and Wong, T. T. W. (2020). A Review of Endogenous and Exogenous Contrast Agents Used in Photoacoustic Tomography with Different Sensing Configurations. *Sensors* 20, 5595. doi:10.3390/s20195595

Xia, J., Huang, C., Maslov, K., Anastasio, M. A., and Wang, L. V. (2013). Enhancement of Photoacoustic Tomography by Ultrasonic Computed Tomography Based on Optical Excitation of Elements of a Full-Ring Transducer Array. *Opt. Lett.* 38, 3140–3143. doi:10.1364/OL.38.003140

Xu, M., and Wang, L. V. (2006). Photoacoustic Imaging in Biomedicine. *Rev. Scientific Instr.* 77, 041101–041598. doi:10.1063/1.2195024

Xu, M., and Wang, L. V. (2005). Universal Back-Projection Algorithm for Photoacoustic Computed Tomography. *Phys. Rev. E* 71, 016706. doi:10.1103/PhysRevE.71.016706

Yao, J., Wang, L., Yang, J.-M., Maslov, K. I., Wong, T. T. W., Li, L., et al. (2015). High-speed Label-free Functional Photoacoustic Microscopy of Mouse Brain in Action. *Nat. Methods* 12, 407–410. doi:10.1038/nmeth.3336

Zha, Z., Zhang, S., Deng, Z., Li, Y., Li, C., and Dai, Z. (2013). Enzyme-responsive Copper Sulphide Nanoparticles for Combined Photoacoustic Imaging, Tumor-Selective Chemotherapy and Photothermal Therapy. *Chem. Commun.* 49, 3455–3457. doi:10.1039/c3cc40608c

Zhang, Y., Cai, X., Choi, S.-W., Kim, C., Wang, L. V., and Xia, Y. (2010). Chronic Label-free Volumetric Photoacoustic Microscopy of Melanoma Cells in Three-Dimensional Porous Scaffolds. *Biomaterials* 31, 8651–8658. doi:10.1016/j.biomaterials.2010.07.089

Zhang, Y., and Wang, L. (2020). Video-rate Ring-Array Ultrasound and Photoacoustic Tomography. *IEEE Trans. Med. Imaging* 39, 4369–4375. doi:10.1109/TMI.2020.3017815

Zheng, S., Li, H., Lai, K., Chen, M., Fu, G., Liu, W.-H., et al. (2018). Noninvasive Photoacoustic and Fluorescent Tracking of Optical Dye Labeled T Cellular Activities of Diseased Sites at New Depth. *J. Biophotonics* 11, e201800073. doi:10.1002/jbio.201800073

Conflict of Interest: The authors declare that the research was conducted in the absence of any commercial or financial relationships that could be construed as a potential conflict of interest.

Publisher's Note: All claims expressed in this article are solely those of the authors and do not necessarily represent those of their affiliated organizations, or those of the publisher, the editors and the reviewers. Any product that may be evaluated in this article, or claim that may be made by its manufacturer, is not guaranteed or endorsed by the publisher.

frontiers in Materials

ORIGINAL RESEARCH
published: 20 October 2021
doi: 10.3389/fmats.2021.731611

Structure-Size Optimization and Fabrication of 3.7 GHz Film Bulk Acoustic Resonator Based on AlN Thin Film

Pingying Jiang[1], Shiping Mao[2], Zaifang An[3], Chunlong Fei[3], Lifei Lou[3], Zhaoxi Li[3], Tianlong Zhao[3], Shiyi Jiang[1]* and Yintang Yang[3]*

[1]The 26th Institute of China Electronics Technology Group Corporation, Chongqing, China, [2]School of Electronic Science and Engineering, University of Electronic Science and Technology of China, Chengdu, China, [3]School of Microelectronics, Xidian University, Xian, China

Traditional radio frequency filters cannot meet the demands of miniaturization, high frequency operation, integration, and broadband capacity in new-generation communication system owing to their larger volumes. A thin film bulk acoustic resonator (FBAR) is therefore suggested as an optimum solution because of its small volume and a good performance. In this study, the COMSOL multiphysics software was used to build 2 D and 3 D finite element models to analyze the harmonic characteristics of the FBAR. Based on the optimized structural parameters, the FBAR was fabricated with series resonant frequency, parallel resonant frequency, and effective coupling coefficient values of 3.705, and 3.82 GHz, and 7.4%, respectively. Compared with the simulated FBAR results, the effective coupling coefficient of the fabricated FBAR declined by only 0.1%, almost achieving the desired performance.

Keywords: FBAR, effective electromechanical coupling coefficient, AlN thin film, apodization, spurious resonance

OPEN ACCESS

Edited by:
Jianguo Ma,
Beihang University, China

Reviewed by:
Zhenghua Qian,
Nanjing University of Aeronautics and Astronautics, China
Bo Hou,
Soochow University, China

****Correspondence:***
Lifei Lou
loulifei@mail.xidian.edu.cn
Shiyi Jiang
38517560@qq.com

Specialty section:
This article was submitted to Smart Materials, a section of the journal Frontiers in Materials

Received: *27 June 2021*
Accepted: *05 August 2021*
Published: *20 October 2021*

Citation:
Jiang P, Mao S, An Z, Fei C, Lou L, Li Z, Zhao T, Jiang S and Yang Y (2021) Structure-Size Optimization and Fabrication of 3.7 GHz Film Bulk Acoustic Resonator Based on AlN Thin Film. Front. Mater. 8:731611. doi: 10.3389/fmats.2021.731611

INTRODUCTION

With the rapid advances in cellular phones, satellite navigation, cloud services, and various other forms of wireless data communication in recent times, filters have become essential to prevent interference between various forms of communication. Such filters are required to have excellent power tolerance, temperature stability, and chip integrability. Typically, several resonators are electrically connected in an appropriate manner to achieve the desired filter characteristics (Hagelauer et al., 2018).

Traditional cavity or dielectric filters usually require a large portion of the space in the circuit (Kirby et al., 2003; Voiculescu and Nordin, 2012; Zhang and Chen, 2013) and are usually the devices with the largest height on a printed circuit board. This is not suitable for the design of microsized on-chip integrated devices. The mechanical resonance frequency of a surface acoustic wave (SAW) resonator is determined by the widths of and spacing between the interdigital electrodes (Mamishev et al., 2004; Kimura et al., 2019). When the resonance frequency is higher than that of the 2G communication band, the sizes of the interdigital electrodes are too small to achieve high process accuracy, which in turn increases the ohmic loss of the device (Bhadauria et al., 2018). A thin film bulk acoustic resonator (FBAR) is a device that is realized by the acoustic resonance of a piezoelectric film in the thickness direction; the FBAR can easily achieve gigahertz or even higher frequency owing to its structural advantages. At the same time, the device is made of silicon, which enables compatibility with semiconductor technology and easy to realize device integration. In addition,

for a given device, the FBAR filter has a higher quality factor and lower loss (Warder and Link, 2015; Lee and Mortazawi, 2016; ZHAO et al., 2019), which is the optimal solution for 5G communications and operation in higher frequency bands (Hara et al., 2018).

The core element of the FBAR is a piezoelectric material, materials such as aluminum nitride (AlN), piezoelectric ceramics (PZT), and zinc oxide (ZnO) are widely used to realize resonators operating at high frequencies. (Schreiter et al., 2004; Huang et al., 2005; Joseph et al., 2018). Among them, AlN has the following advantages: low acoustic attenuation and stable chemical properties; very high velocity and appropriate technology; a fabrication process that is compatible with existing complementary metal-oxide semiconductor (CMOS) processes (Gong et al., 2018; Joseph et al., 2018).

In this study, a 3.7 GHz FBAR based on AlN was designed and fabricated. Its topology consists of an AlN layer as the piezoelectric layer, Mo as the material of the electrodes, a seed layer and a protective layer using AlN, along with Si as the substrate. This resonator is perfectly compatible with currently available semiconductor technologies, which enables easy device integration.

DESIGN AND FABRICATION OF FILM BULK ACOUSTIC RESONATOR

The inverse piezoelectric effect of the piezoelectric material can transform the electrical signals at the electrodes into mechanical resonance. Conversely, mechanical resonance can also be transformed into electric signals based on the positive piezoelectric effect. This ability of a piezoelectric material is the basis of FBAR operation to achieve conversion between acoustics and electrical signals. The FBAR can achieve resonance when an AC electrical signal is applied to the electrodes. A time-varying electric field is generated within the piezoelectric film along the thickness direction that motivates a longitudinal acoustic wave in the film to propagate along the direction of the electric field. The wave established in the piezoelectric film is reflected back and forth at the interface with a large reflection coefficient. Assuming that the acoustic velocity of the piezoelectric material is v, the mechanical resonance condition of the system can be written as follows:

$$\omega_n = (n+1)\cdot\frac{\pi}{2}\cdot\frac{v}{d}, \quad n = 0, 1, 2\ldots \tag{1}$$

where v, $2d$, and ω are the velocity, thickness, and angular frequency of the FBAR, respectively. For FBAR devices, we usually consider the fundamental frequency.

The effective coupling coefficient (K_{eff}^2) (Stoeckel et al., 2018) is an important parameter to analyze the performance of the FBAR; K_{eff}^2 characterizes the energy conversion efficiency of the piezoelectric thin films under the influence of the adjacent structures. The effective coupling coefficient of the FBAR is given by:

$$k_{eff}^2 \approx \frac{\pi^2}{4}\left(\frac{f_p - f_s}{f_p}\right) \tag{2}$$

where f_s and f_p are the series resonant and parallel resonant frequencies of the FBAR, respectively. The bandwidth of the resonator depends on the coupling coefficient. Generally, for a larger effective coupling coefficient, the bandwidth of the device is wider.

Optimization Design of Film Bulk Acoustic Resonator

In this study, the COMSOL multiphysics software was used to build a 2D finite element model of the FBAR. A schematic of the model is shown in **Figure 1** along with material and electrical boundary conditions. The material specifications of the FBAR is listed in **Table 1** (Lakin et al., 2001; Bhugra and Piazza, 2017; Nguyen et al., 2019).

Figure 2 shows the influence of the FBAR structure size on K_{eff}^2. Obviously, as the AlN film thickness increases, K_{eff}^2 first increases and then decreases, as shown in **Figure 2A**. Given a limited range, it is useful to enhance the piezoelectric properties of the piezoelectric layer. **Figure 2B** shows the influence of the thickness ratio of the piezoelectric to electrode layers on K_{eff}^2, where d_{AlN} and d_{Mo} are thicknesses of the AlN piezoelectric layer and Mo electrode layer, respectively. K_{eff}^2 is observed to increase with d_{AlN}/d_{Mo} and tends to be stable beyond a certain value. The

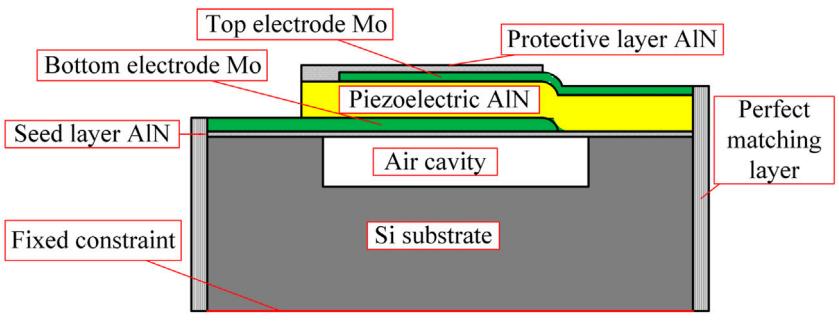

FIGURE 1 | 2D model of the FBAR.

TABLE 1 | Simulation parameters for the film of the FBAR.

Parameter	AlN	Mo	Si
Density (kg/m3)	3,260	10,200	2,181
Young's modulus (GPa)	394	312	150
Poisson ratio	0.25	0.31	0.27
Acoustic loss factor, ηs	2.5×10^{-4}	5×10^{-4}	6×10^{-5}
Dielectric loss factor, ηε	2×10^{-3}	—	—
Elastic matrix (GPa)	$\begin{pmatrix} 4.1 & 1.49 & 0.99 & 0 & 0 & 0 \\ 1.49 & 4.1 & 0.99 & 0 & 0 & 0 \\ 0.99 & 0.99 & 3.645 & 0 & 0 & 0 \\ 0 & 0 & 0 & 1.25 & 0 & 0 \\ 0 & 0 & 0 & 0 & 1.25 & 0 \\ 0 & 0 & 0 & 0 & 0 & 1.305 \end{pmatrix}$	—	—
Coupling matrix (C/m2)	$\begin{pmatrix} 0 & 0 & 0 & 0 & -4.8 & 0 \\ 0 & 0 & 0 & -4.8 & 0 & 0 \\ -0.58 & -0.58 & 1.55 & 0 & 0 & 0 \end{pmatrix}$	—	—
Dielectric constant matrix	$\begin{pmatrix} 9.21 & 0 & 0 \\ 0 & 9.21 & 0 \\ 0 & 0 & 8.9 \end{pmatrix}$	—	—

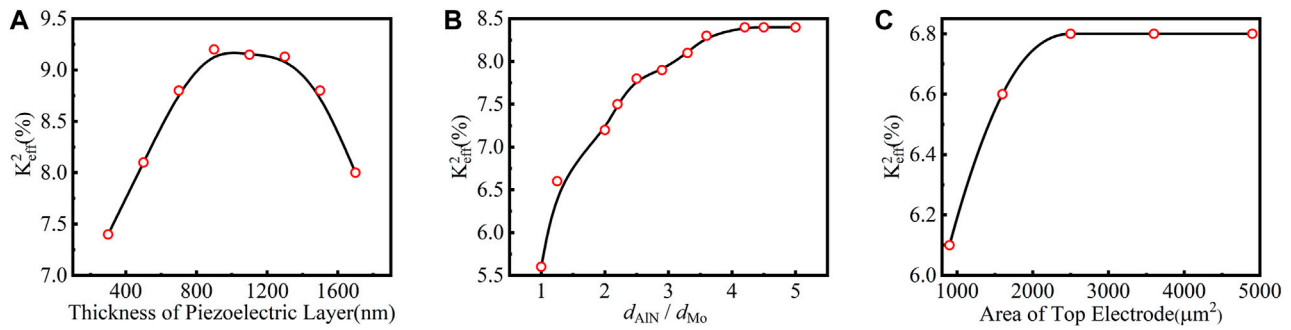

FIGURE 2 | (A) K^2_{eff} of FBAR with varying thicknesses of the piezoelectric layer; **(B)** K^2_{eff} of FBAR with varying thickness ratios of the piezoelectric to electrode layers; **(C)** K^2_{eff} of FBAR with varying areas of the top electrode.

performance of the FBAR can therefore be improved by increasing d_{AlN}/d_{Mo} appropriately. **Figure 2C** shows the influence of different top electrode areas on K^2_{eff}. The areas considered here are 900, 1,600, 2,500, 3,600, and 4,900 μm^2. The simulation results show that K^2_{eff} gradually increases and finally tends to be stable beyond a certain value of the area of the top electrode.

A 3D finite element model was established to analyze the effects of the apodization electrode on the spurious resonance of the FBAR are shown in **Figure 3**. The material and structural details of this model are the same as those of the 2D model.

The Smith chart is most often used to evaluate the impedance matching and designs of matched networks. Herein, the Smith plot also depicts the unwanted resonances or spurious modes by smaller loops. The influence of different electrode shapes on the spurious resonance of the FBAR was analyzed when the structural parameters were constant, as shown in **Figure 4**. Compared with rectangular electrodes, the triangular, apodized quadrilateral, circular, and apodized pentagonal electrodes significantly weaken the spurious resonances. This is because the apodized electrodes increases the propagation distance of the transverse Lamb wave to reduce the probability of forming spurious resonance formation by changing the direction of reflection of

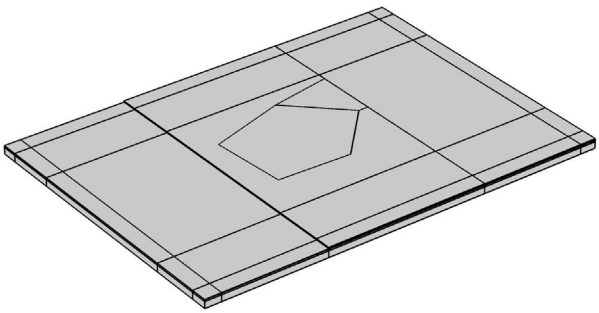

FIGURE 3 | 3D finite element model of the FBAR.

the transverse Lamb wave. The effects of the apodized pentagonal electrode on spurious resonance suppression was maximal in the simulated structures.

Table 2 shows the structural optimization parameters of the FBAR. The thickness of the Mo layer of the top electrode is 130 nm and that of the piezoelectric AlN layer is 540 nm. The lattice orientation of the bottom Mo electrode directly affects the quality of the sputtered AlN piezoelectric film. To ensure that

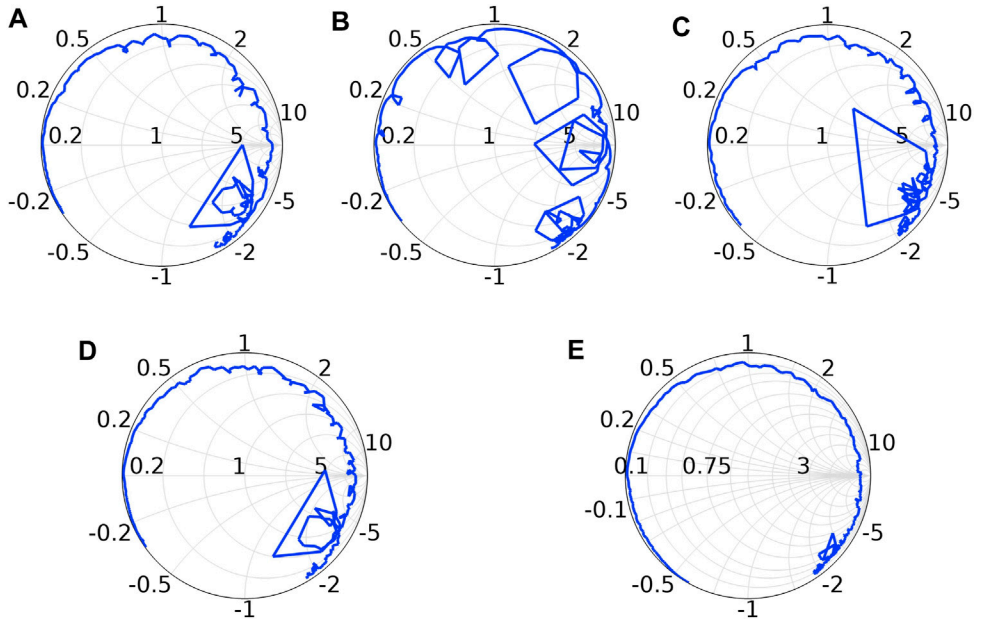

FIGURE 4 | Spurious resonances seen in the impedance Smith chart for different shapes of the top electrode: **(A)** triangle; **(B)** rectangle; **(C)** apodized quadrilateral; **(D)** circle; **(E)** apodized pentagon.

TABLE 2 | Structural optimization parameters of the FBAR.

Structures	Material	Thickness	Length	Width	Shape	Area
Protective layer	AlN	120 nm	—	180 μm	—	—
Top electrode	Mo	130 nm	—	—	Apodized pentagon	3,600 μm^2
Piezoelectric layer	AlN	540 nm	200 μm	180 μm	—	—
Bottom electrode	Mo	180 nm	175 μm	180 μm	—	—
Seed layer	AlN	50 nm	250 μm	180 μm	—	—
air cavity	—	1 μm	100 μm	180 μm	—	—
substrate	Si	10 μm	250 μm	180 μm	—	—

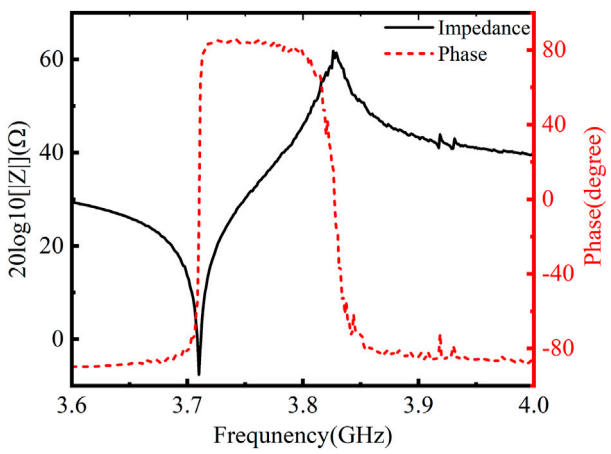

FIGURE 5 | Amplitude and phase of Z plotted for the optimized FBAR.

the bottom Mo electrode has good sputtered quality, its thickness is selected as 180 nm. The protective and seed layers are 120 and 50 nm thick, respectively. The shape of the top electrode of the FBAR is an apodized pentagon whose area is 3,600 μm^2.

The frequency response of the optimized FBAR is shown in **Figure 5**. The impedance and phase are observed to vary with frequency, and only small spurious resonances are seen near the parallel resonance point. f_s and f_p are 3.71 and 3.82 GHz, respectively, and K^2_{eff} is 7.5% based on **Eq. 2**, which agrees with the desired performance characteristics.

Experimental Fabrication

A prototype FBAR was fabricated using the optimized structural parameters. The fabrication process starts with etching the resonator cavity on a silicon substrate. Thermally oxidized silicon dioxide (SiO_2) can protect the substrate when the sacrificial layer is released. Polysilicon is then deposited using PECVD to fill the resonant cavity, next, the seed layer (50 nm)

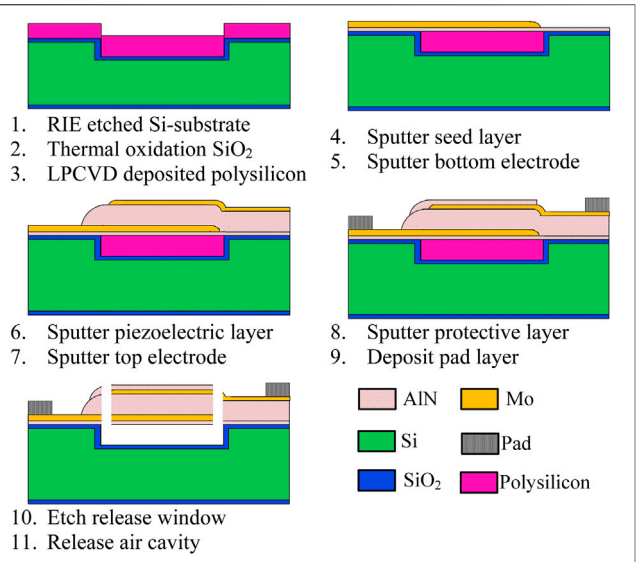

FIGURE 6 | Schematic of the fabrication process of FBAR.

and bottom electrode (180 nm) are sputtered. The former is used to induce the lattice arrangement of the upper film, and the latter is etched to form electrode patterns by ICP-RIE. The piezoelectric layer and top electrode are constructed by sputtering AlN (540 nm) and Mo (130 nm), respectively. The piezoelectric layer should meet the requirements of the c-axis orientation and have high uniformity. Then, the protective layer (120 nm) is sputtered, and the pad layer is deposited by a lift-off process. Finally, the release holes are etched using ICP-RIE, and are distributed around the resonator transducer to release gas into the resonator cavity. **Figure 6** shows the fabrication process for a single FBAR.

A photograph of the fabricated wafer of the FBAR is shown in **Figure 7A**. The scanning electron microscope (SEM) image of the cross-section of a single FBAR is shown in **Figure 7B**. The film quality of each structural layer is observed to meet the requirements, and the sacrificial material in the resonator cavity is completely released.

A microwave probe platform was used to test the fabricated FBAR. **Figure 8** shows the performance curve of FBAR. The f_s and f_p values of the FABR are 3.705 and 3.82 GHz, respectively. There is no obvious spurious resonance near the resonance point, indicating that the general index requirements of the FBAR are met.

COMPARISON AND DISCUSSION

A performance comparison between the experimental and simulated FBARs is shown in **Table 3**. The results of the microwave probe test show that small drifts are observed for the series and parallel resonant frequencies of the FBAR. The K^2_{eff} of the test data is 0.1% lower than the simulated results, thus almost achieving the desired performance.

Figure 9 shows the frequency response comparison between the simulated and test data of the FBAR. Compared with the simulation results, there were some small defects near the series resonance point in the test data. However, the simulated results were consistent with the trends of the test data. The main causes of the discrepancies are as follows:

1) The electrode may be oxidized during the fabtrication of the FBAR, thereby increasing its resistivity.
2) During the patterned etching of the electrode, the amount of etching may be too high and may cause defects.
3) Electromagnetic interference during the performance test of the FBAR may cause the observed discrepancies.

The improvement schemes for the above defects may be considered as follows:

1) Optimizing the thin-film sputtering process of the FBAR to prevent oxidation of the electrode during the fabrication process.

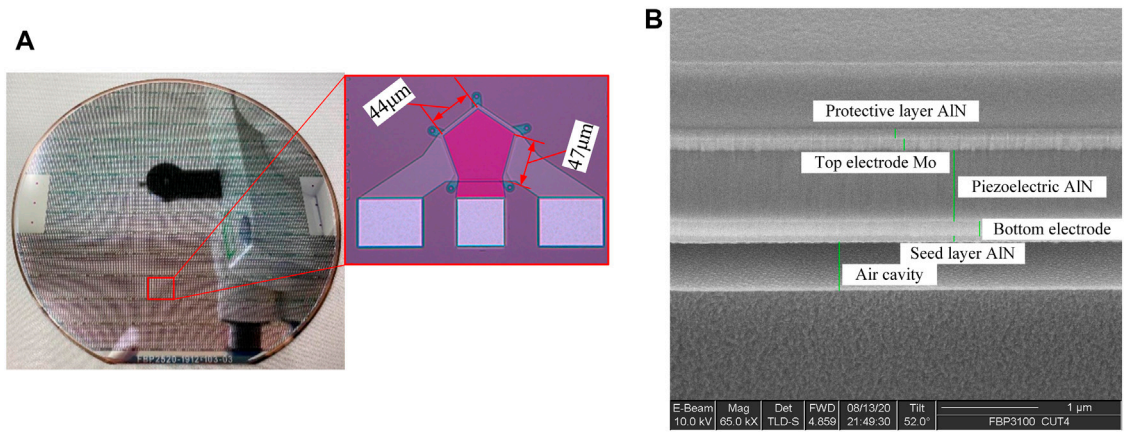

FIGURE 7 | Photographs of the fabricated FBAR: **(A)** wafer; **(B)** cross section as seen under a SEM.

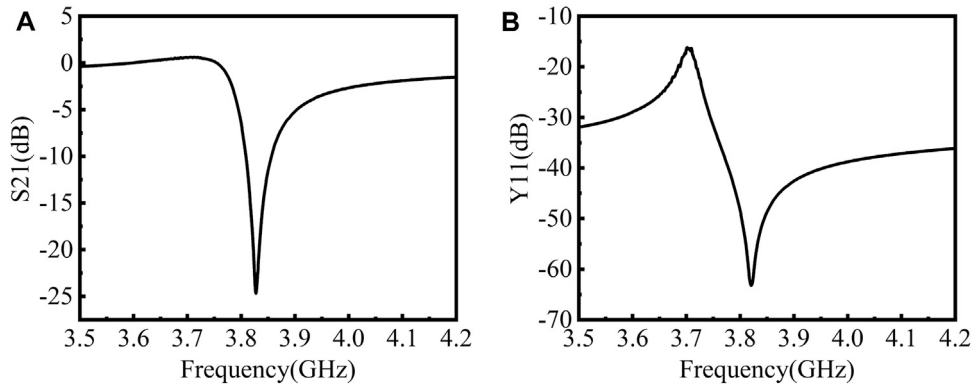

FIGURE 8 | Test results of the fabricated FBAR: **(A)** Transmission coefficient S21; **(B)** Input admittance Y11.

TABLE 3 | Performance comparison between experimental and simulated results of the FBAR.

Performance	f_s(GHz)	f_p(GHz)	K^2_{eff}(%)
Simulation	3.71	3.8263	7.5
Experiment	3.705	3.820	7.4

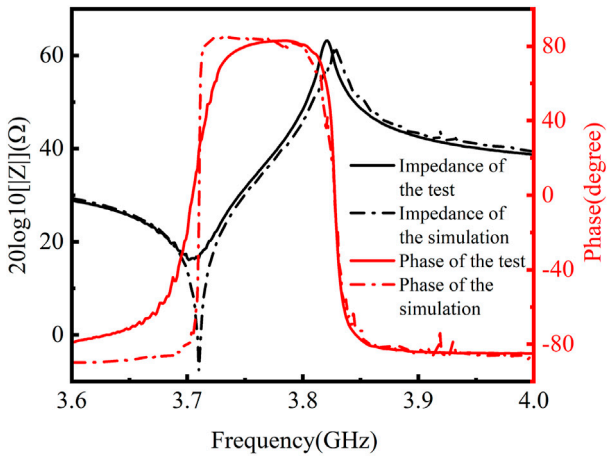

FIGURE 9 | Comparison of the test data and simulated data.

2) To reduce or even eliminate the electrode etching defects, the electrode etching process of FBAR may be optimized to improve the accuracy of electrode patterning.
3) The test process may be calibrated and corrected for errors to achieve de-embedding to overcome the influence of the external environment during the measurement process.

CONCLUSION

In this study, an FBAR was designed and fabricated. Based on 2D and 3D models, the effects of various factors on the performance of FBAR were studied, including the piezoelectric layer thickness, electrode layer thickness, and top electrode area. Using apodization technology, the spurious resonance in the frequency response curve of the FBAR is effectively suppressed. Based on the designed process flow, the FBAR was fabricated, and the SEM image of its cross section exhibited sufficient molded effect. Compared with the simulated results of the FBAR, the frequency response curve was roughly consistent with the trend of the test data, almost achieving the desired performance. Thus, a single FBAR was fabricated with a K^2_{eff} of 7.4%, f_s of 3.705 GHz, and f_p of 3.82 GHz.

DATA AVAILABILITY STATEMENT

The original contributions presented in the study are included in the article/Supplementary Material, further inquiries can be directed to the corresponding authors.

AUTHOR CONTRIBUTIONS

Conceptualization, CF; methodology, PJ, SM, and ZA; software, ZA, PJ, SM, and ZL; validation, CF, PJ, SJ, LL, TZ, and SM; investigation, PJ, SM, and ZA; resources, CF, SJ, and YY; data curation, SM, PJ, and CF; writing—original draft preparation, PJ and ZA; writing—review and editing, CF, SJ, SM, and LL; fabrication PJ, SM, and SJ; supervision, CF, SJ, and LL; project administration, LL and TZ; funding acquisition, CF, SJ, and YY. All authors have read and agreed to the published version of the manuscript.

FUNDING

This work was supported by the Key Projects of National Defense Basic Research Program of National Defense Science and Industry Administration (No: JCKY2019210B003) and the Fundamental Research Funds for the Central Universities (No: XJS211105, JBF211103).

REFERENCES

Bhadauria, A., Panchal, B., and Varghese, S. (2018). "RF Bandpass Filters Using FBAR with Fractal Electrodes," in 2018 IEEE MTT-S International Microwave and RF Conference (Kolkata, India: IMaRC), 1–3. doi:10.1109/IMaRC.2018.8877300

Bhugra, H., and Piazza, G. (2017). *Piezoelectric MEMS Resonators*. Berlin, Germany: Springer International Publishing. doi:10.1007/978-3-319-28688-4

Gong, D., Cai, H., Xia, Y., Ma, S., Liu, H., Chiu, Y., and Jin, Y. (2018). "Fabrication and Characterization of AlN Based Piezoelectric Micromachined Ultrasonic Transducer for Contact Sensing," in 2018 19th International Conference on Electronic Packaging Technology (ICEPT), 1442–1447. doi:10.1109/ICEPT.2018.8480577

Hagelauer, A., Fattinger, G., Ruppel, C. C. W., Ueda, M., Hashimoto, K.-y., and Tag, A. (2018). Microwave Acoustic Wave Devices: Recent Advances on Architectures, Modeling, Materials, and Packaging. *IEEE Trans. Microwave Theor. Techn.* 66 (10), 4548–4562. doi:10.1109/TMTT.2018.2854160

Hara, M., Yano, Y., Ito, H., Toda, M., Ono, T., Kajita, M., Hara, S., Kasamatsu, A., and Ido, T. (2018). "FBAR Oscillator Stabilized by Rb Atomic Resonator for SHF/EHF-band Wireless Devices," in 2018 IEEE International Ultrasonics Symposium (Kobe, Japan: IUS), 1–9. doi:10.1109/ULTSYM.2018.8579685

Huang, C. L., Tay, K. W., and Wu, L. (2005). Fabrication and Performance Analysis of Film Bulk Acoustic Wave Resonators. *Mater. Lett.* 59 (8-9), 1012–1016. doi:10.1016/j.matlet.2004.11.047

Joseph, J., Singh, S. G., and Vanjari, S. R. K. (2018). Piezoelectric Micromachined Ultrasonic Transducer Using Silk Piezoelectric Thin Film. *IEEE Electron. Device Lett.* 39 (5), 749–752. doi:10.1109/LED.2018.2816646

Kimura, T., Omura, M., Kishimoto, Y., and Hashimoto, K. (2019). Comparative Study of Acoustic Wave Devices Using Thin Piezoelectric Plates in the 3-5-GHz Range. *IEEE Trans. Microwave Theor. Techn.* 67 (3), 915–921. doi:10.1109/TMTT.2018.2890661

Kirby, P. B., Potter, M. D. G., Williams, C. P., and Lim, M. Y. (2003). Thin Film Piezoelectric Property Considerations for Surface Acoustic Wave and Thin Film Bulk Acoustic Resonators. *J. Eur. Ceram. Soc.* 23 (14), 2689–2692. doi:10.1016/S0955-2219(03)00147-X

Lakin, K. M., Belsick, J., McDonald, J. F., and McCarron, K. T. (2001). "Improved Bulk Wave Resonator Coupling Coefficient for Wide Bandwidth Filters," in 2001 IEEE Ultrasonics Symposium. Proceedings. An International Symposium (Cat. No.01CH37263) (Atlanta, GA, USA: IEEE), 827–831. doi:10.1109/ULTSYM.2001.991848

Lee, S., and Mortazawi, A. (2016). "BAW Filter Design Method Based on Intrinsically Switchable Ferroelectric BST FBARs," in 2016 IEEE MTT-S International Microwave Symposium (San Francisco, CA, USA: IMS), 1–4. doi:10.1109/MWSYM.2016.7540105

Mamishev, A. V., Sundara-Rajan, K., Yang, F., Du, Y., and Zahn, M. (2004). Interdigital Sensors and Transducers. *Proc. IEEE* 92 (5), 808–845. doi:10.1109/JPROC.2004.826603

Nguyen, N., Johannessen, A., Rooth, S., and Hanke, U. (2019). The Impact of Area on BAW Resonator Performance and an Approach to Device Miniaturization. *Ultrasonics* 94, 92–101. doi:10.1016/j.ultras.2018.11.014

Schreiter, M., Gabl, R., Pitzer, D., Primig, R., and Wersing, W. (2004). Electro-acoustic Hysteresis Behavior of PZT Thin Film Bulk Acoustic Resonators. *J. Eur. Ceram. Soc.* 24, 1589. doi:10.1016/S0955-2219(03)00406-0

Stoeckel, C., Meinel, K., Melzer, M., and Otto, T. (2018). "Thin Film Piezoelectric Aluminum Nitride for Piezoelectric Micromachined Ultrasonic Transducers," in 2018 IEEE SENSORS (New Delhi, India: IEEE), 1–4. doi:10.1109/ICSENS.2018.8589845

Voiculescu, I., and Nordin, A. N. (2012). Acoustic Wave Based MEMS Devices for Biosensing Applications. *Biosens. Bioelectron.* 33 (1), 1–9. doi:10.1016/j.bios.2011.12.041

Warder, P., and Link, A. (2015). Golden Age for Filter Design: Innovative and Proven Approaches for Acoustic Filter, Duplexer, and Multiplexer Design. *IEEE Microwave* 16 (7), 60–72. doi:10.1109/MMM.2015.2431236

Zhang, Y., and Chen, D. (2013). *Multilayer Integrated Film Bulk Acoustic Resonators*. Berlin: Springer.

Zhao, X.-l., Zhao, Z.-n., and Qian, Z.-h. (2019). "Structural Optimization for Uniform Displacement Variations in ZnO FBAR Mass Sensor Using Rectangular Frame-like Driving Electrodes," in 2019 14th Symposium on Piezoelectricity, Acoustic Waves and Device Applications (Shijiazhuang, China: SPAWDA), 1–4. doi:10.1109/SPAWDA48812.2019.9019224

Conflict of Interest: Author PJ is employed by the 26th Institute of China Electronics Technology Group Corporation.

The remaining authors declare that the research was conducted in the absence of any commercial or financial relationships that could be construed as a potential conflict of interest.

frontiers in Materials

REVIEW
published: 18 January 2022
doi: 10.3389/fmats.2021.733358

A Review of UltraHigh Frequency Ultrasonic Transducers

Jun Chen[1], Chunlong Fei[1], Danmei Lin[1], Pengkai Gao[1], Junshan Zhang[2], Yi Quan[3], Dongdong Chen[1], Di Li[1] and YinTang Yang[1]*

[1]School of Microelectronics, Xidian University, Xian, China, [2]School of Equipment Management and Support, University of People's Armed Police, Xi'an, China, [3]School of Xi'an Jiaotong University, Xian, China

The ultrahigh-frequency (UHF) ultrasonic transducers are active in various fields, including nondestructive evaluation in the semiconductor industry, microscopic biological organization imaging in biomedicine, particle manipulation, and so on. In these fields ultrahigh-frequency (UHF) ultrasonic transducers play a critical role in the performance of related equipment. This article will focus on the topic of ultrahigh-frequency ultrasonic transducers' preparation, and reviews three aspects: material selection, focus design, and acoustic energy transmission matching. Provides a summary of the current research status, and puts forward some views on the future development of UHF ultrasound devices.

Keywords: ultrahigh frequency, ultrasonic transducer, piezoelectric material, MEMS technology, acoustic lens, scanning acoustic microscope

OPEN ACCESS

Edited by:
Marcelo J Dapino,
The Ohio State University,
United States

Reviewed by:
Venu Gopal Madhav Annamdas,
Continental, Germany
Tianhong Yan,
China Jiliang University, China

****Correspondence:***
Chunlong Fei
clfei@xidian.edu.cn

Specialty section:
This article was submitted to Smart Materials, a section of the journal Frontiers in Materials

Received: *30 June 2021*
Accepted: *26 October 2021*
Published: *18 January 2022*

Citation:
Chen J, Fei C, Lin D, Gao P, Zhang J, Quan Y, Chen D, Li D and Yang Y (2022) A Review of UltraHigh Frequency Ultrasonic Transducers. Front. Mater. 8:733358. doi: 10.3389/fmats.2021.733358

INTRODUCTION

As an energy conversion device, the ultrasonic transducer can convert electrical energy into sound energy. Ultrasonic transducers excited by different working frequencies can emit ultrasonic waves of different frequencies. KHz-level ultrasound is generally used for large-scale and long-distance detection, like underwater sonar. In 1–10 MHz, the ultrasonic transducer of this frequency band is usually used in the field of large-size parts non-destructive testing. Up to 100 MHz, medical high-frequency ultrasound is roughly distributed in this frequency range. When it is greater than 100 MHz, it is usually collectively referred to as UHF. The UHF ultrasonic transducer can emit ultra-small wavelength ultrasonic waves because of its extremely high center frequency, which makes it a core component in the high-resolution imaging equipment- Scanning Acoustic Microscope (SAM) (**Supplementary Figure S1**). SAM (Makra et al., 2020)is widely used in non-destructive testing, biological microstructure imaging (Fei et al., 2016; Zhang et al., 2017), and biological cell research (Weiss et al., 2007). Moreover, acoustic tweezers (**Supplementary Figure S1**) based on ultra-high frequency ultrasound transducers (Chen et al., 2017; Lim and Shung, 2017) can be used for the manipulation of very small particles, and have great application value in single-cell research and micro-assembly. Therefore, the preparation of UHF ultrasonic transducers is extremely important.

This article will introduce three important aspects in the preparation process of high-frequency ultrasonic transducers. *Introduction* section introduces different materials for UHF transducer and analysis their advantages and disadvantages. *Material Selection of Ultrasound Generation* section present various transducer focus method and emphasize the difference between the low-frequency lens and high-frequency lens. *Focusing Design of Ultrasonic Emission Energy* section describes the acoustic energy transmission matching problem and mentions a new type of metal-polymer structure matching layer for the UHF ultrasonic transducer.

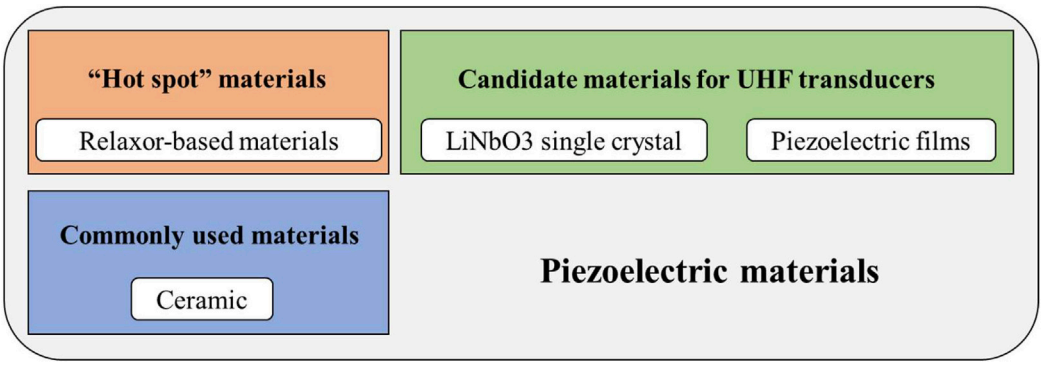

FIGURE 1 | Block diagram of Material selection.

MATERIAL SELECTION OF ULTRASOUND GENERATION

Description of This Section

There are many types of piezoelectric materials. It is necessary to have a general understanding of the existing materials for choosing piezoelectric materials suitable for preparing ultra-high frequency ultrasonic transducers. As shown in **Figure 1**, this section mainly introduces four types of well-known piezoelectric materials. The first type is piezoelectric ceramics, which have long development history and widespread application in various fields for low-cost, good piezoelectric properties. The second class is relaxor-based materials. Whether ceramic or single crystal is the hot research direction of many materials scholars for the advantages of excellent piezoelectric constant and electromechanical coupling coefficient. The third is single-crystal materials, among which LiNbO3 have been many successful cases in the preparation of ultra-high frequency ultrasonic transducers. So it is an optional material; the fourth is piezoelectric film. With the development of MEMS technology, its preparation process has become more and more mature. The convenience of piezoelectric materials' thickness control makes it act a key development direction in UHF transducers' preparation in the future. The follow-up of this section will describe the four materials in terms of their applicability in ultra-high frequency ultrasonic transducer devices' preparation.

Ceramic

Ceramic is a polycrystalline structure composed of many crystal grains of different sizes, and the crystal grains of the same orientation form crystal domains together. Due to the random orientation of the ceramic's crystal domains, from a macroscopic point of view, the ceramic is isotropic, so it was initially considered to have no piezoelectricity, but we can rearrange the crystal domains through polarization to make ceramics piezoelectric. This discovery also led to the rapid development of ceramics in the application of piezoelectric ultrasonic transducers. In 1991, a miniature PZT ceramic high-frequency ultrasonic transducer (20–80 MHz) was reported (Foster et al., 1991) with a center frequency of 45 MHz and a thickness of 48 um. The grain size of ceramics (**Supplementary Figure S2**) is usually unevenly distributed in a few microns or tens of microns (Randall et al., 1998; Haertling, 1999; Kong et al., 2000; Pérez et al., 2005; Kamel and de With, 2008; Sangsubun et al., 2008), this is very close to the thickness of piezoelectric materials. In the process of lapping the ceramic material to the specified thickness, as the material thickness gradually approaches the grain size, its mechanical strength will be significantly reduced, and the material will become fragile. The material may fall off in the form of grains resulting in poor material uniformity. The piezoelectric performance of the target material obtained in this way will greatly reduce, and it may even become unpredictable. This is a fatal weakness that prevents them from being used in UHF devices' production.

Relaxor-Based Materials

Ceramics based on PZT solid solutions have low production costs and good piezoelectric properties. They have been occupying the choice of ultrasonic transducers for many years. Until the emergence of relaxor-based materials, this situation has been broken. Since then, it has been a hot research direction because of their extremely high piezoelectric constant d33 (Park and Shrout, 1997b) and electromechanical coupling coefficient kt (Park and Shrout, 1997a). The performance parameters of several materials are shown in **Table 1** (Chen et al., 2014). Due to the similarities in the properties of different materials in this category, only a few representative materials are listed here.

It can be seen from the table that most relaxor-based materials have d33 as high as 2000 or even greater, and the max kt is higher

TABLE 1 | Performance parameters of relaxor-based materials-thickness vibration mode.

	Cut	d_{33}(pC/N)	k_t	ε_{33}
PZN	001	1,100	0.49	3,600
PZN-0.08 PT	001	2070	0.48	4,200
PMN-0.28 PT	001	2,365	0.63	1,032
PIN-0.40PMN-o.33 PT	001	2,742	0.59	659

than 0.60. Piezoelectric performance is excellent, but the speed of sound of this type of material is usually not high, which will cause the thickness of the material to be thinner under the same center frequency requirement. This will greatly increase the difficulty of processing, and even cannot be manufactured. In addition, the high dielectric constant of the relaxor ferroelectric will make the area of the piezoelectric unit that meets the 50-ohm impedance matching too small, which will greatly increase the difficulty of machining and will also affect the ultrasonic emission intensity. Therefore, although the relaxor ferroelectric has excellent piezoelectric properties, it is not a suitable choice for the preparation of ultra-high frequency ultrasonic transducers due to the limitation of other factors.

LiNbO3 Single Crystal

Since it was invented by Jan Czochralski in 1916 (Uecker, 2014), the growth of bulk single crystals technique (Czochralski Method) has been widely spread and developed, and then the Bridgman method (Chen et al., 2003) using crucibles to prepare single crystals was reported. This method can effectively ensure that the raw material composition ratio is affected by the external environment. Subsequently, based on these two methods, many new preparation methods have been introduced through process improvement. The continuous maturity of single crystal preparation technology has also promoted the research and development of single crystals.

Single crystal has a very high piezoelectric constant d33 and electromechanical coupling coefficient kt, making it a promising candidate for making high-performance transducers. Moreover, unlike polycrystalline ferroelectric ceramics, single crystals are not limited by factors such as crystal grains and porosity and have the potential to produce ultra-high frequency transducers. The grown large-size single-crystal generally needs to be cut into the plate, single crystal has a crystallographic axis, and the cutting direction affects the piezoelectric performance of the single crystal. Different device performance requirements corresponding to different cutting types. A plate cut with its surface perpendicular to the *x*-axis of a crystal is called x-cut, and the same as other axes.

LiNbO3 single crystal with relatively high acoustic velocity, excellent piezoelectric properties, and small dielectric constant, have advantages in manufacture high frequency and large aperture ultrasonic transducers. For better piezoelectric property, we usually choose 36° Y-cut LiNbO3 as the transducer's piezo layer. The detail parameters include thickness mode electromechanical coupling, dielectric permittivity, longitudinal wave velocity is about 0.49, 39, 7,340 m/s, respectively. To make UHF transducers based on LiNbO3, we need to lap it to a few microns, which can be achieved in theory, but the process is quite difficult. To meet the requirements of high-resolution imaging of biological microstructures, Chunlong Fei (Fei et al., 2016) prepared a 100–300 MHz UHF ultrasound transducer. As shown in **Supplementary Figure S3**, you can see on the left that the thickness of the piezoelectric layer of the 300 MHz LN UHF ultrasound transducer is only 9 um, the UBM ultrasound scan image of zebrafish eye on the right, the internal structure of the eye can be distinguished.

As shown in **Figure 2**, Hae Gyun Lim and K. Kirk Shung (Lim and Shung, 2017) prepared an LN piezoelectric layer with a thickness of 7.1 um and used a focus design to generate a UHF probe capable of emitting a 6.5 um width beam. The UHF transducer has a center frequency of up to 400 MHz, which achieves Acoustic tweezers capture a single red blood cell (~7.5 um). Xiaoyang Chen (Chen et al., 2017) used a 6um thick LN to prepare an ultra-high frequency ultrasonic transducer with a resonant frequency of 526 MHz, and achieved selective acoustic tweezers for particles in the range of 3–10 um by changing the excitation, as shown in **Figure 2**.

Although there have been reports of the above-mentioned UHF LN single-crystal devices, it is still extremely difficult to control the thickness of LN materials of a few microns. The preparation process requires a lot of time and effort, and with the further increase of the center frequency, the degree of difficulty may be more than a simple linear increase, so to increase the upper limit of UHF ultrasonic transducers, new materials are needed to provide the feasibility of extremely low thickness control.

Piezoelectric Films

With the development of MEMS technology, piezoelectric film manufacturing technology has also made great progress, which provides a new choice for piezoelectric materials for ultra-high frequency ultrasonic transducers. Films based on traditional ferroelectric materials have excellent piezoelectric properties and mature thickness control technology. So far, many researchers have done a lot of work in this area. As early as 1997, DA Barrow produced a 60um thick PZT film through the sol-gel method (Barrow et al., 1997). This method firstly disperses PZT particles into a PZT sol-gel matrix to achieve a 0–3 ceramic/ceramic composite. Then the ceramic/ceramic composite is spin-coated and distributed on the silicon substrate, followed by sintering and annealing, repeat the above steps layer by layer until the specified thickness is reached. As shown in **Supplementary Figure S4**, it is a 20 um PZT film coated with ten layers. The PZT films prepared by this method have a good piezoelectric constant d33 = 325pC/N.

Subsequently, many UHF transducer devices based on PZT films were published. In 2006, P Marechal improved the sol-gel and introduced a vacuum precursor solution filling method to improve the quality of the film. A 13 um thick PZT film was fabricated on the Pt-substrate, with this film, a 103 MHz ultra-high frequency ultrasonic device was fabricated (Marechal et al., 2006). The pulse-echo test results are shown in the upper part of **Supplementary Figure S5**. The -6 dB bandwidth reaches 70%, and the pulse-echo waveform is also relatively beautiful. Then in 2008, BP Zhu grew PZT films by a ceramic powder/sol-gel solution modified composite method, and prepared a 156 MHz PZT films transducer (Zhu et al., 2008) with a -6 dB bandwidth of 50%, as shown in **Supplementary Figure S5**, the bottom left is the experimental measurement results and the bottom right is the simulation result of PiezoCAD.

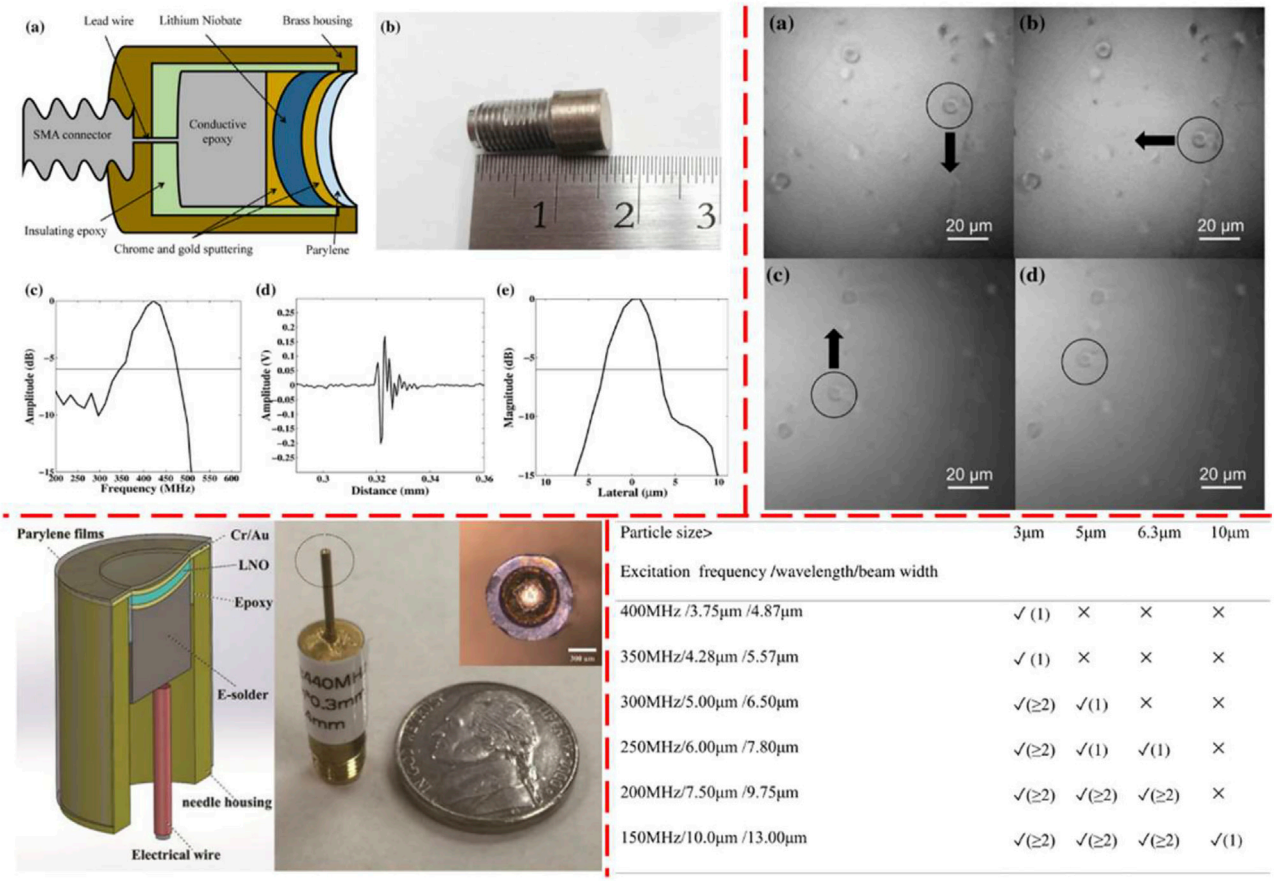

Particle size>	3μm	5μm	6.3μm	10μm
Excitation frequency /wavelength/beam width				
400MHz /3.75μm /4.87μm	√ (1)	×	×	×
350MHz/4.28μm /5.57μm	√ (1)	×	×	×
300MHz/5.00μm /6.50μm	√(≥2)	√(1)	×	×
250MHz/6.00μm /7.80μm	√(≥2)	√(1)	√(1)	×
200MHz/7.50μm /9.75μm	√(≥2)	√(≥2)	√(≥2)	×
150MHz/10.0μm /13.00μm	√(≥2)	√(≥2)	√(≥2)	√(1)

FIGURE 2 | 400 MHz ultra-high frequency ultrasonic transducer structure and performance **(top left)**; 500 MHz ultra-high frequency ultrasonic transducer structure **(bottom left)**; red blood cell acoustic tweezers capture process under microscope **(top right)**; acoustic tweezers capture particles under different excitation results **(bottom right)**.

PiezoCAD is a simulation software derived from the KLM model. When the frequency is not particularly high, the simulation results are still relatively close, but when the frequency continues to increase, many factors that are difficult to consider are introduced by high frequency. The aspects involved in the KLM model may not be enough to ensure the accuracy of the simulation. It seems that the deviation is not particularly large here. The simulation results can still play a certain reference role. In the UHF frequency, the results of simulation through finite element calculation, such as PZFlex, COMSOL, and other software, are relatively more reliable, but as the frequency increases, the simulation time will also increase significantly. XY Chen combined composite ceramic sol-gel film technique with sol-infiltration technique and fabricated up to 300 MHz 0–3 composite PZT films transducer (Chen et al., 2016), the center frequency of 300-MHz is the highest value in a PbTiO3 based ceramic ultrasonic transducers ever reported (**Supplementary Figure S6**).

In consideration of environmental protection, lead-free material films have also been added to the research on the preparation of UHF transducers. ST Lau has done a series of UHF transducer preparations based on lead-free piezoelectric films, the result shown in **Supplementary Figure S7** (Lau S.-t. et al., 2010; Lau S. T. et al., 2010; Lau et al., 2011). K H Lam studied KNN/BNT ultra-high frequency ultrasonic transducer devices in the frequency range of 170–320 MHz. Pulse echo is shown in **Supplementary Figure S8** (Lam et al., 2013b).

The traditional bulk piezoelectric relaxor ferroelectric material has attracted the attention of many researchers due to its extremely high piezoelectric constant and dielectric constant. It has also been seen in the application of film materials. PMN-PT film is considered to can replace the PZT film, but its extremely high dielectric constant will make it difficult to control the ultrasonic transducer device during electrical impedance matching. A feasible solution is to use a composite sol-gel method to composite PMN- PT and PZT according to a certain mixing ratio, then made them into xPMN-PT-(1-x)PZT film (Hsu et al., 2012). While retaining high piezoelectric performance, the dielectric constant is adjusted to a controllable range, such as **Supplementary Figure S9**, on the left is the change in dielectric constant, and on the right is the pulse-echo waveform of an ultra-high frequency transducer made

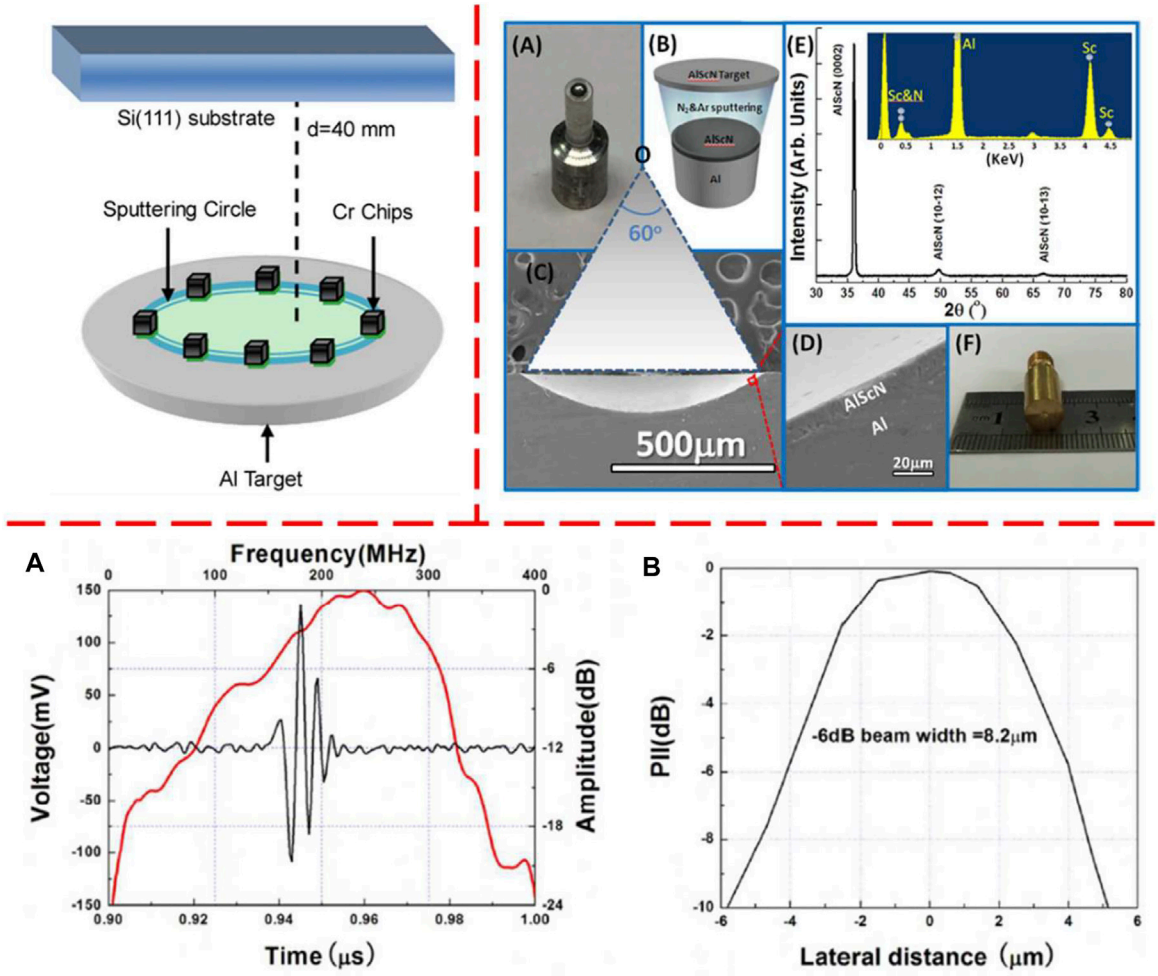

FIGURE 3 | Schematic drawing of the Cr doping sputtering system **(top left)**; preparation of Cr-doped AlN UHF Ultrasonic Transducer **(top right)**; Time-domain pulse/echo response (black line) and frequency spectrum (red line) and resolution of Cr-doped AlN UHF Ultrasonic Transducer **(bottom)**.

of 0.9PMN-PT–0.1PZT composite film. In addition to material composition, it is also a commonly used material modification method to change the crystallographic properties and microstructure of materials through particle doping and to change material properties. These two methods can be combined to provide more possibilities for UHF transducer materials. HS Hsu further adjusted the performance of the xPMN-PT-(1-x)PZT composite film through Ag doping (Hsu et al., 2013) and successfully fabricated an ultra-high frequency ultrasonic transducer device. The results are shown in **Supplementary Figure S10**.

The overall performance of the thin film prepared by the traditional ferroelectric materials has declined, but it is still related to the electrical performance of the bulk material. Furthermore, the particle doping and material composite can be used in the thin film, which will improve the performance of the material. However, there are also shortcomings. The high temperature during the film densification and annealing process cannot be withstood by other materials in the ultrasonic transducer. As a result, the growth of the piezoelectric film is not completely compatible with the manufacturing process of the transducer, and secondary processing operations are usually required for the grown film. It is very difficult to operate a film of several microns, which will greatly affect the repeatability of the preparation of the transducer, the consistency cannot be guaranteed, and the process complexity is high, which is not conducive to mass production.

The semiconductor industry is developing rapidly, and its mature MEMS technology provides a new path to produce UHF transducers. Using ZnO and AlN, which are commonly used in semiconductors, to replace traditional ferroelectric materials to

TABLE 2 | Material parameters of transducer design.

Dielectric properties	Piezoelectric properties	Acoustic properties
$C = \frac{\varepsilon_{33} A}{t}$	$k_t^2 = \frac{e_{33}^2}{c_{33}\varepsilon_{33}}$, d_{33}	$Z_P = \rho c_m$, $f = n\frac{c_m}{2t}$

TABLE 3 | Material analysis summary.

	Advantage	Shortcoming	UHF devices applicability
Ceramic	Low cost, complete variety, good piezoelectric performance	Grain size limitation	No, the material has limitations
Relaxor-based materials	Excellent piezoelectric performance	Large dielectric contant makes impedance (50 Ω) matching difficult, sound velocity is not large enough	No it's difficult to fabricate
LiNbO3 single crystal	Good piezoelectric performance, large sound velocity, no grain size limitation, small dielectric constant	Difficult to realize precise thickness control	Yes, but there is a frequency limit, and it is difficult to reach more higher frequency
Ferroelectric films	Good piezoelectric performance, precise thickness control	Poor compatibility between material growth and transducer preparation	Yes, but manufacturing repeatability needs to be improved
Semiconductor films	Mature technology, precise thickness control	Poor piezoelectric performance	Yes, but material performance needs to be improved

prepare ultra-high frequency ultrasonic transducers, its consistency and reliability will be better in terms of process realization. But in terms of material piezoelectric properties, ZnO and AlN are far inferior to traditional ferroelectric materials. It is also necessary to improve the performance of the material by doping. For example, the piezoelectric constant of AlN piezoelectric film sputtered by Cr doping (Luo et al., 2009) will be improved to a certain extent, as shown in **Figure 3**. E Wistrela also mentioned that XRD and surface topography analysis (Wistrela et al., 2018) can as a straightforward approach to estimate the piezoelectric activity of Cr doped AlN thin films. K San reported a 40–80 MHz Cr-doped AlN ultrasonic transducer (Sano et al., 2018). BP Zhu reported a 200 MHz Cr-doped AlN ultra-high frequency ultrasonic transducer (Zhu et al., 2017), the preparation of the transducer is shown in the upper right of **Figure 3**, the pulse-echo and resolution are shown in **Figure 3** bottom left.

The latest research report that introduces Yb into aluminum nitride (AlN) leads to a large enhancement in the material's piezoelectric response (d33). The maximum d33 is calculated to be over 100 pC/N, which is 20 times higher than that of AlN(Hirata et al., 2021). However, there are no reports of successful preparation of devices from related materials.

Summary of This Section

The selection of piezoelectric materials is the most critical step in the preparation of ultrasonic transducer devices. The choice of materials needs to be considered from two major aspects. One aspect is the process, which determines whether the material can successfully fabricate UHF devices. The thickness of the piezoelectric material is usually half a wavelength at the working frequency. When the working frequency is up to the ultra-high frequency, the thickness control of the piezoelectric material of a few microns is a big problem. Therefore, when selecting the material, it is necessary to consider its growth process, processing difficulty, and whether it can be better compatible with the preparation process of the transducer device to ensure the stability of the preparation process of the transducer. Another aspect is the performance of the material, which determines the final device performance. The parameters

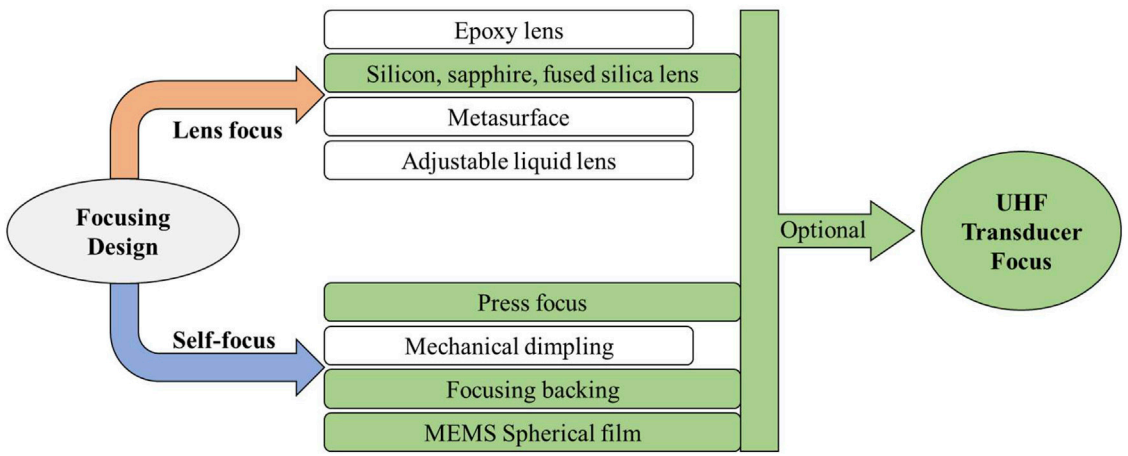

FIGURE 4 | Block diagram of Focusing Method.

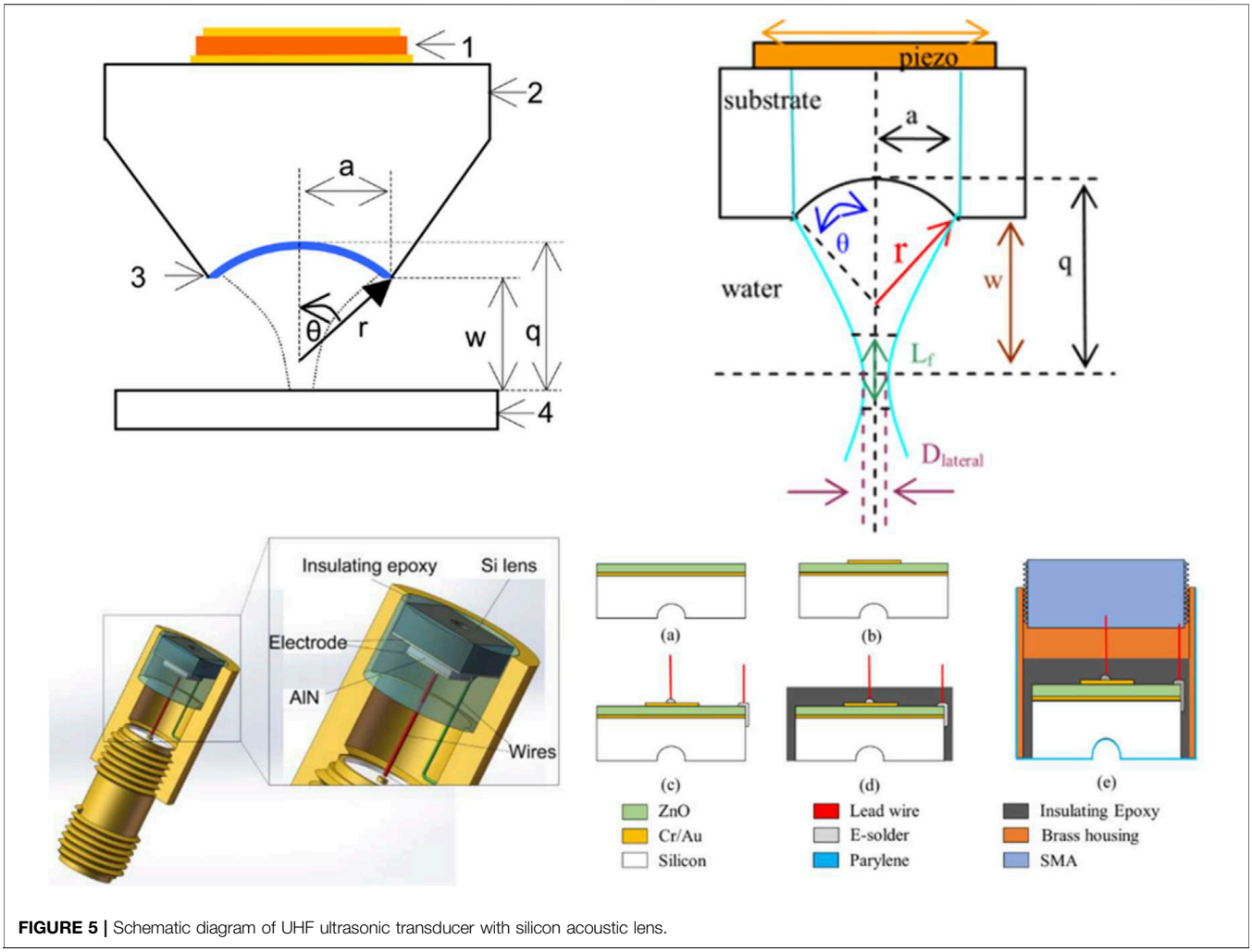

FIGURE 5 | Schematic diagram of UHF ultrasonic transducer with silicon acoustic lens.

in the thickness vibration mode are mainly considered here. Generally, the material parameters considered in the preparation of ultrasonic transducers are piezoelectric constant d_{33}, electromechanical coupling coefficient k_t, dielectric constant ε_{33}, acoustic impedance Z_p, and sound velocity c_m. Compared with conventional devices, UHF devices pay more attention to the speed of sound and dielectric constant. The former determines the final thickness of the piezoelectric material, and the latter determines the final area size of the piezoelectric material when the electrical impedance is matched to 50Ω. Reasonable thickness and area size can ensure the success of preparing UHF transducers. Then we need to consider the piezoelectric constant and electromechanical coupling coefficient, which affect the final signal amplitude and energy loss of the device. The material parameters mentioned above are all in **Table 2**, where n is an odd integer and usually n = 1, it means the lowest resonant frequency. C is the clamped capacitance, A is the area of piezoelectric materials, t is the thickness of piezoelectric materials, e_{33} is the piezoelectric stress constant, c_{33} is the elastic constant, c_m is the speed of sound inside the piezoelectric material, ρ is the density.

There is no best material, only the most suitable material. **Table 3** analyzes and compares the four types of piezoelectric materials' advantages and disadvantages mentioned, and gives an evaluation of the applicability of these four materials in ultra-high frequency ultrasonic devices' preparation.

Focusing Design of Ultrasonic Emission Energy

Description of This Section

The higher the frequency, the greater the attenuation of ultrasonic energy. To concentrate more emitted energy, the focus design of the transducer is usually necessary. Moreover, the UHF device has a higher frequency and smaller thickness, so its focus needs to consider tremendous sound attenuation and difficulty in process realization.

As shown in **Figure 4**, the focus design in this article divides into two directions. One is to achieve focusing by adding a lens to the surface of the piezoelectric material, which includes epoxy lens, metamaterial lens, adjustable liquid lens, Silicon lens, sapphire lens, and fused silica lens. The other is to achieve the

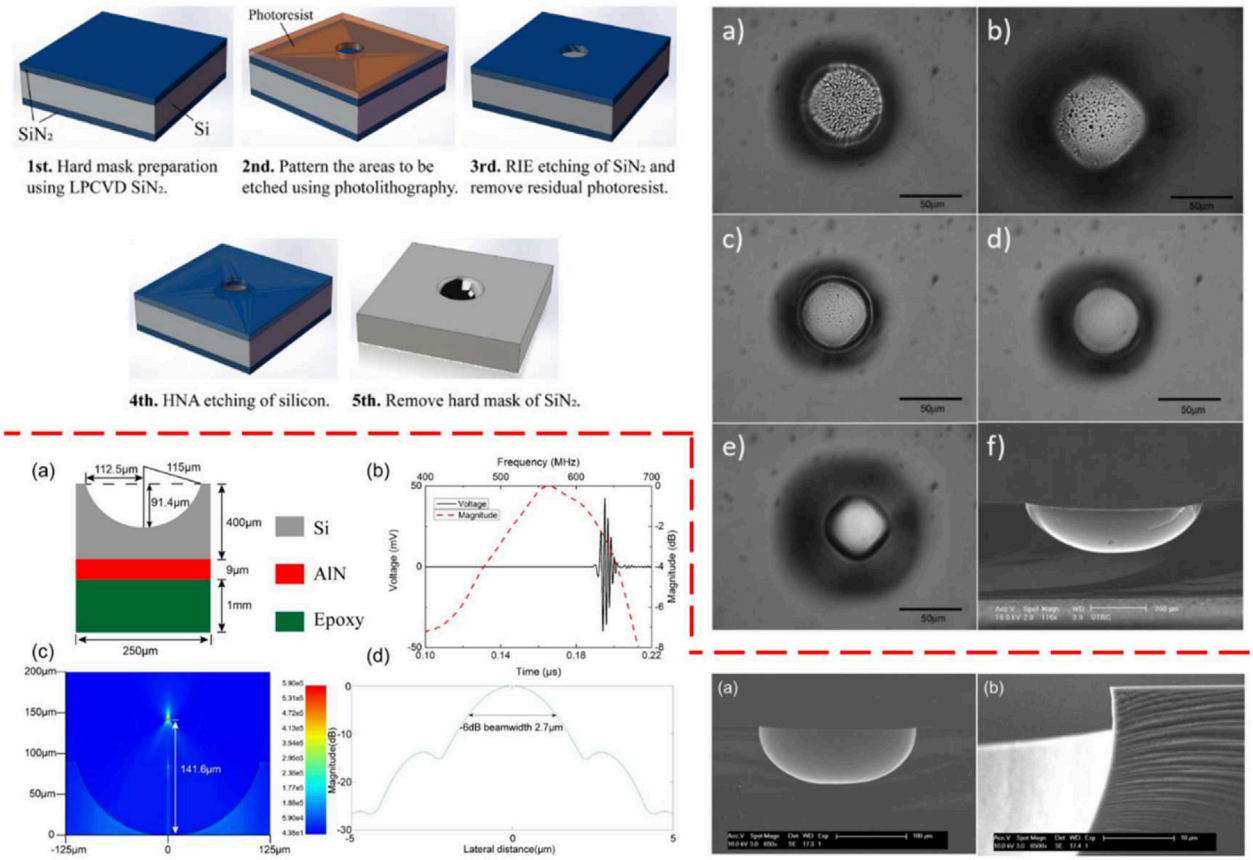

FIGURE 6 | The flow chart of chemical wet etching silicon lens and the SEM photographs of the silicon lens prepared by this method **(top)**; silicon lens simulation and UHF device performance and the SEM photographs of dry-etched silicon lens **(bottom)**.

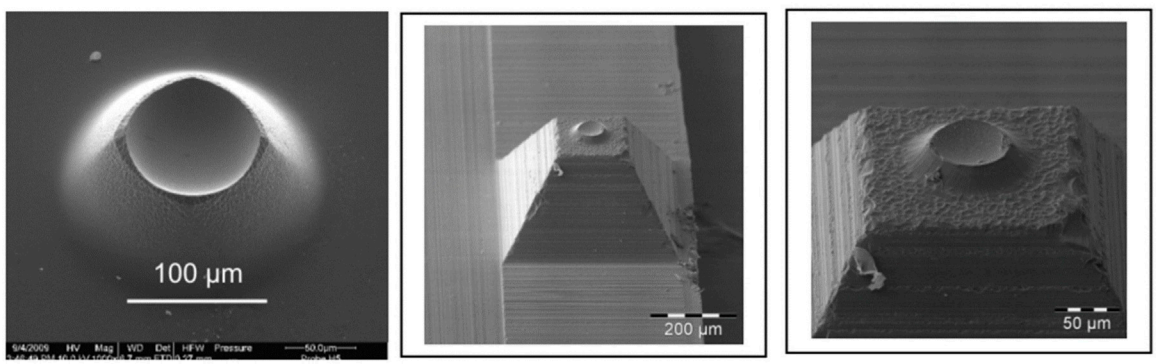

FIGURE 7 | Specially designed acoustic lens for GHz ultrasonic transducer device.

purpose of focusing by changing the shape of the piezoelectric material itself. There present four methods. The first one is to use a small ball to press the piezoelectric material to a focused shape. The second method is to lap the surface of the piezoelectric material with a mechanical grinding wheel. The third way applies a focused shape backing material. The last one combines MEMS technology to fabricate a focused shape piezoelectric material. Considering the difficulty of the process and the final focusing

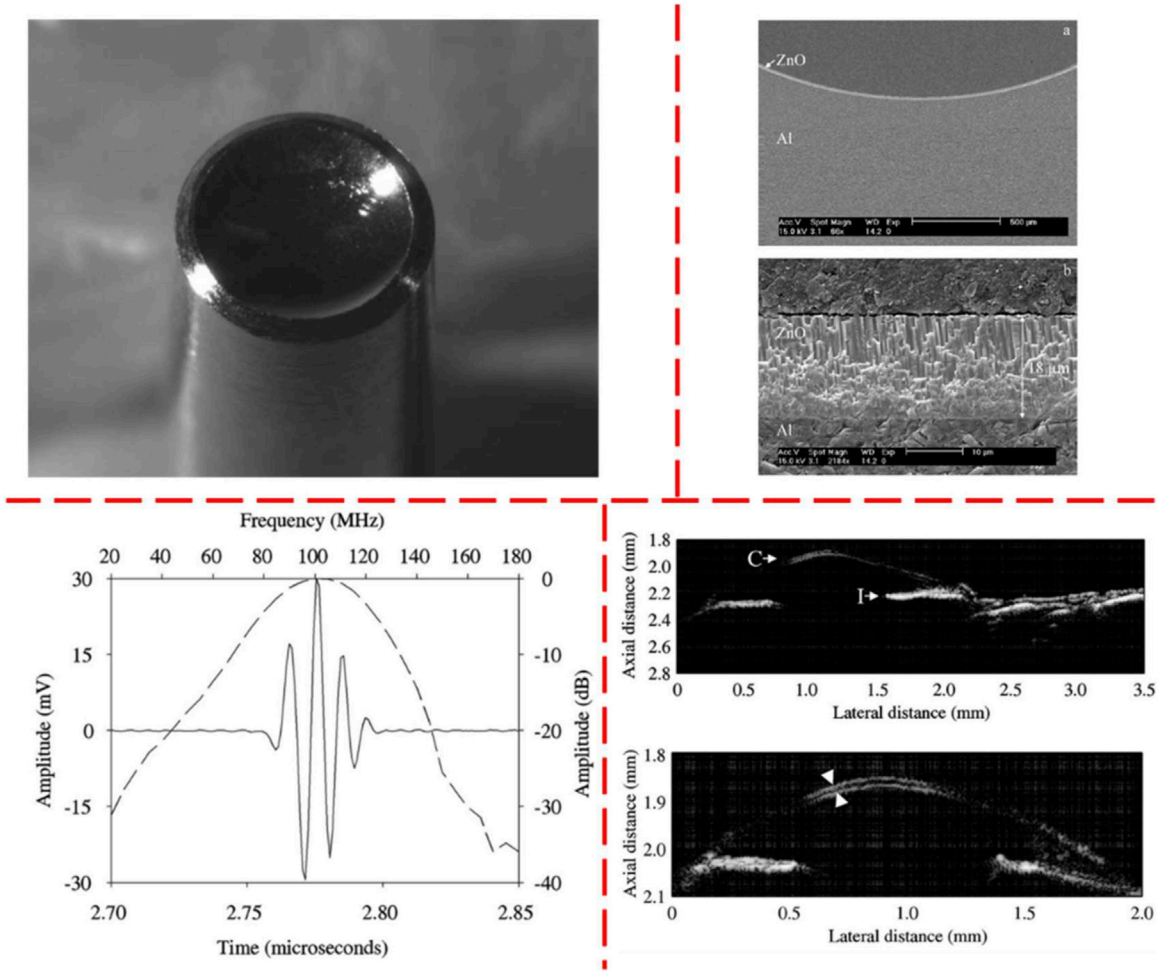

FIGURE 8 | A photograph of 100 MHz ZnO self-focus transducer **(top left)**; The SEM cross section of 100 MHz ZnO self-focus transducer **(top right)**; time-domain pulse/echo response (solid line) and frequency spectrum (dashed line) of 100 MHz ZnO self-focus transducer **(bottom left)**; High resolution ultrasound image of zebrafish eye **(bottom right)**.

effect, the focusing methods adapt to ultra-high frequency ultrasound devices' fabrication have been marked in green in the figure for easy viewing. The following content will illustrate these focusing methods.

Press Focus

Generally speaking, the most commonly used focusing method is spherical pressure focusing (Fei et al., 2018b), which uses a small ball to press a piezoelectric material to a spherical concave surface through a weight (**Supplementary Figure S11**). This method is simple and the cost is low, but the piezoelectric material in the UHF device is very thin. Using this method will often cause the piezoelectric material to break, and finally, make the performance of the device more difficult to predict, and the consistency is difficult Guaranteed. (Cannata et al., 2000).

TABLE 4 | UHF ultrasonic transducer acoustic lens material properties.

	Sapphire	Fused quartz	Si(100)
Acoustic velocity (***m/s***)	11,100	5,900	8,430
Acoustic impedance ($10^6 kg/m^2 \cdot s$)	40	15.6	19.8
Loss at 1 GHz (***dB/cm***)	0.2–0.5	12.1	6.5

Mechanical Dimpling

Another commonly used focus method is mechanical dimpling (Lam et al., 2012; Chen et al., 2013; Fei et al., 2018a). As shown in **Supplementary Figure S12**, the upper left is 5 MHz mechanical focusing PMN–PT single crystal, the top right is the surface morphology of the piezoelectric material after mechanical digging, and the bottom is the production flow chart of the 35 MHz PMN-PT IVUS mechanical focusing transducer. It can be seen in that the mechanical digging is performed on the piezoelectric material through a circular grinding wheel. The surface is made by pressing and polishing, but it is impossible to perform machining on the surface of the piezoelectric material of the ultra-high frequency device of a few microns.

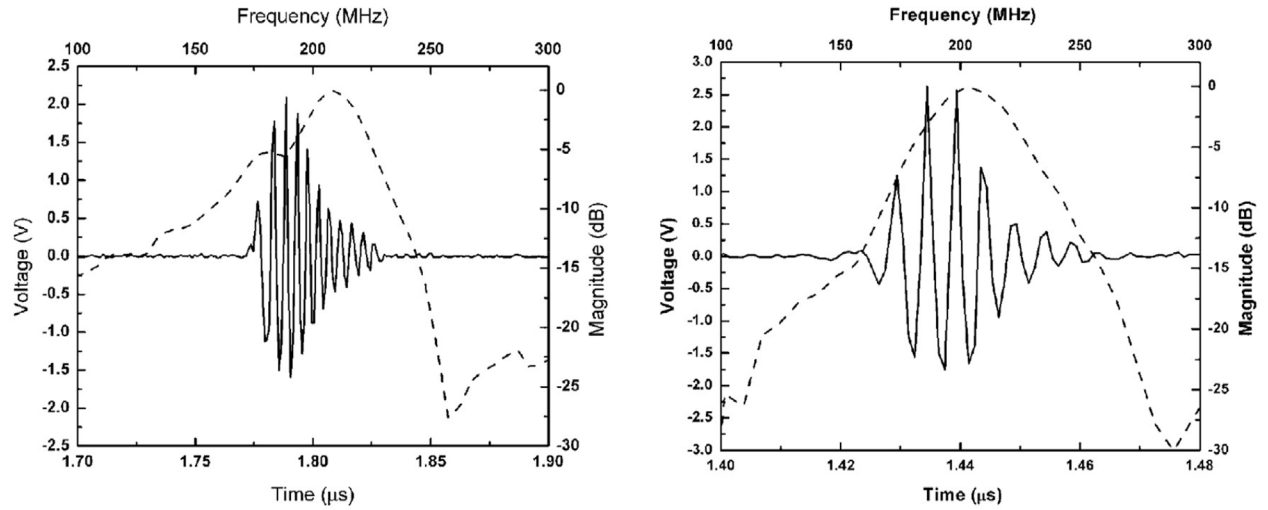

FIGURE 9 | Time-domain pulse/echo response (solid line) and frequency spectrum (dashed line) of the 200 MHz LiNbO3PF transducer **(left)**; Time-domain pulse/echo response (solid line) and frequency spectrum (dashed line) of the 200 MHz ZnO SF transducer **(right)**.

Acoustic Metasurface

Acoustic metasurface (**Supplementary Figure S13**) is a relatively novel way of sound field control (Al Jahdali and Wu, 2016; Zhu et al., 2016), but its structure usually has a large attenuation. Furthermore, with the frequency increases, the fabrication of metasurface structure is harder to realize, which makes it very difficult to play a role in the range of UHF applications. However, it can play a great role in regulating a specific sound field.

Adjustable Focus

There is an unconventional, but very interesting lens, as shown in **Supplementary Figure S14**. It can flexibly change the focus point by injecting liquid to control the curvature of the lens (Li et al., 2021b; Li et al., 2021c). It is hard to apply in UHF ultrasonic devices, but some special occasions may play a miraculous effect.

Silicon Lens

In the low-frequency range, epoxy can be considered to prepare a lens (Cannata et al., 2003), the epoxy lens is easy to mold and the prepared lens surface is smooth. Sapphire, fused quartz, and silicon are usually used in ultrahigh-frequency ultrasonic devices. Acoustic lenses are made by machining or etching firstly, and then ZnO is sputtered on the surface of the lens as piezoelectric materials to make UHF ultrasonic transducers, as shown in **Figure 5** (Kushida et al., 1988; Hashimoto et al., 1991; Vispute et al., 1997; Molarius et al., 2003; Jakob et al., 2009). This production process is relatively reliable and repeatable.

In 2017, CL Fei prepared a silicon lens through chemical wet etching. The preparation process and preparation effect are shown in the upper part of **Figure 6**. By sputtering a ZnO piezoelectric layer on this lens, a 300 MHz UHF device was successfully prepared (Fei et al., 2017). Then D Li and CL Fei reported on the silicon lens prepared by dry etching, and successfully prepared a 500 MHz AlN ultra-high frequency ultrasonic transducer (Li et al., 2018), the performance of the silicon lens and the transducer, as shown in **Figure 6** below.

Jakob mentioned in the article that the shape of the lens in **Figure 7** can not only reduce the interference of the edge echo but also can concentrate more energy in the target imaging area, reducing the divergence of the beam side lobes. This kind of acoustic lens can be applied to the ultrasonic scanning microscope of the GHz level. However, the realization of this kind of lens is more complicated, and the cavity needs to be etched by the wet method, and then the excess part of the edge is removed by the dry method (Jakob et al., 2007; Jakob et al., 2009). Some acoustic lens materials are listed in **Table 4** for reference (Hashimoto et al., 1991).

Focusing Backing

Since the acoustic lens will introduce a certain amount of attenuation, self-focusing of piezoelectric materials (Zhou et al., 2007; Jakob et al., 2009; Zhu et al., 2017) may be a better method. In this method, a focusing backing substrate is prepared in advance, and then piezoelectric material is sputtered on it, to avoid the attenuation caused by the acoustic lens. But in this way, the choice of the backing base material is more important. If the acoustic impedance of the backing material is too large from the piezoelectric material, the ultrasonic energy propagating after the phase cannot be absorbed, which will result in a larger ring in the echo signal. Al has many advantages, such as good processability, easy to process into spherical focusing grooves, good electrical conductivity, acoustic impedance closer to ZnO compared to other metals, higher melting point, and not being affected by the operating temperature during the preparation of piezoelectric materials. It is suitable to be a base material for self-focusing UHF transducers. JM Cannata fabricated a 100 MHz self-focusing UHF device using Al as the substrate (Cannata et al., 2008) and performed high-resolution imaging of zebrafish eyes (**Figure 8**). KH Lam also chose Al as the substrate. A 200 MHz self-focusing UHF device was fabricated on the substrate (Lam et al., 2013a), and the performance of the LN spherical pressure focusing UHF device was compared at the same

TABLE 5 | Summary of focusing methods.

	Advantage	Shortcoming	UHF devices applicability
Epoxy lens	Simple molding, low cost	Large attenuation	No
Silicon, sapphire, fused silica lens	Low attenuation, high surface smoothness	Complex process, high cost	Suitable for ultrahigh frequency, recommended method
Metasurface	Design flexibility	Large attenuation, complex process	No
Adjustable liquid lens	Adjustable focus	Not burst enough	No
Process focus	Easy to operate, low cost	Damage to piezoelectric materials, poor consistency	Applicable, but the consistency of equipment performance is difficult to guarantee
Mechanical dimpling	Easy to operate, low cost	Not suitable for microfabrication	No
Focusing backing	Easy to operate, low cost	Relay on machining accuracy	Applicable, there is an upper limit for machining
MEMS Spherical film	Good repeatability	Complex process, high cost	Applicable and developable direction

frequency. In **Figure 9**, it illustrates the effectiveness of the method of preparing UHF self-focusing by sputtering ZnO film with Al as the substrate, and the process stability of this method is much better than LN spherical pressure focusing.

MEMS Spherical Film

There is another way to realize transducer self-focus, which is a complete MEMS process. As shown in **Supplementary Figure S15**, the dome-shaped-diaphragm transducers (DSDT) (Feng et al., 2005) fabrication uses spherical balls to precisely shape wax molds, onto which parylene is deposited as a support layer for the DSDT. Piezoelectric ZnO film is sputter-deposited on the parylene dome diaphragm. E-Solder silver epoxy is placed and cured on the back surface to function both as an acoustic backing and as structural support. Quarter wavelength thick parylene is deposited on the front side of the wafer for acoustic matching. The fabrication technique for the DSDTs is meant for low-cost mass production of the devices for high-frequency biomedical imaging. This method successfully prepared a 200 MHz UHF transducer.

Summary of This Section

Through the broader understanding of ultrasonic transducers' focusing method, we can understand the difference between UHF devices' focusing and low-frequency devices' focusing. **Table 5** presents these focusing methods' summary, which can compare the differences of these methods more intuitively.

ACOUSTIC ENERGY TRANSMISSION MATCHING

Description of This Section

When the ultrasonic wave is emitted from the ultrasonic transducer into the propagation medium, due to the large difference in acoustic impedance between the piezoelectric material and the propagation medium, most of the energy will be reflected, which leads to the low working efficiency of the ultrasonic device (**Figure 10**). In the low-frequency range, ceramics can be composited (Smith, 1986; Hou et al., 2018; Lin et al., 2018; Fei et al., 2019; Chen et al., 2020; Lin et al., 2020) to make the material acoustic impedance close to the propagation medium, improving energy transmission efficiency. The metamaterials mentioned in *Material Selection of Ultrasound Generation* section also have applications in acoustic impedance matching (Li et al., 2017; Liu et al., 2018). These two methods both perform impedance matching by changing the spatial structure of the piezoelectric material. Although very effective, these operations are difficult to achieve in the UHF range. Therefore, we usually prefer to select the method by adding a matching layer to the piezoelectric material or lens surface for acoustic impedance matching in UHF. As the simplest and most effective matching method, quarter-wavelength matching (Kossoff, 1966; Desilets et al., 1978; Rhee et al., 2001) has been active from the initial Mason model (Mason, 1948; Sittig, 1972) to the improved KLM model (Krimholtz et al., 1970; Leedom et al., 1971). Although easy to use, this method requires materials with specific acoustic impedance for matching. To obtain the matching layer with specified acoustic impedance, it is a general method by dope high acoustic impedance particles into low acoustic impedance materials. However, it is difficult to get a few microns or even sub-micron size for the doped particle. For this problem, the Mass-spring model (Toda and Thompson, 2010) and the Transmission line matching network (Ma et al., 2015) are introduced for the UHF ultrasonic devices' matching layer design. Furthermore, they also provide a good solution for the precise control of the matching layer's thickness. The research situation of these two methods will show in the follow-up.

Novel Polymer-Metal Matching Layer

In 2010, M. Toda and M. Thompson (Toda and Thompson, 2010) proposed a novel multi-layer polymer-metal structure for use in ultrasonic transducer impedance matching (Toda and Thompson, 2012; Brown et al., 2014) which is based on mass-spring model. In **Figure 11** (Fei et al., 2015) we can see, after adding a metal-polymer structure matching layer to the ultrasonic transducer, its echo amplitude and bandwidth have been improved effectively. This method does not require materials with specific acoustic impedance and only needs to design metal and polymer layers of different thicknesses in combination with material characteristics to achieve the purpose of improving acoustic energy transmission. This laminated matching layer is conducive to the batch

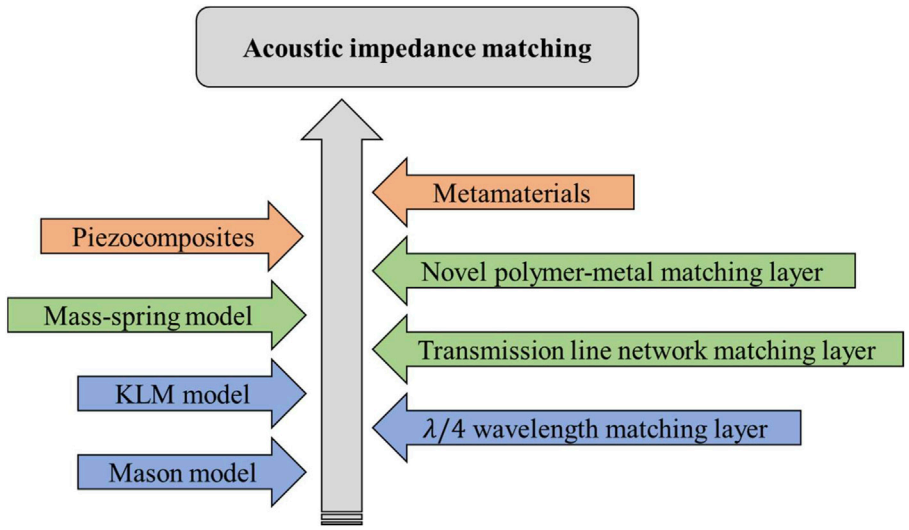

FIGURE 10 | Block diagram of Acoustic impedance matching (Rathod, 2020).

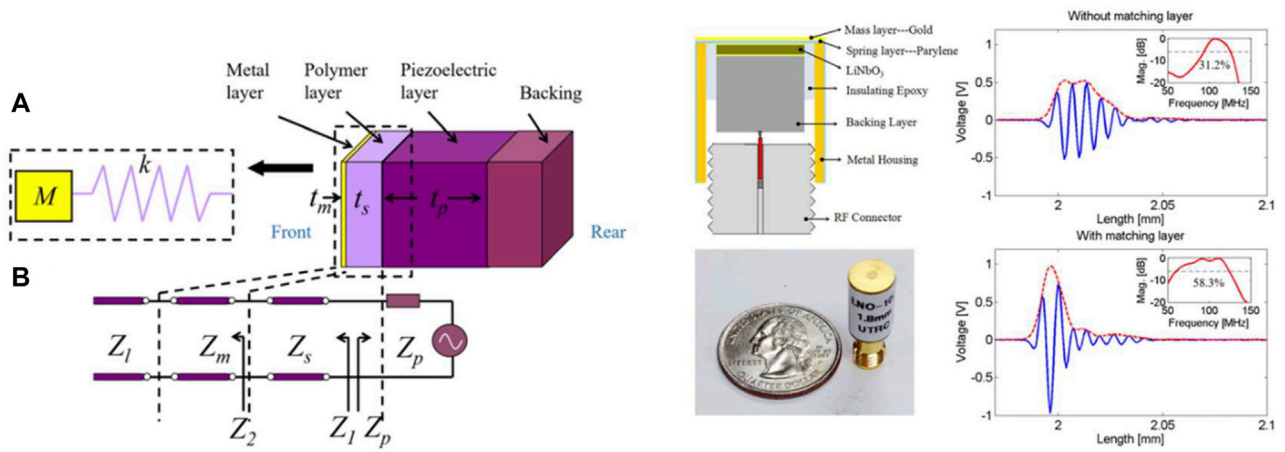

FIGURE 11 | Schematic diagram of the metal polymer matching layer based on mass-spring and its practical application in the transducer.

operation of the matching layer of the transducer and provides a feasible idea for the effective matching of ultra-high frequency ultrasonic devices.

Transmission Line Network Matching Layer

The transmission line matching network is implemented based on the KLM model. The acoustic impedance matching layer is designed by equating the acoustic parameters to the transmission line parameters and connecting them with the acoustic ports of the KLM model as shown in **Figure 12** (Yang et al., 2020). It can be seen from the figure that after adding the matching layer, the echo does have a significant improvement. Therefore, the transmission line matching network is also an effective way to UHF transducer's energy transmission matching.

Summary of This Section

Piezoelectric composites and metamaterials are not suitable for improving the acoustic energy transmission matching of ultra-high frequency ultrasonic devices due to the difficulty of actual operation in the high-frequency range. The traditional quarter matching layer is not suitable for UHF ultrasonic devices due to the specific acoustic impedance. Mass-spring and transmission line matching networks can achieve high-efficiency acoustic energy transmission by combining multi-layer materials with different acoustic impedances. Theoretically speaking, the design and implementation process of the matching layer is compatible with the MEMS processing technology, with high repeatability and good development prospects. However, we should also consider the attenuation caused by the multi-layer matching layer

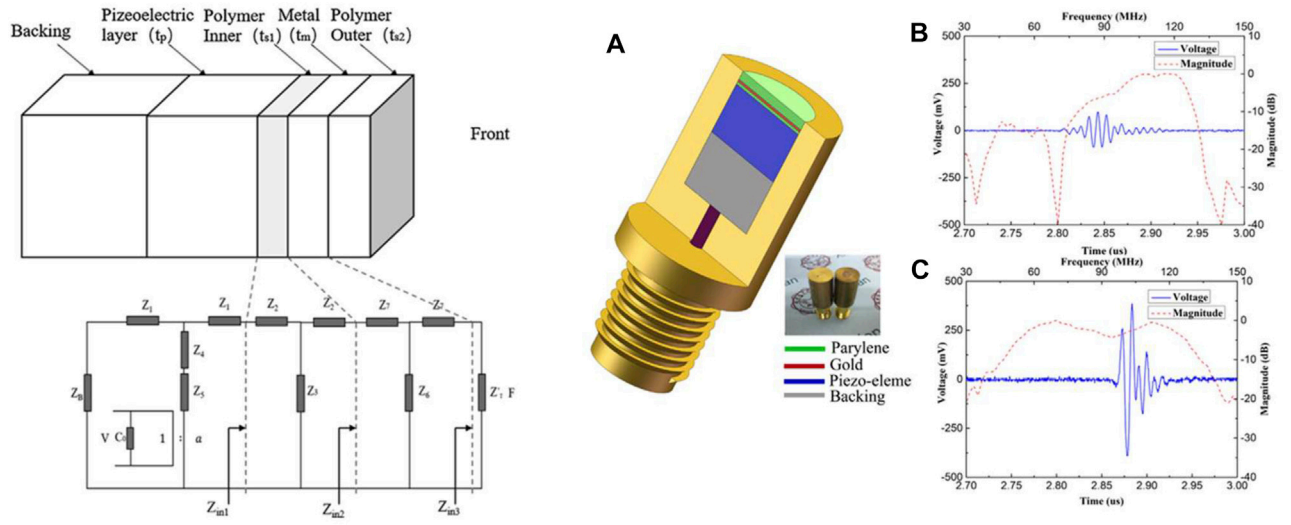

FIGURE 12 | Schematic diagram of the metal polymer matching layer based on transmission line matching network and its practical application in the transducer.

itself when designing the matching layer, so the acoustic impedance matching effect and the impact of material attenuation should consider comprehensively. Artificial intelligence (Li et al., 2021a) has become popular in recent years is good at finding the optimal solution among multiple factors. In the design of multi-layer matching layers, there may be a lot of room for development.

CONCLUSION

This article starts with the introduction of the selection of materials for UHF ultrasonic transducers. First, it explains the reasons why the most commonly used ceramic materials cannot be used in the preparation of UHF devices and then mentions the more popular relaxation-based materials, but they also have disadvantages Therefore, it is not suitable for making UHF devices. The excellent material properties of LN single crystal make it occupy a place in UHF devices, from 100 to 500MHz, but its difficult processing flow makes it difficult to break through the higher frequency limit. In addition, the processing flow is unstable, and the uniformity of the device caused by this makes it difficult to carry out mass production.

Things are always moving forward. The development of piezoelectric film materials has injected new impetus into the preparation of UHF transducers. Piezoelectric films prepared based on traditional ferroelectric materials solve the problem of difficult thickness control, and the piezoelectric films retain the excellent piezoelectric properties of bulk piezoelectric materials to a certain extent, and the UHF devices prepared by them have better performance. But this method can only be said to be a step to improve the thinning of piezoelectric materials in the traditional transducer manufacturing process. Due to the high temperature of densification and annealing during the preparation of piezoelectric film materials, the preparation of piezoelectric films and the production of transducers cannot be completely compatible. This leads to secondary processing of the prepared piezoelectric film, which is also quite difficult in actual operation. How to grow the piezoelectric film and the preparation of the transducer has good process compatibility is a very critical issue, and it is hoped that this problem can be solved through continuous process improvement in the future.

The development of the semiconductor industry has made MEMS technology increasingly mature, and piezoelectric films made of ZnO and AlN, which are commonly used semiconductor materials, have also joined the family of ultra-high frequency ultrasonic transducers. The mature MEMS technology makes the piezoelectric film and the transducer preparation compatible and does not require secondary processing. The preparation of the piezoelectric film is a step included in the MEMS transducer preparation process. This gives a better guarantee for the consistency of UHF devices and provides a basis for mass production. But all things have advantages and disadvantages. The disadvantage of using semiconductor materials to replace traditional ferroelectric materials is that the piezoelectric performance is relatively poor. Piezoelectric materials determine the final performance of the device, so the problem here is how to improve the piezoelectric performance of the material. There have been a few reports on this aspect of research, such as the above-mentioned modification of Sc doping and Yb doping to improve the piezoelectricity of AlN. This is a key issue that requires more researchers to join.

In addition to material selection, the focus design of UHF ultrasound devices is another key point. At present, the most

commonly used focusing methods in UHF ultrasound devices are acoustic lens focusing and self-focusing. There are also a certain number of reports on UHF ultrasound devices in this regard. This article also mentioned more focusing methods currently used in low-frequency bands, such as spherical pressure focusing, mechanical focusing, and acoustic lens focusing. There are also some interesting focusing methods, such as ultrasonic super-surface, liquid lens focusing. By understanding these various focusing methods, we can diverge our thinking. When we encounter problems in the focus design of UHF ultrasound devices, it may provide us with clever solutions.

The last key point mentioned in this article is the problem of acoustic energy transmission. As we all know, the propagation of sound requires a medium. In the application of UHF ultrasonic transducers, the medium we mentioned is usually water, and the acoustic impedance of water is only 1.5MRlays, but piezoelectric materials are often much larger than this. If no matching layer is added, the acoustic energy is directly emitted from the piezoelectric material into the water, and most of the energy will be reflected due to the large acoustic impedance difference. This will cause the device to work very inefficiently. The traditional quarter acoustic impedance matching layer has explained why it is not suitable for UHF ultrasonic devices. A new design method of metal-polymer structure matching layer is mentioned, and its applicability in ultra-high frequency ultrasonic devices is explained.

AUTHOR CONTRIBUTIONS

JC was responsible for collecting, sorting out relevant information and writing the paper. Other authors provided advice and help. All authors contributed to the article and approved the submitted version.

FUNDING

This work was supported by the National Natural Science Foundation of China (No: 61974110), the Key Projects of National Defense Basic Research Program of National Defense Science and Industry Administration (JCKY2019210B003), the Natural Science Foundation of Shaanxi Province (No: 2020JM-205, 2021JM-253), and the Fundamental Research Funds for the University of People's Armed Police (No: WJY201923, WJY202147).

SUPPLEMENTARY MATERIAL

The Supplementary Material for this article can be found online at: https://www.frontiersin.org/articles/10.3389/fmats.2021.733358/full#supplementary-material

Supplementary figure S1 | Schematic diagram of acoustic tweezers (left) and ultrasound scanning microscope (right).

Supplementary figure S2 | Ceramic grains under the microscope.

Supplementary figure S3 | A photograph of LN transducer and cross section of piezoelectric layer (left); High resolution ultrasound image of zebrafish eye (right).

Supplementary figure S4 | Cross section of 20 um PZT film.

Supplementary figure S5 | Pulse echo and FFT of 100 MHz PZT thick film transducer (top); Experimental pulse echo and FFT of 150 MHz PZT thick film transducer (bottom left); Simulated pulse echo and FFT of 150 MHz PZT thick film transducer (bottom right).

Supplementary figure S6 | A photograph of 300 MHz transducer (top left); Schematic diagram of 0–3 composite PZT film (top right); time-domain pulse/echo response (solid line) and frequency spectrum (dashed line) of 100–300 MHz transducer (bottom).

Supplementary figure S7 | A photograph of 193 MHz KNN-LSO needle planar transducer (top left); schematic diagram of 225 MHz KNN/BNT piston focusing transducer (bottom left); time-domain pulse/echo response and frequency spectrum of 193 MHz KNN-LSO needle planar transducer (top right); time-domain pulse/echo response and frequency spectrum of 225 MHz KNN/BNT piston focus transducer (lower right).

Supplementary figure S8 | Time-domain pulse/echo response (solid line) and frequency spectrum (dashed line) of 170–320 MHz KNN/BNT transducer.

Supplementary figure S9 | Frequency curve of the dielectric coefficient of xPMN-PT-(1-x)PZT composite film under different PZT doping ratios (left); time-domain pulse/echo response (solid line) and frequency spectrum (dashed line) of 0.9PMN-PT–0.1PZT composite film transducer (right).

Supplementary figure S10 | Ferroelectric hysteresis loops of PMN-PT-PZT composite film under different Ag doping concentration (top left); curve of influence of Ag concentration on the dielectric constant of PMN-PT-PZT composite film at 1 KHz (top right); a photograph of silver-doped PMN-PT-PZT needle transducer (bottom left); time-domain pulse/echo response (solid line) and frequency spectrum (dashed line) of silver-doped PMN-PT-PZT needle transducer (bottom right).

Supplementary figure S11 | Preparation process of spherical pressure focusing transducer.

Supplementary figure S12 | A photograph of needle type mechanical focused ultrasound transducer (top left); piezoelectric materials after mechanical dimpling under optical microscope (top right); IVUS mechanical focus transducer preparation process (bottom).

Supplementary figure S13 | Two types of acoustic metasurface lenses and simulation diagram of the focusing effect of two acoustic metasurface lenses.

Supplementary figure S14 | Schematic and physical image of liquid lens.

Supplementary figure S15 | The flow chart of prepare Dome-Shaped-Diaphragm Transducers (left) and photographs of Dome-Shaped-Diaphragm Transducer (right).

REFERENCES

Al Jahdali, R., and Wu, Y. (2016). High Transmission Acoustic Focusing by Impedance-Matched Acoustic Meta-Surfaces. *Appl. Phys. Lett.* 108 (3), 031902. doi:10.1063/1.4939932

Barrow, D. A., Petroff, T. E., Tandon, R. P., and Sayer, M. (1997). Characterization of Thick lead Zirconate Titanate Films Fabricated Using a New Sol Gel Based Process. *Journal Applied Physics* 81, 876–881. doi:10.1063/1.364172

Brown, J., Sharma, S., Leadbetter, J., Cochran, S., and Adamson, R. (2014). Mass-spring Matching Layers for High-Frequency Ultrasound Transducers: a New Technique Using Vacuum Deposition. *IEEE Trans. Ultrason. Ferroelect., Freq. Contr.* 61 (11), 1911–1921. doi:10.1109/TUFFC.2014.006480

Cannata, J. M., Ritter, T. A., Wo-Hsing Chen, W.-H., and Shung, K. K. (20002000). Design of Focused Single Element (50-100 MHz) Transducers Using Lithium Niobate. *IEEE Ultrason. Symp.* 2, 1129–1133. doi:10.1109/ULTSYM.2000.921524

Cannata, J. M., Ritter, T. A., Wo-Hsing Chen, W., Silverman, R. H., and Shung, K. K. (2003). Design of Efficient, Broadband Single-Element (20-80 MHz) Ultrasonic

Transducers for Medical Imaging Applications. *IEEE Trans. Ultrason. Ferroelect., Freq. Contr.* 50, 1548–1557. doi:10.1109/TUFFC.2003.1251138

Cannata, J. M., Williams, J. A., Zhou, Q. F., Sun, L., Shung, K. K., Yu, H., et al. (2008). Self-focused ZnO Transducers for Ultrasonic Biomicroscopy. *Journal Applied Physics* 103, 084109. doi:10.1063/1.2907716

Chen, D., Hou, C., Fei, C., Li, D., Lin, P., Chen, J., et al. (2020). An Optimization Design Strategy of 1-3 Piezocomposite Ultrasonic Transducer for Imaging Applications. *Mater. Today Commun.* 24, 100991. doi:10.1016/j.mtcomm.2020.100991

Chen, H., Xia, H., Wang, J., Zhang, J., Xu, J., and Fan, S. (2003). Growth of LiNbO3 Crystals by the Bridgman Method. *Journal Crystal Growth* 256, 219–222. doi:10.1016/S0022-0248(03)01361-7

Chen, X., Fei, C., Chen, Z., Chen, R., Yu, P., Chen, Z., et al. (2016). Simulation and Fabrication of 0-3 Composite PZT Films for Ultrahigh Frequency (100-300 MHz) Ultrasonic Transducers. *Journal Applied Physics* 119, 094103. doi:10.1063/1.4942857

Chen, X., Lam, K. H., Chen, R., Chen, Z., Yu, P., Chen, Z., et al. (2017). An Adjustable Multi-Scale Single Beam Acoustic Tweezers Based on Ultrahigh Frequency Ultrasonic Transducer. *Biotechnol. Bioeng.* 114, 2637–2647. doi:10.1002/bit.26365

Chen, Y., Lam, K.-H., Zhou, D., Yue, Q., Yu, Y., Wu, J., et al. (2014). High Performance Relaxor-Based Ferroelectric Single Crystals for Ultrasonic Transducer Applications. *Sensors* 14, 13730–13758. doi:10.3390/s140813730

Chen, Y., Lam, K. H., Zhou, D., Cheng, W. F., Dai, J. Y., Luo, H. S., et al. (2013). High Frequency PMN-PT Single crystal Focusing Transducer Fabricated by a Mechanical Dimpling Technique. *Ultrasonics* 53 (2), 345–349. doi:10.1016/j.ultras.2012.06.017

Desilets, C. S., Fraser, J. D., and Kino, G. S. (1978). The Design of Efficient Broad-Band Piezoelectric Transducers. *IEEE Trans. Son. Ultrason.* 25, 115–125. doi:10.1109/T-SU.1978.31001

Fei, C., Chiu, C. T., Chen, X., Chen, Z., Ma, J., Zhu, B., et al. (2016). Ultrahigh Frequency (100 MHz-300 MHz) Ultrasonic Transducers for Optical Resolution Medical Imagining. *Sci. Rep.* 6, 28360. doi:10.1038/srep28360

Fei, C., Hsu, H.-S., Vafanejad, A., Li, Y., Lin, P., Li, D., et al. (2017). Ultrahigh Frequency ZnO Silicon Lens Ultrasonic Transducer for Cell-Size Microparticle Manipulation. *Journal Alloys Compounds* 729, 556–562. doi:10.1016/j.jallcom.2017.09.113

Fei, C., Lin, P., Li, D., Wu, Y., Wu, R., Chen, J., et al. (2019). Fabrication and Characterization of High-Sensitivity Ultrasonic Transducers with Functionally Graded Design. *IEEE Sensors J.* 19 (16), 6650–6654. doi:10.1109/jsen.2019.2905625

Fei, C., Ma, J., Chiu, C. T., Williams, J. A., Fong, W., Chen, Z., et al. (2015). Design of Matching Layers for High-Frequency Ultrasonic Transducers. *Appl. Phys. Lett.* 107 (12), 123505. doi:10.1063/1.4931703

Fei, C., Yang, Y., Guo, F., Lin, P., Chen, Q., Zhou, Q., et al. (2018a). PMN-PT Single Crystal Ultrasonic Transducer with Half-Concave Geometric Design for IVUS Imaging. *IEEE Trans. Biomed. Eng.* 65 (9), 2087–2092. doi:10.1109/TBME.2017.2784437

Fei, C., Zhao, T., Wang, D., Quan, Y., Lin, P., Li, D., et al. (2018b). High Frequency Needle Ultrasonic Transducers Based on Lead-Free Co Doped Na0.5Bi4.5Ti4O15 Piezo-Ceramics. *Micromachines* 9 (6), 291. doi:10.3390/mi9060291

Feng, G.-H., Sharp, C. C., Zhou, Q. F., Pang, W., Kim, E. S., and Shung, K. K. (2005). Fabrication of MEMS ZnO Dome-Shaped-Diaphragm Transducers for High-Frequency Ultrasonic Imaging. *J. Micromech. Microeng.* 15, 586–590. doi:10.1088/0960-1317/15/3/021

Foster, F. S., Ryan, L. K., and Turnbull, D. H. (1991). Characterization of lead Zirconate Titanate Ceramics for Use in Miniature High-Frequency (20-80 MHz) Transducers. *IEEE Trans. Ultrason. Ferroelect., Freq. Contr.* 38, 446–453. doi:10.1109/58.84289

Haertling, G. H. (1999). Ferroelectric Ceramics: History and Technology. *Journal American Ceramic Society* 82, 797–818. doi:10.1111/j.1151-2916.1999.tb01840.x

Hashimoto, H., Tanaka, S., and Sato, K. (1991). "Silicon Acoustic Lens for Scanning Acoustic Microscope (SAM)," in TRANSDUCERS '91: 1991 International Conference on Solid-State Sensors and Actuators. Digest of Technical Papers, San Francisco, CA, USA, 24-27 June 1991 (IEEE), 853–859. doi:10.1109/SENSOR.1991.149019

Hirata, K., Mori, Y., Yamada, H., Uehara, M., Anggraini, S. A., and Akiyama, M. (2021). Significant Enhancement of Piezoelectric Response in AlN by Yb Addition. *Materials* 14, 309. doi:10.3390/ma14020309

Hou, S., Yang, X., Fei, C., Sun, X., Chen, Q., Lin, P., et al. (2018). Fabrication of PMN-PT/Epoxy 2-2 Composite Ultrasonic Transducers and Analysis Based on Equivalent Circuit Model. *J. Elec. Materi.* 47 (11), 6842–6847. doi:10.1007/s11664-018-6603-0

Hsu, H.-S., Benjauthrit, V., Wei, Q., Huang, Y., Zhou, Q., and Shung, K. K. (2013). Silver Doped 0.9PMN-PT-0.1PZT Composite Films for Very High Frequency Ultrasonic Transducer Applications. *Appl. Phys. A.* 111, 459–463. doi:10.1007/s00339-013-7558-x

Hsu, H.-S., Benjauthrit, V., Zheng, F., Chen, R., Huang, Y., Zhou, Q., et al. (2012). PMN-PT-PZT Composite Films for High Frequency Ultrasonic Transducer Applications. *Sensors Actuators A: Phys.* 179, 121–124. doi:10.1016/j.sna.2012.02.031

Jakob, A., Bender, M., Knoll, T., Lemor, R., Lehnert, T., Koch, M., et al. (2009). "Comparison of Different Piezoelectric Materials for GHz Acoustic Microscopy Transducers," in 2009 IEEE International Ultrasonics Symposium, Rome, Italy, 20-23 Sept. 2009 (IEEE), 1722–1725. doi:10.1109/ULTSYM.2009.5442024

Jakob, A., Weiss, E. C., Knoll, T., Bauerfeld, F., Hermann, J., and Lemor, R. (2007). "P2E-5 Silicon Based GHz Acoustic Lenses for Time Resolved Acoustic Microscopy," in 2007 IEEE Ultrasonics Symposium, New York, NY, USA, 28-31 Oct. 2007 (IEEE), 1605–1608. doi:10.1109/ULTSYM.2007.404

Kamel, T. M., and de With, G. (2008). Grain Size Effect on the Poling of Soft Pb(Zr,Ti)O3 Ferroelectric Ceramics. *Journal European Ceramic Society* 28, 851–861. doi:10.1016/j.jeurceramsoc.2007.08.010

Kong, L. B., Zhu, W., and Tan, O. K. (2000). Preparation and Characterization of Pb(Zr0.52Ti0.48)O3 Ceramics from High-Energy ball Milling Powders. *Materials Letters* 42, 232–239. doi:10.1016/S0167-577X(99)00190-1

Kossoff, G. (1966). The Effects of Backing and Matching on the Performance of Piezoelectric Ceramic Transducers. *IEEE Trans. Son. Ultrason.* 13 (1), 20–30. doi:10.1109/T-SU.1966.29370

Krimholtz, R., Leedom, D. A., and Matthaei, G. L. (1970). New Equivalent Circuits for Elementary Piezoelectric Transducers. *Electron. Lett.* 6 (13), 398–399. doi:10.1049/el:19700280

Kushida, K., Takeuchi, H., Kanda, H., and Yamaguchi, S. (1989). 100 MHz Band Ultrasonic Transducers Utilizing Epitaxially Grown ZnO Films. *Jpn. J. Appl. Phys.* 28, 260. doi:10.7567/JJAPS.28S1.260

Lam, K. H., Chen, Y., Cheung, K. F., and Dai, J. Y. (2012). PMN-PT Single crystal Focusing Transducer Fabricated Using a Mechanical Dimpling Technique. *Ultrasonics* 52 (1), 20–24. doi:10.1016/j.ultras.2011.06.004

Lam, K. H., Hsu, H.-S., Li, Y., Lee, C., Lin, A., Zhou, Q., et al. (2013a). Ultrahigh Frequency Lensless Ultrasonic Transducers for Acoustic Tweezers Application. *Biotechnol. Bioeng.* 110, 881–886. doi:10.1002/bit.24735

Lam, K. H., Ji, H. F., Zheng, F., Ren, W., Zhou, Q., and Shung, K. K. (2013b). Development of lead-free Single-Element Ultrahigh Frequency (170-320MHz) Ultrasonic Transducers. *Ultrasonics* 53 (5), 1033–1038. doi:10.1016/j.ultras.2013.01.012

Lau, S.-t., Li, X., Zhang, X., Zhou, Q., Shung, K. K., Ji, H., et al. (2010a). "High Frequency Ultrasonic Transducer with KNN/BNT 0–3 Composite Active Element," in 2010 IEEE International Ultrasonics Symposium, San Diego, CA, USA, 11-14 Oct. 2010 (IEEE), 76–79. doi:10.1109/ULTSYM.2010.5935849

Lau, S. T., Ji, H. F., Li, X., Ren, W., Zhou, Q., and Shung, K. K. (2011). KNN/BNT Composite Lead-Free Films for High-Frequency Ultrasonic Transducer Applications. *IEEE Trans. Ultrason. Ferroelect., Freq. Contr.* 58, 249–254. doi:10.1109/TUFFC.2011.1793

Lau, S. T., Li, X., Zhou, Q. F., Shung, K. K., Ryu, J., and Park, D.-S. (2010b). Aerosol-deposited KNN-LSO lead-free Piezoelectric Thick Film for High Frequency Transducer Applications. *Sensors Actuators A: Phys.* 163, 226–230. doi:10.1016/j.sna.2010.08.020

Leedom, D. A., Krimholtz, R., and Matthaei, G. L. (1971). Equivalent Circuits for Transducers Having Arbitrary Even- or Odd-Symmetry Piezoelectric Excitation. *IEEE Trans. Son. Ultrason.* 18 (3), 128–141. doi:10.1109/T-SU.1971.29608

Li, D., Fei, C., Zhang, Q., Li, Y., Yang, Y., and Zhou, Q. (2018). Ultrahigh Frequency Ultrasonic Transducers Design with Low Noise Amplifier Integrated Circuit. *Micromachines* 9 (10), 515. doi:10.3390/mi9100515

Li, Z., Chen, D., Fei, C., Li, D., Feng, W., and Yang, Y. (2021a). Optimization Design of Ultrasonic Transducer with Multimatching Layer. *IEEE Trans. Ultrason. Ferroelect., Freq. Contr.* 68 (6), 2202–2211. doi:10.1109/TUFFC.2021.3059671

Li, Z., Guo, R., Chen, D., Fei, C., Yang, X., Li, D., et al. (2021b). An Efficient Optimization Design of Liquid Lens for Acoustic Pattern Control. *IEEE Trans. Ultrason. Ferroelect., Freq. Contr.* 68 (5), 1546–1554. doi:10.1109/TUFFC.2020.3040174

Li, Z., Guo, R., Fei, C., Li, D., Chen, D., Zheng, C., et al. (2021c). Liquid Lens with Adjustable Focus for Ultrasonic Imaging. *Appl. Acoust.* 175, 107787. doi:10.1016/j.apacoust.2020.107787

Li, Z., Yang, D.-Q., Liu, S.-L., Yu, S.-Y., Lu, M.-H., Zhu, J., et al. (2017). Broadband Gradient Impedance Matching Using an Acoustic Metamaterial for Ultrasonic Transducers. *Sci. Rep.* 7 (1), 42863. doi:10.1038/srep42863

Lim, H. G., and Shung, K. K. (2017). Quantification of Inter-erythrocyte Forces with Ultra-high Frequency (410 MHz) Single Beam Acoustic Tweezer. *Ann. Biomed. Eng.* 45, 2174–2183. doi:10.1007/s10439-017-1863-z

Lin, P., Fei, C., Hou, S., Zhao, T., Chen, Q., Quan, Y., et al. (2018). 0.36BiScO3-0.64PbTiO3/Epoxy 1-3 Composite for Ultrasonic Transducer Applications. *IEEE Sensors J.* 18 (14), 5685–5690. doi:10.1109/jsen.2018.2837868

Lin, P., Zhang, L., Fei, C., Li, D., Wu, R., Chen, Q., et al. (2020). Novel Multi-Layer-Composites Design for Ultrasonic Transducer Applications. *Compos. Structures* 245, 112364. doi:10.1016/j.compstruct.2020.112364

Liu, C., Luo, J., and Lai, Y. (2018). Acoustic Metamaterials with Broadband and Wide-Angle Impedance Matching. *Phys. Rev. Mater.* 2 (4), 045201. doi:10.1103/PhysRevMaterials.2.045201

Luo, J. T., Fan, B., Zeng, F., and Pan, F. (2009). Influence of Cr-Doping on Microstructure and Piezoelectric Response of AlN Films. *J. Phys. D: Appl. Phys.* 42, 235406. doi:10.1088/0022-3727/42/23/235406

Ma, J., Steer, M. B., and Jiang, X. (2015). An Acoustic Filter Based on Layered Structure. *Appl. Phys. Lett.* 106 (11), 111903. doi:10.1063/1.4915100

Makra, A., Bost, W., Kallo, I., Horvath, A., Fournelle, M., and Gyongy, M. (2020). Enhancement of Acoustic Microscopy Lateral Resolution: A Comparison between Deep Learning and Two Deconvolution Methods. *IEEE Trans. Ultrason. Ferroelect., Freq. Contr.* 67 (1), 136–145. doi:10.1109/TUFFC.2019.2940003

Marechal, P., Levassort, F., Holc, J., Tran-Huu-Hue, L.-P., Kosec, M., and Lethiecq, M. (2006). High-frequency Transducers Based on Integrated Piezoelectric Thick Films for Medical Imaging. *IEEE Trans. Ultrason. Ferroelect., Freq. Contr.* 53, 1524–1533. doi:10.1109/TUFFC.2006.1665110

Mason, W. P. (1948). *Electromechanical Transducers and Wave Filters*. D. Van Nostrand Company.

Molarius, J., Kaitila, J., Pensala, T., and Ylilammi, M. (2003). Piezoelectric ZnO Films by r.F. Sputtering. *Journal Materials Science-Materials Electronics* 14, 431–435. doi:10.1023/A:1023929524641

Park, S.-E., and Shrout, T. R. (1997b). Ultrahigh Strain and Piezoelectric Behavior in Relaxor Based Ferroelectric Single Crystals. *Journal Applied Physics* 82, 1804–1811. doi:10.1063/1.365983

Pérez, J. A., Soares, M. R., Mantas, P. Q., and Senos, A. M. R. (2005). Microstructural Design of PZT Ceramics. *J. Eur. Ceram. Soc.* 25, 2207–2210. doi:10.1016/j.jeurceramsoc.2005.03.031

Randall, C., Kim, N., Kucera, J., Cao, W., and Shrout, T. (1998). Intrinsic and Extrinsic Size Effects in fine-grained Morphotropic-Phase-Boundary lead Zirconate Titanate Ceramics. *Journal American Ceramic Society* 81, 677–688.

Rathod, V. T. (2020). A Review of Acoustic Impedance Matching Techniques for Piezoelectric Sensors and Transducers. *Sensors (Basel)* 20 (14), 4051. doi:10.3390/s20144051

Rhee, S., Ritter, T. A., Shung, K. K., Wang, H., and Cao, W. (2001). "Materials for Acoustic Matching in Ultrasound Transducers," in 2001 IEEE Ultrasonics Symposium. Proceedings. An International Symposium (Cat. No.01CH37263), Atlanta, GA, USA, 7-10 Oct. 2001 (IEEE), 1051–1055. doi:10.1109/ULTSYM.2001.991900

Sangsubun, C., Watcharapasorn, A., and Jiansirisomboon, S. (2008). Densification and Microstructure of lead Zirconate Titanate Ceramics Fabricated from a Triol Sol-Gel Powder. *Current Applied Physics* 8, 61–65. doi:10.1016/j.cap.2007.04.009

Sano, K., Karasawa, R., and Yanagitani, T. (2018). ScAlN Thick-Film Ultrasonic Transducer in 40-80 MHz. *IEEE Transactions Ultrasonics Ferroelectrics Frequency Control* 65, 2097–2102. doi:10.1109/TUFFC.2018.2865791

Seung-Eek Park, S., and Shrout, T. R. (1997a). Characteristics of Relaxor-Based Piezoelectric Single Crystals for Ultrasonic Transducers. *IEEE Trans. Ultrason. Ferroelect., Freq. Contr.* 44, 1140–1147. doi:10.1109/58.655639

Sittig, E. K. (1972). "5 - Design and Technology of Piezoelectric Transducers for Frequencies above 100 MHz," in *Physical Acoustics*. Editors W. P. Mason and R. N. Thurston (Academic Press), 221–275. doi:10.1016/b978-0-12-395670-5.50010-6

Smith, W. A. (1986). "Composite Piezoelectric Materials for Medical Ultrasonic Imaging Transducers - A Review," in Sixth IEEE International Symposium on Applications of Ferroelectrics, Bethlehem, PA, USA, 8-11 June 1986 (IEEE), 249–256. doi:10.1109/ISAF.1986.201136

Toda, M., and Thompson, M. (2012). Detailed Investigations of Polymer/metal Multilayer Matching Layer and Backing Absorber Structures for Wideband Ultrasonic Transducers. *IEEE Trans. Ultrason. Ferroelectrics, Frequency Control.* 59 (2), 231–242. doi:10.1109/TUFFC.2012.2183

Toda, M., and Thompson, M. (2010). Novel Multi-Layer Polymer-Metal Structures for Use in Ultrasonic Transducer Impedance Matching and Backing Absorber Applications. *IEEE Trans. Ultrason. Ferroelectrics, Frequency Control.* 57 (12), 2818–2827. doi:10.1109/TUFFC.2010.1755

Uecker, R. (2014). The Historical Development of the Czochralski Method. *Journal Crystal Growth* 401, 7–24. doi:10.1016/j.jcrysgro.2013.11.095

Vispute, R., Talyansky, V., Trajanovic, Z., Choopun, S., Downes, M., Sharma, R., et al. (1997). High Quality Crystalline ZnO Buffer Layers on Sapphire (001) by Pulsed Laser Deposition for III-V Nitrides. *Applied Physics Letters* 70, 2735–2737. doi:10.1063/1.119006

Weiss, E. C., Anastasiadis, P., Pilarczyk, G., Lemor, R. M., and Zinin, P. V. (2007). Mechanical Properties of Single Cells by High-Frequency Time-Resolved Acoustic Microscopy. *IEEE Transactions Ultrasonics Ferroelectrics Frequency Control* 54 (11), 2257–2271. doi:10.1109/tuffc.2007.530

Wistrela, E., Schmied, I., Schneider, M., Gillinger, M., Mayrhofer, P., Bittner, A., et al. (2018). Impact of Sputter Deposition Parameters on the Microstructural and Piezoelectric Properties of CrxAl1 (-) N-X Thin Films. *Thin Solid Films* 648, 76–82. doi:10.1016/j.tsf.2018.01.003

Yang, X., Fei, C., Li, D., Sun, X., Hou, S., Chen, J., et al. (2020). Multi-layer Polymer-Metal Structures for Acoustic Impedance Matching in High-Frequency Broadband Ultrasonic Transducers Design. *Appl. Acoust.* 160, 107123. doi:10.1016/j.apacoust.2019.107123

Zhang, T., Chen, R., Zhang, Z., Li, R., Tang, X., Wang, X., et al. (2017). "High Frequency Single crystal Ultrasonic Transducers up to 100 MHz for High Resolution Ophthalmic Imaging Applications," in 2017 IEEE International Ultrasonics Symposium, Washington, DC, USA, 6-9 Sept. 2017 (IEEE), 1. doi:10.1109/ULTSYM.2017.8092279

Zhou, Q. F., Sharp, C., Cannata, J. M., Shung, K. K., Feng, G. H., and Kim, E. S. (2007). Self-focused High Frequency Ultrasonic Transducers Based on ZnO Piezoelectric Films. *Appl. Phys. Lett.* 90 (11). doi:10.1063/1.2712813

Zhu, B., Fei, C., Wang, C., Zhu, Y., Yang, X., Zheng, H., et al. (2017). Self-Focused AIScN Film Ultrasound Transducer for Individual Cell Manipulation. *ACS Sensors* 2, 172–177. doi:10.1021/acssensors.6b00713

Zhu, B., Wu, D., Zhou, Q., Shi, J., and Shung, K. (2008). Lead Zirconate Titanate Thick Film with Enhanced Electrical Properties for High Frequency Transducer Applications. *Applied Physics Letters* 93, 012905. doi:10.1063/1.2956408

Zhu, Y.-F., Fan, X.-D., Liang, B., Yang, J., Yang, J., Yin, L.-l., et al. (2016). Multi-frequency Acoustic Metasurface for Extraordinary Reflection and Sound Focusing. *AIP Adv.* 6 (12), 121702. doi:10.1063/1.4968607

Conflict of Interest: The authors declare that the research was conducted in the absence of any commercial or financial relationships that could be construed as a potential conflict of interest.

Publisher's Note: All claims expressed in this article are solely those of the authors and do not necessarily represent those of their affiliated organizations, or those of the publisher, the editors and the reviewers. Any product that may be evaluated in this article, or claim that may be made by its manufacturer, is not guaranteed or endorsed by the publisher.

Advantages of publishing in Frontiers

OPEN ACCESS
Articles are free to read for greatest visibility and readership

FAST PUBLICATION
Around 90 days from submission to decision

HIGH QUALITY PEER-REVIEW
Rigorous, collaborative, and constructive peer-review

TRANSPARENT PEER-REVIEW
Editors and reviewers acknowledged by name on published articles

Frontiers
Avenue du Tribunal-Fédéral 34
1005 Lausanne | Switzerland

Visit us: www.frontiersin.org
Contact us: frontiersin.org/about/contact

REPRODUCIBILITY OF RESEARCH
Support open data and methods to enhance research reproducibility

DIGITAL PUBLISHING
Articles designed for optimal readership across devices

FOLLOW US
@frontiersin

IMPACT METRICS
Advanced article metrics track visibility across digital media

EXTENSIVE PROMOTION
Marketing and promotion of impactful research

LOOP RESEARCH NETWORK
Our network increases your article's readership